

Development of a Microfluidic Platform for Size-Based Enrichment and Immunomagnetic Isolation of Circulating Tumour Cells

by

Hadi Esmaeilsabzali

M.A.Sc., Electrical Engineering, Iran University of Science and Technology, 2006
B. Eng., Biomedical Engineering, Shahid Beheshti University of Medical Sciences, 2003

Thesis Submitted in Partial Fulfillment of the
Requirements for the Degree of
Doctor of Philosophy

in the
School of Mechatronic Systems Engineering
Faculty of Applied Sciences

© Hadi Esmaeilsabzali
SIMON FRASER UNIVERSITY
Summer 2017

Copyright in this work rests with the author. Please ensure that any reproduction or re-use is done in accordance with the relevant national copyright legislation.

Approval

Name: Hadi Esmaeilsabzali

Degree: Doctor of Philosophy

Title: Development of a Microfluidic Platform for Size-Based Enrichment and Immunomagnetic Isolation of Circulating Tumour Cells

Examining Committee:

Chair: Dr. Behraad Bahreyni
Associate Professor

Dr. Edward J. Park
Senior Supervisor
Professor

Dr. Timothy V. Beischlag
Senior Co-Supervisor
Professor

Dr. Ash Parameswaran
Supervisor
Professor

Dr. Bonnie L. Gray
Internal Examiner
Professor
School of Engineering Science

Dr. Yu Sun
External Examiner
Professor
Department of Mechanical & Industrial Engineering
University of Toronto

Date Defended/Approved: August 16, 2017

Ethics Statement



The author, whose name appears on the title page of this work, has obtained, for the research described in this work, either:

- a. human research ethics approval from the Simon Fraser University Office of Research Ethics

or

- b. advance approval of the animal care protocol from the University Animal Care Committee of Simon Fraser University

or has conducted the research

- c. as a co-investigator, collaborator, or research assistant in a research project approved in advance.

A copy of the approval letter has been filed with the Theses Office of the University Library at the time of submission of this thesis or project.

The original application for approval and letter of approval are filed with the relevant offices. Inquiries may be directed to those authorities.

Simon Fraser University Library
Burnaby, British Columbia, Canada

Update Spring 2016

Abstract

Cancer is a leading cause of death worldwide. Efforts to improve the longevity and quality of life of cancer patients are hindered by delays in diagnosis of tumours and treatment deficiency, as well as inaccurate prognosis that leads to unnecessary or inefficient treatments. More accurate biomarkers may address these issues and could facilitate the selection of effective treatment courses and development of new therapeutic regimens. Circulating tumour cells (CTCs), which are cancer cells that are shed from tumours and enter the vasculature, hold such a promise. Therefore, there is much interest in the isolation of CTCs from the blood. However, this is not a trivial task given the extreme scarcity of CTCs in the circulation.

In this thesis, the development of a microfluidic immunomagnetic approach for isolation of CTCs is presented. First, the design, microfabrication, and experimental evaluation of a novel integrated microfluidic magnetic chip for sensitive and selective isolation of immunomagnetically labelled cancer cells from blood samples is reported. In general, to ensure the efficient immunomagnetic labelling of target cancer cells in a blood sample, an excessive number of magnetic beads should be added to the sample. When an immunomagnetically labelled sample is processed through the chip, not only cancer cells but also free magnetic beads that are not bonded to any target cells would be captured. The accumulation of these beads could disrupt the capture and visual detection of target cells. This is an inherent drawback associated with immunomagnetic cell separation systems and has rarely been addressed in the past. Therefore, the design, microfabrication, and characterization of a microfluidic filter for continuous size-based removal of free magnetic beads from immunomagnetically labelled blood samples is presented next. Connected in tandem, the two chips developed in this work form a microfluidic platform for size-based enrichment and immunomagnetic isolation of CTCs. Preclinical studies showed that the proposed approach can capture up to 75% of blood-borne prostate cancer cells at clinically-relevant low concentrations (as low as 5 cells/mL) at an acceptable throughput (200 μ L/min). The retrieval and successful propagation of captured prostate cancer cells is also investigated and discussed in this thesis.

Keywords: BioMEMS; Cancer; Circulating Tumour Cells; Immunomagnetic Cell Separation; Single-Cell Research; Microfluidics

To My Parents, Esmat and Karim

Acknowledgements

I am fortunate to have had Dr. Edward Park as my senior supervisor during my PhD studies. Without his broad interdisciplinary vision, continuous guidance, and capacity to form fruitful collaborations with other researchers, this work would have not been possible. I thank him for giving me the freedom to pursue my research ideas while providing me with constructive directions. I appreciate his encouragement, patience, and support throughout these years.

Dr. Timothy Beischlag has been significantly influential in my PhD research. Working with him helped me in defining the scope of my research and learning the skills and concepts that I would not have known otherwise. He taught me scientific writing and the significance of self-criticism and perseverance in research. I am grateful to him for all the lessons.

I am thankful to Dr. Ash Parameswaran for his original ideas and willingness to advise on microfabrication issues whenever I needed his valuable expertise.

I would like to thank Dr. Nikolai Dechev for his guidance and support during the early stages of my PhD studies. I am also appreciative to Dr. Frank Lee, Dr. Gratien Prefontaine, and the Faculty of Health Sciences for their support and hospitality.

I have been lucky to work with several amazing lab-mates over the past few years. Their accompany made this occasionally bumpy PhD journey enjoyable, and it would not be an overstatement to say I learned something new from each and every of them. Thank you, Kelly Sakaki, Shabnam Massah, Samaneh Khakshour, Jung Keun Lee, Mark Labrecque, Rebecca Moncur, Shazina Khan, Beryl Luk, Mandeep Takhar, Julienne Jagdeo, and Kevin Tam, for your friendship and fun memories.

I cannot begin to express how grateful I am to my parents, Esmat and Karim, and my brothers, Bahram, Shahram, and Kourosh, for their love and support. Hearing their voice was all the motivation I needed to firmly get back to work when I was having a frustrating day in the lab.

Table of Contents

Approval.....	ii
Ethics Statement.....	iii
Abstract.....	iv
Dedication.....	v
Acknowledgements.....	vi
Table of Contents.....	vii
List of Tables.....	x
List of Figures.....	xi
List of Acronyms.....	xiii
Introductory Image.....	xv
Chapter 1. Introduction.....	1
1.1. Background.....	1
1.2. Thesis Outline.....	2
1.3. Motivation.....	2
1.4. Literature Review.....	6
1.4.1. Carcinogenesis, Metastasis, and Circulating Tumour Cells.....	6
1.4.2. CTC Detection and Isolation: Principles and Methods.....	10
Nucleic acid-based methods for CTC detection.....	11
Physical properties-based methods for CTC isolation.....	13
Antibody-based methods for CTC detection and isolation.....	19
1.5. Contributions.....	31
Chapter 2. An Integrated Microfluidic Magnetic Chip for Immunomagnetic Isolation of Cancer Cells.....	34
2.1. Microfluidic Immunomagnetic Cell Isolation.....	34
2.1.1. Background.....	34
2.2. Theory.....	35
2.3. Materials and Methods.....	38
2.3.1. PSMA and Prostate Cancer.....	38
2.3.2. Immunomagnetic Labelling.....	41
Indirect Labelling Using Tetrameric Antibody Complex (TAC) Technology.....	42
Direct Labelling Using Anti-mouse IgG Coated Magnetic Beads.....	42
Indirect Labelling Using Streptavidin-Biotin Interaction.....	43
2.3.3. Microfluidic Magnetic Separation Mechanism.....	44
First-Generation Microfluidic Magnetic Chip.....	44
Second-Generation Microfluidic Magnetic Chip.....	47
2.3.4. Macro-to-Micro Interfacing.....	53
2.3.5. Cell Line and Cell Culture.....	53
2.4. Microfabrication.....	53
2.4.1. Magnetic Component Microfabrication.....	54
2.4.2. Microfluidic Component Microfabrication.....	56

2.5.	Results	59
2.5.1.	Immunomagnetic Labelling Efficiency and Experimental Optimization	59
2.5.2.	Microfabrication	61
	Magnetic Component Microfabrication	61
	Microfluidic Component Microfabrication	64
2.5.3.	Cell Capture Experiments	65
	Experiments Using First-Generation Devices	65
	Experiments Using Second-Generation Devices	67

Chapter 3. A Microfluidic Platform for Size-Based Enrichment and Immunomagnetic Isolation of Rare Cancer Cells from Blood Samples.....78

3.1.	Background	78
3.2.	Continuous Microfluidic Size-Based Particle Separation.....	79
3.3.	Materials and Methods	79
3.3.1.	Magnetically-Enhanced Active Size-Based Cross Flow Filtration (MASCFF)	79
	Background and Theory	79
	Design.....	81
3.3.2.	Deterministic Lateral Displacement (DLD)	82
	Background and Theory	82
	Design.....	83
3.3.3.	Multiorifice Flow Fractionation (MOFF)	85
	Background and Theory	85
	Design.....	87
3.4.	Microfabrication	89
3.5.	Results	90
3.5.1.	Microfabrication	90
3.5.2.	Qualitative Characterization of Efficiency of Filters to Remove Free Magnetic Beads	92
3.5.3.	Quantitative Characterization and Cell Capture Experiments.....	94
	Experimental Setup and Sample Preparation	94
	Specificity and Sensitivity of MOFF Filter	95
	Effect of Blood Cells on MOFF Filtration Specificity.....	97
	Capture of LNCaP Cells from Spiked Blood Samples	97
3.6.	Summary and Discussion	98

Chapter 4. Retrieval and Propagation of Immunomagnetically Captured Cancer Cells101

4.1.	Background	101
4.2.	Effect of Immunomagnetic Labelling on Viability of LNCaP Cells	101
4.3.	Biocompatibility of the Microfluidic Magnetic Cell Separation System	103
4.4.	Retrieval and Propagation of Captured LNCaP Cells.....	103
4.5.	Summary and Discussion	105

Chapter 5. Conclusion and Future Work 106

References.....	112
Appendix A. Machine Vision-Based Localization of Nucleic and Cytoplasmic Injection Sites on Low-Contrast Adherent Cells	144
Appendix B. Localized, Macromolecular Transport for Thin, Adherent, Single Cells Via an Automated, Single Cell Electroporation Biomanipulator	156
Appendix C. COMOSL CFD Optimization of the Microfluidic Manifold Structure	168

List of Tables

Table 3.1	Summary of the filtration performance of MASCF, DLD, and MOFF designs	100
-----------	---	-----

List of Figures

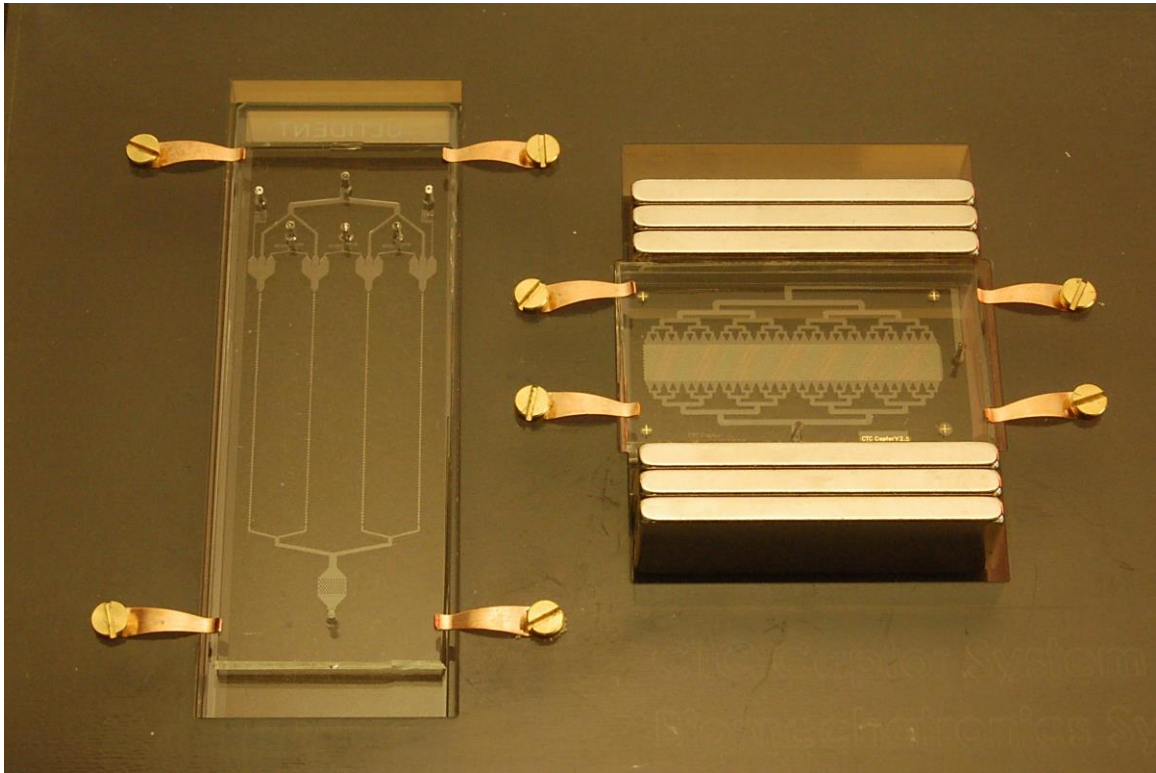
Figure 1.1 Simplified framework for the metastatic cascade.....	9
Figure 1.2 SEM view of different size-based filters.....	14
Figure 1.3 Schematic of different microfluidic size/deformity-based filters.....	15
Figure 1.4 Layout of various microfluidic size-dependent hydrodynamic filters.....	16
Figure 1.5 The DEP/G-FFF principle for cell separation.....	18
Figure 1.6 Automated quantitative FISH analysis of CTCs.....	22
Figure 1.7 Various direct and indirect methods for immunomagnetic labeling approaches.....	25
Figure 1.8 A microfluidic bio-chip for immunomagnetic capture of CTC.....	27
Figure 1.9 Microfluidic magnetophoretic isolation of cancer cells in a microchannel.....	28
Figure 1.10 Microfluidic adhesion-based isolation of CTCs.....	30
Figure 2.1 Simplified demonstration of different forces acting on a magnetically labelled cell in a microfluidic device.....	35
Figure 2.2 The molecular structure of PSMA.....	39
Figure 2.3 Bi-specific TAC-mediated labelling of target cancer cells using magnetic particles.....	42
Figure 2.4 Direct labelling using Pan Mouse IgG coated beads.....	43
Figure 2.5 Indirect labelling using the streptavidin-biotin interaction.....	43
Figure 2.6 The first-generation integrated microfluidic-magnetic chip.....	45
Figure 2.7 COMSOL simulation of the magnetic component of the integrated chip.....	46
Figure 2.8 Photographs of different first- and second-generation magnetic chips.....	48
Figure 2.9 Different microtrap shapes and configurations studied in second-generation prototypes.....	49
Figure 2.10 General structure of different bifurcation designs.....	50
Figure 2.11 COMSOL CFD results showing streamlines in a second-generation microfluidic component.....	52
Figure 2.12 Schematic of a microfluidic component with an embedded herringbone mixer.....	52
Figure 2.13 The fabrication process for the magnetic component.....	56
Figure 2.14 The fabrication process for the microfluidic component.....	57
Figure 2.15 The fabrication process for the microfluidic component with embedded herringbone mixer.....	59
Figure 2.16 LNCaP cells immunomagnetically labelled using different direct and indirect approaches.....	61
Figure 2.17 SEM view of different permalloy microtrap structures.....	62
Figure 2.18 SEM EDS elemental analysis of different permalloy structures.....	63
Figure 2.19 AFM and SEM views of the “edge effect” on Sawtooth structures.....	63
Figure 2.20 SEM views of the master SU-8 mold embedded arrays of herringbone mixer.....	64

Figure 2.21 Isolation of immunomagnetically labelled LNCaP cells from a binary cell solution (LNCaP/Jurkat)	66
Figure 2.22 The experimental setup for experiments using second-generation prototypes	68
Figure 2.23 LNCaP cells captured on different magnetic microtrap designs	69
Figure 2.24 Capture efficiency of Sawtooth and Pillar designs	70
Figure 2.25 Effect of an embedded Herringbone mixer on capture efficiency	71
Figure 2.26 Comparison of capture efficiency of different immunomagnetic labelling protocols	71
Figure 2.27 Photograph of the finalized second-generation integrated microfluidic chip	73
Figure 2.28 Capture efficiency for spiked LNCaP cells at very low concentrations	74
Figure 2.29 Accumulation of extra unbonded magnetic beads on the chip	75
Figure 2.30 Capture efficiency for LNCaP cells from spiked and lysed blood samples. .	76
Figure 3.1 The general principle of cross-flow filtration	80
Figure 3.2 A general schematic of a typical MASCFE device.	81
Figure 3.3 The general principle of DLD particle separation.	83
Figure 3.4 Experimental data for calculation of the critical diameter in DLD devices.....	84
Figure 3.5 A schematic of a typical DLD device design.	85
Figure 3.6 The general principle of MOFF.	86
Figure 3.7 A schematic of a typical MOFF device.....	88
Figure 3.8 COMSOL CFD simulation to optimize hydraulic resistance values at the MOFF microchannel outlet.	89
Figure 3.9 Photographs of different microfluidic filter prototypes.	90
Figure 3.10 Different SEM views of a MASCFE SU-8 mold.	91
Figure 3.11 Different SEM views of DLD and MOFF filters.	92
Figure 3.12 Examples of target cell loss in MASCFE filters.	93
Figure 3.13 DLD malfunction due to accumulation of air bubbles within the device.	94
Figure 3.14 The experimental setup and the microfluidic platform for size-based enrichment and immunomagnetic isolation of cancer cells from spiked blood samples.	95
Figure 3.15 Specificity and sensitivity analysis of MOFF filter.....	96
Figure 3.16 Capture efficiency of the platform for labelled LNCaP cells seeded in blood sample	97
Figure 3.17 Capture efficiency of the platform for LNCaP cells spiked in blood sample	98
Figure 4.1 Effect of immunomagnetic labelling on LNCaP cells	102
Figure 4.2 Validation of the biocompatibility of the magnetic chip	103
Figure 4.3 Retrieval and propagation of captured LNCaP cells on the magnetic chip ..	104

List of Acronyms

CTC	Circulating tumour cells
SCE	Single cell electroporation
MDR	Multidrug resistance
CSC	Cancer stem cells
PB	Peripheral blood
PFS	Progression free survival
OS	Overall survival
EMT	Epithelial to mesenchymal transition
ECM	Extracellular matrix
GF	Growth factor
HIF	Hypoxia-inducible factor
WBC	White blood cell
RBC	Red blood cell
PCR	Polymerase chain reaction
CK	Cytokeratin
EpCAM	Epithelial cell adhesion molecule
PSA	Prostate-specific antigen
CEA	Carcinoembryonic antigen
EGFR	Epidermal growth factor receptor
FISH	Fluorescence in situ hybridization
AMD	Automated digital microscopy
FAST	Fiber-optic array technology
EPISPOT	EPithelial ImmunoSPOT
ELISPOT	Enzyme-linked immunosorbent spot
MFD	Magnetic flux density
FDA	Food and Drug Administration
PSMA	Prostate-specific membrane antigen
PCa	Prostate Cancer
ADT	Androgen-depravation therapy
mCRPC	Metastatic castration-resistant prostate cancer
QOL	Quality of life
AR	Androgen receptor

AR-V7	Androgen receptor splice variant 7
PDMS	Polydimethylsiloxane
CFD	Computational fluid dynamics
SEM	Scanning electron microscopy
EDS	Energy dispersive X-ray spectroscopy
XPS	X-ray photoelectron spectroscopy
CMP	Chemical mechanical polishing
AFM	Atomic force microscopy
BSA	Bovine serum albumin
EDTA	Ethylenediaminetetraacetic acid
PBS	Phosphate-buffered saline
GFP	Green fluorescent protein
MASCFF	Magnetically-enhanced active size-based cross flow filtration
DLD	Deterministic lateral displacement
MOFF	Multiorifice Flow Fractionation
DRIE	Deep reactive ion etching
ICC	Immunocytochemistry
DAPI	4',6-diamidino-2-phenylindole
MET	Mesenchymal to epithelial transition
DEP	Dielectrophoresis
FDA	Food and Drug Administration



Chapter 1.

Introduction

1.1. Background

Biomedical research may significantly benefit from the exceptional potential of single-cell studies. By avoiding inaccuracies that are inherent to data-averaging over cell cultures, which are caused by intercellular signaling or heterogeneity of cell populations, single-cell studies can contribute to a clearer understanding of cells and their functions. Such a knowledge may lead to a range of unique solutions for substantial human health issues [1]. Considering the necessity of developing efficient tools for single-cell studies, my PhD research was focused on two areas: 1) development of a novel image processing algorithm for automated localization of injection sites on thin adherent cells for robotic single-cell electroporation/injection purposes, and 2) development of a novel microfluidic platform for size-based enrichment and immunomagnetic isolation of circulating tumour cells (CTCs) from blood samples.

During my PhD studies, I was initially involved in the development of an automated robotic single-cell electroporation (SCE) system. In particular, I proposed the necessary problem of automated machine vision-based localization of electroporation sites on the nucleus as well as the cytoplasm of thin adherent cells, and developed and implemented a novel image processing algorithm for localization of such sites on these cells. I published the results of this work in *Medical & Biological Engineering & Computing* [2], which can be found in Appendix A. We then demonstrated the ultimate practical application of this algorithm for fully automated *in vitro* electroporation of single 3T3 fibroblasts using a robotic SCE manipulator that had been developed by Dr. Kelly Sakaki, my then lab-mate. We published the results of this work in *IEEE Transactions on Biomedical Engineering* [3], which can be found in Appendix B.

Following the completion of this project, I became interested in the CTC isolation problem. For the rest of my PhD studies, my research was focused on CTCs, their clinical and biological significance, and their isolation from blood samples. This thesis presents this part of my PhD research.

1.2. Thesis Outline

This thesis is composed of five chapters. The rest of Chapter 1 discusses the clinical and biological significance of CTCs and reviews different principles and techniques used for detection and isolation of these cells from blood samples. Then, in Chapter 2, the development of a novel integrated microfluidic magnetic chip for immunomagnetic isolation of cancer cells is presented. Chapter 3 describes the development and integration of a microfluidic filter for continuous size-based removal of free magnetic beads from immunomagnetically labelled blood samples. Chapter 4 reports the retrieval and propagation of captured cancer cells. Finally, Chapter 5 concludes the thesis and discusses the future works.

1.3. Motivation

Cancer is the second leading cause of death worldwide. In 2015, cancer claimed 8.7 million lives, and this number is expected to pass 13 million by 2030 [4]. However, according to the World Health Organization, at least 30% of these deaths are preventable. Early diagnosis and treatment of the primary tumour, which may prevent its subsequent metastasis, and development of more efficient therapies against the metastasized cancer, which accounts for 90% of cancer-related mortalities, are believed to be the key factors to win the *War on Cancer*. In particular, the efficiency of existing anti-metastatic therapies is mainly hampered by the heterogeneity of cancer cells as well as their peculiar interactions with the secondary host organs. Personalized targeted therapies that can be prescribed dynamically and according to the existing molecular characteristics of cancer cells may significantly improve the quality of treatment. However, even if the metastatic lesions are detected and anatomically accessible for sampling, performing multiple regular biopsies is an impractical task. CTCs, which are cancer cells that are actively and/or passively detached from primary or secondary tumours and entered the circulation, could be ideal specimens that: a) can be obtained regularly and less invasively and b) provide the real-time single-cell-level data required for effective identification of therapeutic targets [5] [6].

CTCs can also be readily exploited in basic cancer research where the majority of the existing knowledge is based on mice models and cancer cell lines, both of which may not correctly represent the cancer problem [7]. For instance, single cell profiling of CTCs from breast cancer patients and its comparison with several breast cancer cell lines has

shown considerable molecular differences between these cells, questioning the usefulness of studies performed on immortalized cell lines [8]. Furthermore, histological analysis of the primary tumour samples may not be as useful, given that metastatic cancer cells could be genetically different from primary tumour cells. For example, CTCs detached from HER2-negative primary tumours in some breast cancer patients become HER2-positive, indicating that cancer cells may experience further mutations after breaking off from the primary tumour [9]. Hence, studying CTCs can shed more light on the transient and still-not-clearly-understood phase of cancer by which the malignancy metastasizes to other organs. CTCs may also improve our understanding about the natural selection process of multidrug resistance (MDR) and how it relates to major events in the metastatic cascade or stem cell properties in CTCs [10] [11]. The identification and characterization of CTCs with characteristics of cancer stem cells (CSC) that may represent the true progenitors of metastatic tumours has now become a topic of attention [12]. The CSC model for carcinogenesis and metastasis is built on a hierarchical framework which predicts that tumour-derived cells with tissue progenitor characteristics, colloquially termed CSCs, can initiate and drive tumour spread through their intrinsic self-renewal capacity and the ability to maintain the tumour by giving rise to different types of non-CSCs [13]. It has been suggested that it is during the differentiation of CSCs that epigenetic factors could lead to the emergence of chemorefractory cells that are responsible for the MDR effect in many cancers [11]. Although it has been assumed that tumour-initiating CSCs are extremely rare (0.0001- 0.1% of tumour cells) [14], some studies have identified CSC properties in up to 25% of tumour cells [12]. A possible explanation for such a discrepancy is the difference in xenograft models used to assess the tumorigenic capability of these cells. Identification and molecular analysis of circulating CSCs, which could be different from those residing in primary tumours, may provide additional insight into the nature of these cells. If accepted, the CSC model may realign many of the previously held notions on the classic clonal evolution theory of cancer development. A direct consequence of such a model would state that by targeting CSCs, metastasis can be managed [15] [16].

Aside from their applications in basic and translational cancer research, the quantitative and qualitative characterization of CTCs found in the peripheral blood (PB) has been proposed as an accurate and less invasive clinical biomarker for diagnostic, prognostic, and pharmacological purposes [17] [18] [19] [20] [21]. The haematogenous

spread of cancer can be an early event in carcinogenesis, meaning that the growth of a primary tumour and a metastatic lesion could happen in parallel [22]. For instance, in nearly 5% of breast cancer patients, at least one overt metastasis is detectable at the time of initial tumour diagnosis, while 30-40% of patients may have developed occult metastases [20]. Thus, CTCs may be detected in the PB even before the symptoms of the primary tumour are revealed and can be used for early diagnosis of cancer [17] [20] [23]. Several prospective studies on patients with metastatic cancers of different organs have indicated that a higher number of CTCs at the baseline or any time during the therapy is associated with a shorter progression free survival (PFS) and overall survival (OS) [20] [21] [24] [25] [26] [27] [28] [29]. The prognostic value of CTCs has also been investigated in patients with primary non-metastatic cancers, where the presence of as low as one CTC per a 7.5-mL sample prior to tumour resection has been correlated with a reduced OS [30]. For such patients, CTC count may also be useful as a surrogate marker to assess the relapse risk after tumour removal [31]. CTC counts can also be exploited as a surrogate endpoint to evaluate the efficiency of anti-metastasis therapies [32]. In other words, instead of using serological markers that occasionally lack the required sensitivity and specificity (e.g., due to a prolonged “spike” that is often observed in the marker level after administration of the drug [33]), or waiting for up to months to determine the response of a particular treatment using radiographic imaging, regular monitoring of CTC counts has been suggested as a rapid and accurate method for evaluating the treatment.

Investigating the clinical significance of the frequency of CTCs has initially been the major focus of many studies. However, it is worth noting that genomic and proteomic characterization of CTCs offers far more valuable information than the mere CTC frequency does and could ideally be used in precision oncology for development of individualized therapeutic regimens. For instance, while the SWOG S0500 trial results showed that switching to an alternative line of therapy solely based on persistent high CTC frequency does not benefit patients [34], other studies have lately demonstrated that molecular analysis of CTCs and selecting the treatment accordingly may indeed improve the survival of prostate cancer patients [35]. Moreover, as mentioned earlier, it has been proposed that a subpopulation of CTCs is the precursor for the formation of subsequent secondary tumours in distant sites [5]. The over-expression of vimentin, putatively known as an epithelial to mesenchymal transition (EMT) marker, correlates well with accelerated tumour growth, invasion, and poor prognosis [36]. In addition, CTCs expressing CD44, but

not all CTCs, have been associated with a lower OS and increased metastatic activity of cancer [37]. Recently, it has been suggested that true metastasis initiating cells may have an intermediate phenotype partially displaying both epithelial and mesenchymal qualities [5]. Thus, not only their frequency but also the molecular determinants of individual CTCs can be screened and evaluated as potentially more accurate biomarkers for early detection, PFS, OS, and treatment efficiency [17].

Since PB sampling is performed easily, CTCs can be frequently counted and analyzed, without the increased invasiveness, cost, and often low efficiency associated with other clinical assays. For instance, in a study involving 138 breast cancer patients, inter-reader variability for the radiological assessment of the tumour and the associated CTC count has been reported to be 15.2% and 0.7%, respectively, which indicates the *precision* of CTCs as clinical biomarkers [38]. Moreover, the median OS of patients with radiologically favorable prognosis but unfavorable CTC counts has been significantly shorter compared to that of patients with the same radiological prognosis and favorable CTC counts (15.3 versus 26.9 months). Also, patients with unfavorable radiological prognosis but favorable CTC counts has shown significantly longer OS compared with those patients with the same radiological prognosis and unfavorable CTC counts (19.9 versus 6.4 months). Such findings support the *accuracy* of CTCs for cancer prognosis.

Considering the aforementioned applications for CTCs, two main subjects are now being increasingly studied: a) further characterization of the correlation between CTCs and cancer diagnostic, prognostic, and pharmacodynamic indices, and b) development of more efficient techniques for detection, isolation, and retrieval of CTCs from blood samples. In the next section, these techniques are classified and reviewed according to their basic working-principles. The advantages and potential drawbacks of each method are outlined and discussed. CTC detection and isolation is a highly interdisciplinary problem. Hence, in addition to physical, chemical, and engineering expertise, an understanding of the biological aspects involved in this problem is necessary. Accordingly, a brief biological background about the CTC problem has been provided first.

1.4. Literature Review

1.4.1. Carcinogenesis, Metastasis, and Circulating Tumour Cells

The formation and spread of a cancer is a complex process that is not fully understood. Whether it is triggered by internal stimuli (e.g., random or inherited mutations, hormones, or immune conditions) or environmental/acquired factors (e.g., tobacco, diet, radiation, or viral infections), a cancer results from the accumulation of multiple mutations within the malignant cells. In majority of cases, it is not the primary tumour but its spread to distant organs that eventually compromises the function of the host organ and is associated with mortality. For instance, the average 5-year survival rate for patients with localized and metastatic prostate cancers is 100% and 29%, respectively [39]. Hence, although significant improvements have been achieved in curing the localized cancer (e.g., tumour resection followed by systematic post-surgery adjuvant therapies), few efficient treatments for the metastasized disease have been devised. In spite of the vast amount of knowledge acquired about the metastatic cascade during the last two decades, there still remain many unknowns about this process [40]. In general, the carcinogenesis, including the primary tumour formation and its subsequent metastasis, can be considered as a Darwinian process consisting of a sequence of events that can be summarized in four broad categories (see Figure 1.1):

1) Primary tumour formation and growth: The formation of a primary tumour essentially results from: i) exceeding access of mutant cells to growth signals (i.e. either the ability to independently synthesize the required growth factors (GF), such as TGF α in sarcoma, or the over-expression of GF receptors on the cell surface, such as HER2/neu in mammary carcinomas), and ii) their insensitivity to inhibitory signals (e.g., disruption of pRb pathways, resulting in malfunctioning of growth-inhibitory signals such as TGF β [40]. Together, these mutations result in an abnormal pattern of mitotic cell division and evasion of cell death by blocking apoptosis (i.e. the programmed cell death) or regulation of autophagic and necrotic mechanisms, which leads to the formation of a solid tumour [41]. Once the growing primary tumour reaches a certain size, rapidly dividing mutant cells surpass the available nutrition and oxygen (i.e. hypoxia), which results in neovascularisation triggered by hypoxia-inducible factor (HIFs). HIFs, along with other pathways that also control the expression of GFs in tumour cells, trigger the expression of angiogenesis-promoting factors, such as VEGF and angiopoietin-1 and -2 [42] [43].

II) Epithelial to mesenchymal transition (EMT) and Intravasation: It has been shown that the activation of HIF and the subsequent expression of angiogenesis and a variety of other factors (e.g., laminin), through pleiotropic effects, result in the reduced expression of E-cadherin. The downregulation of E-cadherin reduces the cell-cell adhesion and increases the motility of tumour cells [44]. This is a critical event in the EMT, which is a phenotypic change in tumour cells and a crucial stage in the metastatic cascade [45] [46]. The EMT process is further characterized by a change in the expression of cell-ECM adhesion molecules (e.g., integrins), downregulation of epithelial markers (e.g., cytokeratin), and upregulation of mesenchymal markers (e.g., vimentin), although the relative extent of these phenotypic alterations in cancer cells is somewhat unclear. The EMT process in metastatic cancer cells is highly complex and still mostly unknown; however, it is believed that it is a hallmark of metastasis and is closely correlated with CSCs and, perhaps, MDR [47] [10] [11] [36]. It has been proposed that EMT is able to induce CSC properties in non-CSCs [48].

Following the EMT process, cancer cells adopt and exhibit a motile, invasive phenotype, which increases the likelihood that they detach from the tumour body and migrate within the neighboring tissue (i.e. local invasion). The invasion process is governed by complex molecular mechanisms that predominantly result in cytoskeleton modification, localized proteolysis of the surrounding tissue, and cell-ECM dynamic interactions that mediate the motility of cancer cells (either as a single cell or an aggregate of cells) through tissues [49]. The invasive phenotype of some cancer cells then enables them to enter the circulation by traversing the basement membrane, interstitial spaces, and endothelial barriers of the internal network of blood vessels formed by the angiogenesis. This process, known as intravasation, ultimately allows the invading cancer cells to initiate regional or distant metastases. It is worth reemphasizing that, contrary to canonical models, intravasation could be an early event in carcinogenesis, even before the primary tumour is diagnosed [22]. This has been investigated in a pancreatic cancer model, where it has been shown that EMT and dissemination of cancer could happen during the pre-malignancy stage when the primary tumour has not entirely developed [50].

III) Hematogenous spread of cancer: Once the tumour cells enter the circulation, inadequate or inappropriate cell-matrix interactions could result in disintegration of the majority of cells through a process known as anoikis. However, it has been suggested that the expression of anoikis inhibitors, such as the protein XIAP, in a subpopulation of these

cells makes them resistant to apoptosis [51]. Surviving CTCs, which are believed to be non-proliferative in the circulation [52], travel to other parts of the body until, due to either their different size or molecular adhesion, they are arrested in capillary beds at specific organs [53] [49] [40]. It should be noted that a majority of secondary tumours are formed at organs (e.g., bone, liver, lung, and brain) that are not directly connected to lymph nodes, where cancer cells floating in lymph vessels are collected. This implies that if cancer cells only enter the lymph vessels, reach a lymph node, and establish a limited metastasis there, these lesions will later shed other tumour cells into the blood circulation. Thus, cancer cells that are carried by the blood circulation, i.e. CTCs, are associated with the majority of fatal metastatic malignancies.

IV) Extravasation and secondary tumour formation: Tumour cells that are already captured at capillary beds, penetrate through the layer of endothelial cells and invade the host organ by crossing the interstitium and parenchyma [54]. The cancer cells then undergo another phenotypic alteration known as the mesenchymal to epithelial transition (MET), which, contrary to the EMT process, is associated with the reappearance of epithelial traits in those cells that have successfully invaded and inhabited the host organ. Similar to EMT, the MET process is also not fully understood, and different molecular mechanisms have been suggested or are still being investigated [55] [56].

Whether or not a cancer cell that has settled in the secondary organ regains its ability to proliferate and colonize in the new environment is contingent upon many unknown and known parameters, which mainly include the molecular makeup of the cancer cell, its new environment, and their interactions. These three factors collectively determine all major qualities (e.g., the ability to synthesize the required GFs) that cancer cells should possess to initiate the growth of a secondary micrometastasis, which is defined as an aggregate of tumour cells smaller than 2 mm but larger than 0.2 mm in diameter. Some *in vivo* observations in murine models has suggested that the micrometastasis formation may also begin intravascularly once the successful cancer cells are arrested on the vascular endothelium [57]. A micrometastasis then can grow to become a macrometastasis (i.e. a secondary metastatic tumour larger than 2 mm in diameter) provided that enough oxygen and nutrients are accessible, which requires the angiogenesis in the secondary tumour [49] [58].

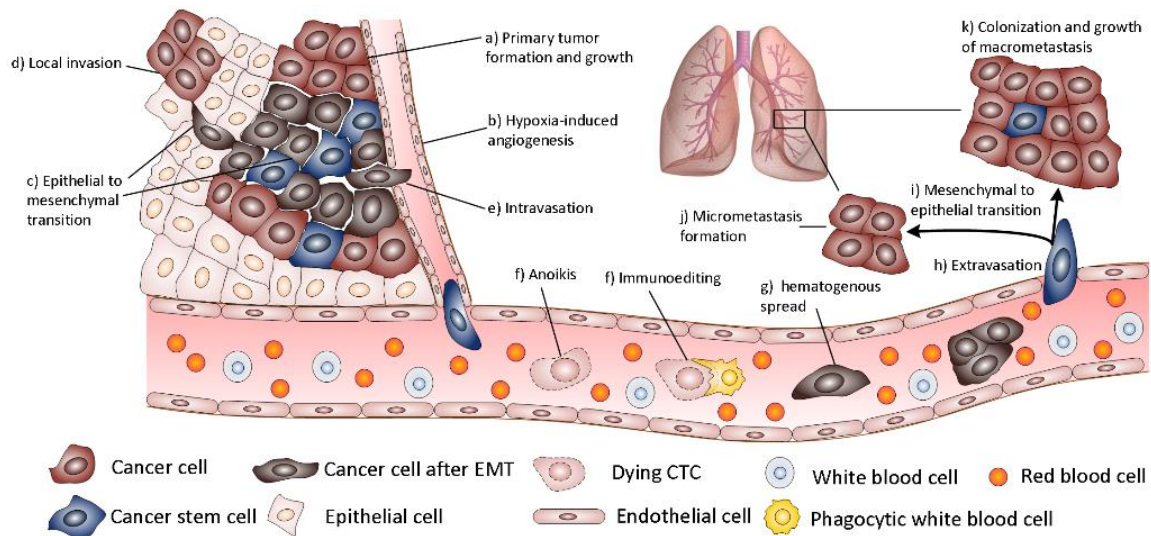


Figure 1.1 A simplified framework for the metastatic cascade: I) The formation and growth of a primary tumour within an epithelial tissue is often accompanied by hypoxia-induced angiogenesis, which allows the rapidly dividing tumour cells to have access to oxygen and required nutrition. The primary tumour itself is composed of a heterogeneous population of cells, some of which may display stem cell properties. II) Cancer cells in the primary tumour may undergo EMT, which enables them to become more invasive. Such a phenotypic modification along with a series of complex pathways, which are mainly responsible for reduced cell-extracellular matrix (ECM) adhesion, increase the motility of cancer cells and set the stage for local invasion and intravasation. III) Once tumour cells enter the circulation, majority of them will be destroyed by anoikis or the immune system. IV) At some point, which is believed to be determined by specific physical and molecular interactions between CTCs and the secondary host organ (e.g. lung), surviving CTCs, which may have stem cells properties, leave the circulation. These cancer cells then experience a series of phenotypic changes, which results in the colonization of the host organ and the formation of a micrometastasis or a macrometastasis.

It should be noted that in addition to the naturally occurring preoperative spread of CTCs from the primary or secondary neoplasms, cancer cells could also enter the circulation during the surgical resection of the tumour or from its microscopic residues (i.e. minimal residual disease (MRD)) after the surgery [20]. Regardless of the mode by which they enter the circulation and considering the aforementioned framework, CTCs may have different fates:

- 1) Anoikis, disintegration by immunoediting, or transition to a dormant state while remaining in the circulation [59],
- 2) Cell death following extravasation,

- 3) Forming occult micrometastases and becoming dormant for a long period of time (5-25 years) without subsequent aggressive proliferation (possibly due to deficient angiogenesis) [60],
- 4) Successfully developing a malignant macrometastasis.

Hence, the metastatic process is inefficient, and only the “fittest” CTCs end up initiating a metastatic tumour. It is believed that a tumour on average throws $\sim 1 \times 10^6$ cells/gram of tumour into the circulation daily. However, the majority ($\sim 85\%$) of CTCs undergo anoikis and generally will be lysed within a few hours after intravasation [61]. Only a small fraction ($\sim 0.1\%$) may remain alive in the circulation after 24 hours, among which only a few cells ($< 0.01\%$) are progenitors of a metastatic tumour [62]. Thus, although CTCs are quite rare, their spread in the circulation is a necessary condition for cancer metastasis [20].

1.4.2. CTC Detection and Isolation: Principles and Methods

Two factors make the detection and isolation of CTCs challenging: i) CTCs are rare in the circulation of cancer patients and ii) there is no one marker that can reliably and efficiently distinguish these cells from other blood-borne cells. Herein, the word *detection* refers to direct or indirect identification of CTCs in a sample, while the word *isolation* indicates the separation of CTCs from all other cells in a sample. To exploit the full potential associated with CTCs, high-purity isolation of viable CTCs is as important as their detection. A variety of techniques have been developed for these purposes [63] [64] [65]. Based on their basic working-principles, in this section, different CTC detection and isolation methods have been classified into three major categories; namely, nucleic acid-based, physical properties-based, and antibody-based.

Due to the extremely low frequency of CTCs compared to blood cells, such as white blood cells (WBC) ($\sim 7 \times 10^6$ cells/mL), red blood cells (RBC) ($\sim 5 \times 10^9$ cells/mL), and platelets ($\sim 3 \times 10^8$ cells/mL), an initial enrichment step may precede some of the CTC detection and isolation methods. The enrichment should be considered as a preliminary sample preparation step, by which the majority of blood cells are removed from the sample to improve the relative concentration of CTCs. The enriched sample is then processed further for detection or isolation of CTCs. Common methods for sample enrichment include density gradient centrifugation, RBC lysis, positive or negative immunomagnetic

separation, and size-based filtration. The first two methods eliminate RBCs and platelets from the sample, leaving CTCs and WBCs for further processing in the subsequent steps. Density gradient centrifugation is based on the lower density of CTCs and nucleated blood cells (i.e. WBCs) and uses a density gradient medium to separate these cells of similar density from other blood constituents. Common issues in CTC enrichment by this method are the entrapment of CTCs within RBCs and the mixing of blood with the gradient medium during the layering process, both of which may result in CTC losses. The latter issue can be partly addressed by placing a porous membrane on top of the gradient media to prevent the mixing (e.g., OncoQuick®, Greiner Bio-One, Germany) [63]. Another variation of sample enrichment by centrifugation is enabled by RosetteSep™ (STEMCELL Tech., BC, Canada), which removes RBCs and WBCs from the sample. A mixture of antibodies that specifically crosslink RBCs to each other and to WBCs are used to form cell rosettes consisting of multiple RBCs and WBCs. Due to the higher density of these clusters, they can be effectively separated from CTCs. A comparison of this approach and a regular density gradient method has favoured the RosetteSep™ system [64]. Sample enrichment can also be performed by RBC lysis. Although CTC loss also happens during this process, a comparison between gradient centrifugation and RBC lysis has favoured the latter approach [65]. Superior enrichment results can be obtained using immunomagnetic and size-based methods that are employed to remove both RBCs and WBCs. The basic working-principles used in these methods are also exploited in CTC isolation methods.

Nucleic acid-based methods for CTC detection

Nucleic acid-based methods identify specific DNA or mRNA molecules in the sample to indirectly detect the presence of CTCs in a sample. To this end, specific primers are employed in polymerase chain reaction (PCR) to target known DNA or mRNA (i.e. cDNA) molecules that are extracted from the enriched sample and supposedly associate with CTC-specific genes. These genes either code for tissue-, organ-, or tumour-specific proteins or polypeptides, or, more specifically, contain known mutations, translocations, or methylation patterns found in cancer cells [66].

Owing to the fundamental amplification principle of PCR, the nucleic acid-based approach offers the highest sensitivity for CTC detection [67] [68]. It can effectively pick out the signal from an extremely small amount of the marker in the sample, meaning that a single CTC can be detected in a large sample volume (e.g., 1 CTC in $5-10 \times 10^6$ nucleated

blood cells or >5 mL of blood). CTC detection using mRNA molecules is generally more effective. Free DNA molecules, which could have been released by necrotic or apoptotic CTCs, are stable in the circulation and can affect the PCR result and produce false-positive detections. Contrarily, mRNA molecules are unstable and will be rapidly degraded in the circulation. Hence, they can be associated with the presence of living CTCs for the most part, which makes them a superior marker for CTC detection. Accordingly, reverse transcription PCR (RT-PCR) is the major technique employed for nucleic acid-based detection of CTCs. Multiplex RT-PCR assays, such as commercially available AdnaTest kits (AdnaGen, Germany) in which the expression of multiple transcripts can be measured simultaneously, have also been used for this purpose [69]. Considering the genetic heterogeneity of CTCs, a multiplex PCR assay may provide improved sensitivity and specificity rates [70].

A crucial factor that dictates the efficacy of a nucleic acid-based approach is the specificity of the selected marker. Cancers of epithelial tissues constitute 85% of cancers. As such, epithelial-specific genes, such as those coding for different subtypes of cytokeratin (CK, an epithelial-specific intracytoplasmic protein) and epithelial cell adhesion molecule (EpCAM, a cell-surface glycoprotein), which should normally be absent in the PB, are among the most widely used tissue-specific markers. Organ-specific markers, such as genes coding for prostate-specific antigen (PSA) (prostate), mammaglobin (breast), and MUC-1 (breast, pancreatic, intestinal, and other glandular cancers), as well as tumour-specific markers (e.g., carcinoembryonic antigen (CEA), epidermal growth factor receptor (EGFR), and HER-2 genes) have also been employed [70] [71].

Nucleic acid-based CTC detection offers impressive sensitivity, yet its specificity reduces the overall accuracy of this approach. False-positive signals from tissue- and organ-specific markers could legitimately originate from a small number of non-cancerous cells that have entered the circulation due to inflammation, invasive diagnostic biopsies, or during the tumour resection surgeries [72]. Moreover, none of the markers that have been employed so far are entirely CTC-specific, and studies have confirmed that they can also be detected in blood cells. For instance, the expression of CK-19, a major marker used for CTC detection, has also been observed in immune cells [73]. Another issue that affects the specificity of these methods paradoxically arises from their high sensitivity. Since a tiny amount of mRNA or DNA in the sample can potentially be detected by this technique, sample contamination, illegitimate transcription (i.e. ubiquitously very low

amount of any gene in any cell type) [74], and pseudogenes (i.e. genes lacking intronic sequences) can unfavourably be amplified, causing false-positive results. This problem can be addressed using quantitative real-time PCR (qRT-PCR), in which a cut-off value can be set to distinguish between transcripts from tumour and non-tumour cells. However, the selection of the cut-off value poses another challenge, as the level of transcripts in different subjects and between different samples is variable and cannot be estimated easily and reliably [73]. The aforementioned issues emphasize the necessary role of a truly CTC-specific marker that can improve the specificity and sensitivity of nucleic acid-based and, as will be discussed later, antibody-based methods. Nonetheless, even if such optimal markers are found, nucleic acid-based methods have a major inherent drawback: CTCs have to be lysed before the PCR process, which prevents their direct observation, enumeration, and further analysis.

Physical properties-based methods for CTC isolation

Physical properties of cells, including size, mechanical plasticity, and dielectric properties, can be exploited to isolate CTCs from the blood.

Isolation of CTCs based on size and mechanical plasticity

Size-based isolation mainly relies on the larger size of CTCs (20-30 μm) compared to that of blood cells (8-12 μm). Based on this difference, several approaches have been proposed and include size-based membrane filters, size/deformation-based microfluidic chips, and size-based hydrodynamic methods.

In its simplest form, size-based isolation of CTCs has been realized using track-etched polycarbonate filters [75] (see Figure 1.2.a). The filter is a porous membrane containing numerous randomly distributed 8- μm -diameter holes that allow blood constituents to cross but capture the supposedly larger CTCs. Microfabrication techniques have been used to build microfilters with controlled distribution, size, and geometry of the pores (see Figure 1.2.b and c) [76] [77] [78]. In addition to producing precise dimensions, microfabrication allows the integration of sensing or manipulation mechanisms within the filter [77]. Although simple and easy-to-use, membrane filters do not offer a high purity and capture many blood cells (e.g., up to 3000 WBCs from a 1-mL sample [76]). Hence, they are often used as an enrichment step preceding nucleic acid- or antibody-based detection methods.

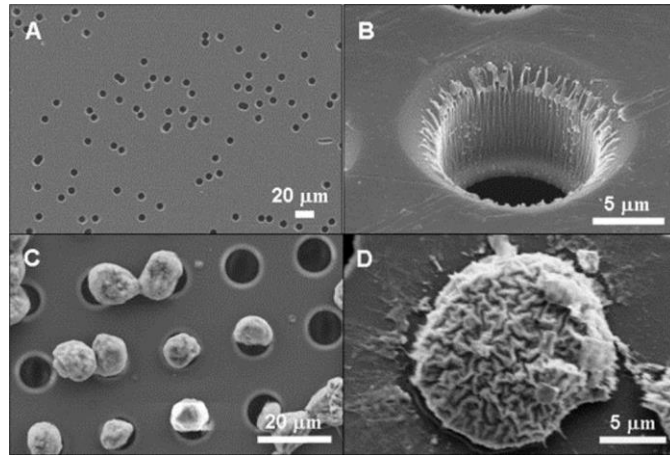


Figure 1.2 Scanning electron microscopy (SEM) images of: (a) commercial track-etched membranes. The random distribution of pores results in the formation of larger holes by fusion of neighboring holes. (b) A microfabricated hole in a parylene membrane filter. (c) Captured cells on a parylene membrane with controlled distribution and size of holes. (d) SEM view of a captured CTC [77].

Size-based isolation of CTCs can be performed in a microfluidic setting, where the integration of precisely defined topography of micro-structures (traps) with the laminar flow in microchannels offers novel solutions for cell separation [79]. In addition to size disparity, the difference in mechanical properties of CTCs and blood cells has often been exploited in such devices. While the inherent deformability and smaller size of blood cells allow them to easily pass through micron-sized barriers (e.g., capillaries), CTCs that are presumably larger and stiffer might be captured. Several methods have been proposed to realize this principle (see Figure 1.3). For instance, in a pool-dam structure consisting of a series of pools that are partially connected by micron-sized gaps (Figure 1.3.a), the width of each gap can be designed so that different cells, i.e. CTCs, WBCs, and RBCs, are filtered by the associated dam and captured in corresponding pools [80]. Despite the promising results reported in the preliminary studies (e.g., recovery rate of 99.9% for high concentrations of cancer cells in spiked samples), this approach has not been further investigated for the isolation of low-abundance cancer cells or in a clinical setting. In another study, a microfluidic chip made of a wide microchannel (60 mm × 30 mm × 20 μm) whose floor is covered by arrays of micron-sized obstacles with four successively decreasing clearances (i.e. 20, 15, 10, and 5 μm) has been reported (Figure 1.3.b) [81]. It has been shown that different cancer cells with different sizes can be captured at different locations along the device, while majority of blood cells can move through.

In a more efficient size-based microfluidic approach, arrays of crescent-shaped traps composed of three adjacent micro-pillars have been used to capture CTCs from the whole blood (see Figure 1.3.c) [82]. Such a design allows higher flow rates to be used and prevents channel clogging by accumulation of cells and other debris between closely packed obstacles. More importantly, the proposed design enables the isolation of single or double CTCs per each trap, making their automatic vision-based enumeration and analysis practical. By reversing the flow direction, the trapped cells have been retrieved and cultured successfully, showing the ability of this device to isolate viable CTCs.

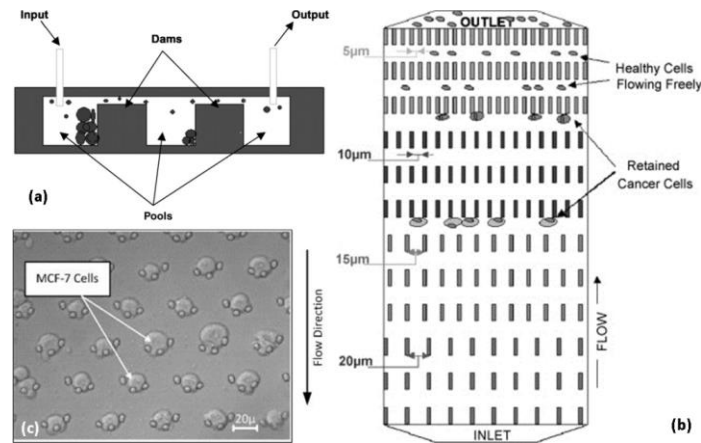


Figure 1.3 (a) Schematic of a pool-dam chip. The decreasing width of gaps between successive pools allows the separation of CTCs in the first pool, followed by WBCs and RBCs in the subsequent pools [80]. (b) Schematic of arrays of obstacles with decreasing distances. Larger CTCs are trapped between the obstacles, while smaller blood cells move freely [81]. (c) Isolation of cancer cells by crescent-shaped traps. The distance between each of the three micropillars is 5 µm which presumably results in the capture of larger cancer cells and not blood cells [82].

Size-dependent hydrodynamic forces acting on cells in a microchannel can also be exploited for CTC isolation. For example, the formation of vortices in lateral reservoirs at both sides of a microchannel has been investigated for the isolation of CTCs [83]. As the sample flows in the microchannel, the interaction of two major hydrodynamic forces (i.e. shear-gradient lift and wall effect lift) pushes the larger cancer cells into the vortices in reservoirs but does not affect the trajectory of smaller blood cells. The recovery rate for this method has been theoretically associated with the size of the target cell and the Reynolds number in the microchannel. The principle of Dean-coupled inertial migration has also been employed for CTC isolation [84] [85] [86]. The principle states that, for a particle in a spiral microchannel, the ratio of the inertial lift force, which is present in any Poiseuille flow, to the Dean drag force, defined as the centrifugal force present in a spiral

microchannel, is proportional to the third power of the particle diameter. Hence, by adjusting the microchannel width and the Reynolds number (i.e. flow rate), different cells migrate to different location along the width of the microchannel and can be subsequently isolated at designated outlets (Figure 1.4.a and 1.4.b). Using this approach, 96% and 92% of cancer and blood cells have been isolated from diluted blood samples, respectively [86].

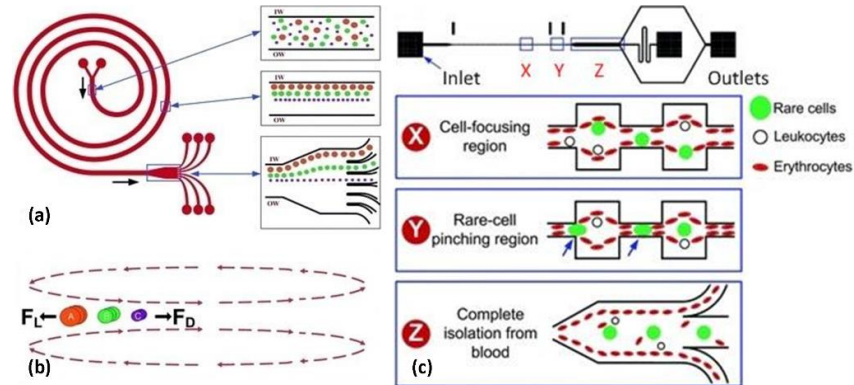


Figure 1.4 (a) The layout of a spiral microchannel used for cell isolation based on Dean-coupled inertial migration. The particles (cells) in the mixture are focused on designated locations as they move within the microchannel and are collected at the associated outputs. (b) The principle of Dean-coupled inertial migration, which explains that the net force experienced by different particles in a spiral microchannel is proportional to the third power of their diameter. Hence, based on their size, particles are equilibrated at certain positions along the width of the microchannel, with larger cells closer to the microchannel wall [85]. (c) Layout of the device used for size-dependent inertial-based isolation of CTCs. Shear-modulated inertial lift force first pushes the cells toward the sidewalls, while a pinching region focuses larger CTCs at the center. When the pinched-flow enters a wider region, blood cells tend to stay close to the sidewalls and CTCs move straight to the bifurcated outlet where different cells are isolated separately [87].

Microfluidic flow fractionation, which combines the effect of hydrodynamic focusing and pinched flow in a microfluidic setting, has also been studied for isolation of cancer cells [87] [88]. The inertial lift force together with a series of contraction–expansion features along the microchannel act on cells to form a pinched flow with smaller blood cells close to the microchannel sidewalls and larger cancer cells in the middle (Figure 1.4.c). Once the pinched flow enters a wider V-shaped outlet, the inertial lift force keeps the smaller blood cells close to the sidewalls, while larger CTCs, driven by the inertial hydrodynamic force, continue their straight trajectory until they are collected at the designated exit (recovery rate: ~80-90%) [87] [88]. Using this approach, CTCs have been isolated from clinical blood samples with 79% sensitivity [88]. Since target cancer cells are not physically trapped in this approach (see Figure 4.c), the sample can be reprocessed through serially

connected devices to improve the purity of isolation or be sent to another device for downstream manipulation [87]. I used the basic principle of multiorifice flow fractionation for development of a size-based filter for pre-processing and enrichment of immunomagnetically labelled blood samples, which is explained in Chapter 3.

Although size-based isolation of CTCs is simple and label-free, the non-specificity of size as a biomarker could affect the efficiency of this approach. Morphological analysis of CTCs has shown that these cells are morphologically heterogeneous with either round or oval shapes and sizes varying from 4 μm to 30 μm [89]. Furthermore, in addition to our experimental observations, other biomechanical studies on primary and immortalized cancer cells show that due to degradation of the stiff cytoskeleton (mainly during EMT), cancer cells become more plastic [90]. Such pathways are responsible for the ability of the CTC to avoid the sieving action of the pulmonary microvasculature. Hence, the fundamental principle used to isolate CTCs in size/deformation-based methods may ignore more invasive, perhaps metastasis-initiating CTCs or CSCs [48].

An antibody-mediated size-based approach has been proposed to address some of these issues [91]. To address the size heterogeneity of CTCs and its overlap with that of WBCs, cancer cells have been labelled with microbeads that specifically attach to surface antigens (e.g., EpCAM). This labeling will increase the size of cancer cells by creating a layer of microbeads on the cell surface, which helps setting a clear cut-off for the size of non-target cells. It has also been proposed that labeling the cancer cells with solid microbeads will reduce the deformation of the cell-microbeads complex and increases the recovery rate (e.g., 20% vs. 92%). However, uniform surface labeling of target cells may not be achieved in practice, which can affect the main assumption employed in this approach.

Electrokinetic isolation of CTCs

Cells can be considered as dielectric particles, meaning that they are electrically neutral but polarizable [92]. Hence, while they are in an electric field (DC or AC), electric dipoles moments are induced in cells [93]. The magnitude and direction of these dipole moments mainly depend on the dielectric properties of the cells. These properties are themselves dominated by the polarity and conductivity of the cell membrane and the cytoplasm, and can be experimentally determined using the single-shell model [92]. Depending on their phenotype, physiological state, and morphology, different cells have

different dielectric properties, which is the basic principle employed for electrokinetic isolation of CTCs [94] [95]. In practice, when different cells are exposed to a spatially inhomogeneous AC field, based on dielectric properties of cells and the carrying medium as well as the frequency and amplitude of the field, they will experience different electrokinetic forces. These forces can be used for characterization and isolation of cells through electrorotation (i.e. the rotary motion of cells in a rotating AC field) and dielectrophoresis (DEP) (i.e. the repulsive or attractive translational motion of cells in a non-uniform AC field), respectively [96] [97].

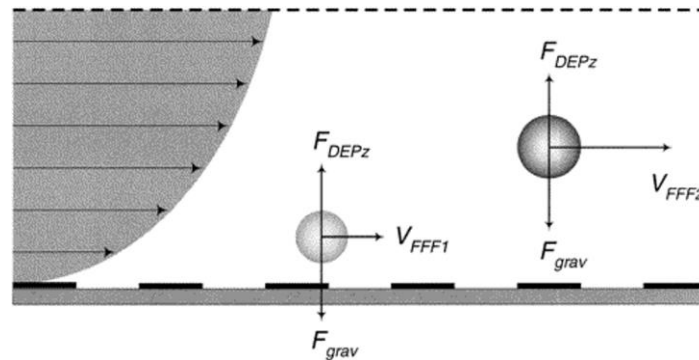


Figure 1.5 The DEP/G-FFF principle for cell separation. Different cells are levitated at different heights determined by the collective effect of DEP and gravity (F_{DEPz} and F_{grav}). After cells reach their equilibriums, a parabolic laminar flow having different velocity profiles at different heights ($V_{FFF2} > V_{FFF1}$) collects the cells at the same output but at different times. Cells within the faster profile (V_{FFF2}) are collected first, followed by the cells lie within the slower profile (V_{FFF1}) [98].

The DEP force is inversely proportional to the length scale, making it more effective for micro-scale cell isolation using integrated microfluidic-electronic devices [99] [93]. Accordingly, a general design for devices used for DEP-based isolation of cancer cells consists of a micro-scale chamber or channel with arrays of electrodes at its floor to produce the non-uniform AC field. The isolation can be realized either by capturing cancer cells on the electrode by attractive DEP force, or by immobilizing the cancer cells within the medium by balancing the repulsive DEP force and gravitational and hydrodynamic forces (i.e. Dielectrophoretic/gravitational field-flow fractionation (DEP/G-FFF)) (see Figure 1.5) [100] [98]. Using these methods, DEP-based isolation of cancer cells from mixed cell samples has been demonstrated, and high recovery and purity rates (>95%) for samples with different cancer cell concentrations (e.g., one cancer cell mixed with 3×10^5 blood cells) have been reported [100] [98]. Viability tests have confirmed the non-invasiveness of the relatively high strength electrical fields ($>2.5 \times 10^4$ V/m) employed in

this method. Nevertheless, the main disadvantage associated with the above methods is their low throughput, as sample processing is accomplished on a non-continuous basis (i.e. a stop-flow sequence) and the volume processed in each run is too small (e.g., 30-50 μL) for a typical CTC assay.

To address this issue, a device with a larger chamber capable of processing larger volumes (up to 4.5 mL) at can be used [101]. However, the sensitivity of this device has significantly decreased for large sample volumes. For example, for a 4.5 mL sample containing cancer cells mixed with $\sim 5 \times 10^6$ blood cells (1:1000 ratio), the recovery rate has been reduced to 10%, as the majority of cancer cells were co-eluted with blood cells. As the sample volume was decreased by 9 fold (i.e. 100 cancer cells mixed with $\sim 2 \times 10^5$ blood cells), the recovery rate increased to 92%. These results indicate that a non-continuous “batch-wise” method may not be a suitable approach, given that the number of blood cells in a real blood sample is higher than the values used in these works. More efficient continuous-flow microfluidic approaches have also been reported. In one study, a DEP module has been integrated with a size-based hydrodynamic step, which has been employed as the enrichment stage to remove excess blood cells [102]. Another approach employed a separate elute flow to continuously remove the levitating blood cells, while cancer cells remain within the attractive DEP field at lower heights within the chamber and are continuously collected at a separate outlet [103].

DEP-based isolation of CTCs is also label-free and delivers viable cells, but some factors may affect their application in practice. For instance, dielectric characteristic of cells can gradually change due to ion leakage, meaning that the isolation should be completed within a short duration after the sample processing starts [101]. This is not an easy task given the large sample volumes required for CTC isolation assays and the relatively slow sample processing rates achieved so far. Furthermore, the electrical conductivity of the carrying medium must be carefully adjusted to a sufficiently low value, which is not achievable for whole blood samples.

Antibody-based methods for CTC detection and isolation

All antibody-based methods are built upon a single biochemical principle, that is, antibody-antigen specific binding. These methods are the most common and effective approaches for both detection and isolation of CTCs. Antibody-based detection mainly refers to immunocytochemistry (ICC) by visual examination of cells, although other non-

visual detection techniques, such as Raman spectroscopy, photoacoustic flowmetry, and nuclear magnetic resonance, have also been used [74] [104] [105] [106]. Antibody-based CTC isolation is realized using an antibody-mediated “matrix” to which CTCs are specifically bound and, either directly or indirectly, captured. The matrix could assume two major forms: magnetic particles or a modified surface within a vessel (mostly, a microchannel). Considering the specificity of the principle employed in antibody-based isolation methods, they can theoretically achieve simultaneous detection and isolation of CTCs. However, due to the lack of a truly specific surface antigen for CTCs, this has not confidently been accomplished in practice. Herein, antibody-based methods for detection and/or isolation of CTCs are classified as ICC, immunomagnetic, and adhesion-based methods, which are reviewed in the following subsections.

The performance of any antibody-based method partly depends on the antigen (marker) that it employs. Various antigens have been exploited for detection or isolation of CTCs, among which EpCAM and different subtypes of CK are by far the most frequently used markers. However, many studies have now confirmed that not all CTCs express these markers, which may be a consequence of the EMT process. Given that the EMT process has been associated with CSCs, it is likely that any method based on these markers neglect this important subpopulation of CTCs. However, since the prognostic value of CTCs detected using such epithelial markers has been demonstrated in several clinical studies, it may be assumed that these cells (i.e. EpCAM+ and/or CK+) are surrogates of the more prominent metastasis-initiating cells or CSCs [107]. Several organ- or tumour-specific markers, such as CEA, EGFR, PSA, HER-2, MUC-1, EphB4, IGF-1R, cadherin-11, and TAG-72, have also been reported for antibody-based detection and isolation of CTCs, which has already been reviewed in several other studies (e.g., [108]). In short, none of the markers reported so far have offered the ideal performance (i.e. high expression and specificity) required for effective detection and isolation of all CTCs, with the major issue being the lack of expression by a subpopulation of CTCs. Of equal significance is the development of antibodies that specifically and readily bind to target antigens. In order to be employed in ICC or immunomagnetic methods, these antibodies should themselves be covalently conjugated to fluorophore molecules or paramagnetic particles or beads. In adhesion-based methods, chemical derivatization techniques are usually used to link the antibodies to a capture surface to which target cells should selectively adhere.

Immunocytochemistry (ICC) methods for CTC detection

CTC detection by ICC mainly refers to direct visual examination of the enriched sample to find the specifically antibody-labelled target cells. A CTC is often defined as a CK+/DAPI+/CD45- intact cell [109]. In particular, the CD45-negativity is used to increase the detection specificity by ruling out WBCs that might be illegitimately positive for the CTC marker(s). The biological and clinical significance of such cells (e.g., CD45+/CK+/DAPI+) is still unknown, although some have speculated that these cells could be phagocytic WBCs that have engulfed a CTC, or cancer stem cells that have acquired hematopoietic characteristics [110]. The nuclear dye DAPI is used to exclude positively scored cell fragments and debris. Interestingly, it has been reported that all EpCAM+/CK+/CD45- objects, regardless of their DAPI status, are prognostic [111]. In principle, ICC can be considered as the most reliable and specific method for CTC detection, although ideal performance may not be achievable in practice. In addition to sensitivity and specificity of markers, the efficiency of the optical techniques employed to interrogate the cells affects the performance of ICC methods. In general, two main approaches can be envisioned for this purpose, namely, flow cytometry and image cytometry.

The principle of flow cytometry, including the fluorescence-activated cell sorting (FACS), has usually been employed for in-house detection, enumeration, and separation of immunofluorescently labelled CTCs [112]. A multi-parameter protocol allows the evaluation of several fluorescent labels simultaneously, increasing the detection specificity [113]. However, flow cytometry has not consistently offered the high sensitivity required for detecting CTCs [114]. Aside from technical limitations and detection resolution, this may also originate from the variations in antigen expression, which could result in a poor gating definition. CTC detection through image cytometry is more popular and mainly refers to the immunofluorescence microscopy [115]. The main advantage of image cytometry is the possibility of incorporating several markers as well as different molecular (e.g., fluorescence in situ hybridization (FISH)) or cytomorphological (e.g., N/C ratio) assays in the detection procedure, which improves the specificity of detection [116]. Image cytometry by manual examination of numerous slides, even after sample enrichment, is not a practical task. Thus, a variety of laboratory or commercial automated digital microscopy (ADM) systems have been employed for this purpose. In addition to higher-than-manual throughput and repeatability, ADM systems can offer computerized post-processing analysis of the image data (see Figure 1.6) [117] [118].

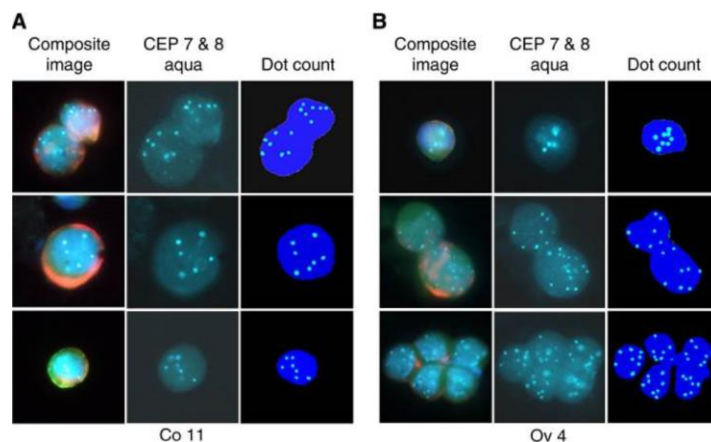


Figure 1.6 Automated quantitative FISH analysis of detected CTCs from colorectal (panel A) and ovarian (panel B) cancer patients. In each panel, the left column depicts detected CTCs at $\times 100$ magnification labelled for EpCAM (green), CK-7/8 (Cy5), and DAPI (blue). The middle column shows FISH results for chromosome 7 and 8, and the last column is a pseudo colored map of detected FISH signals (dots) within the nucleus of each CTC. Based on the automatic enumeration of dots, the system confirms the identity of detected CTCs [117].

Sensitivity and throughput of image cytometry methods can be improved using more efficient optical techniques. A modified ADM system, the laser scanning cytometry is another image cytometry technique used for the detection of CTCs [119]. It can be considered as a 2D flow cytometry system that exploits a monochromatic laser beam to scan and analyze the slides through rigorous image processing algorithms. Higher sensitivity and speed compared to conventional ADMs have been achieved, thanks to the effective excitation and shorter exposure times possible using the laser [120]. Higher throughputs can be achieved using another optical technique called the fiber-optic array technology [121]. Enabled by an array of optical fibers, this technology exploits a laser raster over a very large field of view (e.g., 50 mm) to rapidly scan a large substrate (9.5cm \times 4.5cm) on which immunofluorescently labelled cells are fixed.

CTC detection by image cytometry is a popular approach that has also been employed by the CellSearch[®] system (Veridex, NJ, USA), which is the only clinically approved assay for CTC detection (see “Immunomagnetic methods for CTC isolation” for details). By skipping the enrichment step and examining all nucleated cells in the sample, another image cytometry system, the HD-CTC assay has achieved \sim 99% detection sensitivity [122]. Since the sample has not been subjected to any enrichment process, this method has also been able to detect CTC aggregates in some samples [123]. Whether these circulating CTC aggregates have been broken off from the tumour body or have

formed intravascularly after CTCs dock on the endothelial wall of the blood vessels is not known. However, they may have a high clinical significance as it has been postulated that they can more easily lodge in the capillary beds and initiate a micrometastasis [123].

EPithelial ImmunoSPOT (EPISPOT), a modification of the enzyme-linked immunosorbent spot (ELISPOT) assay, can also be classified as a novel antibody-based approach that only detects living CTCs and has prognostic significance for a variety of carcinomas [124] [125]. CTCs are detected based on a “footprint,” which is created by secretion of one or more CTC-specific proteins after the negatively-enriched sample is cultured on a surface covered by antibodies against those proteins. After removing the cells from the surface, a secondary set of fluorophore-conjugated antibodies are employed to label the captured proteins on the surface. Since proteins are only secreted by viable CTCs, this method only detects living CTCs. Since the surface can be treated with different antibodies, the expression of several proteins can be analyzed concurrently.

Immunomagnetic methods for CTC isolation

Almost all cells, except for deoxyhemoglobin RBCs, are either diamagnetic or very weakly magnetic [126]. Hence, a magnetic field can be used to effectively isolate CTCs from the blood if their magnetic property is selectively modified. To this end, CTCs can be tagged using antibody-conjugated magnetic beads (diameter: 0.5-5 μ m) or nanoparticles (diameter: 50-250nm) that often bind to a specific surface antigen, although intracellular antigens can also be targeted [127] [128]. Once immunomagnetically labelled, the sample is exposed to a non-uniform magnetic field, causing the labelled cells to migrate towards the regions of higher magnetic flux density (MFD) where they are captured [129]. Except for the intracellular labeling which entails membrane permeabilization, immunomagnetic methods yield viable cells as magnetic labels often do not interfere with the biological function (e.g., gene expression profile [130]) of cells.

In general, the performance of an immunomagnetic method is determined by three factors, including a) the expression and specificity of the target antigen and the binding quality of the associated antibody, b) the efficiency of immunomagnetic labeling process and magnetic particles, and c) the magnetic separation mechanism that isolates labelled cells. Immunomagnetic methods have often been employed as an effective enrichment step. However, by optimizing these factors, particularly the separation mechanism, the

principle of immunomagnetic cell separation can simultaneously achieve high recovery and purity rates, rendering single-step detection and isolation of CTCs [131] [130].

An overexpressed surface antigen could increase the uptake of immunomagnetic particles, which in turn reinforces the magnetic force acting on cells and facilitates their isolation. EpCAM has often been used for this purpose; however, as it was explained earlier, the expression of EpCAM may vary among CTC subpopulations [132]. In the lack of an ideal marker, one approach to partially overcome this issue is to use a “cocktail” of antibodies to target multiple antigens [133]. Another approach, which is independent of the phenotype of CTCs, is to negatively isolate CTCs by lysing RBCs and using specific markers (e.g., CD45 or CD61) to magnetically remove WBCs from the sample [134] [135] [136]. Such an approach is not biased by a particular CTC marker and leaves the CTCs untouched. However, since WBCs largely outnumber CTCs, to achieve an acceptable purity, the separation method should have a very high recovery rate. In other words, even a small percentage of non-recovered WBCs will translate to a large number of background cells and reduce the purity.

In addition to the target antigen and its antibody, both the labeling protocol (i.e. direct or indirect labeling and the reagents) and the magnetic particles (i.e. their size and composition) can also affect the performance of immunomagnetic methods [136] [137]. The binding between primary antibody and magnetic particles could be achieved either directly or indirectly through secondary antibodies that are already bound to magnetic particles and can specifically bind to a specific epitope on the primary antibody (see Figure 1.7). Compared to a direct (single-step) method, an indirect (two-step) approach can potentially achieve a higher labeling efficiency (i.e. magnetic particle density per cell). For instance, up to a 15-fold increase in the labeling efficiency has been observed for an indirect approach when a proper chemistry was employed [138]. The improved performance of an indirect method can be related to the ability of each primary antibody to attach to more than one magnetic particle through several secondary antibodies that bind to the primary antibody. Moreover, a secondary ligand-receptor interaction with a strong affinity and fast dynamics could improve the immunomagnetic labelling significantly. The size of magnetic particles can also affect the overall efficiency. For instance, for an overexpressed surface antigen, using larger particles could actually reduce the overall magnetic load due to steric hindrance [139].

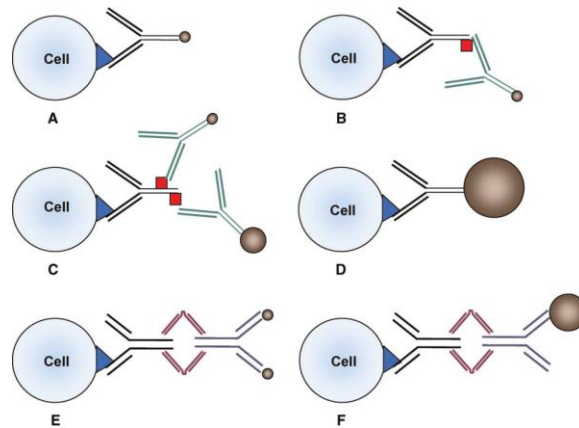


Figure 1.7 Various direct and indirect methods for immunomagnetic labeling [136]. Protocols A and D show direct labeling using magnetically-labelled primary antibodies. Protocols B and C depict the indirect labeling using magnetically-labelled secondary antibodies that bind a hapten-conjugated primary antibody attached to a surface antigen. Protocols E and F represent another indirect labeling approach using tetrameric antibody complex (TAC) structures that bind to the surface antigen and a receptor (often dextran) on the magnetic particles.

Macro-scale Separation Structures

The third factor affecting the performance of an immunomagnetic approach is the magnetic separation mechanism used to capture labelled target cells. In general, the separation can be realized at macro or micro scales. Macro-scale methods offer a higher throughput and have often been employed for enrichment purposes. In batch-wise separation approach, the whole labelled sample is subjected to a magnetic field at once, resulting in the migration of labelled cells to the regions of higher MFD. Different mechanisms have been designed based on this concept, ranging from a simple test tube placed next to a permanent magnet (e.g., EasySep™, STEMCELL Tech., BC, Canada) to more complex mechanized platforms (e.g., CellSearch® system). An alternative approach which can effectively process larger volumes is the continuous-flow separation, in which the sample is continuously fed through the separation module. This module either contains a magnetically activated filter (e.g., steel wool columns) to capture and retain the labelled cells or use the principle of magnetophoresis to selectively deviate the labelled cells within the flow and collect them at designated outputs [140] [141].

Combining immunomagnetic sample enrichment and image cytometry, the CellSearch® system is still the only Food and Drug Administration (FDA)-approved platform for detection and enumeration of CTCs. The sample preparation and cell labeling in this system is performed using an automated module. The enriched labelled sample

(e.g., ~300 μ L extracted by lysing a 7.5-mL blood sample) is then transferred to a magnetic cartridge that is loaded into a four-color ADM. Once loaded, the magnetic cartridge is activated, causing the magnetically EpCAM-labelled cells to migrate and attach to the surface of the cartridge which is then scanned for different labels separately. The detection results should be reviewed by an operator for final verification. High degree of repeatability and inter- or intra-assay accordance have been reported for this system, thanks to the automated sample preparation procedure as well as the stringent criteria used to define a CTC (i.e. CK+/DAPI+/CD45- intact cells with round or oval morphology) [142] [143]. The CellSearch[®] system has been employed in numerous large-scale clinical studies that are associated with the majority of current data about the clinical utility of CTCs.

While the CellSearch[®] assay has not generally detected CTCs in healthy blood samples, the number of CTC-positive patients as well as the frequency of CTCs detected in these patients tends to be low [144] [89]. In addition to possible cell loss during aggressive preprocessing (e.g., lysing RBCs), this reduced detection sensitivity could also arise from the immunomagnetic labelling step that only selects EpCAM+ cells [145] [146]. For instance, a comparative study involving 48 breast cancer patients has reported that using CK along with EpCAM for the immunomagnetic enrichment step could increase the recovery rate up to 20% [127].

Although the isolation of a single cancer cell spiked into a minimum volume of 1 mL of blood has been achieved by such macro-scale methods, significant variations can be observed in the reported recovery rates (10-90%) with an average close to 50-60% [147] [148] [149]. This can in part be explained by the steep decrease in the MFD gradient (hence, the magnetic force) as one moves away from the maximum MFD point. In other words, the magnetic gradient created by a separation structure can readily manipulate the labelled cells only within a limited distance. This renders some macro-scale mechanisms, whose length scale may vary between a few millimeters to a few centimeters, less effective. A clever approach has been proposed by continuously relocating the regions of high MFD gradient within the sample and close to all labelled cells [130]. The system is essentially a robotic arm that is equipped with a magnetic rod covered by a thin plastic layer with minimum nonspecific adherence to non-target cells. Isolation of EpCAM-labelled CTCs from the whole blood samples contained in a multiwell plate has been achieved by automatically sweeping the magnetic rod within the wells.

Micro-scale Separation Structures

Taking advantage of microfabrication and microfluidic technologies, the sample can be processed at a scale small enough to effectively exploit the strong MFD gradient created in close vicinity (i.e. several micrometers) of a magnetic source. The isolation efficiency in an immunomagnetic microfluidic chip is mainly governed by an equilibrium between hydrodynamic and magnetic forces acting on the labelled cells [150]. The controllable dynamics of laminar flows in microchannels and, therefore, the net force acting on labelled target cells can be adjusted such that labelled cells are either captured at regions of maximum MFD, or deterministically moved and collected at specified regions in the microchannel [129] [141]. For example, micro-scale immunomagnetic capture of CTCs has been realized by simply securing a rectangular microchannel on top of a stack of permanent magnets (see Figure 1.8) [131]. As the sample flows in the microchannel, the MFD gradient created between adjacent magnets attracts and immobilizes the EpCAM-labelled cancer cells on the microchannel floor. Another design consisting of a straight microchannel with several square indentations at its sidewall has been used to isolate CTCs from murine cancer models [151]. The magnetic field gradient created by a permanent magnet placed beside the chip pulls the EpCAM-labelled cells towards the sidewall where they eventually enter and get trapped in microfabricated indentations.

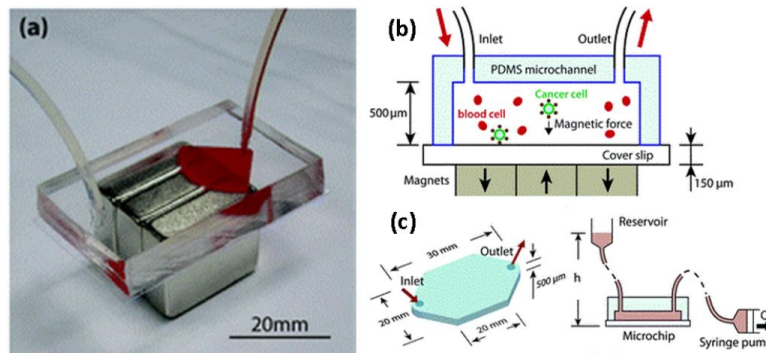


Figure 1.8 (a) and (c) the microfluidic chip used for immunomagnetic isolation of cancer cells from whole blood. Magnet blocks are used to create the magnetic field gradient required to attract magnetically labelled cells at the bottom of the microchannel as depicted in (b). The sample is continuously pumped through the microchannel, causing the non-captured (blood) cells to exit the chip [131].

Micro-magnetophoretic isolation of cancer cells can be performed by incorporating microfabricated magnetic concentrators within a microchannel to produce the MFD gradient required to selectively deviate and collect the flowing labelled cells [152] [91]. An

alternative magnetophoretic approach consisting of a straight microchannel with two current-carrying wires at both sides has been reported by Plouffe and colleagues [153] (Figure 1.9). Taking advantage of the laminar nature of flow in microchannels, the sample has been separated into two streams to efficiently sheath a buffer solution at the center of the microchannel. Once the current is passed through the wires, a magnetic field is created, forcing the labelled cells to move from both sample streams into the buffer collection stream.

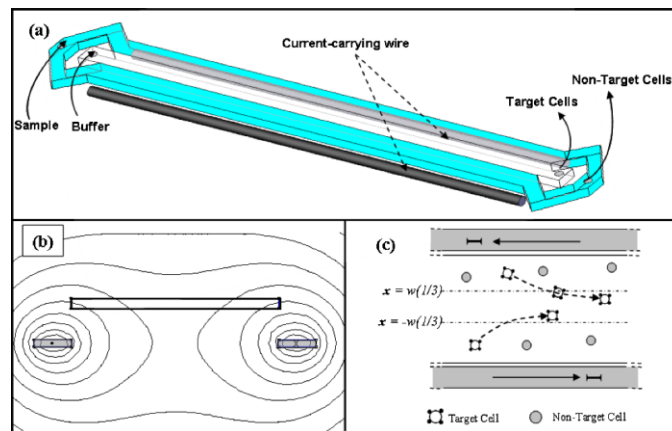


Figure 1.9 Isolation of cancer cells by magnetophoretic displacement in a microchannel. (a) The device composed of a straight microchannel with two wires at each side. A buffer collection solution splits the sample solution into two separate streams at both sides. (b) A cross-sectional illustration of the device showing a magnetic field created by the anti-parallel current in wires. (c) A top view of the microchannel showing magnetic entities (i.e. labelled cancer cells) moving away from the high magnetic flux regions into the collection stream [153].

Adhesion-based methods for CTC isolation

Adhesion-based methods rely on the affinity of CTCs to a capture surface whose biochemical and, occasionally, topographical properties have been modified. It has been shown that modifying topographical properties of an antibody-coated surface can enhance the cell adhesion up to 10 folds by increasing the local interactions between the nano-structured surface and membrane features without compromising the cell viability [154]. Unlike immunomagnetic methods, adhesion-based isolation of CTCs does not require labeling the cells prior to the isolation process. Adhesion-based CTC isolation can be performed either in batch-wise (static) or in continuous-flow microfluidic modes, although the latter approach is far more efficient and common [155] [156]. In batch-wise adhesion-based assays, the sample is first incubated on the capture surface for a given duration. Next, non-adherent, supposedly non-target cells are washed off, leaving CTCs attached

to the surface. For example, a proprietary collagen-coated surface has been employed to detect and isolate CTCs from patients with metastatic and local carcinomas of different origins [157] [158]. Due to the tendency of metastatic cancer cells to invade collagenous tissues (e.g., the bone matrix), it has been suggested that this method captures the more invasive subpopulation of CTCs.

The sensitivity and selectivity of adhesion-based methods can be improved using continuous-flow microfluidic approaches in which the flow dynamics can be adjusted such that the target cells can effectively interact with the capture surface while any non-specific adhesion is prevented by the hydrodynamic shear. The adhesion of target cells to the capture surface in a microfluidic device is characterized by a balance between the hydrodynamic force and the affinity and dynamics of the ligand-receptor binding [156] [159] [160]. Accordingly, several parameters affect the adhesion efficiency, including the microchannel's Reynolds number (i.e. the flow rate), cell-surface collision frequency, and probability of cell adhesion following a collision [155] [161]. The flow rate affects duration as well as frequency of collisions, both of which can also be increased by expanding the effective area of the capture surface [162]. The flow rate also determines the hydrodynamic shear acting on both target and non-target cells. Ideally, it should be high enough to achieve a reasonable throughput and purity, while the recovery rate and cell viability are not compromised [163]. The probability of bond formation following a collision depends on the affinity and dynamics of the receptor-ligand bond, the expression of the receptor on CTCs, and the concentration and orientation of binding sites on the ligands that coat the capture surface [161] [164].

Microfluidic adhesion-based isolation of CTCs can be achieved by running the sample through a straight microchannel whose inner surface has been coated with an antibody against CTCs. However, the highly laminar streamlines developed in such a microchannel prevent cell-surface collision (see Figure 1.10.a). To address this issue, a passive mixing mechanism can be employed to disrupt the laminar flow in a straight microchannel and increase the diffusive movement of cells at practical flow rates (Figure 10.b) [165]. Another approach to increase the frequency of collisions is to employ a curvilinear (e.g., sinusoidal) design for the microchannel [166]. Regardless of the flow rate, the dynamics governing the flow in such a design shifts the cells towards one of the antibody-coated sidewalls, allowing a high throughput without sacrificing the sensitivity. Based on this design, a microfluidic chip composed of several parallel microchannels

whose walls are coated with an anti-EpCAM antibody or an anti-prostate-specific membrane antigen (PSMA) aptamer has been developed and used for isolation of different cancer cell lines from spiked blood samples [167] [168]. The adhesion efficiency can be further improved if instead of a flat surface, a nano-structured [169] [170].

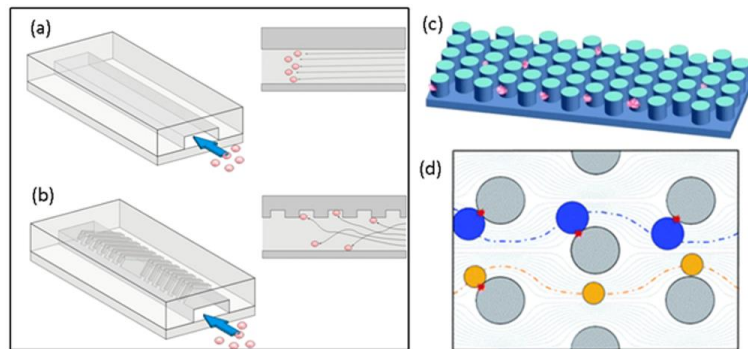


Figure 1.10 (a) Cells flowing within the laminar streamlines in a straight microchannel do not come in contact with the capture surface. (b) A passive mixing mechanism, known as herringbone mixer, composed of micron-sized grooves in the upper surface of the microchannel can increase the diffusive movement of cells and the cell-surface collision frequency [165]. (c) Increasing the effective capture surface by inclusion of microposts in a straight microchannel. Adopted from [171]. (d) A modified geometrical and spatial configuration of microposts can increase the recovery rate and purity by maximizing CTC-micropost collisions and minimizing blood cell-micropost collisions. CTCs and blood cells are depicted in blue and yellow, respectively [172].

The collision frequency can also be increased by expanding the effective surface area using 3D structures (e.g., microposts) within the microchannel (Figure 1.10.c). This approach was first introduced in the CTC-Chip, a wide silicon-based microchannel containing an array of 78,000 microposts activated against EpCAM [173]. Due to the high rate of collisions enabled by the dense array of microposts, it has been shown that varying expressions of EpCAM by target cells does not affect the recovery rate. By further improving the relative alignment of microposts, minimum collision between blood cells and microposts has been achieved, while the frequency of CTC-micropost collisions has been maximized (Figure 1.10.d) [172]. Other variations of the micropost-enabled immunocapture, including different material (e.g., a polydimethylsiloxane (PDMS)-based chip [174]), different micropost size and distribution [161], or different ligands and receptors (e.g., using oligonucleotide aptamers instead of antibodies or using the streptavidin-biotin affinity [161] [175]), have also been reported. In particular, using the streptavidin-biotin affinity for adhesion-based isolation of CTCs can potentially increase

the recovery rate as target cells can be labelled against multiple surface antigens using a cocktail of biotinylated antibodies [176].

To avoid the lengthy processes of surface derivatization, commercially available immunomagnetic microbeads have been used to create capture beds within the microchannels. For instance, self-assembled microposts can be created by vertically stacking biofunctionalized microbeads over a microfabricated pattern defined at the bottom of the microchannel [177] [178]. Although these methods are easy to implement some issues, including low throughput to prevent collapsing the self-assembled microposts or channel clogging due to accumulation of microbeads may hinder their application in practice.

The process by which CTCs adhere to the endothelium prior to their extravasation can also be mimicked to capture these cells [179]. For this purpose, the inner lumen of a microtube can be coated with E-selectin and a CTC-specific antibody, followed by a layer of halloysite nanotubes. The nanotubes physically engage the flowing cells, which then make transient bonds with E-selectin, decelerate, and start rolling on the surface of microtube. CTCs are then captured by the specific (and usually slower) bonding between specific antibodies and surface antigens.

1.5. Contributions

The main goal of the research presented in this thesis was to develop a system capable of isolating rare cancer cells from blood samples with high sensitivity (>65%) at a practical throughput ($\geq 100 \mu\text{L}/\text{min}$). This goal was achieved by successfully accomplishing several sub-goals, resulting in the following contributions:

- 1- *A comprehensive critical review of the CTC isolation problem:* A critical review of the biological and clinical significance of CTCs as well as different methods for their isolation from the blood was performed in the initial phase of this research. The objective of this review was to gain a solid understanding of the CTC problem and state-of-the-art technologies used for CTC detection and isolation. This study was published in the high impact factor journal *Biotechnology Advances* in 2013 and has been cited by other researchers

frequently (77 citations according to Google Scholar and 48 citations according to Web of Science as of June 15th, 2017) [180].

- 2- *Design, microfabrication, and experimental characterization of a novel integrated microfluidic magnetic chip for immunomagnetic isolation of cancer cells:* During this phase of the project, the basic working-principle of an integrated microfluidic magnetic chip was first developed. Next, proof-of-principle experiments were carried out using several prototypes. The final optimized device was then rigorously tested under different experimental conditions. The macro-to-micro interfacing was also optimized through empirical evaluation of different protocols and configurations. The results confirmed that the proposed chip can capture immunomagnetically labelled cells with close to 100% sensitivity at very low concentrations (<20 cells/mL). These preliminary findings were published in *Biomedical Microdevices* [181].
- 3- *Design, microfabrication, and experimental evaluation of a novel microfluidic chip for magnetically-enhanced active size-based cross-flow filtration of magnetic particles:* An inherent problem in immunomagnetic cell isolation is the non-specific capture and accumulation of free unbonded magnetic particles by the magnetic separation mechanism employed to capture immunomagnetically labelled target cells. These redundant beads not only could affect the magnetic capture of target cells, but also hinder the visual detection of captured cells and might compromise their viability. To fundamentally address this issue, these particles should be removed from the labelled sample before it is exposed to the magnetic separation mechanism. To this end, the basic working principle of a novel magnetically-enhanced active size-based approach based on the general principle of microfluidic cross-flow filtration was proposed. Several prototypes with extremely low feature sizes and high aspect ratios were fabricated. Experimental observations concluded that due to the intrinsic plasticity of cancer cells, this method may not be highly effective for this particular application. However, the proposed filtration principle would be a practical approach for sensitive and specific separation of magnetic particles from diamagnetic entities. We are planning to further optimize and examine the performance of this approach for such applications in the near future.

- 4- *Design, microfabrication, and experimental analysis of a microfluidic platform for size-based enrichment and immunomagnetic isolation of rare cancer cells from spiked blood samples:* To address the free magnetic particles problem mentioned earlier, another filter based on the principle of microfluidic multiorifice flow fractionation was designed and fabricated. The filter, which was able to remove ~80% of free magnetic particles with ~85% specificity, was then integrated with the magnetic chip, forming a microfluidic platform for two-stage size-based enrichment and immunomagnetic isolation of cancer cells from blood samples. Experimental analyses of this platform confirmed that it can capture blood-borne prostate cancer cells with high sensitivity (up to ~75%) at clinically meaningful low concentrations (5-20 cells/mL) and a practical throughput (200 μ L/min). We are currently preparing a manuscript to present these latest results in *Lab on a Chip*.

Although not entirely relevant to the scope of this thesis, another contribution during my PhD studies was the following:

- 5- *Development and experimental verification of a novel machine-vision system for automated localization of nucleic and cytoplasmic micromanipulation sites on low-contrast adherent cells:* Adherent cells include a wide range of mammalian cells and are usually thin with highly irregular morphologies. As such, the automated micromanipulation of these cells is a beneficial yet challenging task. As a member of a team working on the development of a robotic automated SCE system, I proposed the necessary problem of machine vision-based automated localization of micromanipulation sites on the nucleus as well as the cytoplasm of thin adherent cells, and developed and implemented a novel image processing algorithm for this purpose. The results of this work were published in *Medical & Biological Engineering & Computing* and *IEEE Transactions on Biomedical Engineering* [2] [3]. It should be noted that the knowledge and skills I acquired during this first part of my PhD research are closely linked and will be subsequently applied to the next phase of my research on CTCs for automated machine-vision based enumeration and analysis of captured CTCs.

Chapter 2.

An Integrated Microfluidic Magnetic Chip for Immunomagnetic Isolation of Cancer Cells

2.1. Microfluidic Immunomagnetic Cell Isolation

2.1.1. Background

As thoroughly discussed in the previous chapter, a variety of principles can potentially be employed for CTC isolation. Among these, antibody-based approaches are the most effective techniques. To recapitulate, antibody-based isolation of CTCs, which for the most part is based on specific surface antigens (or markers) that are expressed by cancer cells, has been realized at both macro and micro scales, either directly on a functionalized capture bed or indirectly using immunomagnetic particles. The specificity of the antibody-antigen affinity when augmented with the magnetic force that can be applied on immunomagnetic particles can offer highly sensitive and selective solutions for cell isolation from blood samples. The magnetic force exerted on a magnetic entity, such as a magnetically labelled cell, partly depends on the strength and gradient of the flux density produced by the magnetic source [129] [182]. This magnetic source could be an electromagnet, a permanent rare earth magnet, or some soft magnetic material that should in turn be magnetized by a primary source. Regardless of the type of source, the MFD drops quickly ($\propto 1/r^3$) as the distance (r) from the source increases, reducing the force experienced by labelled cells and hence the sensitivity of cell capture [150]. Taking advantage of microfabrication and microfluidic technologies, the sample can be processed at a scale small enough to effectively exploit the strong magnetic force created in close vicinity (ideally several micrometers) of the magnetic source, thereby increasing the sensitivity of magnetic cell capture.

Therefore, I chose to study a microfluidic immunomagnetic approach in my research on the isolation of CTCs from the blood. Such an approach has occasionally been employed for CTC isolation by other researchers [91] [131] [134] [183]. However, in majority of these works, cell separation is accomplished via magnetophoresis, where labelled cells are deflected from the continuous flow in a microfluidic channel, either by an

external source or a series of soft magnetic structures (e.g., wires) embedded inside the microfluidic channel. These cells are then collected at a separate outlet for off-chip enumeration or characterization. In the proposed method in this thesis, cancer cells are captured at addressable locations on the chip, which would facilitate the automated *in-situ* enumeration and analysis of single cells using machine vision.

2.2. Theory

Almost all cells, including blood constituents, are either diamagnetic or very weakly magnetic [126]. Therefore, a magnetic force can be used to exclusively isolate target cancer cells from the blood provided their magnetic property is selectively modified using magnetic particles that specifically bind to a certain surface marker on the cancer cells. Once the sample is exposed to a non-uniform magnetic field, the field gradient forces immunomagnetically labelled cancer cells to migrate towards regions with the highest MFD where they are eventually captured [129] [150]. The isolation of cells in such a framework is characterized by the interaction of several magnetic and hydrodynamic forces acting on labelled cells. These forces include diffusion (i.e. Brownian motion (F_B)), gravity (F_g), buoyancy (F_b), inertia (F_i), Stokes' drag (F_d), and magnetic force (F_m) (see Figure 2.1).

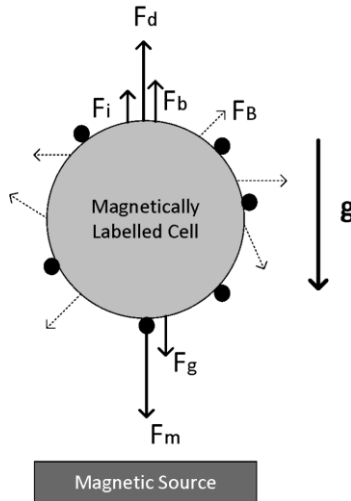


Figure 2.1 A simplified 2D demonstration of different forces acting on a magnetically labelled cell in a microchannel. The magnetic source in this figure could represent a magnetic micro-concentrator or a region of high MFD. Black circles represent magnetic particles/beads.

The Brownian motion within the fluid can be calculated using the random walk theory [184]:

$$\Delta\vec{r} = \sqrt{2D\Delta t} \quad (2.1)$$

where Δr is the diffusive movement in Δt seconds at any direction for a cell whose diffusion constant is D . The diffusion constant is calculated using the Stokes-Einstein equation:

$$D = \frac{K_B T}{6\pi\eta R_c} \quad (2.2)$$

where K_B , T , η , and R_c are the Boltzmann's constant, temperature, viscosity of the carrying medium (e.g., blood or buffer), and the average cell diameter, respectively. Assuming that a cell's journey within the carrying medium at the room temperature (25 °C) lasts <10 seconds (before it is captured), the maximum Brownian motion of the cell in the blood and the buffer would be 0.295 μm and 0.700 μm , respectively. Thus, considering the typical characteristic dimension of different prototypes studied in this research (i.e. the microchannel height = 55 \pm 5 μm), the Brownian motion can be safely neglected.

The counteracting forces of gravity and buoyancy are calculated, respectively, as follows:

$$\vec{F}_g = V_c \rho_c \mathbf{g} \quad (2.3)$$

$$\vec{F}_b = -V_c \rho_b \mathbf{g} \quad (2.4)$$

where V_c , ρ_c , and ρ_b are cell volume, and cell and the carrying medium density values, respectively. Considering typical densities of a cell (1.077 \times 10³ kg/m³) and the blood (1.060 \times 10³ kg/m³) [185] [186], it can be assumed that these forces cancel each other [187]. Since the Reynolds number for the proposed prototypes in this research remains very small (e.g., \ll 1), the inertial force can also be neglected [186].

Considering these assumptions, labelled cells are mainly affected by drag and magnetic forces. Drag is a hydrodynamic resistance experienced by labelled cells while the magnetic force exerted on magnetic particles that are bonded to the cells pull them

toward the regions of high MFD. Assuming a laminar flow within the device and a spherical shape for the cells, the drag can be calculated using Stokes' Law as follows:

$$\vec{F}_d = 6\pi\eta R(\vec{v}_f - \vec{v}_c) \quad (2.5)$$

where η , R , \vec{v}_c , \vec{v}_f are fluid viscosity, cell radius, cell velocity, and flow velocity, respectively. The magnetic force experienced by a labelled cell can be estimated by integrating the magnetic force exerted on each magnetic particle (or bead) attached to the cell. For a single magnetic particle, the magnetic force is calculated as follows:

$$\vec{F}_m = (\vec{m} \cdot \nabla) \vec{B} \quad (2.6)$$

where \vec{m} and \vec{B} are total magnetic moment and the MFD, respectively. The total magnetic moment of a particle is found by multiplying its effective magnetic volume (V_p) by its volumetric magnetization (\vec{M}). The volumetric magnetization in turn is defined as $\vec{M} = \Delta\chi\vec{H}$, in which \vec{H} is the magnetic field strength and $\Delta\chi$ is the difference between the volumetric magnetic susceptibility of the particle (χ_p) and that of the medium (χ_f). Given $\vec{B} = \mu_0\vec{H}$, the magnetic force exerted on a single magnetic particle can be written as:

$$\vec{F}_m = \frac{V_p\Delta\chi}{\mu_0} (\vec{B} \cdot \nabla) \vec{B} \quad (2.7)$$

where μ_0 is the magnetic permeability of vacuum. Taking the Maxwell equation ($\nabla \times \vec{B} = 0$) into account, equation (2.7) can be rewritten as follows:

$$\vec{F}_m = \frac{1}{2\mu_0} \Delta\chi V_p \nabla \vec{B}^2 \quad (2.8)$$

If a cell is labelled with N particles, the magnetic force exerted on the cell will be [188]:

$$\vec{F}_m = N \frac{1}{2\mu_0} \Delta\chi V_p \nabla \vec{B}^2 \quad (2.9)$$

Thus, the sensitivity and selectivity of an immunomagnetic cell isolation approach are largely determined by the collective effect of the following factors:

- (a) the expression and specificity of marker and the quality of associated antibody (i.e. N)

(b) the quality of immunomagnetic labelling process and magnetic particles (i.e. $N, \Delta\chi, V_p$)

(c) the magnetic separation mechanism used to capture labelled cells (i.e. $\nabla\vec{B}^2$)

The performance of a microfluidic immunomagnetic approach is also governed by an equilibrium between hydrodynamic drag and magnetic forces acting on labelled cells. The controllable dynamics of laminar flows in a microfluidic chip and, therefore, the net force acting on labelled cells can be adjusted such that they are captured at a practical throughput. By optimizing all these factors, particularly the magnetic separation mechanism, the principle of immunomagnetic cell separation can simultaneously achieve high recovery and purity rates. In the next section, I have explained my approach for design and optimization of these factors.

2.3. Materials and Methods

2.3.1. PSMA and Prostate Cancer

A key factor defining the performance of an immunomagnetic cell isolation approach is the expression and specificity of the marker and the quality of the associated antibody (i.e. N in (2.9)). Ideally, a CTC marker should be expressed on the surface of all target cancer cells but almost absent on other circulating non-tumour or blood cells. PSMA, also known as glutamate carboxypeptidase II, N-acetyl- α -linked acidic dipeptidase I, or folate hydrolase, has nearly such qualities for prostate cancer cells. Physiologically, PSMA contains a binuclear zinc site and acts as an enzyme (glutamate carboxypeptidase (GCPII)) on small molecule substrates, including folate, the anticancer drug methotrexate, and the neuropeptide N-acetyl-L-aspartyl-L-glutamate [189]. The enzymatic role of PSMA in the function of prostate cells is not fully understood, but it can potentially be employed for designing prodrugs [189] [190]. Structurally, PSMA is a type II transmembrane glycoprotein with a large extracellular polypeptide chain (707/750 amino acids) (see Figure 2.2)

PSMA is overly expressed in prostate cancer cells and nonprostatic solid tumour neovasculature and expressed at lower levels in other tissues including healthy prostate, kidney, liver, small intestine, and brain [189]. It has been shown that the PSMA expression

increases with prostate cancer aggressiveness and androgen-independence [189] [191] [192] [193] [194]. Therefore, while its large extracellular domain and over-expression can increase the sensitivity of labelling, the fact that PSMA is dominantly observed on prostate tumour cells and its expression level is associated with the malignancy of the tumour make it a highly specific marker for the isolation of CTCs in prostate cancer. It should be noted that the majority of immunomagnetic CTC isolation systems, including the FDA-approved CellSearch® system, only capture prostate cancer cells that sufficiently express EpCAM. However, it has been shown that the EpCAM expression among cancer cells varies significantly, which may be a direct consequence of the EMT process [46]. For example, it has been shown that only 40-70% of PSMA-positive CTCs express variable levels of EpCAM [195]. Moreover, given that the EMT process has been associated with metastasis-initiating cancer cells [10] [11] [48], it is likely that such systems neglect an important subpopulation of CTCs [196] [197]. Thus, in this study, PSMA was selected as the marker and was targeted using a highly efficient proprietary monoclonal antibody that had been developed by our collaborators at the British Columbia Cancer Agency.

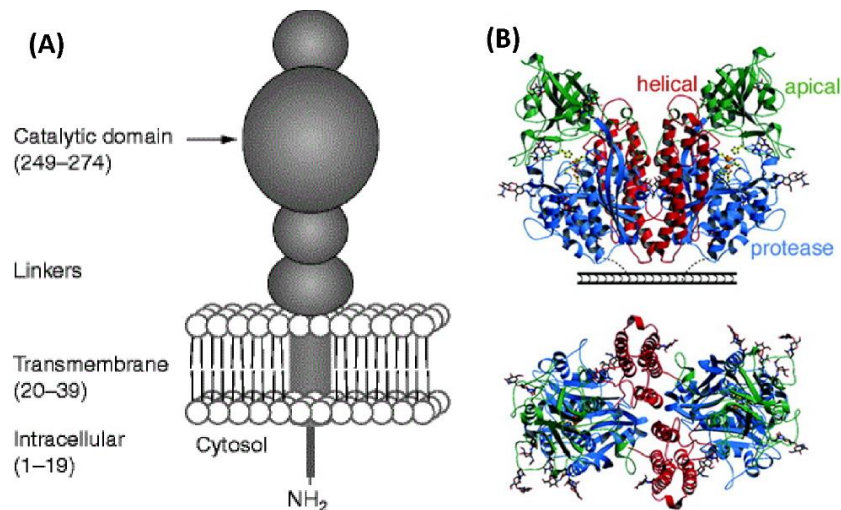


Figure 2.2 (a) The simplified molecular structure of PSMA [190] (b) Ribbon diagrams of side and top view of PSMA [189]

It is worth emphasizing that prostate cancer (PCa) is the most prevalent non-cutaneous malignancy and the second most fatal form of cancer among men [198]. PCa is usually diagnosed as a localized disease through digital rectal exam or PSA screening. The latter has been criticized for its high false positive rate, resulting in over-diagnosis or overtreatment of early/benign neoplasms [199]. Given that PCa is largely driven by the androgen axis, the management of local PCa often involves surgical or medical castration,

radiation therapy, or a combination of both. While majority of patients treated for localized PCa go on to live without significant complications for years, others (~30%) will present with metastatic spread of malignancy to distant sites, mostly to bone. In majority of cases, the metastatic disease continues to progress despite ongoing first-line androgen-deprivation therapy (ADT) and castrate levels of testosterone. Such a condition is known as metastatic castration-resistant prostate cancer (mCRPC), which is the lethal form of PCa. Prior to the approval of docetaxel (an anti-mitotic chemotherapy agent from the taxane family) that was followed by five other therapies (i.e. abiraterone, enzalutamide, cabazitaxel, radium-223 dichloride, and sipuleucel-T), treatment options for mCRPC patients were merely palliative. The introduction of these agents is changing the therapeutic landscape of mCRPC, providing oncologists with an armamentarium of therapies that have shown survival benefit through tumour growth inhibition [199]. Additionally, other novel agents (e.g., custirsen, cabozantinib, etc.) are being investigated in late-phase clinical trials and may soon be added to this list. Nevertheless, the sequence by which these therapies are applied for individual patients is not entirely optimized to maximize the benefit and minimize the toxicity and cost. Despite patient stratification based on symptoms, existing guidelines almost follow a one-size-fits-all approach that is based on meta-analysis of data from clinical trials [200] [201]. Such data may be differentially biased by prior treatments or not portray real-world populations, for example by accruing patients with a certain performance status and skipping those with a poor status or asymptomatic patients.

Precision oncology, in which predictive molecular biomarkers are employed and screened to identify particular drugs that benefit a patient, can improve both the survival and quality of life (QOL) of mCRPC patients. Given the molecularly heterogeneous nature of cancer and the selection pressure exerted on cancer cells during each line of treatment, it is necessary to monitor these biomarkers continuously [202]. However, considering that bone is the major site of metastasis in PCa, performing multiple biopsies is anatomically impractical. CTCs could be ideal specimens that can be obtained relatively easily and regularly, and provide the real-time single-cell level molecular data about the malignancy. As an example, it has been shown that mCRPC patients whose CTCs express androgen receptor (AR) splice variant 7 (AR-V7) develop resistance against anti androgen-axis agent abiraterone and enzalutamide, but benefit from docetaxel and cabazitaxel [35] [203]. Resistance to these taxane-based chemotherapy agents will also emerge in mCRPC

patients at some point. While the exact mechanisms of resistance against these agents are not known, some molecular biomarkers, such as β III-tubulin (an isoform of β -tubulin, the main target of these agents), have been suggested as a predictive marker for efficiency these compounds [204]. Additionally, upregulated expression of a MDR transporters, P-glycoprotein and MDR1 protein, is another putative mechanism of taxane resistance in mCRPC [204]. Therefore, probing CTCs for significant expression of such markers allows the physician to withdraw such highly toxic treatments and switch to another line of therapy. Thus, precision oncology based on longitudinal screening of the frequency and molecular signature of CTCs that can serve as both an intermediate endpoint for the efficiency of current treatment and a predictive biomarker for selection of the next line of therapy may improve survival and QOL of mCRPC patients.

Resistance to abiraterone (an androgen synthesis inhibitor) and enzalutamide (an antagonist of AR) implies that AR signaling pathways, which are essential for survival and growth of PCa cells, manage to remain active during therapy with these agents. Intratumoural androgen biosynthesis and alterations of AR signaling play roles in the development of resistance to such systemic hormonal therapies. Further research on these mechanisms may provide a clearer insight into pathways involved in PCa progression, novel biomarkers to predict treatment efficiency, and new targets for therapies. In particular, identification of novel therapeutic targets may provide treatment options for those cases with rare but highly aggressive driving mutations, such as small cell/neuroendocrine PCa (2% of all diagnosed PCa). The molecular etiology of PCa is not fully understood, partly due to lack of adequate access to metastatic lesions that are mostly homed to bone. Furthermore, the heterogeneity of tumour cells may not be captured by local biopsies. CTCs, on the other hand, can be obtained less-invasively and more accurately represent tumours.

2.3.2. Immunomagnetic Labelling

In addition to the target marker and its antibody, both the labelling method (i.e. direct or indirect labelling) and the magnetic particles (i.e. their size and composition) also affect the performance of an immunomagnetic cell isolation method (i.e. N , $\Delta\chi$, V_p in (2.9)) [137] [139]. Several labelling approaches were empirically evaluated in this research, which are explained next.

Indirect Labelling Using Tetrameric Antibody Complex (TAC) Technology

Initially, an indirect immunomagnetic labelling protocol based on the TAC technology was studied [205]. Bi-specific TAC molecules are made by bridging a mouse anti-dextran antibody (Do-It-Yourself Selection Kit (Cat#: 18098), STEMCELL Tech., BC, Canada) and the anti-PSMA antibody using an antibody against Fc region of the both mouse IgG1 antibodies. This TAC then recognizes PSMA-expressing cancer cells at one end and dextran-coated magnetic particles at the other end (see Figure 2.3). The sample is first incubated with the TAC, allowing the anti-PSMA/PSMA interaction to happen. Dextran-coated particles (50-500nm) are then added to the sample, and it is incubated further to form dextran/anti-dextran interaction.

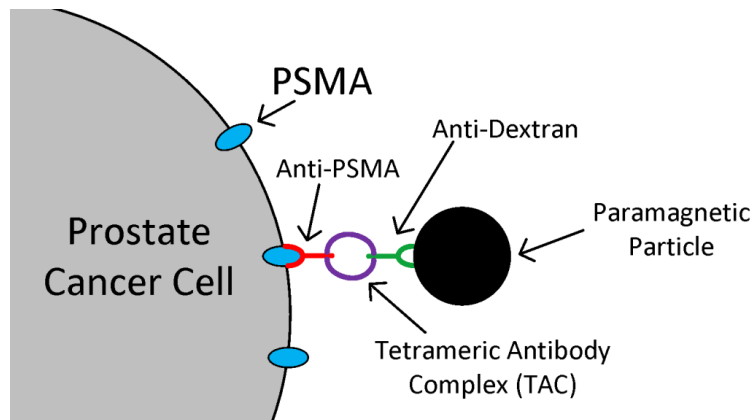


Figure 2.3 Bi-specific TAC-mediated indirect labelling of target cancer cells using magnetic particles.

Direct Labelling Using Anti-mouse IgG Coated Magnetic Beads

Dynabeads[®] Pan Mouse IgG (Cat#: 11041, Invitrogen, CA, USA) magnetic beads were also examined for direct labelling of prostate cancer cells. The beads (4.5 μm in diameter) are already coated with a monoclonal human anti-mouse IgG antibody that in turn recognizes the anti-PSMA mouse IgG1 monoclonal antibody (Fc specific). Once the beads are coupled with the anti-PSMA antibody, they can be incubated with the sample to allow the anti-PSMA/PSMA interaction (see Figure 2.4).

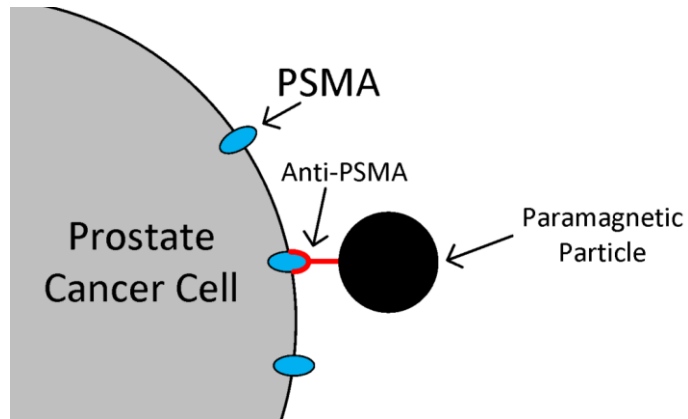


Figure 2.4 Direct labelling using Pan Mouse IgG coated beads

Indirect Labelling Using Streptavidin-Biotin Interaction

As an alternative indirect labelling approach, the performance of Streptavidin-coupled Dynabeads® (Cat#: 11205D, 65601, Invitrogen, CA, USA) magnetic beads was also evaluated. This approach takes advantage of the strong affinity and rather fast binding kinetics of the streptavidin-biotin interaction. The beads are already coupled with streptavidin. Using an EZ-Link™ Sulfo-NHS-LC-Biotinylation Kit (Cat#: 21435, ThermoFisher Scientific, MA, USA), the anti-PSMA antibody can be biotinylated by targeting its primary amine groups. The sample is first incubated with the biotinylated anti-PSMA antibody (forming the anti-PSMA/PSMA interaction), followed by incubation with streptavidin-coupled magnetic beads (forming the streptavidin-biotin interaction).

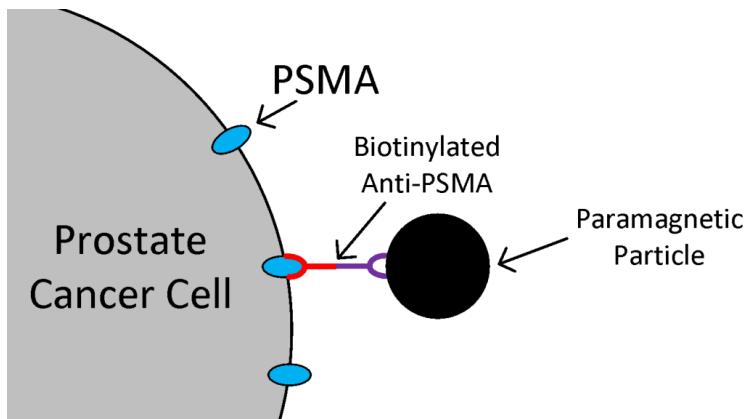


Figure 2.5 Indirect labelling using the streptavidin-biotin interaction

2.3.3. Microfluidic Magnetic Separation Mechanism

The third and most influential factor dominating the performance of an immunomagnetic cell separation approach is the magnetic separation mechanism employed to capture labelled cells (i.e. $\nabla \overline{B}^2$ in (2.9) and the F_a-F_m equilibrium). Several prototypes for continuous-flow microfluidic immunomagnetic isolation of CTCs were designed, fabricated, and tested, which is described in this section.

First-Generation Microfluidic Magnetic Chip

A magnetic microarray for batch-wise single cell sorting of immunomagnetically labelled cells from a unary cell solution with a relatively small volume (80-100 μL) was developed by our group in 2009 [206]. Based on this earlier work, the first-generation integrated chip was initially developed to assess the feasibility of continuous-flow microfluidic immunomagnetic isolation of CTCs using the magnetic capture principle employed in this microarray. The first-generation chip is essentially made of such a magnetic microarray component enclosed by a microchannel (see Figure 2.6).

Magnetic Component

The magnetic component of the chip is designed and built based on the exceptional magnetic properties of permalloy as well as established techniques for microfabrication of permalloy structures [207] [208]. A nickel-iron (80%-20%) alloy, permalloy, is a soft magnetic material with high permeability and low coercivity. Therefore, in the presence of an external magnetic field, permalloy absorbs magnetic field lines and becomes highly magnetized (due to its high permeability), while it loses its magnetism once the field is removed (due to its low coercivity). The magnetic component is composed of thousands of magnetic microtraps that are fabricated on a glass substrate. These microtraps are formed by geometrically modifying permalloy strips (6-10 μm thick, 120 μm wide, 30 μm apart), creating arrays of numerous sawtooth dentations at both sides of each strip (see Figure 2.7). When the direction of the external “activating” magnetic field is parallel to the longer axes of the permalloy strips (i.e. S and N poles at both ends of strips), the highest MFD spots will be formed at the center of each dentation. The strong field gradient produced by these MFD hot spots causes the sawtooth dentations to act almost as individual micromagnets or magnetic microtraps. When the external magnetic field is large enough, permalloy strips become saturated. As a result, the MFD and therefore the

field gradient produced by microtraps across the chip become nearly identical. With the maximum MFD at the center of each sawtooth microtrap, the MFD gradient vectors and therefore the magnetic force on a labelled cell around each microtrap point into the center of the microtrap. Thus, a magnetically labelled cell would be pulled into and captured on a microtrap when it gets sufficiently close (i.e. a few μm) to it (see Figure 2.7 for more details).

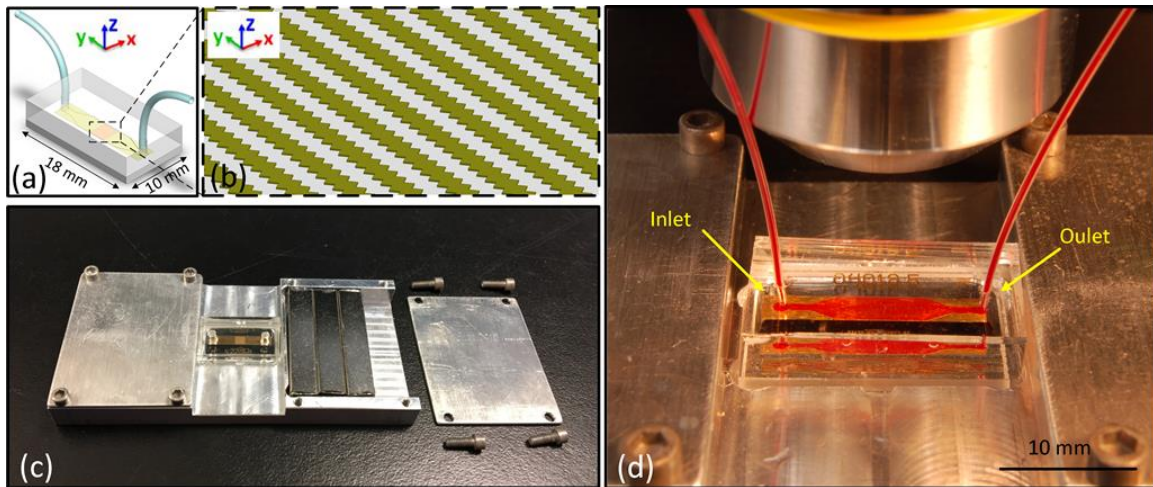


Figure 2.6 (a) A schematic of the first-generation integrated microfluidic magnetic chip. The top (transparent) part is a PDMS microfluidic component in which a $55 \pm 5\text{-}\mu\text{m}$ microchannel is embedded. The bottom (gray and golden) part is the magnetic component. (b) The magnetic microtrap bed area ($2.4 \times 2.8 \text{ mm}^2$), where magnetic sawtooth microtraps are fabricated on permalloy strips (golden). Cells will be trapped at the valleys defined by the shape of these magnetic microtraps. (c) Magnetic adaptor designed and fabricated to activate the chip and hold it on the microscope stage. (d) Chip-adaptor assembly while processing a blood sample.

Microfluidic Component

The microfluidic component of the first-generation device consists of a straight microchannel ($W \times L \times H = 2.4 \text{ mm} \times 2.8 \text{ mm} \times 55 \mu\text{m}$) that is fabricated in PDMS using standard soft lithography [209]. The internal surface of the PDMS microfluidic component is activated by a brief exposure to air plasma and irreversibly bonded on top of the magnetic component to create the integrated chip. The chip is magnetically activated when it is placed in an external magnetic field in the desired direction created by an adaptor designed and fabricated to hold a stack of N-52 rare earth magnets at either side of the chip (Figures 2.6 and 2.7). The sample is continuously run through the microchannel and over magnetic microtraps whose higher MFD would pull the anti-PSMA labelled cells toward the center of microtraps where the MFD is the highest. COMSOL simulation results

indicated that the MFD gradient created by permalloy microtraps can effectively manipulate labelled cells within 30 μm ; therefore, considering the size of a typical cancer cell (20 μm), the height of microchamber was set to 55 ± 5 μm .

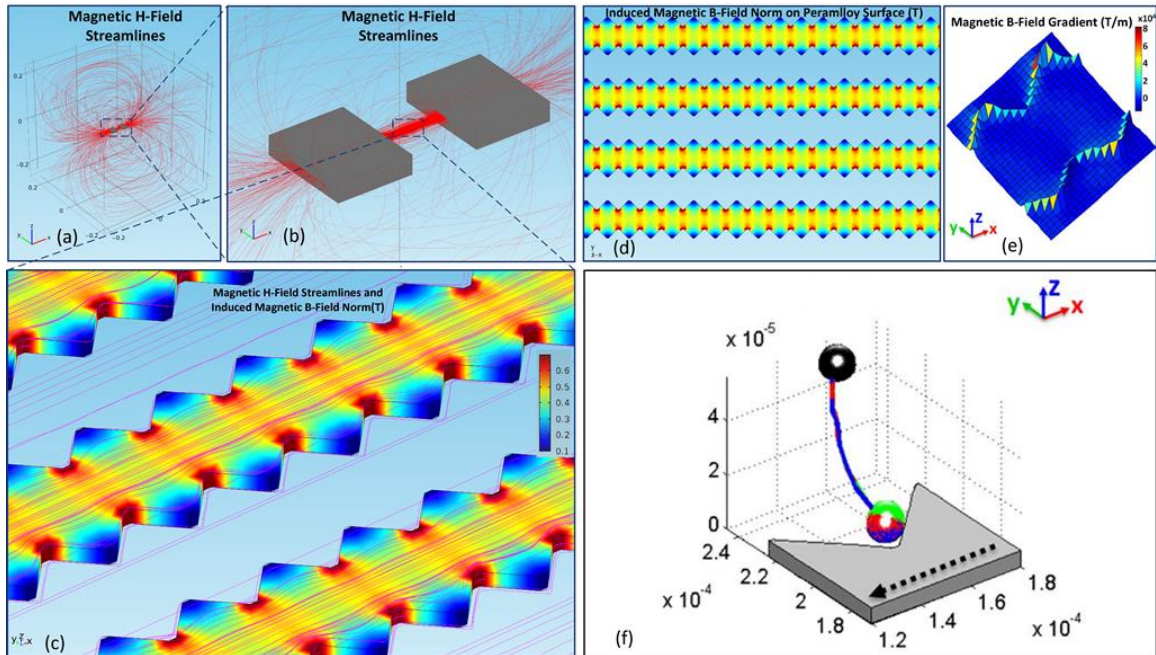


Figure 2.7 COMSOL simulation of the magnetic component of the integrated chip. Finite element models were defined and solved in COMSOL Multiphysics® V.5.1 (COMSOL Inc., CA, USA). Magnetic models were developed using AC/DC Module (Magnetic Fields, No Currents Interface). The magnetic model only takes into account magnetic components (i.e. the external “activating” permanent magnets and the permalloy strips). All other components have a relative permeability equal to 1 with no remnant magnetism and therefore are not considered in this model. (a) Magnetic H-field lines (red streamlines) generated by a pair of permanent magnets (dark cubes). The medium is a 500 mm³ cube filled with air. (b) The high permeability of permalloy strips located between two magnets provides a path with a lower magnetic reluctance, attracting magnetic field lines. (c) As magnetic field lines pass through permalloy strips, due to the narrower width of strips between sawtooth dentations, magnetic field lines redirect and squeeze through these area, causing a maximum MFD (B-field) to be formed at the center of each sawtooth dentation. (d) The maximum MFD formed at the center of microtraps across the device is nearly identical once the permalloy is saturated. (e) The MFD gradient as plotted at 15 μm above the substrates shows that the gradient value is the highest at the center of each dentation [210]. (f) Simulated cell path close to the magnetic microtrap [210]. The arrow shows the flow direction.

Preliminary experiments using first-generation prototypes confirmed the assumption that the proposed microfluidic immunomagnetic approach can capture labelled cells once they reach magnetic microtraps within the chip. This can be mainly associated with the high MFD gradient produced at microtraps and the overexpression of

PSMA, which, in turn, increases the magnetic particle load on labelled cells. Moreover, minimum non-specific adhesion of non-target cells on the chip surface was observed, which can be mainly explained by the hydrodynamic shear experienced by all cells in the microchannel. While these results confirmed the potential of the proposed approach in general, some factors rendered the first-generation device far from being practically useful. The effective magnetic microtrap bed in this design was too small ($2.4 \times 2.8 \text{ mm}^2$), which reduced the recovery rate significantly. In practice, not all cancer cells are labelled equally, and those cells that carry less magnetic particles would experience a smaller magnetic force. Therefore, if not successfully captured within this limited trapping area, these cells would simply be missed. A larger magnetic microtrap bed area could improve the recovery rate by increasing the rate of capturing those cells that were missed by previous microtraps. Furthermore, the small width of the magnetic microtrap bed on the magnetic component (hence, the microchannel width) significantly reduced the maximum allowable flow rate (i.e. throughput). Considering the direction of the magnetic field required to activate the chip in this design, this small flow rate (which translates to a relatively small hydrodynamic shear at the inlet) also resulted in the stoppage of many labelled cells at the macro-to-micro interfacing, tubing, and the chip inlet, which prevented them from entering the microchannel and reaching microtraps.

Second-Generation Microfluidic Magnetic Chip

Having the proposed microfluidic immunomagnetic cell isolation working principle verified using the first-generation chip, second-generation prototypes were designed, fabricated, and tested to address the issues mentioned earlier and further optimize the cell capture performance (see Figure 2.8). Like the first-generation device, all second-generation prototypes are composed of two parts: a permalloy-based magnetic component and a PDMS-based microfluidic counterpart that are irreversibly bonded and together form an integrated microfluidic magnetic chip.

Magnetic Component

Several modifications were considered while designing the magnetic component of second-generation prototypes. The overall size and, particularly, the width of the magnetic microtrap bed area was significantly increased (up to 10X) in all designs. Not only does this increase the effective size of the magnetic capture bed, but it also allows up to 10X increase in throughput without jeopardizing the recovery rate. The dimensions

were designed with the main consideration being the strength of the external magnetic H-field generated by the pair of N-52 rare earth magnets used to magnetize permalloy-based microtrap structures. Earlier experimental observations showed that the best cell capture performance is achieved when the magnets are placed ~30 mm away from each other. Therefore, the magnetic component's dimension along the external magnetic field's direction was set to 25-30 mm.

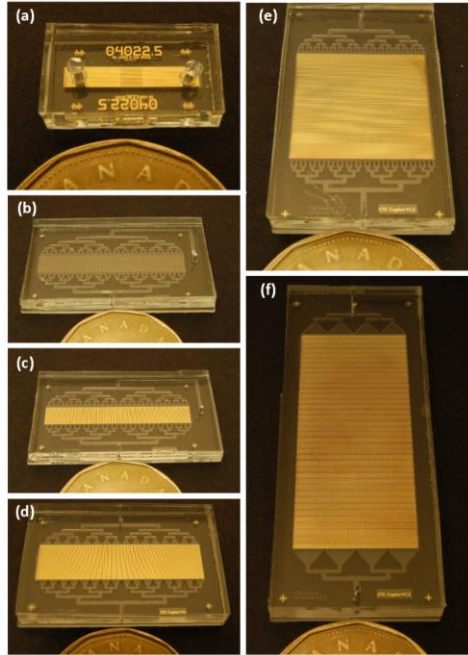


Figure 2.8 A first-generation device (a) along with a few second-generation prototypes (b-f). Notice the difference in the overall size and the magnetic capture bed area among different prototypes. In all second-generation prototypes, the chip outlet is located close the bottom of photographs.

The effects of the microtrap shape and size and the direction of external magnetization field were also investigated. While preliminary experiments using second-generation prototypes based on the original sawtooth design showed high recovery rates, the occasional capture of double or multiple cells on a single microtrap rendered an initial objective of capturing single cells per single microtrap unattainable. To address this issue, individual physically-separated magnetic microtrap structures (as opposed to multiple sawtooth microtraps on a single permalloy strip) were studied. It was assumed that such a design would provide enough MFD to capture labelled cells but the smaller physical footprint of each microtrap structure (and its corresponding MFD) would hinder the capture of subsequent cells on a previously occupied microtrap. Three different designs for the shape of microtraps were studied, namely: Pillar, Star, and Double-Dentation.

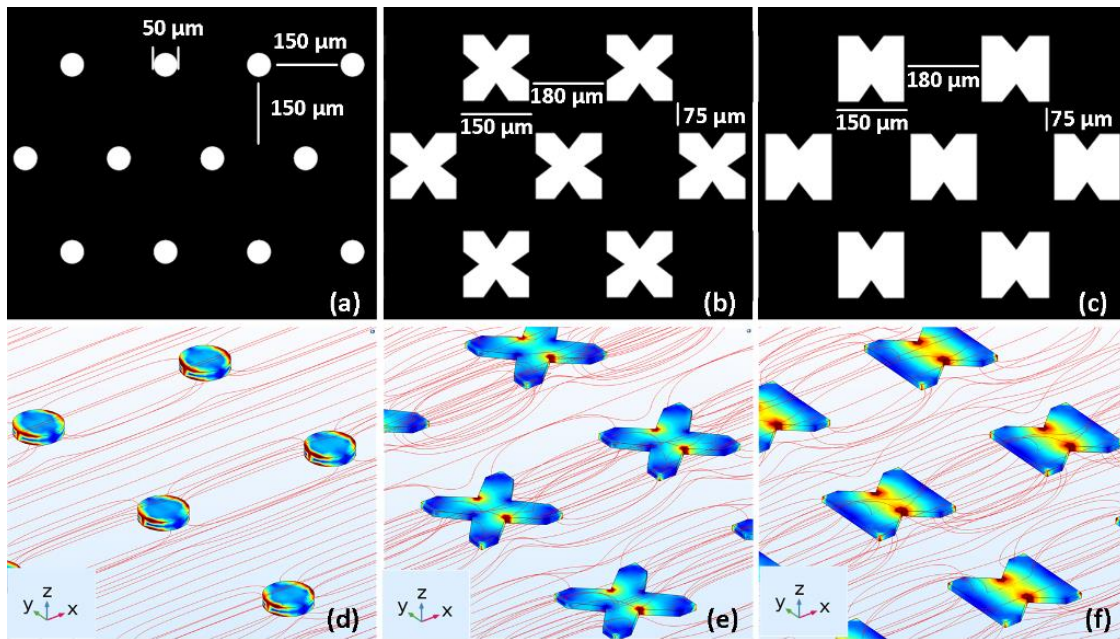


Figure 2.9 Different microtrap shapes (a: Pillar, b: Star, c: Double-Dentation) and configurations studied in second-generation prototypes. (d)-(f) Magnetic H-field lines (red) and induced magnetic B-fields within microraptraps. The fluid flow direction in (d) is aligned with the x-axis, whereas it is parallel to the y-axis in (e) and (f).

Furthermore, the composition of electroplated permalloy microstructures was empirically adjusted to achieve the nominal iron-to-nickel ratio (80:20), which is associated with the optimal behaviour (i.e. maximum permeability and minimum coercivity) of permalloy. To this end, several tests were carried out in which permalloy structures were electroplated at different current density values using the previously established bath recipes [208] [211].

Microfluidic Component

The microfluidic component in all second-generation prototypes is made of a microfluidic flow distribution manifold and a central microchamber. The manifold itself is composed of a network of bifurcation microchannels and diffusers (see Figures 2.8 and 2.11). The microchamber encloses microtraps and carries the sample flowing over microtraps. Considering the overall size of second-generation devices, the width and length of microchambers should be in the centimeter scale, while its height would be in the micrometer scale. To efficiently deliver a sample from the chip inlet to such a microchamber with a uniform flow across its width, a microfluidic flow distribution manifold is needed. The manifold uses a network of bifurcations to sequentially split the incoming flow and ultimately, through diffusers, deliver a uniform flow across the microchamber and

over microtraps. Note that having an even flow across the width of a microchamber is essential, as the magnetic capture is governed by an equilibrium between hydrodynamic drag (F_d) and magnetic (F_m) forces acting on the labelled cells. An uneven flow across the microchamber translates into different values for the drag force acting on cells at different locations and would consequently result in difference in the capture efficiency across the microchamber. Increasing the number of diffusers improves the uniformity of the flow and its velocity; however, it increases the number of bifurcation generations, which, in turn, increases the length of the manifold and the overall length of the chip. However, the length of prototypes is generally limited and is dictated by the size and intensity of the external magnetic H-field, which magnetizes permalloy-based magnetic microtraps. A weak H-field would reduce the $\nabla \vec{B}^2$ associated with microtraps and could hamper the recovery rate. To design the manifold, several general bifurcation structures, such as Tee, Tree, and Circular, were initially studied [212] [213] [214] (see Figure 2.10). It was concluded that the Tee structure has the highest overall hydraulic resistance and its flow uniformity is not ideal, but it is the most compact structure. Since having the minimum length along the direction of the external magnetic field had the highest priority in designing the manifold, a Tee structure with rounded corners for branches was selected (Figure 2.10.b).

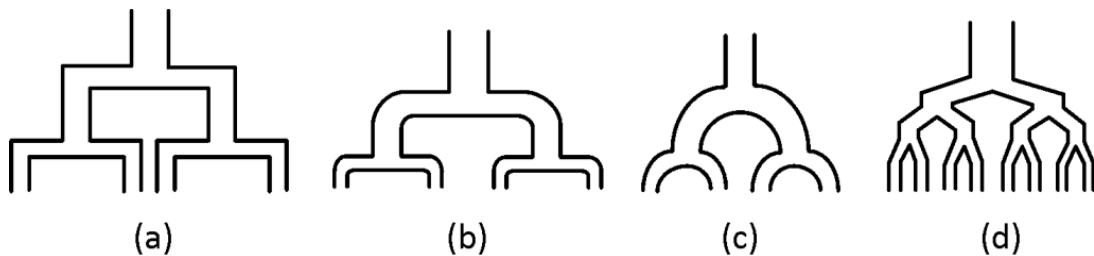


Figure 2.10 General structure of different bifurcation designs studied for developing second-generation prototypes: (a) Tee, (b) Tee with rounded corners, (c) Circular, and (d) Tree.

Considering the constant depth of microchannels and the microchamber across the microfluidic component ($55 \pm 5 \mu\text{m}$), to further design the manifold, the width and length of each branch should be designed. To define the width of each branch, the width of the last generation branch (directly connected to diffusers) was determined first, and the remaining upstream generations were defined accordingly. For instance, for a 32-mm-wide microchamber that is fed by 32 diffusers (this value is optimized empirically via computational fluid dynamics (CFD) simulation – see Appendix C), each diffuser would feed a 1-mm-wide area of the microchamber. Assuming that the width of the last

generation bifurcation microchannel expanded by a diffuser should be $>1/5$ of that of the diffuser, the width of such a microchannel would be set to 250 μm . Both COMSOL CFD simulations and our earlier experiments had shown that such a value would be large enough to minimize the hydraulic resistance but small enough to provide enough shear stress to prevent cell stoppage at diffusers. Having this width defined, several approaches can be used to design the width of upstream branches. A constant width for all other branches increases the overall hydraulic resistance of the manifold significantly, which could easily break the chip due to a high pressure at the inlet. To reduce this resistance and the required power, the width of each upstream generation can be proportionally increased. These values were designed based on Murray's principle and optimized through CFD simulation to ensure the flow uniformity [215]. The length of each branch was defined such that a fully developed flow is attained at the end of each branch. Considering the dimensions of microchannels in the manifold, the typical entrance length for all branches is $<100 \mu\text{m}$. To confirm a fully developed flow and account for fabrication errors, the length of branches was set to 200-300 μm . Finally, the size of diffusers feeding the microchamber can also affect the uniformity of the flow in the microchamber. For example, relatively longer diffusers provide a better uniformity [216]. The final size of diffusers was chosen based on CFD simulations (see Appendix C). Figure 2.11 depicts the flow profile in the microfluidic component of a second-generation prototype.

Given the small Reynolds number associated with typical nominal flow rates used in second generation prototypes, the flow within the microchamber is highly laminar. As such, labelled cells flowing within the streamlines will move towards microtraps only if the magnetic force (F_m) exerted on them overcomes the hydrodynamic drag force (F_d). Since the PSMA expression is not equal on all target cancer cells, some cells may not adsorb and carry enough magnetic particles/beads to experience enough magnetic pull when they arrive at the magnetic capture bed. To address this issue, the F_d - F_m balance can be altered by breaking the laminar flow streams and inducing a diffusive movement of cells inside the microchamber, allowing cells, including those with less magnetic particle/bead load, to get closer to microtraps and experience a larger F_m . To this end, a passive herringbone mixer was designed and implemented in the microchamber to increase the diffusive movement of the cells when they arrive at microtraps [217] [218]. The mixer is composed of herringbone arrays of 50x50 μm (widthxdepth) grooves incorporated in the upper surface of the microchamber (see Figure 2.12).

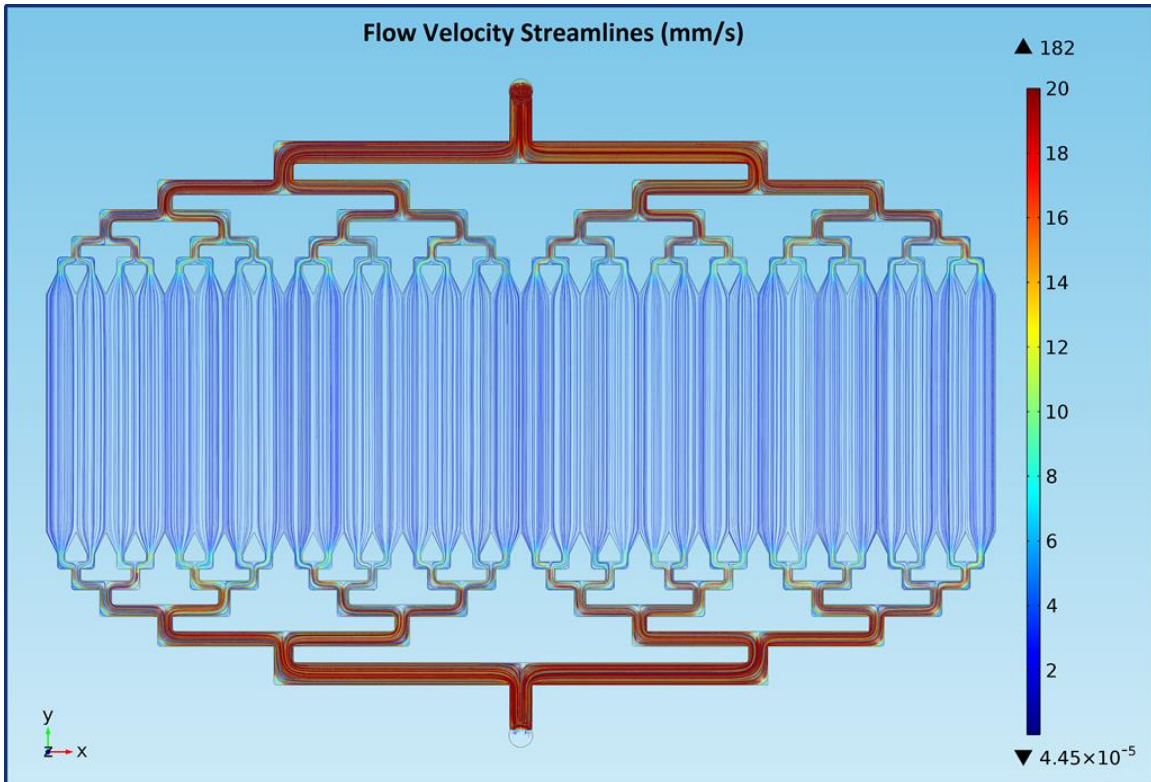


Figure 2.11 COMSOL CFD results showing uniform flow streamlines in a second-generation microfluidic component, which allows the sample to be distributed evenly over the underlying magnetic microtraps. The velocity numerical values are associated with the nominal flow rate (100 $\mu\text{L}/\text{min}$) at the chip inlet (top). The interaction between the fluid flow and permalloy strips located at the bottom of the microchamber were not taken into account in the microfluidic model. Finite element models were defined and solved in COMSOL Multiphysics® V.5.1. Microfluidic models were developed using Fluid Flow Module (Laminar Flow Interface).

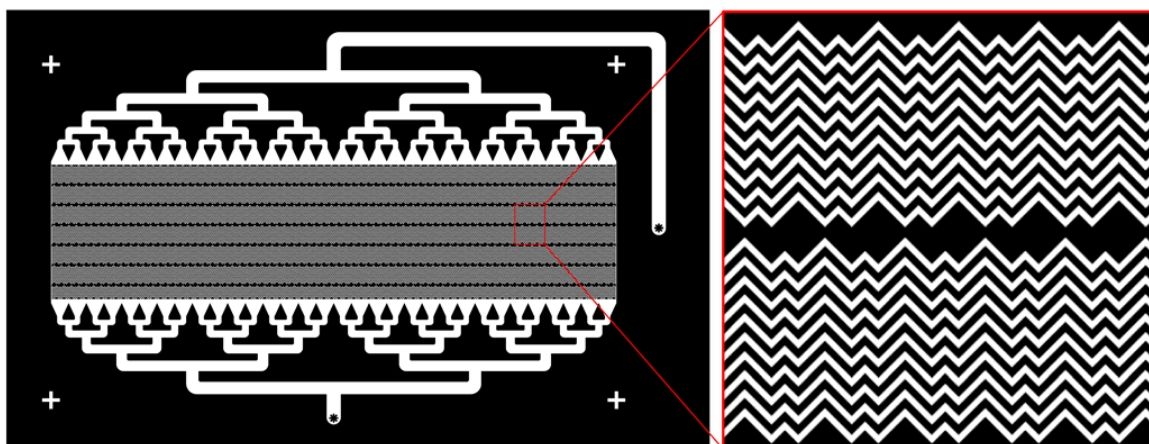


Figure 2.12 A schematic of a second-generation microfluidic component with enhanced mixing capability of sample within the microchamber. The mixing is achieved by arrays of herringbone grooves embedded in the inner surface of microchamber.

2.3.4. Macro-to-Micro Interfacing

In addition to the three specific key elements that affect the performance of a microfluidic immunomagnetic CTC isolation method (i.e., the marker and antibody, the immunomagnetic labelling protocol, and the magnetic separation mechanism), there are other general factors (e.g., conditions under which the blood sample is drawn, kept, and handled) that also influence the efficiency of any CTC isolation method [180]. In particular, for microfluidic approaches, the macro-to-micro interfacing is a critical consideration [219]. Referring to components involved in delivering the sample from the outside world to the microfluidic device, an optimal macro-to-micro interface should minimize dead volumes and possibility of cell loss prior to delivery of the sample to the device, and enable the easy and efficient transfer of different agents (e.g., priming agent, wash buffers, labelling agents, etc.) to the device from the outside world. After experimental evaluation of several components and configurations (i.e. pumps, reservoirs, tubing, interconnections, inlet designs, etc.), the optimized macro-to-micro interfacing with almost zero cell loss, <20 μ L dead volume, and capability of applying multiple agents without disturbing the normal function of the microfluidic device was also developed in this research. Further details of this interfacing are discussed later in the Results Section (page 67).

2.3.5. Cell Line and Cell Culture

LNCaP cells, a prostate cancer cell line, were selected as the target cancer cell for all experiments. LNCaP cells are androgen-sensitive cells that mimic the specific *in vivo* characteristics of prostate carcinoma cells and are extensively used in prostate cancer research [220]. LNCaP cells (Cat#: CRL-1740, ATCC, VA, USA) were generally maintained in 10-mm culture plates in Corning's RPMI 1640 medium (Cat#: CA45000-396, VWR, ON, Canada) supplemented with 10% fetal bovine serum (FBS) (Cat#: 16000-036, Invitrogen, CA, USA), 1% Penicillin–Streptomycin (Cat#: 15140-12, Invitrogen, CA, USA). The cells were cultured for <30 passages, after which a fresh batch of cells was thawed and used.

2.4. Microfabrication

As mentioned earlier, all prototypes are composed of two parts: a permalloy-based magnetic component and a PDMS-based microfluidic counterpart that are fabricated

separately. The two components are then treated with air plasma using a BD-20AC corona discharger (Electro-Technic, IL, USA) [221], precisely positioned using a precision alignment stage (ABM, CA, USA), and baked to irreversibly bond and form the integrated chip. The magnetic and microfluidic components are fabricated as follows.

2.4.1. Magnetic Component Microfabrication

The magnetic component of all devices (first- and second-generation) is fabricated via a through-mask electroplating process (see Figure 2.13):

(1) A RCA cleaned 1 mm thick 4" Borofloat glass wafer (University Wafer, MA, USA) was used as the substrate.

(2) A 30-nm thick Cr adhesion layer and a 120-nm thick Au seed layer were sputtered on the substrate.

(3) PMGI SF-19 photoresist (MicroChem, MA, USA) was spun at 4000 rpm for 30 seconds and baked at 180°C for 2 min, yielding a 200-nm thick adhesion layer for the electroplating mask.

(4) AZ-9260 photoresist (Capitol Scientific, TX, USA) was spun and patterned to create the electroplating mask. It was spun at 2250 rpm for 30 seconds and baked at 110°C for 7 min to achieve a thickness of $15 \pm 1 \mu\text{m}$. The wafer was then cooled down to the room temperature and soaked in deionized (DI) water for 10 min to hydrate the coated film.

(5) The wafer was blown dry with N₂, and the photoresist layer was exposed in a contact mask aligner with the nominal dose.

(6) The exposed photoresist was then developed in 4:1 DI:AZ-400K developer (Capitol Scientific, TX, USA) until the endpoint was visually determined (approximately 6 min). The wafer was rinsed in DI water and blown dry with N₂.

(7) A plasma ashing process was performed for 3 min at 80 mTorr and 150 W with a gas flow of 15 sccm O₂ to obtain a clean gold seed layer for the subsequent electrodeposition step.

(8) The electroplating bath was prepared in a 4L PYREX beaker as follows: 39 g/L $\text{NiCl}_2 \cdot 6\text{H}_2\text{O}$, 16.3 g/L $\text{NiSO}_4 \cdot 6\text{H}_2\text{O}$, 25 g/L H_3BO_4 , 1.5 g/L $\text{C}_7\text{H}_4\text{NNaO}_3\text{S} \cdot x\text{H}_2\text{O}$ (for stress adjustment), 25 g/L NaCl, 1.4 g/L $\text{FeSO}_4 \cdot 7\text{H}_2\text{O}$ in DI water [208]. All chemicals were obtained from Sigma-Aldrich, ON, Canada. The solution pH was adjusted to 2.7. The electroplating setup included a custom-made wafer holder with multiple contact points (OAI/Idonus, CA, USA). A 5"x5" nickel plate suspended ~5 cm away directly in front of the wafer holder in the bath was used as the anode. A magnetic stirrer was used to continuously mix the bath. For different magnetic microtraps designs, the electrodeposition was performed at an experimentally optimized current density and time at the clean-room temperature (19°C), yielding an average thickness of 10 μm . The wafer was then removed from the bath, rinsed with DI water, and blown dry in N_2 .

(9) Following the electrodeposition, the photoresist mold was lifted off by dipping the wafer in acetone accompanied by ultrasonic agitation.

(10) The seed layer was then removed in a TFAC gold etchant solution that had been heated to 65°C. Note that TFAC is a potentially toxic cyanide-based gold etchant, but it does not attack the permalloy. Following a thorough rinse in running DI water, the Cr adhesion layer was removed by dipping the wafer in a TFE Cr etchant at the clean-room temperature for 30 seconds. Both etchants were obtained from Transene Co. Inc., MA, USA.

(11) To ensure biocompatibility, the permalloy structures were encapsulated by a 200-nm gold layer that was electroless-deposited using the Bright Electroless Gold solution (Transene Co. Inc., MA, USA) at 90°C for 8 min.

(12) The wafer was then diced into individual chips using a saw machine.

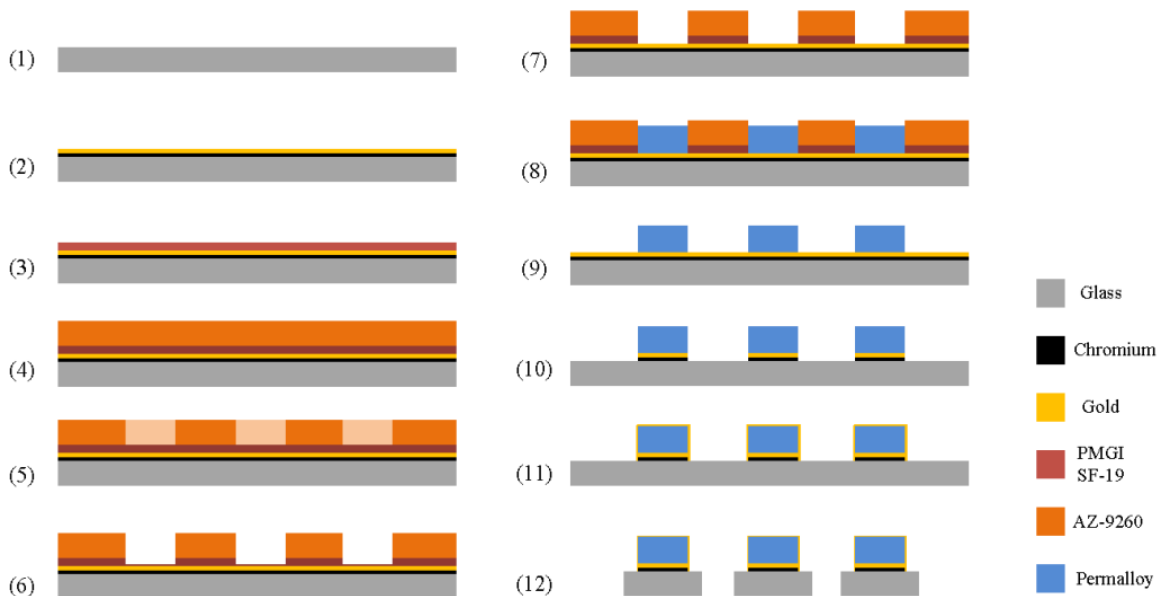


Figure 2.13 The fabrication process for the magnetic component

2.4.2. Microfluidic Component Microfabrication

Except for devices with an embedded herringbone mixer in the microchamber, the microfluidic component of all devices was fabricated using soft lithography as follows [209] (see Figure 2.14):

(1) A RCA cleaned 0.5 mm thick 4" silicon wafer (University Wafer, MA, USA) was used as the substrate to fabricate the SU-8 mold.

(2) SU-8 2035 photoresist (MicroChem, MA, USA) was spun at 2250 rpm for 30 seconds to achieve the nominal thickness of $55 \pm 5 \mu\text{m}$. It is worth noting that unlike the 2050 formulation, the lower viscosity of the 2035 formulation greatly helps reducing the formation of bubbles when the photoresist is poured on the wafer.

(3) The photoresist was soft baked at 65°C for 3 min, followed by 6 min at 95°C and another 3 min at 65°C . The wafer was then cooled to the room temperature.

(4) The photoresist was exposed in a contact mask aligner with the nominal dose.

(5) The hard bake was performed similar to the soft bake (step 3).

(6) The unexposed photoresist was developed in SU-8 developer (MicroChem, MA, USA) until the endpoint was visually determined (approximately 5 min). The

wafer was then rinsed in fresh SU-8 developer followed by isopropanol (IPA) and blown dry with N₂.

(7) The post exposure bake was performed at 120°C for 7 min.

(8) To build the microfluidic component, PDMS and the cross-linking agent (SYLGARD® 184, Dow Corning, MI, USA) were mixed (10:1, by weight), degassed, and casted over the SU-8 mold that had been placed in an aluminum dish. The PDMS sample was cured in a convection oven at 80°C for 3 hours.

(9) The PDMS cast was then carefully pilled off and parts were cut using a blade.

(10) Inlet and outlet holes were made using a MP10-UNV punch machine (SYNEO, TX, USA).

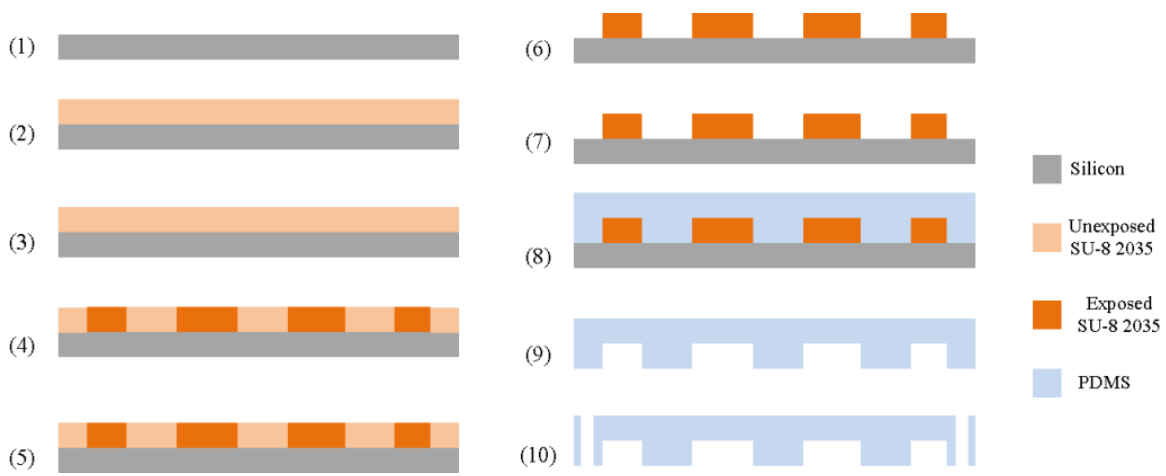


Figure 2.14 The fabrication process for the microfluidic component

For microfluidic components with a herringbone mixer, another recipe was developed to fabricate a two-layer SU-8 mold structure as follows (see Figure 2.15):

(1) A RCA cleaned 0.5 mm thick 4" silicon wafer (University Wafer, MA, USA) was used as the substrate to fabricate the SU-8 mold.

(2) The first SU-8 2035 photoresist layer (MicroChem, MA, USA) was spun at 2250 rpm for 30 seconds to achieve the nominal thickness of $55 \pm 5 \mu\text{m}$.

(3) The photoresist was soft baked at 65°C for 5 min, followed by 7 min at 95°C and another 5 min at 65°C. The wafer was then slowly cooled to the room temperature.

(4) The photoresist was exposed in a contact mask aligner with the nominal dose.

(5) The hard bake was performed similar to the soft bake (step 3) followed by cool down to the room temperature.

(6) The second SU-8 2035 photoresist layer (MicroChem, MA, USA) was spun on top of the first layer at 2250 rpm for 30 seconds to achieve the nominal thickness of 55 ± 5 μm .

(7) The second layer photoresist was soft baked at 65°C for 7 min, followed by 15 min at 95°C. The wafer was then gradually cooled to the room temperature.

(8) The perimeter of wafer where the alignment marks were located was carefully developed without affecting other structures on the wafer. This was achieved by tilting the wafer and leaving its edge in SU-8 developer for 10 min. The developed areas were then carefully washed with IPA and blown dry with N₂.

(9) The photoresist layer was exposed in a contact mask aligner with the empirically optimized dose. This dose is normally a third of the required dose for the first layer.

(10) The hard bake was performed similar to the soft bake (step 3) followed by gradual cool down to the room temperature.

(11) The unexposed photoresist (both first and second layers) was developed in SU-8 developer (MicroChem, MA, USA) until the endpoint was visually determined (approximately 7 min). The wafer was then rinsed in fresh SU-8 developer followed by IPA and blown dry with N₂.

(12) The post exposure bake was performed at 120°C for 10 min.

(13) To build the microfluidic component, PDMS and the cross-linking agent (SYLGARD® 184, Dow Corning, MI, USA) were mixed (10:1, by weight), degassed,

and casted over the SU-8 mold that had been placed in an aluminum dish. The PDMS sample was cured in a convection oven at 80°C for 3 hours.

(14) The PDMS cast was then carefully pilled off and parts were cut using a blade, and inlet and outlet holes were made using a MP10-UNV punch machine (SYNEO, TX, USA).

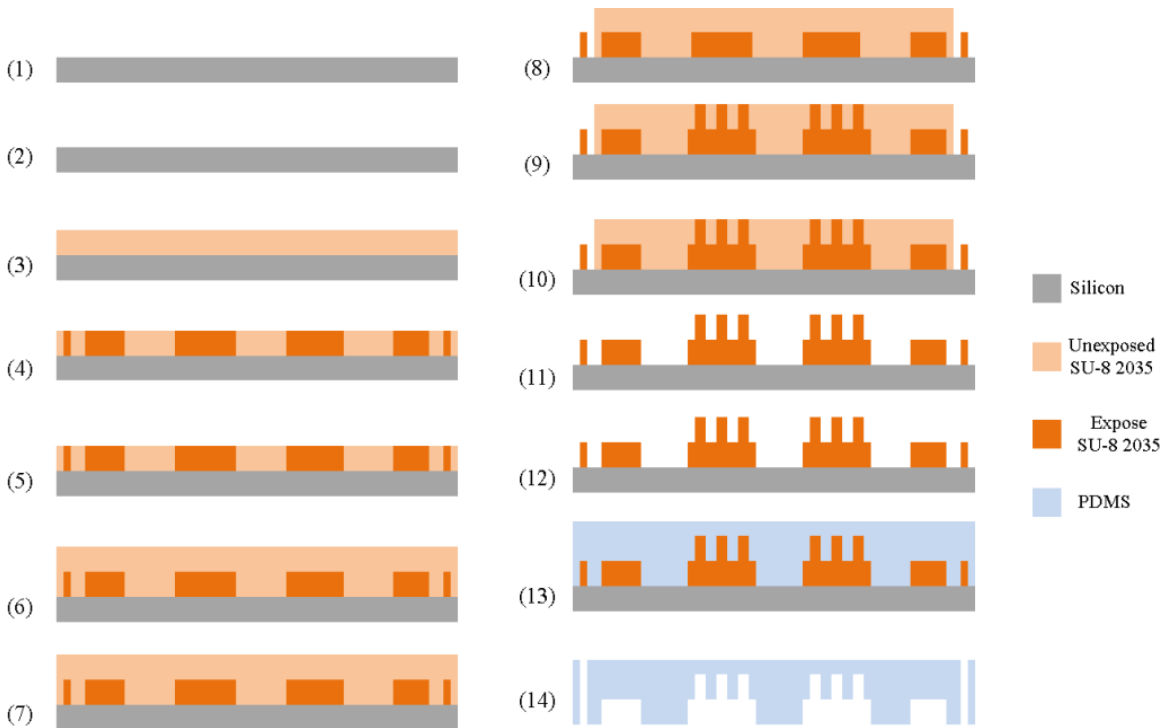


Figure 2.15 The fabrication process for the microfluidic component with embedded herringbone mixer

2.5. Results

2.5.1. Immunomagnetic Labelling Efficiency and Experimental Optimization

As previously explained, three different labelling approaches were experimentally evaluated in this research. Indirect labelling of LNCaP cells using the TAC technology was generally performed by first thoroughly mixing and incubating the sample with the PSMA-based TAC cocktail at a suggested concentration of 1.5 µg/mL at the room temperature for 15 minutes. Magnetic particles (50 or 500nm) were then added to the sample, and it was further incubated at the room temperature for another 15 minutes. Due to the

extremely small size of magnetic particles used in this approach, it was not possible to visualize and precisely measure the magnetic particle load per cell (see Figure 2.16.a). However, as it is discussed later in this section, multiple experiments using both first- and second-generation devices indicated that the relatively small magnetic force associated with the overall low magnetic particle load per cell (due to the small size of particles) makes this labelling approach suboptimal for a continuous-flow microfluidic approach. This is mainly because in such approaches moving cells within the device are exposed to the magnetic field for a short period of time (<10 seconds) and if they are not captured during this limited exposure, they will be missed. Therefore, relatively higher magnetic forces are necessary for a continuous-flow microfluidic approach.

Direct labelling of LNCaP cells was achieved by incubating the sample with 4.5 μm beads (coupled with the anti-PSMA antibody) at the room temperature or 4° C and at different concentrations for 45 minutes on a rocker. Labelling optimization studies was performed by titrating increasing concentrations of beads and evaluating the labelling efficiency. It was concluded that to achieve 100% labelling efficiency (defined as having at least one bead per a target cell), the bead concentration should be $> 5 \times 10^7$ beads/mL. It was later found that minimizing the bead concentration is a vital requirement to improve the overall performance of the system, as free beads could intervene with the capture and visual detection of cells on the chip. In addition, the fairly large size of these beads (see Figure 2.16.b) could negatively affect the capture process, as the very large magnetic force associated with these beads could deviate and sometimes stop labelled cells moving in the flow distribution manifold, preventing them from reaching magnetic microtraps.

Finally, indirect labelling based on the streptavidin-biotin interaction that has a strong affinity and fast binding kinetics and using smaller beads (1 and 2.8 μm) was also evaluated. LNCaP cells were labelled by first incubating the sample with the biotinylated anti-PSMA antibody followed by incubating the sample with magnetic beads at the room temperature on a vortex mixer (see Figure 2.16.c and 2.16.d). The effect of both incubation times was experimentally studied and it was concluded that the labelling efficiency (as defined previously) can be achieved by 40 minutes and 50 minutes for antibody and bead incubation durations, respectively. Furthermore, the antibody and beads concentrations were optimized using titration studies (1-1.5 $\mu\text{g/mL}$ and 1×10^7 beads/mL, respectively). In general, this approach proved to be the most efficient and practical labelling method for the proposed immunomagnetic cell isolation strategy in this research.

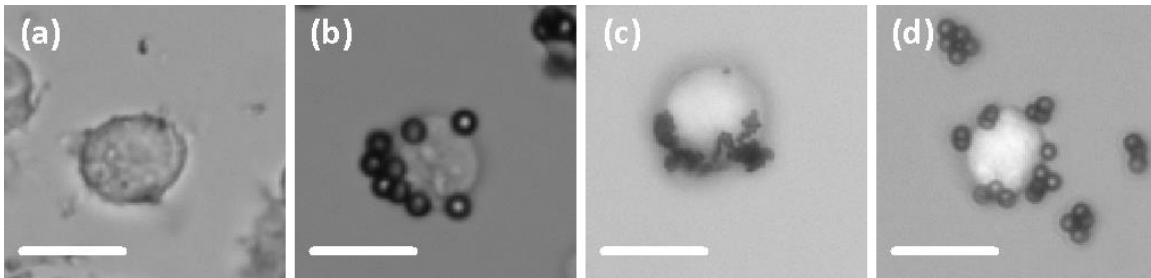


Figure 2.16 LNCaP cells immunomagnetically labelled using (a) indirect approach using the TAC technology and 50-500nm particles, (b) direct approach using anti-mouse IgG coated 4.5 μm beads, (c) indirect approach using streptavidin-coated 1 μm beads, and (d) indirect approach using streptavidin-coated 2.8 μm beads. Scale bars represent 20 μm .

2.5.2. Microfabrication

Magnetic Component Microfabrication

Several prototypes with different designs for the shape and size of magnetic microtraps were fabricated (see Figure 2.17). A critical step in the microfabrication of magnetic components was the electrodeposition of permalloy. The final composition of deposited alloy is a function of the composition of plating bath, the electroplating setup (e.g., the type and size of connections on the cathode, i.e. the electroplating mold), and the current density. To improve the quality of deposited permalloy structures and achieve the nominal composition (i.e. 80% Ni:20% Fe), an established bath composition was first adopted [208], and a custom-made wafer holder with multiple contact points on the perimeter of the mold to provide a uniform electric field (hence, deposition) was acquired. To optimize the remaining variable, i.e. the current density, several structures at different current densities were deposited, and their composition was measured. The elemental analysis of electrodeposited permalloy structures was performed via the energy dispersive X-ray spectroscopy (EDS) technique using two scanning electron microscopy (SEM) systems, the Aspex Explorer and the Helios NanoLab 650 (FEI, OR, USA). It was found that using a current density of 14.5 mA/cm^2 , the composition was in agreement with the nominal values for the most part (see Figure 2.18). However, the measured composition values for relatively small structures (e.g., 30-50 μm posts), showed a noticeable offset from the nominal value, whereas the composition of larger structures on the same device agreed with the nominal value. This discrepancy could have been caused due to the limitations in the accuracy of measurements for smaller structures using the technique used in this study. A more accurate measurement could have been performed using more

advanced material analysis methods, such as X-ray photoelectron spectroscopy (XPS), which was not pursued in this study.

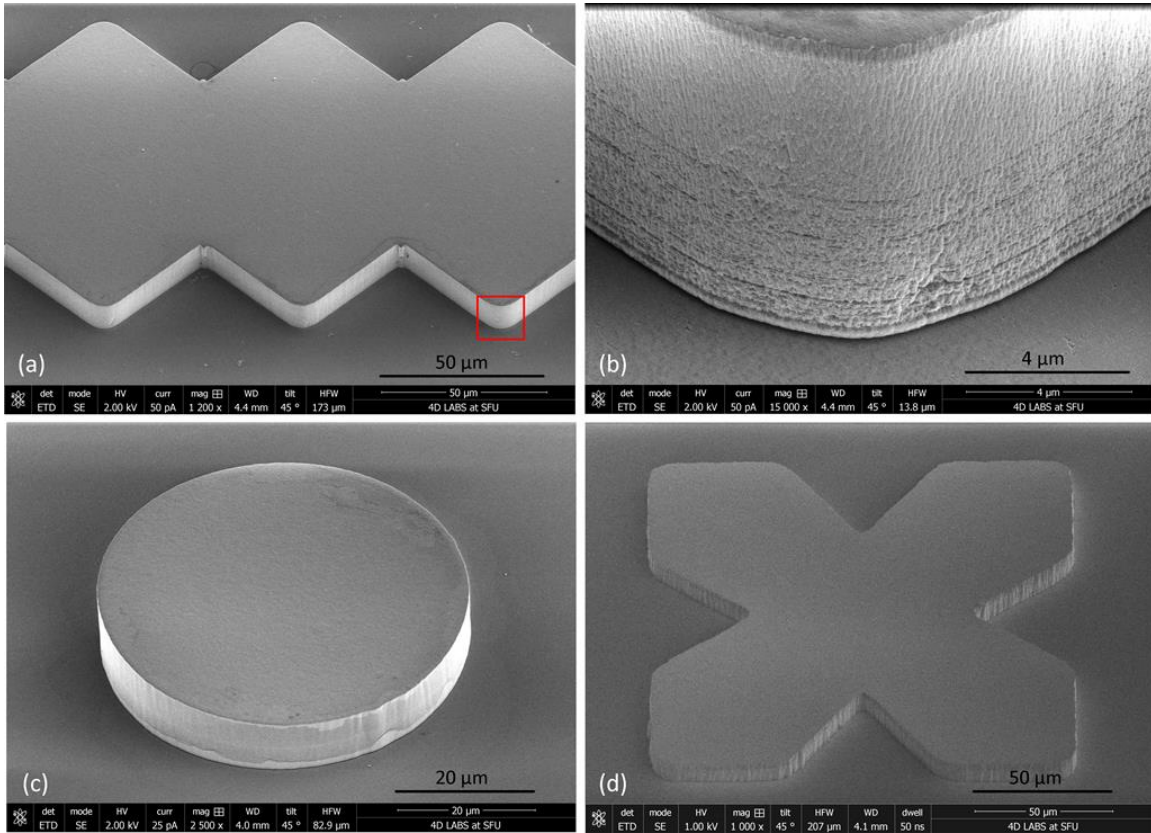


Figure 2.17 SEM view of different permalloy microtrap structures: (a) a Sawtooth structure, (b) closer view of the structure in (a) marked by a red rectangle showing various deposited layers, (c) a Pillar structure, and (d) a Star structure.

Another issue concerning electrodeposited permalloy structures was the difference in the thickness of structures across the wafer as well as across the same structure (see Figure 2.19). This is a well-known phenomenon that happens because of the so-called “edge effect” resulting from increased electrodeposition rate due to current crowding happening on edges of individual features on the plating mold as well as across the wafer [222] [223] [224]. Using the custom-made wafer holder with multiple contact point reduced this effect (<10% thicker at sharp edges). More uniform thickness could have been achieved using the chemical mechanical polishing (CMP) process [225]. However, it was concluded that since such a thickness nonuniformity will not affect the overall cell capture performance of the chips, the CMP process was not necessary.

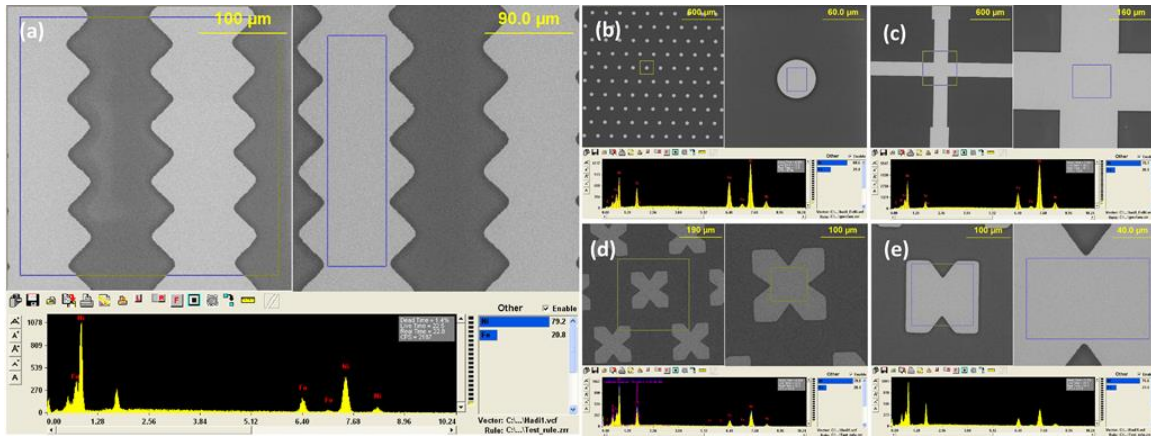


Figure 2.18 SEM EDS analysis of different permalloy structures (light gray). On each panel, the spectroscopy diagram and the bar chart on the bottom row represent constituent elements of the area bounded by the blue rectangle in the right image. On average and at the experimentally the optimized current density, the deposited alloy contains $20\pm 3\%$ nickel and $80\pm 3\%$ iron. The measured permalloy composition values for different structures in this figure are as follow: (a) Sawtooth structure: 79.2%Ni:20.8%Fe, (b) Pillar structure: 68.6%Ni:31.4%Fe, (c) A large alignment mark on the same wafer as for the Pillar structures in (b): 79.1%Ni:20.9% Fe, (d) Star structure: 79.9%Ni:20.1%Fe, and (e) Double-Dentation structure: 76.6%Ni:23.4%Fe.

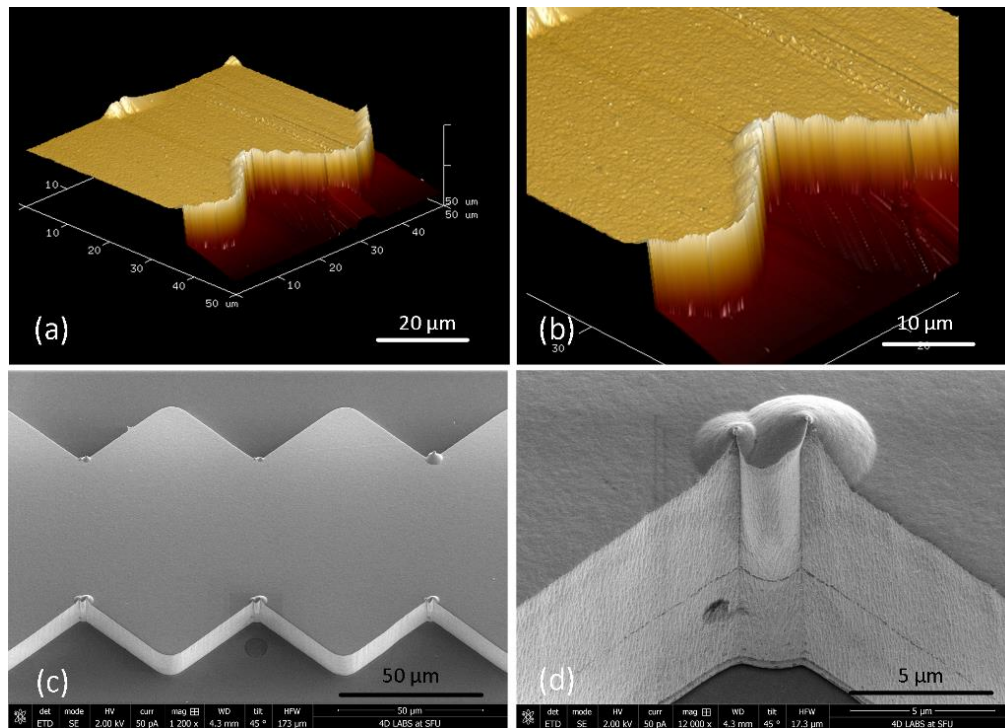


Figure 2.19 The “edge effect” on Sawtooth structures as observed using an atomic force microscopy (AFM) (a-b) and SEM (c-d). (a-b) Structures deposited using a simple wafer holder with two contact point, resulting in more pronounced thickness nonuniformity. (c-d) Improved thickness uniformity when a wafer holder with multiple contact points is used. Thickness nonuniformity is only observed at sharp corners due to the higher rate of current crowding at these locations.

Microfluidic Component Microfabrication

For each microfluidic component design, a master SU-8 mold was initially fabricated and used to cast future PDMS microfluidic parts. Figure 2.20 shows the master SU-8 mold used to cast the PDMS microfluidic component with embedded arrays of herringbone mixer.

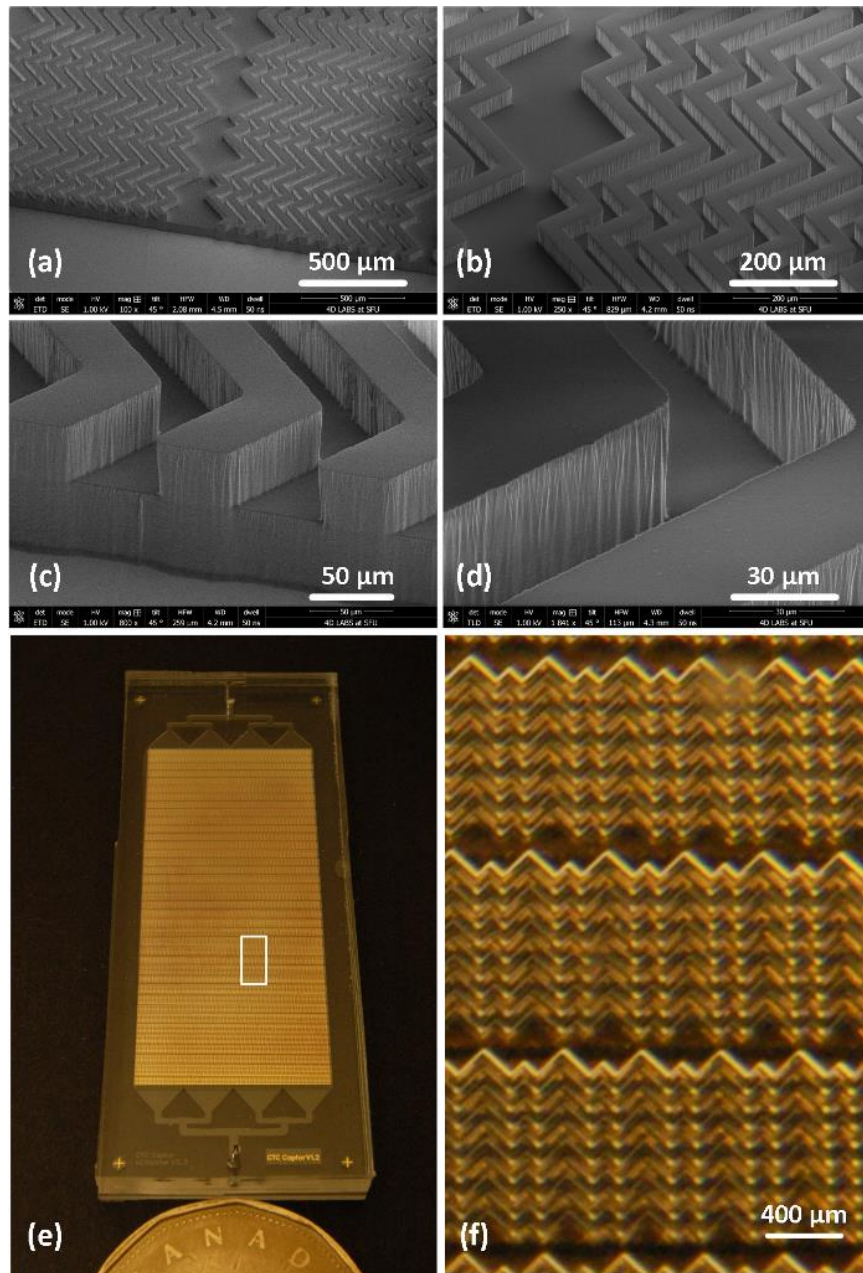


Figure 2.20 (a)-(d) Different SEM views of the master SU-8 mold used to cast the microfluidic component with embedded arrays of herringbone mixer. (e) A second-generation prototype with herringbone mixer embedded in the PDMS component. (f) Closer view of arrays of herringbone mixer highlighted by a white rectangle in (e).

2.5.3. Cell Capture Experiments

Experiments Using First-Generation Devices

Experimental Setup and Sample Preparation

The experimental setup used for these experiments consisted of two major components: an image acquisition system and a pump to continuously run the sample through the chip. The image acquisition system was made of a customized CX-41 Olympus upright microscope equipped with fluorescence, transmission, and reflection modes (Olympus Canada Inc., ON, Canada) and an Infinity-1 CMOS color camera (Lumenera Corporation, ON, Canada). A PHD-2000 syringe pump (Harvard Apparatus, MA, USA) was used to deliver the sample from a 5mL syringe (BD, ON, Canada) to the device at a given flow rate via a Luer-Lok needle and a piece of 0.020" ID×0.060" OD Tygon microbore tubing (Cat#: UZ-06420-02, Cole-Parmer, QC, Canada).

LNCaP cells were immunomagnetically labelled using either 500 nm particles or 4.5 µm beads as explained previously. Jurkat cells, a lymphoid leukemia cell line that was used as a non-target cell in binary solution experiments, were cultured similar to LNCaP cells. For experiments involving blood samples, blood was drawn from healthy Sprague-Dawley rats and kept in Vacutainer® tubes (Cat#: 367862, BD, ON, Canada) at 4°C for no more than 6 hours before each experiment.

Cell Capture Results

Several experiments were initially performed to qualitatively evaluate the feasibility of the proposed immunomagnetic microfluidic cell capture principle and the performance of first-generation devices. Then, to investigate the recovery rate and the macro-to-micro interfacing, isolation of magnetically labelled LNCaP cells (using 500 nm particles) suspended in the buffer solution (3mM EDTA and 1% w/v BSA in PBS) was studied. The recovery rate was defined as the ratio of the number of captured LNCaP cells on the chip to the actual number of cells initially seeded in a sample. Different concentrations of labelled LNCaP cells were suspended in buffer (50-5×10⁴ cells/mL), and the sample was processed at an average flow rate of ~10 µL/min. While it was not possible to reliably count the number of captured cells for higher concentrations of LNCaPs, it was observed that majority of LNCaP cells that had successfully arrived at the magnetic microtrap bed

would be captured. For lower concentrations (50 cells/mL), the recovery rate was 15-25% (n=3).

Next, in order to study the capture specificity (i.e. purity rate), isolation of magnetically labelled LNCaP cells from a binary cell solution (LNCaP/Jurkat) was studied. LNCaP cells were immunomagnetically labelled using 500 nm particles and mixed with Jurkat cells (1×10^6 cells/mL) at different LNCaP:Jurkat ratios (1:100, 1:1000, and 1:10,000) and processed at $\sim 10 \mu\text{L}/\text{min}$. No significant non-specific adhesion or capture of Jurkat cells on the chip was observed, and the recovery rate for LNCaP cells at low concentrations remained at 10-25% (n=3) (see Figure 2.21). Isolation of magnetically labelled LNCaP cells (500 nm particles) from a whole blood sample was also attempted (n=3). A pooled whole blood sample was seeded with 5×10^2 immunomagnetically labelled LNCaPs, diluted 5X, and processed at $\sim 10 \mu\text{L}/\text{min}$. None of the target LNCaP cell was detected on the chip. Moreover, although no major clogging issues were encountered, the non-specific adhesion of blood cells on the chip was noticeable.

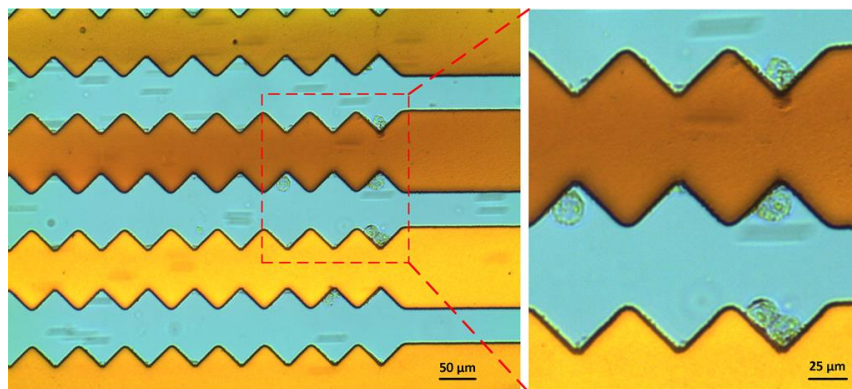


Figure 2.21 Isolation of magnetically labelled LNCaP cells from a binary cell solution (LNCaP/Jurkat). As expected, LNCaP cells are captured at the center of dentations where the MFD is the highest. Notice Jurkat cells ($\sim 10 \mu\text{m}$ in size) moving within the streamlines without being affected. The inset shows a closer view of captured LNCaP cells. Golden layers are gold-coated permalloy structures and blue surface is the glass substrate.

Discussion

As explained earlier, stoppage and loss of target cells at the chip inlet and macro-to-micro interfacing caused by the combined effect of the low flow rate and the external activating magnetic field resulted in an overall low recovery rate. The stoppage issue was worse when $4.5 \mu\text{m}$ beads were used to label LNCaP cells, as these beads created a much stronger magnetic force and resulted in losing many more cells before they arrive

at the magnetic microtrap bed. Moreover, a syringe pump that was used to drive the sample through the chips does not allow a proper mixing of the sample (resulting in cell sedimentation) and changing the running sample (e.g., priming agent, cell sample, wash buffer) without forming bubbles. The low flow rate used in experiments with first-generation chips (hence, the corresponding low hydrodynamic shear) was also caused a noticeable non-specific adhesion of blood cells on the chip. These issues were addressed in designing second-generation devices, which is further discussed next.

Experiments Using Second-Generation Devices

Experimental Setup and Sample Preparation

The experimental setup used for experiments using second-generation devices is depicted in Figure 2.22. The image acquisition system was upgraded with an ORCA-Flash 4.0 CMOS camera (Hamamatsu, CA, USA) that was employed for high speed imaging. Moreover, either an MFCS-FLEX or an MFCS-EZ precision pneumatic pump together with a FLOWELL flow measurement system (all from Fluigent, Paris, France) were used for flowing the sample through the chip. The configuration of this pneumatic pump not only allows applying multiple reagents (priming buffers, the sample, wash buffers, fluorescent labelling reagents, etc.) easily and without forming bubbles, but it also enables frequent mixing of the blood sample to prevent cell sedimentation. A LabVIEW® (National Instruments, TX, USA) program was used for feedback control of the flow rate. The macro-to-micro interfacing was set up by connecting a sample reservoir (Cat#:713124, Nordson, OH, USA) to the chip's inlet via a PTFE tubing (Cat#: RK-06417-21, Cole Parmer, QC, Canada). The sample reservoir was connected to the pneumatic pump's output via a detachable adaptor (Cat#: 7012338, Nordson, OH, USA), allowing easy access to the sample reservoir. All microfluidic connections and adaptors were purchased from IDEX Health & Science, WA, USA. The individual components of this macro-to-micro interfacing setup were carefully chosen after experimental evaluation of different parts and configurations to minimize dead volumes and cell loss.

Prior to processing samples, the chips were primed by flowing either 0.1% w/v Tween-20 or 95% EtOH solutions. The latter showed superior performance for wetting the generally hydrophobic surface of glass and PDMS, and prevent bubble formation. This is due to the low surface tension of ethanol, allowing it to adhere to the surface of glass and PDMS easily. Next, to block any non-specific adsorption, the chips were treated with a 1%

w/v BSA solution in PBS. BSA attaches to and saturates the surface of PDMS or glass, preventing proteins on the cell membrane to non-specifically (due to non-polar interactions) bind to PDMS or glass.

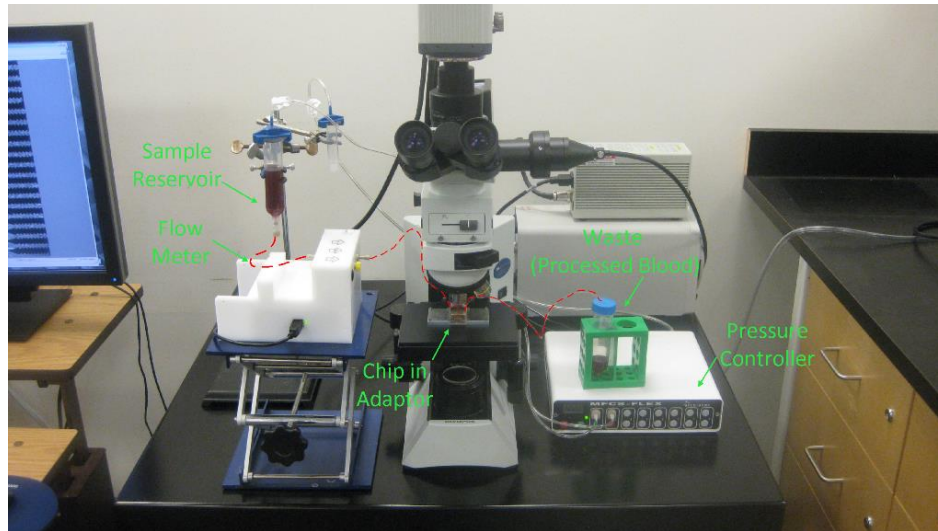


Figure 2.22 The experimental setup. The red dashed-line highlights the path to and from the chip via PTFE tubing.

LNCaP cells were immunomagnetically labelled using 500 nm particles or 2.8 μm beads as explained earlier. For some experiments, LNCaP cells that were previously infected to express green fluorescent protein (GFP), which was later utilized to confirm the identity of captured cells on the chip, were used. Otherwise, the fluorescent labelling of LNCaP cells was performed using a CellTracker™ Green CMFDA Fluorescent Kit (Cat#: C7025, ThermoFisher Scientific, MA, USA). For experiments involving blood samples, blood was drawn from either healthy Sprague-Dawley rats or CD-1 retired breeder mice and kept in Vacutainer® tubes (Cat#: 367862, BD, ON, Canada) at 4°C for no more than 6 hours before each experiment. The animals were purchased from Charles River Laboratories (MI, USA). All procedures performed involving animals were in accordance with the ethical standards of Simon Fraser University (Protocol#: 1056E-12, University Animal Care Committee).

Before each experiment, LNCaP cells were rinsed with PBS and dissociated using the buffer solution (3mM EDTA and 1% w/v BSA in PBS). The cells were then collected and diluted in a larger volume of the buffer solution. To accurately prepare samples, a 5- μL aliquot of the cell solution was placed on the corner of a coverslip or a tube cap. The cells were counted three times under the fluorescence microscope and then mixed into an

appropriate volume of whole blood or buffer to achieve desired concentrations. Coverslips or tube caps were then checked again for any remaining cells, confirming the exact number of cells seeded in the sample.

Performance of Different Second-Generation Designs

Several second-generation prototypes with various designs were experimentally tested. These prototypes were mainly different in the following aspects:

Effect of Magnetic Microtrap Shape and Size

To achieve an initial objective of capturing single cancer cells per individual magnetic microtraps, the performance of different microtrap designs was first investigated qualitatively. These experiments showed that at the same cancer cell concentration (10^3 cells/mL), all four designs performed almost similarly in that they occasionally captured more than a single cell per a magnetic microtrap site. The Sawtooth and Pillar design showed a slightly better performance and captured more single cells (see Figure 2.23). Therefore, a series of experiments were next performed to quantitatively evaluate and compare the recovery rates of these two designs ($n=3$ for each concentration). LNCaP cells were fluorescently and magnetically labelled ($2.8 \mu\text{m}$ beads) and suspended in the buffer solution at three different concentrations (5-500 cells/mL) and processed at $\sim 100 \mu\text{L}/\text{min}$. The recovery rate was defined as the ratio of the number of captured LNCaP cells on the chips to the actual number of cells initially seeded in the sample. Figure 2.24 summarizes the results. The recovery rates for the Pillar and Sawtooth designs were $93.50 \pm 4.44\%$ and $98.65 \pm 1.81\%$, respectively. A two-tailed T-test confirmed that the Sawtooth design offers a better recovery rate ($P = 0.01$).

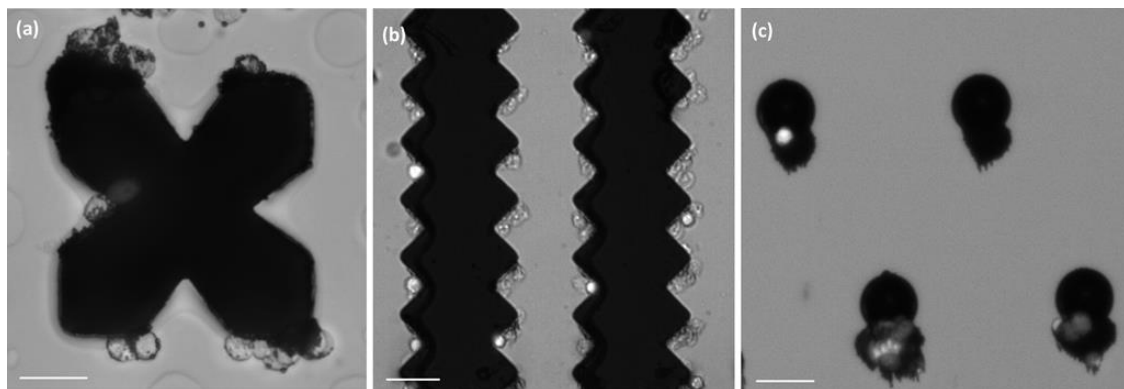


Figure 2.23 LNCaP cells captured on different magnetic microtrap designs: (a) Star, (b) Sawtooth, and (c) Pillar. All scale bar represents $50 \mu\text{m}$.

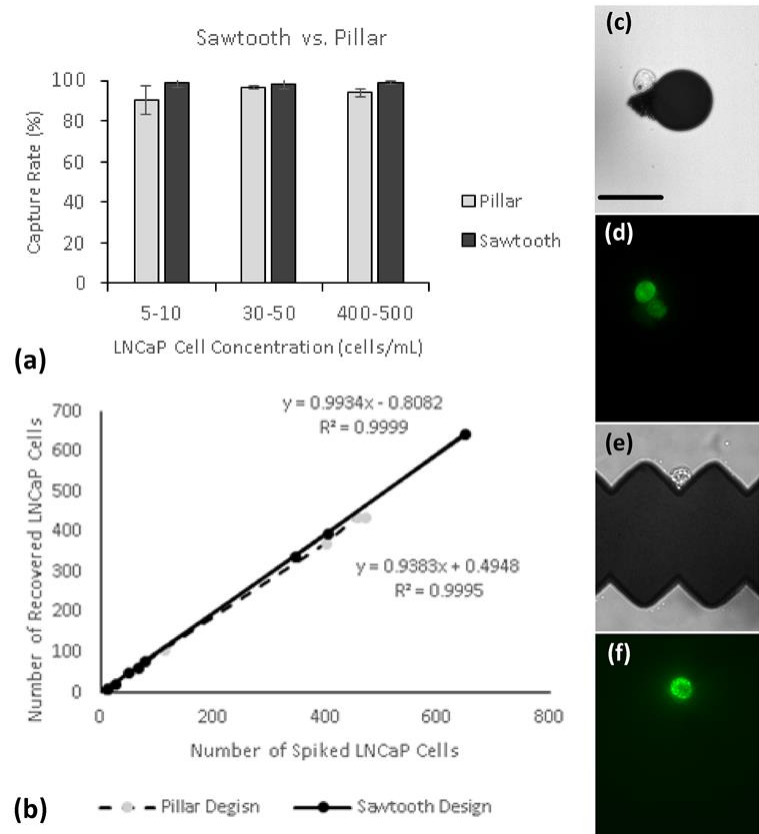


Figure 2.24 (a) Efficiency of Sawtooth and Pillar designs for recovery of LNCaP cells from buffer at different concentrations ($n \geq 3$). Error bars represent standard deviation at each concentration. (b) Regression analysis of efficiency for various cell concentrations. The plot shows number of LNCaP cells seeded versus number of LNCaP cells recovered. (c) and (d) Bright-field and fluorescence images of two LNCaP cells captured on a Pillar structure. (e) and (f) Bright-field and fluorescence images of a single LNCaP cell captured on a Sawtooth structure. Scale bar represents 50 μm.

Effect of Embedded Herringbone Mixer

To study how a passive herringbone mixer could change the recovery rate, the performance of devices with and without a mixer was also evaluated ($n=5$ for each type). All devices had a Sawtooth magnetic microtrap design. LNCaP cells were fluorescently and magnetically labelled (2.8 μm beads) and seeded in healthy blood samples at a concentration of 30-50 cells/mL. The blood samples were then diluted with buffer (1:5) and processed at an average flow rate of 100 μL/min. Figure 2.25 summarizes the capture results. The recovery rates for devices with and without a herringbone mixer were $90.27 \pm 4.04\%$ and $90.81 \pm 3.03\%$, respectively. A two-tailed T-test concluded that there is no significance different in the recovery rates of two designs ($P=0.82$).

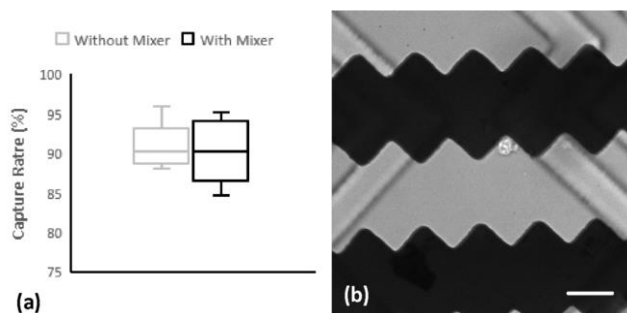


Figure 2.25 (a) Recovery rate of devices with and without an embedded herringbone mixer (n=5 for each test). (b) A bright-field image showing an LNCaP cell captured on the microtrap and embedded herringbone grooves on the inner surface of the PDMS microchamber. Scale bar represents 50 μm.

Effect of Immunomagnetic Labelling Method

A series of blood experiments were also performed to assess the capture efficiency of two different immunomagnetic labelling approaches. LNCaP cells were first fluorescently stained. The cells were then immunomagnetically labelled using either the TAC technology and 500nm magnetic particles or the streptavidin-biotin interaction and 2.8 μm magnetic beads. Next, the labelled cells were seeded in healthy blood samples at three different clinically meaningful concentrations (30-300 cells/mL). The samples were diluted with buffer (1:5) and processed at an average flow rate of 100 μL/min using devices with Sawtooth microtraps and without a herringbone mixer (n=3 for each concentration). Figure 2.26 summarizes the capture results. The recovery rates for immunomagnetic labelling using the TAC technology and 500nm magnetic particles and the streptavidin-biotin interaction and 2.8 μm magnetic beads were 61.14±9.82% and 92.69±6.32%, respectively. These results confirmed the earlier observation that immunomagnetic labelling using the latter approach indeed improves the recovery rate significantly.

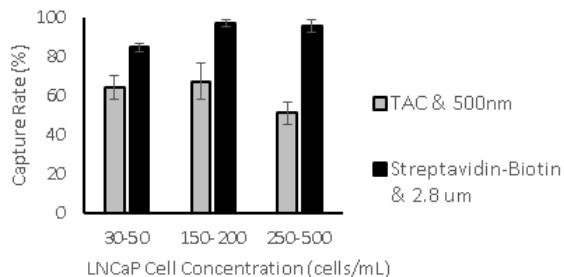


Figure 2.26 Comparison of recovery rate for LNCaP cells labelled using either the TAC technology and 500nm magnetic particles or the streptavidin-biotin interaction and 2.8 μm magnetic beads. Error bars represent standard deviation at each concentration.

Summary and Discussion

The primary objective of this series of experiments was to select the most efficient chip design and immunomagnetic labelling protocol for the next round of experiments that would more closely mimic the isolation of CTCs from clinical blood samples. To this end, the effects of these two major factors, i.e. the magnetic separation mechanism and the immunomagnetic labeling approach, were studied independently. Therefore, for these experiments, LNCaP cells that were confirmed to be immunomagnetically labelled seeded in blood or buffer. This approach allowed studying the performance of different devices without considering another variable, i.e. the immunomagnetic labelling efficiency. Studying the effect of magnetic bead/particle size later confirmed that immunomagnetic labelling using 2.8 μm beads increase the recovery rate considerably.

Based on these experiments, it was concluded that the Sawtooth design for magnetic microtraps would have the highest recovery rate among other designs. It was also concluded that since CTCs are extremely rare, the capture of multiple cells on one microtrap would be an irrelevant issue as it was subsequently confirmed by experiments involving clinically relevant low LNCaP cell concentrations. It was also noticed that when they are labelled with 2.8 μm magnetic beads, at least 85% of LNCaP cells were captured on the three first rows of microtraps nearest to the diffusers. Moreover, in some cases, LNCaP cells were captured on the tip of permalloy strips. The remaining cells were distributed across the chip on different locations. Given the working principle of the device, this can be explained. As mentioned earlier, PSMA is highly expressed by LNCaP and prostate cancer cells. Thus, the majority of cells were labeled with sufficiently high number of beads, rendering a strong magnetic pull that overcomes the hydrodynamic drag force on cells within a few hundred microns of their journey in the microchamber. For the remaining cells, however, the magnetic particle load may not be as high. As such, it takes more time for the magnetic force to gradually pull the cells downward. For blood samples, except a few cases involving blood clots that had been formed in the sample reservoir and entered and blocked the device (data not included), the non-specific capture of blood cells on the chip was generally negligible, making the proposed strategy highly specific.

It was also observed that while the use of herringbone mixer did not increase the overall recovery rate, it caused some blood cells or target LNCaP cells to be trapped inside the grooves. Moreover, these grooves sometimes affected the visual analysis capability

of the system (in particular at high magnifications). As such, it was concluded that a herringbone mixer would not have a significant advantage and was not included in the final design. Finally, the high recovery rate of LNCaP cells in all experiments confirmed that the optimized design and implementation of the macro-to-micro interfacing would not result in any cell loss.

Isolation of Rare LNCaP Cells from Spiked Blood Samples

Having the final device design and immunomagnetic labelling method determined (see Figure 2.27), this series of experiments were designed and carried out to closely simulate the capture of CTCs from clinical blood samples.

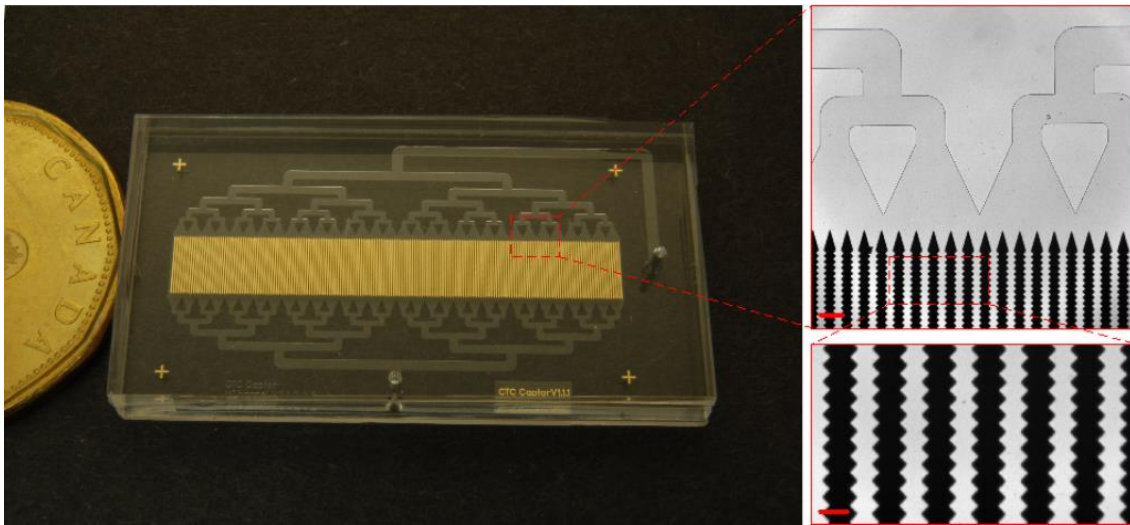


Figure 2.27 A photograph of the finalized second-generation integrated microfluidic chip. The chip is composed of a magnetic component (bottom piece) and a PDMS microfluidic component (top piece) that are irreversibly bonded. Golden structures in the photograph are 10- μm -thick geometrically patterned permalloy strips that are enclosed by the central microchamber, which is connected to the inlet (top right) via a microfluidic flow distribution manifold. Patterned permalloy strips (black) and the resulting Sawtooth magnetic microtraps as seen under the microscope are shown in the magnified insets on the right. Scale bars on the top and bottom insets represent 500 μm and 100 μm , respectively.

Capture Efficiency at Very Low Target Cell Concentrations and In-situ Staining of Captured Cells

The performance of the device to capture cancer cells at very low concentration that mimics clinical blood samples and the ability of the proposed system for *in situ* staining of captured cells was first studied in a number of blood experiments ($n=5$). GFP expressing LNCaP cells were magnetically labelled and seeded in healthy blood samples at very low

concentrations (≤ 10 cells/mL). The chips were primed, and samples were processed as explained earlier. Once blood samples were fully processed, the chips were washed with the buffer solution to remove any non-specifically adhered blood cells. The captured cells' nuclei were then labeled with a nucleic acid stain to differentiate cell debris (GFP+, Hoechst-) from positively scored captured LNCaP cells (i.e. GFP+, Hoechst+). The recovery rate was $87.50 \pm 9.12\%$. Figure 2.28 summarizes the results.

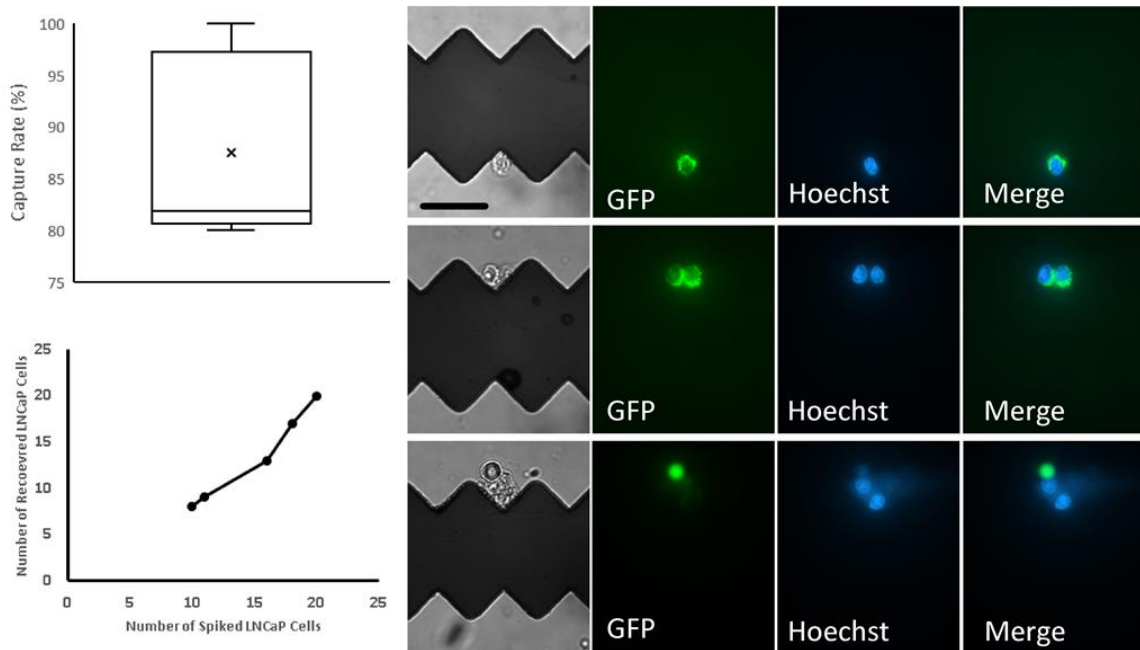


Figure 2.28 The box and whisker plot (top left) represents the recovery rate for rare LNCaP cells seeded in blood. The line plot shows number of LNCaP cells initially seeded (horizontal axis) versus number of LNCaP cells recovered (vertical axis) (n=5). The first two rows on the panel on the left show single and double LNCaP cells capture on microtraps. The bottom row displays an LNCaP cell captured along with and being attacked by two macrophages. Scale bar represents 50 μm .

Capture of LNCaP Cells from Spiked Blood Samples

The objective of these experiments was to evaluate the performance of the chip for capturing LNCaP cells from spiked blood samples that fully mimic clinical blood samples (n=5). Prior to these experiments, the immunomagnetic labelling protocol was empirically optimized to achieve maximum labelling efficiency for LNCaP cells spiked in whole blood sample using minimum number of beads per sample volume. Next, LNCaP cells were fluorescently labelled and spiked in healthy blood samples at clinically relevant low concentrations (5-50 cells/mL). The spiked blood samples were then immunomagnetically labelled according to the optimized protocol, diluted with buffer (1:5),

and processed at 100 $\mu\text{L}/\text{min}$. Once the chips were washed with the buffer solution to remove non-specifically adhered blood cells, they were inspected under the microscope to detect and count captured LNCaP cells. In all five trials, only <15% of spiked LNCaP cells were detectable, which was mainly due to the accumulation of magnetic beads on the chip (see Figure 2.29). These extra beads completely buried captured cells, quenching their fluorescence signals and preventing their visual detection under the microscope. To address this issue, which is an inherent problem in immunomagnetic cell isolation [134] [226], either the number of beads used for the immunomagnetic labelling should be reduced or a mechanism should be put in place to remove extra unbonded beads after the immunomagnetic labelling process is completed.

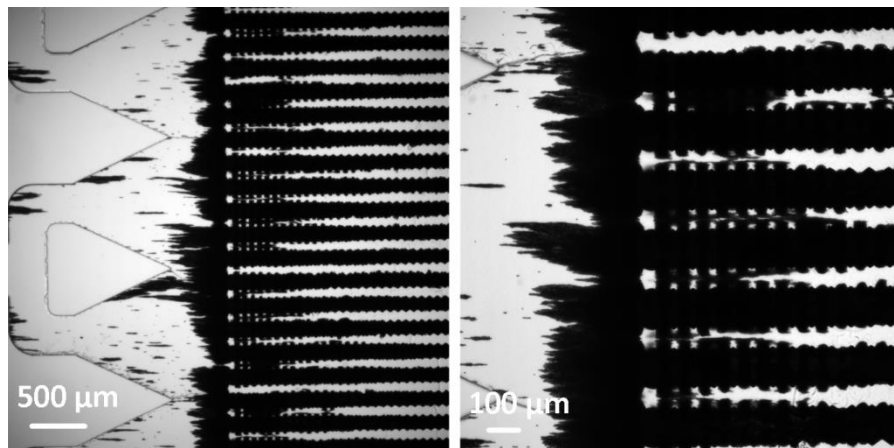


Figure 2.29 Accumulation of extra unbonded magnetic beads on the chip.

To reduce the number of beads needed to efficiently label target cancer cells, the sample volume should also be reduced. This can only be done by lysing RBCs and resuspending remaining nucleated cells (i.e. WBCs and cancer cells) in a smaller volume of buffer. This approach has been employed in many immunomagnetic methods, such as the CellSearch[®] system. To assess the recovery rate using this approach, several experiments were carried out ($n=5$). Prior to experiments, the immunomagnetic labelling protocol was optimized again to achieve maximum labelling efficiency of cancer cells in lysed spiked blood samples using a minimum number of beads per volume. It was confirmed that the minimum number of beads needed for efficient labelling is almost linearly dependent on the sample volume. Next, fluorescently labelled LNCaP cells were spiked in healthy blood samples, and the spiked blood samples were lysed using the BD Pharm Lyse buffer (Cat #: 555899, BD Bioscience, ON, Canada) for 15 minutes at the room temperature. The lysed blood sample was then centrifuged at 400g for 10 minutes,

the supernatant was carefully removed, and the pellet was resuspended in the buffer and centrifuged at 400g for another 10 minutes. The supernatant was carefully removed and the pellet was resuspended in 300 μ L of the buffer solution. The immunomagnetic labelling of target cells was then performed according to the experimentally optimized protocol, and the labelled sample was diluted in a larger volume of the buffer solution and processed at the nominal flow rate. Following the buffer wash, the chip was inspected under the microscope to detect and count captured LNCaP cells. The recovery rate was $51 \pm 9.75\%$. The results are summarized in Figure 2.30. As expected reducing the number of beads enabled the visualization of captured cells. It was assumed that the relatively low recovery rate associated with lysed blood samples might have mainly been caused by the preprocessing of spiked blood samples (i.e. lysing, pipetting, etc.) and not the failure to visually detect the cells due to the captured beads on the chip. To confirm this assumption, immunomagnetically labelled LNCaP cells were seeded in a buffer solution containing the same number of magnetic beads used for immunomagnetic labelling of lysed spiked blood samples, and this sample was processed under the same condition. The chip was then inspected and of the 11 LNCaP cells originally seeded in the sample, 9 captured cells were detected on the chip. This confirmed the assumption that the low recovery rate associated with lysed spiked blood samples was, for the most part, caused by relatively harsh preprocessing of blood samples.

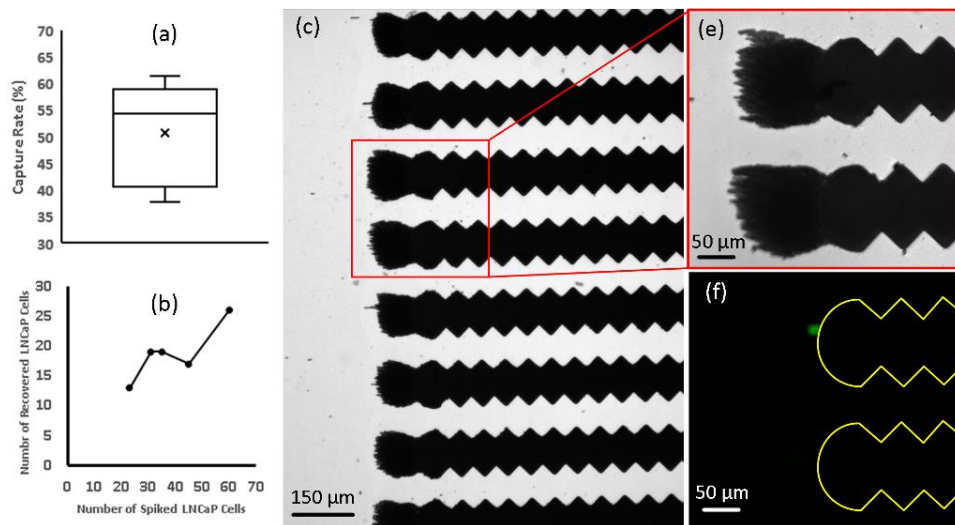


Figure 2.30 (a) Capture efficiency for LNCaP cells from spiked and lysed blood samples (n=5). (b) Number of LNCaP cells originally spiked in blood (horizontal axis) versus number of LNCaP cells recovered (vertical axis). (c) A view of a portion of the chip showing extra magnetic beads accumulated on permalloy strips accumulation. (e) and (f) Magnified views of microtraps with a captured LNCaP cell.

Summary and Discussion

The objective of this series of experiments was to evaluate the performance of the proposed integrated microfluidic magnetic chip for isolation of LNCaP cells from spiked blood samples that closely mimic clinical blood samples from cancer patients. It was first confirmed that the chip can capture cells at very low concentration with high sensitivity if the cancer cells were adequately labelled. In case of 2.8 μm beads, only a single bead was needed for a cell to be captured once it reached the magnetic microtrap bed. Next, a series of experiments was carried out to study the performance of the chip for capturing LNCaP cells from spiked samples. Titration studies had previously shown that in order to efficiently label rare spiked LNCaP cells in blood samples, $>1.5 \times 10^7$ beads/mL should be used. Once the sample is labelled and processed through the chip, not only labelled LNCaP cells but also all unbonded magnetic beads were captured on magnetic microtraps. Experiments showed that this enormous number of free magnetic beads captured on magnetic microtraps can effectively hide captured LNCaP cells, preventing them from being visualized and detected.

To address this issue and reduce the number of magnetic beads, several experiments were performed in which the effect of lysing blood and using smaller number of magnetic beads were studied. It was concluded that while lysing the blood sample, reducing the sample volume, and using significantly smaller number of magnetic beads eliminated the previous issue, the harsh preprocessing and frequent transfer of blood samples (lysing, pipetting, centrifuging) would result in cell loss and deleteriously affect the recovery of spiked cells. Minimizing the number of steps involved in isolating CTCs from blood samples is indeed a critical factor to reduce the possibility of inadvertent cell loss, an effect which might be more severe for extremely rare CTCs. An alternative solution to reduce the number of free magnetic beads on the chip is to use a particle separation mechanism to remove extra unbonded beads after the target cells are labelled in blood samples. This topic was extensively studied in my PhD research and is discussed in the next chapter.

Chapter 3.

A Microfluidic Platform for Size-Based Enrichment and Immunomagnetic Isolation of Rare Cancer Cells from Blood Samples

3.1. Background

Experimental optimization studies showed that to ensure the efficient immunomagnetic labelling of target cancer cells in a blood sample, an excessive number of magnetic beads should be added to the sample (e.g., $>1.5 \times 10^7$ beads/mL in case of 2.8 μm streptavidin-coated beads). However, once the labelled blood sample is processed, those beads that have not been bonded to any cells would also be captured by the same magnetic separation mechanism used to capture immunomagnetically labelled target cells, as, by virtue of their working principle, magnetic separation mechanisms are not magnetically specific, i.e. any magnetic entity exposed to the separation mechanism would be captured. The capture and high-density accumulation of an immense number of magnetic beads on the small footprint of a microfluidic chip could hamper the visual detection of captured cells on the chip. To address this issue and improve the quality of detection, either the number of magnetic beads initially used for immunolabelling of target cells should be reduced, or extra unbonded magnetic beads should be removed from the sample after the labelling process is completed and before the labelled sample is exposed to the magnetic separation mechanism (e.g., the magnetic chip). The former option mandates reducing the sample volume, which can be done by lysing RBCs and resuspending remaining nucleated cells in a much smaller volume of an appropriate buffer. Experiments using this approach showed that such aggressive preprocessing of blood samples could result in accidental target cell loss, thereby reducing the overall recovery rate.

To explore the second option, i.e. refining immunomagnetically labelled blood samples by removing unbonded free magnetic beads, three different microfluidic filters were designed, microfabricated, and tested, which is presented in this chapter.

3.2. Continuous Microfluidic Size-Based Particle Separation

The separation and sorting of micron-sized particles is an established field of research in microfluidics, resulting in the development of a variety of techniques for this purpose over the past decade [227]. Majority of the principles discussed for CTC isolation in Chapter 1 can potentially be applied for the separation of a specific group of particles from a heterogenous population. In brief, continuous-flow microfluidic separation of particles can be accomplished either passively based on the particle size, and interactions between particles, fluid flow fields, and microstructures, or actively using an external magnetic, ultrasonic, electric, or acoustic field to manipulate and specifically separate target particles [227]. Given the definite size of magnetic beads in the case of this study, size-based separation deemed to be the most specific and effective principle for removal of extra magnetic beads from immunomagnetically labelled samples. In the proposed framework, the two microfluidic chips, i.e. the filter and the magnetic chip, would be connected in tandem. The blood sample initially passes through the filter, where unbonded magnetic beads are removed. The refined “bead-free” sample then enters the magnetic chip, where immunomagnetically labelled target cancer cells are captured. It should be noted that similar general strategy has been used by Ozkumur et al. to remove free magnetic beads before microfluidic magnetophoretic isolation of immunomagnetically labelled cells [228]. In the next section, three different microfluidic filters for continues-flow size-based removal of free magnetic beads from blood samples are studied.

3.3. Materials and Methods

3.3.1. Magnetically-Enhanced Active Size-Based Cross Flow Filtration (MASCFF)

Background and Theory

Microfluidic cross-flow filtration is generally a passive size-based particle separation technique that has been used for blood fractionation or cell separation from a heterogenous sample [229] [230] [231]. As shown in Figure 3.1, the separation is realized through numerous precisely-defined slits (or apertures) that are incorporate in a barrier that separates two parallel microchannels: the sample microchannel, where the original unprocessed sample flows, and the collection microchannel, where separated target

particles are collected and carried away. The filtration direction is perpendicular to the flow direction in the sample microchannel (hence, the name “cross-flow” filtration). Particles smaller than the slit size would move through the slits and enter the collection microchannel whereas larger particles stay in the sample microchannel and eventually exit through the refined sample outlet towards the downstream device or process.

Normally, all particles are scattered and flow across the sample microchannel, and only those particles that reach the slits are subject to filtration. To improve the cross-flow filtration efficiency, all particles must be pushed toward the slits. This has usually been done by hydrodynamically focusing the sample using a sheath flow or via centrifugal force created by serpentine curved microchannels [229] [230] [231]. Considering the inherent magnetic properties of beads in the case of free magnetic beads, a magnetic field can be used to actively deviate and pull the beads moving in the sample microchannel towards the filtration slits, where they can be removed from the sample. Based on this idea, a novel MASCFF device was developed and tested to remove extra free magnetic beads from immunomagnetically labelled blood samples.

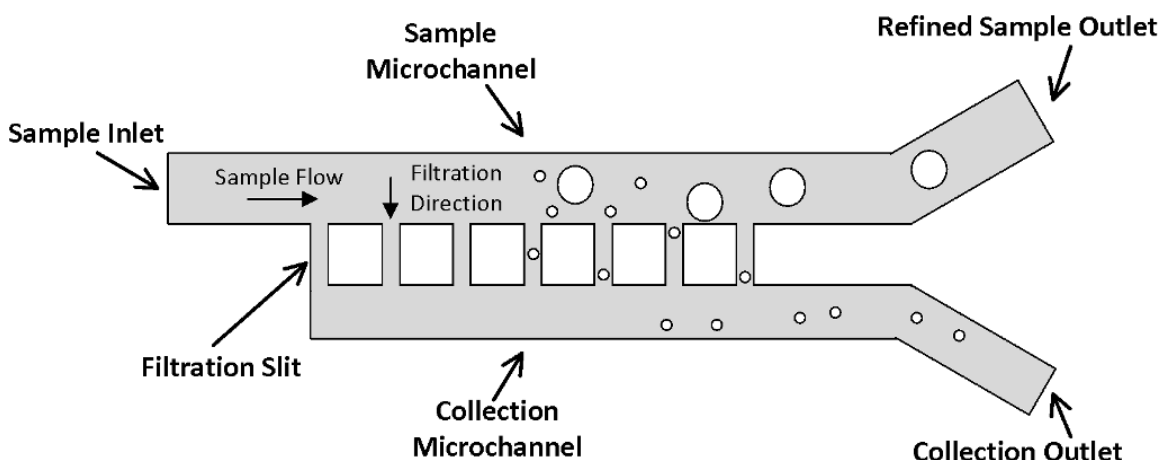


Figure 3.1 The general principle of cross-flow filtration. The original unprocessed sample enters and moves within the sample microchannel, which is separated from the collection microchannel via a barrier containing numerous slits with a precisely-defined size. Smaller particles (in this case, unbonded magnetic beads) pass through filtration slits, enter the collection microchannel and are discarded via the collection outlet. Larger particles (in this case, labelled cancer cells and other blood cells) may not pass through these slits, so they continue moving within the sample microchannel and eventually reach the downstream process or device (in this case, the magnetic chip).

Design

The general schematic of a typical MASCF device is shown in Figure 3.2.

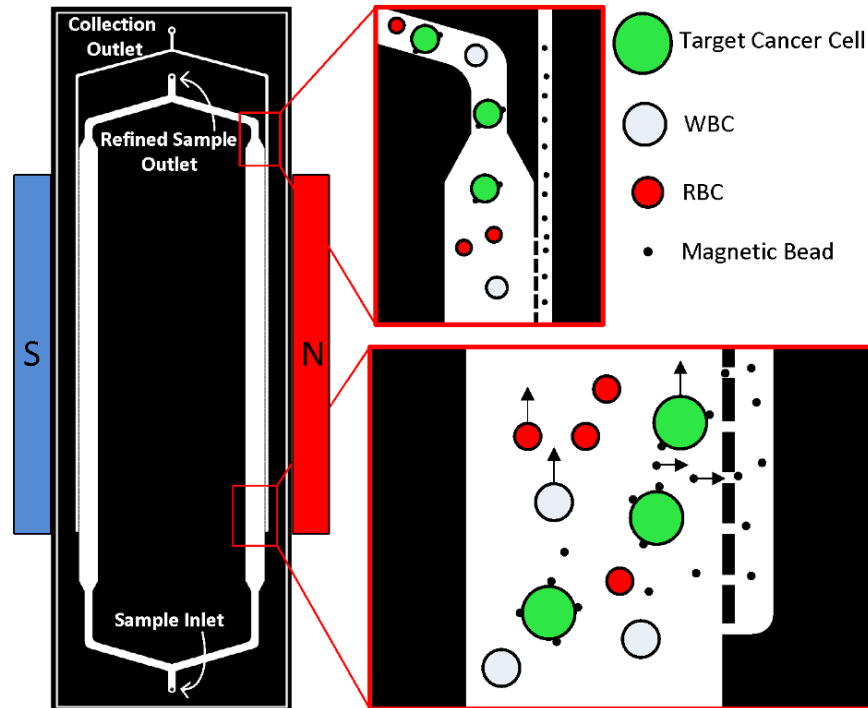


Figure 3.2 A general schematic of a typical MASCF device designed for removing free magnetic beads from immunomagnetically labelled blood samples. The insets are for illustration purposes only and are not to scale.

The proposed symmetrical design of the device includes a pair of sample and collection microchannels at each side. Each pair of microchannels are connected via numerous 5- μm -wide side slits. As the immunomagnetically labelled blood sample flowing in the wider sample microchannel is exposed to the MFD gradient created by a pair of permanent magnets located at each side of the device, magnetic beads, as well as magnetically labelled target cells, would be pulled toward the narrower collection microchannel, where free magnetic beads would pass through the slits and enter the collection microchannel. However, due to the larger size of labelled cells, they would experience a larger hydrodynamic drag force, resulting in a relatively smaller net lateral displacement toward the collection microchannel. Therefore, not all labelled cells would reach the filtration slits. Instead they would continue moving in the sample microchannel and exit the filter via the refined sample outlet. Those labelled cells that would reach the slits would not be able to pass through them and would move within slower streamlines near the microchannel wall and eventually exit the filter via the outlet. The flow rate at the

sample inlet can be adjusted such that the flow velocity in each sample microchannel would be high enough to result in the desired scenario for cells and particles.

The critical dimensions in designing the proposed device are the width of the sample microchannel and the width and height of filtration slits. The width of the sample microchannel was designed to ensure a laminar flow at typical flow rates (<200 $\mu\text{L}/\text{min}$). The width of filtration slits was set to 5 μm , which is large enough to allow free 2.8 μm magnetic beads to pass through and enter the collection microchannel. Two different heights for these slits were considered: 55 μm and 5 μm .

3.3.2. Deterministic Lateral Displacement (DLD)

Background and Theory

DLD is another passive continuous-flow microfluidic particle separation technique that is based on precise interactions of particles, fluid streamlines, and arrays of micron-sized obstacles within a microchannel [232] [233]. The principle of DLD has been implemented in a variety of modified designs and employed for high resolution separation of particles and cells by many researchers [234].

In brief, a DLD device is composed of an array of micron-size obstacles (or microposts) located within a microchannel (see Figure 3.3). The microposts are specifically arranged in several rows, where the center-to-center distance between two neighboring microposts in each row (λ) and, therefore, the gap between two microposts (g) is fixed. Each row is shifted laterally at a set distance ($\Delta\lambda = \epsilon\lambda$) from the predecessor row. Therefore, after $N = 1/\epsilon = \lambda/\Delta\lambda$ rows, the microposts will be in the same lateral position as those in the first row. The flow passing between two neighboring microposts can be considered as N separate streamlines that do not mix (due to low Reynolds number in the microchannel). For a particle whose size is smaller than the critical dimension (D_c) and flowing within a given streamline (e.g., 1 on the first row in Figure 3.3), it remains in the same streamline throughout the microchannel. Therefore, after a full period of N rows ($N=3$ in Figure 3.3), that particle stays in the same lateral position within the microchannel (e.g., 1 on the forth row in Figure 3.3). This mode is often known as the “zigzag” mode. For a particle whose size is larger than D_c , it will be bumped into the neighboring streamline in going from one row to the next row. Therefore, by the end of one full period of rows, the larger particle would be laterally displaced by λ units or $\theta = \tan^{-1}(\epsilon)$ degrees.

This mode is often known as the “displacement” mode. This basic principle constitutes the separation mechanism in all DLD devices.

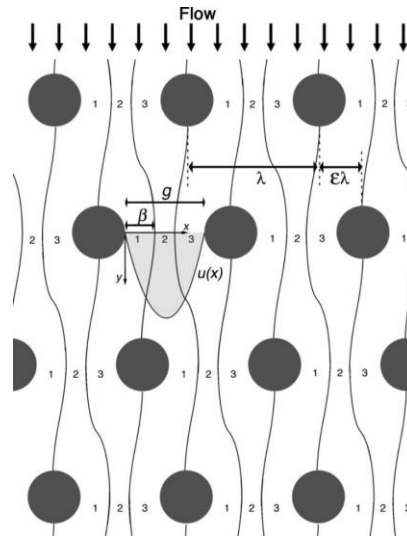


Figure 3.3 The general principle of DLD particle separation. In this example, each post is laterally displaced by $\lambda/3$, meaning that the fluid passing between two neighboring microposts is split to 3 separate streamlines and after 3 rows, microposts will be in the same lateral position [233].

Design

To design a DLD device, several parameters should be defined. These include the micropost shape and diameter (D_P), the gap between two microposts (g), and the period of lateral row shifting (N). To prevent any clogging issues, the value of g should be bigger than size of the largest particle in the sample. However, this value cannot be too big, as it will increase the length of the device. Similarly, a large micropost would increase the overall length of the device. In addition to microfabrication difficulties, an extremely small micropost would increase the shear rate [234]. The value of N partly defines the critical diameter (D_C). Therefore, it cannot be too large (or it will reduce the specificity of separation), but it cannot be too smaller either (or it will reduce the sensitivity of separation).

Several analytical or empirical formulas have been proposed by others to approximate the value of D_C . Inglis et al. analytically calculated this value as follows [233]:

$$D_c = 2\beta = 2\alpha \cdot G \cdot \varepsilon \quad (3.1)$$

where β is the width of the stream next to each micropost (see Figure 3.3). A correction factor (α) was defined to approximate β based on the gap size and value of $\epsilon=1/N$ as follows:

$$\alpha = \sqrt{N/3} \quad (3.2)$$

Davis proposed an empirical formula to estimate the value of D_c as follows [235]:

$$D_c = 1.4G\epsilon^{0.48} \quad (3.3)$$

Based on several experimental and analytical studies, Inglis et al. compiled a plot to approximate the value of critical diameter (D_c) given the values of row shift fraction ($\epsilon=1/N$) and g as follows [233]:

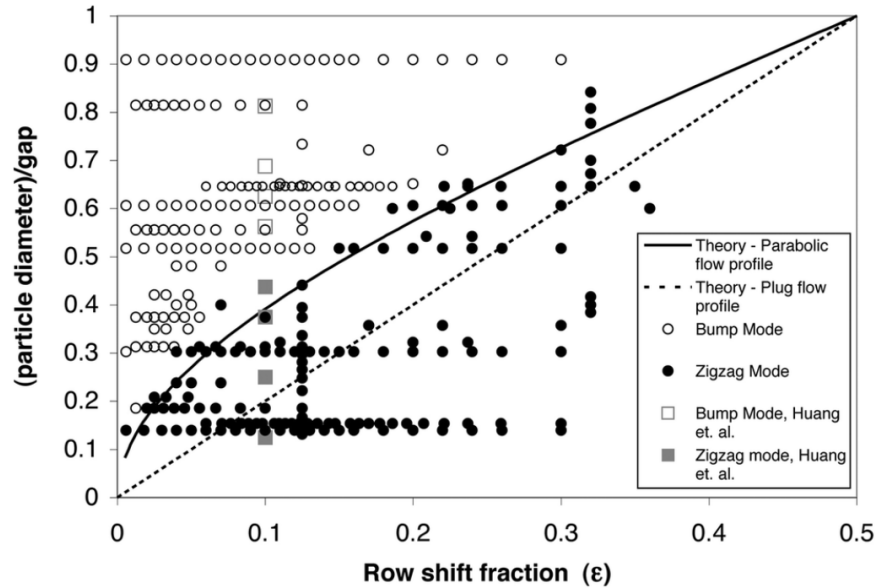


Figure 3.4 Experimental data for the critical diameter divided by the gap size (vertical) versus the row shift fraction (horizontal) [233].

Using these criteria, different prototypes were designed with two different gap sizes (25 μm or 30 μm), micropost shapes (circle or ellipsoid), micropost sizes (25 μm or 30 μm), and row shift fraction values (1/30 or 1/40). The corresponding D_c values were 4-6 μm . Such a value would result in a zigzag mode motion for unbonded free magnetic beads and some RBCs but a displacement mode motion for target labelled cells that are considerably larger. A schematic of a typical DLD design is shown in Figure 3.5.

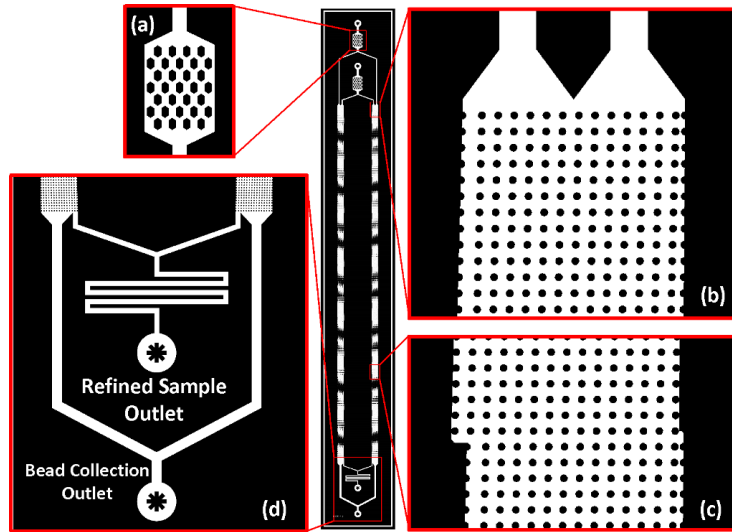


Figure 3.5 A schematic of a typical DLD device (center). The device is composed of two parallel DLD modules at each side. (a) A filter to remove particles and debris larger than the gap size between two microposts to prevent clogging issues. (b) A magnified view of the entrance to the DLD module. The blood sample is fed from the right inlet and a sheath flow is fed from the left inlet. (c) After a full period, the larger particles are laterally moved by λ . In order to displace these target particles across the microchannel width, the DLD unit should be repeated several times. (d) Target labelled cancer cells and other larger blood cells displace along the microchannel would be collected at the left outlet, while unbound magnetic bead and some RBCs would be collected at the right outlet. The output hydraulic resistance for the refined sample outlet (left) is adjusted to allow proportional collection of fluid at each outlet. All drawing, including the insets, are to scale.

3.3.3. Multiorifice Flow Fractionation (MOFF)

Background and Theory

MOFF is also a passive continuous-flow microfluidic particle separation technique that, unlike the previous methods, is achieved in a nonlaminar flow where inertial forces are dominant and the Reynolds number is large ($\gg 1$). Particle separation via MOFF is mainly realized by the collective effect of two inertial forces acting on all particles in a nonlaminar flow in a microchannel: the inertial lift force and the momentum-change-induced inertial force [236] [237]. The inertial lift force itself is the net effect of two forces, i.e. a shear-gradient-induced lift force and a wall-effect-induced lift force. In brief, the shear-gradient-induced lift force causes particles to migrate away from the center of microchannel, and the wall-effect-induced lift force repels particles away from the microchannel wall [236] [238] [239]. The other major inertial force responsible for MOFF particle separation, i.e. the momentum-change-induced inertial force, is essentially

caused by a mismatch between fluid and particle trajectories. Note again that due to nonlaminar nature of flow in MOFF, unlike the case of a laminar flow where particles follow the flow pattern due to a strong viscous drag force, the inertial force becomes the dominant factor in defining the particle migration. As shown in Figure 3.6, in the MOFF particle separation, the mismatch between fluid and particle trajectories is induced by the microchannel's specific geometry containing multiple expansion/contraction units [236].

While all particles flowing in the microchannel would be influenced by the MOFF effect, their behaviour could be correlated with the particle Reynolds number (Re_p), which, in addition to the microchannel dimensions and fluid properties, also depends on the particle size, and is defined as follows:

$$Re_p = Re_c \frac{d^2}{D_h^2} = \frac{\rho U_m d^2}{\mu D_h} \quad (3.4)$$

where D_h is the hydraulic diameter of the microchannel, Mm is the maximum flow velocity in the microchannel (corresponding to contraction regions), ρ is the fluid density, μ is fluid dynamic viscosity, and d is the particle diameter. Experimental studies by other researchers concluded that for $0.5 < Re_p < 1$, particles tend to concentrate close to the walls at both side of the microchannel, whereas for particles with $4.5 < Re_p < 12$, particles would focus in the middle of the microchannel [236] [240]. The focused particles then can be collected at separate outlets at the end of the MOFF microchannel. As mentioned in Chapter 1, the principle of MOFF, either independently or in combination with other cell isolation techniques, has also been used for isolation of CTCs from blood [240] [241].

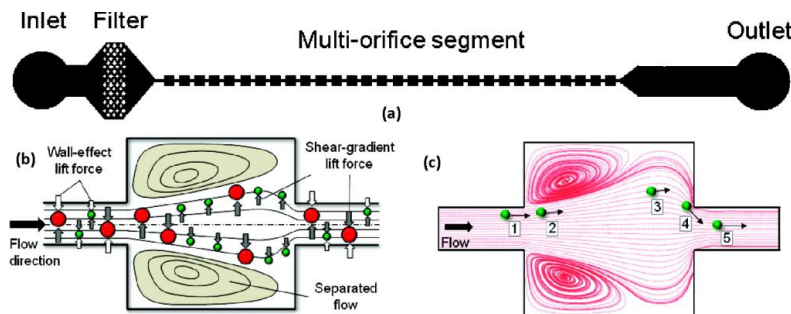


Figure 3.6 The general principle of MOFF. (a) A typical MOFF device with multiple alternating expansion/contraction units along the microchannel. (b) The inertial lift force, which is the net effect of the shear-gradient-induced lift force and the wall-effect-induced lift force acting on particles all along the MOFF microchannel. (c) The momentum-change-induced inertial force resulting from a mismatch between fluid and particle trajectories caused by alternating expansion/contraction units in the MOFF microchannel [236].

Design

A schematic of a typical MOFF device designed to remove extra magnetic beads from an immunomagnetically labelled blood sample is shown in Figure 3.7. To design an MOFF device, two basic parameters should initially be defined, that is, U_m and D_h . U_m ultimately depends on the volumetric flow rate by which the sample is pumped through the MOFF device, and D_h is defined as follows:

$$D_h = \frac{2ab}{(a+b)} \quad (3.5)$$

where a and b are the width and height of the microchannel as measured at the contraction regions, respectively. The height of microchannel is constant across the device ($55 \pm 5 \mu\text{m}$). The width of microchannel cannot be too small as it would result in device malfunction due to clogging. However, it cannot be too large either, as it would increase the hydraulic diameter (D_h) and negatively affect the particle focusing at nominal flow rates. Therefore, to design the MOFF device, first the nominal flow rate range was set ($\sim 200 \mu\text{L}/\text{min}$), and then the particle Reynolds number was calculated for target cells ($d=20 \mu\text{m}$) and magnetic beads ($d \sim 3 \mu\text{m}$) based on different values for the microchannel width at the contraction regions. These results showed that at an average flow rate of $200 \mu\text{L}/\text{min}$ and using a $40\text{-}\mu\text{m}$ wide contraction region, the value of Reynolds number for magnetic beads and target cancer cells would approximately be 0.4 and 15, respectively. Several studies done by other researcher concluded that the size-dependent particles distribution across the width of MOFF microchannel would stabilize after the sample passes through at least 80 expansion/contraction units. Therefore, the length of proposed MOFF microchannels was set based on this number. To improve the throughput, four MOFF modules were connected in parallel on a single chip.

At the end of each MOFF microchannel module is located an outlet structure that gradually expands and eventually leads to three separate exits (see Figure 3.7.e). The central exit collects the target cancer cells that would be focused in the middle, and the two lateral exits collect magnetic beads and some RBCs that would be concentrated at both sides of the MOFF microchannel. The shape of outlet and the width of each exit were optimized via CFD simulation and experimental observations. A wide central exit would prevent cancer cell loss but increase the number of non-specifically collected free magnetic beads. A narrower central exit would have the reverse effect. The hydraulic

resistance at each exit should be adjusted such that proportional volumes of fluid are collected through each exit. If this value is not adjusted properly, the focused lines of target cells and magnetic beads would be interrupted once they arrive at the outlet.

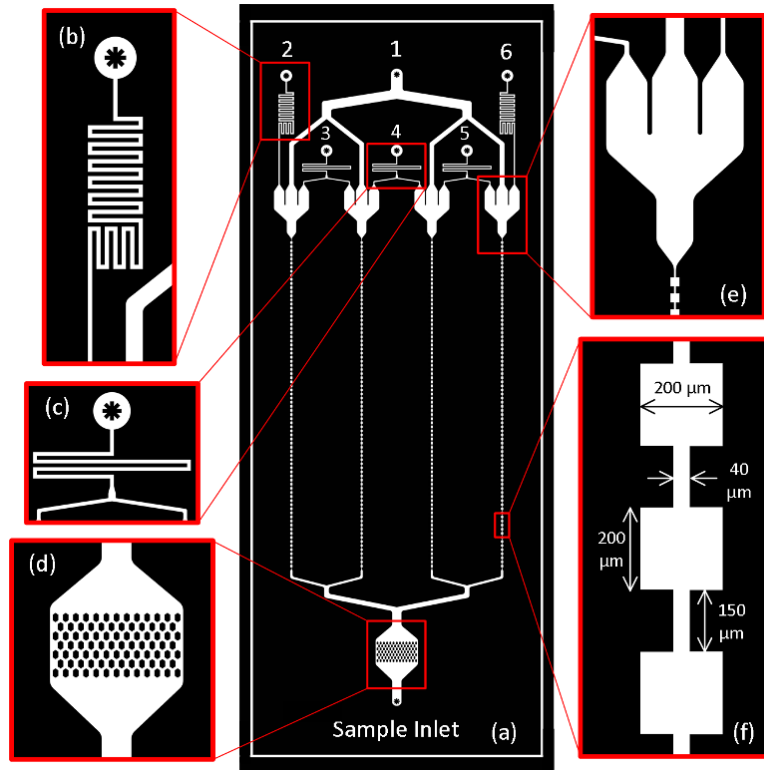


Figure 3.7 A schematic of a typical MOFF device designed for extra magnetic beads removal from immunomagnetically labelled samples. (a) The device (75×25mm) is composed of four separate MOFF modules that are connected in parallel and are fed via a single sample inlet (bottom). The refined (bead-free) sample from all four modules would be combined and collected at Outlet 1, which is located at the top center of the chip. Outlets 2-6 collect extra magnetic beads and a portion of RBCs filtered out by each MOFF module. To efficiently fit four modules on one chip, some outlets from each module were combined. (b) and (c) To collect proportional volumes of fluid at each exit, the hydraulic resistance of each exit was adjusted using CFD simulations. (d) A filter was designed to block larger particles and blood debris from reaching the MOFF microchannels. (e) At the end of each MOFF microchannel is located an outlet structure with three exits. The middle exit collects cells focused in the center (that is, target cancer cells and some blood cells), and two lateral exits collect magnetic beads and a portion of RBCs (smaller particles) focused on both side of the MOFF microchannel. (f) The dimensions of MOFF module. There are 80 contraction/expansion units along each MOFF microchannel module. All drawing, including the insets, are to scale.

CFD simulations were used to precisely design the hydraulic resistance at each exit. Preliminary experiments showed that, when the volumetric flow rate of fluid passing through each exit is proportional to the width of each exit (see Figure 3.8.b and c), not all

target cancer cells would be collected at the central exit. This was due to the fact that not all target cells were focused in the center of the MOFF microchannel, and some cells left the MOFF module via lateral exits. Therefore, the hydraulic resistance at the central exit was modified such that relatively more fluid is collected via this exit (1.3x that of lateral exits - see Figure 3.8.d and e). This would result in collecting as many target cancer cells as possible at the central exit although some magnetic beads would be collected, too.

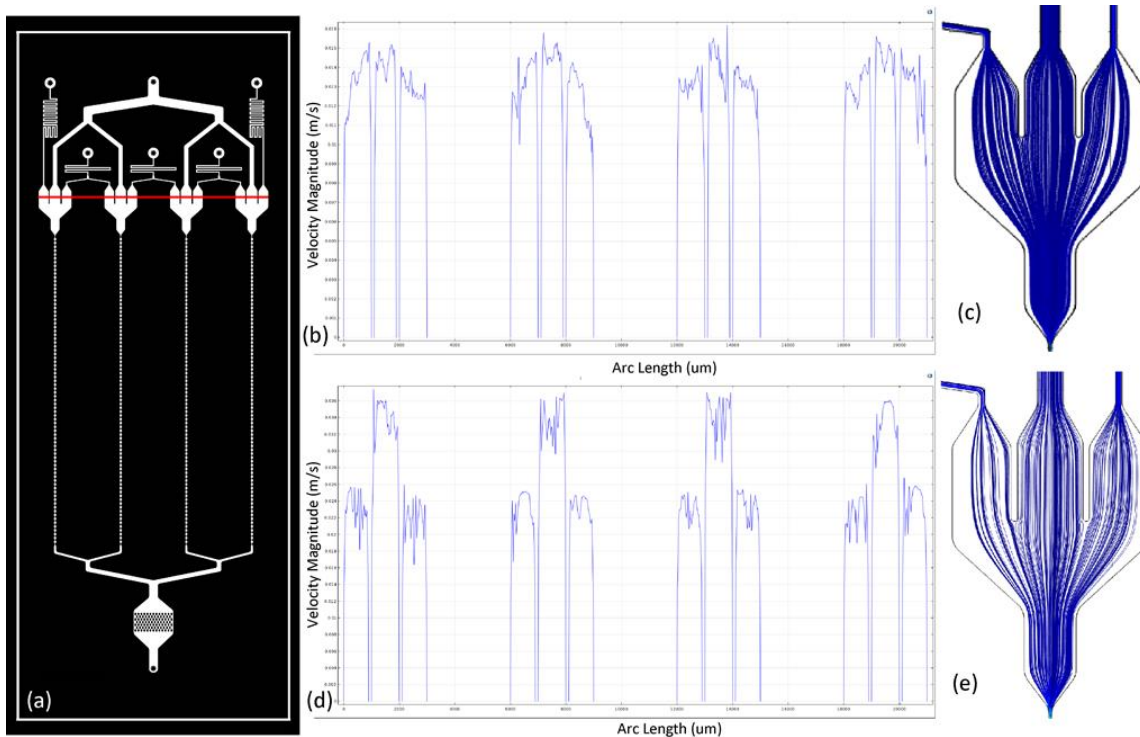


Figure 3.8 COMSOL simulation to optimize hydraulic resistance at MOFF microchannel outlet. (a) A schematic of a typical MOFF device and an arc (red line) along which the flow velocity profile is measured. (b) and (c) Flow velocity magnitude across all outlets and streamlines for a sample outlet when the outlet hydraulic resistance was set to collect proportional flow at each exit (based on the width of each exit). (d) and (e) Flow velocity magnitude across all outlets and streamlines for a sample outlet when the outlet hydraulic resistance was set to collect 1.3x volumetric flow at the central exit where cancer cells are collected.

3.4. Microfabrication

All devices were fabricated using soft lithography and PDMS casting (see Figure 2.14 for the process). Due to the unusually high aspect ratio of features designed in some filters (e.g., the slits in MASCFF and microposts in DLD), the recipe was experientially optimized to allow fabrication of such features in SU-8 and PDMS. Because of the typically

small feature sizes present in all filters, prior to casting PDMS, SU-8 molds were silanized with (tridecafluoro-1,1,2,2-tetrahydrooctyl) trichlorosilane (Sigma-Aldrich, ON, Canada). Such a treatment allows the baked PDMS to be easily pilled off the SU-8 mold and prevents any damage to small features on both the mold and the PDMS cast. Once the inlet and outlet holes were punched in the PDMS part, its inner surface was activated using the air plasma and was irreversibly bonded to a glass substrate.

3.5. Results

3.5.1. Microfabrication

Based on different designs explained earlier, several prototypes were fabricated and analyzed (see Figure 3.9).

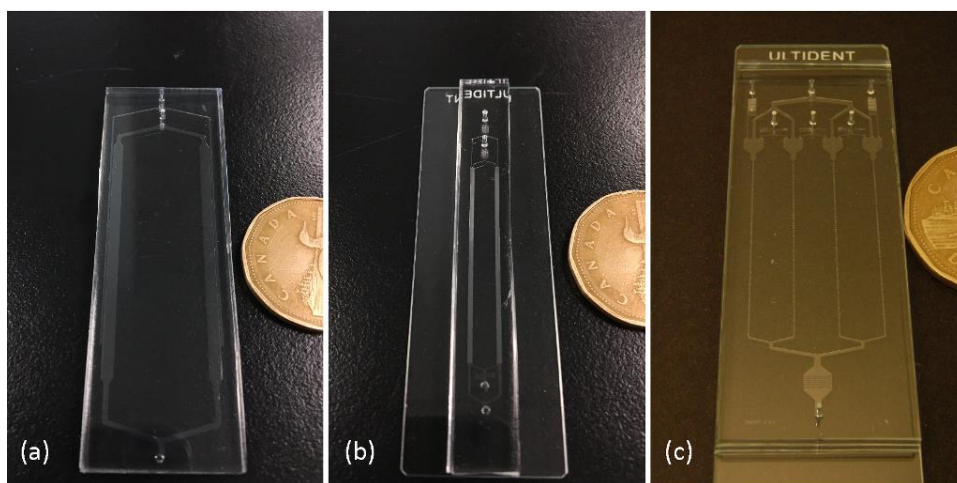


Figure 3.9 Photographs of different microfluidic filter prototypes: (a) MASCF device, (b) DLD device, (c) MOFF device.

While soft lithography is a well-established microfabrication technique, the main challenge associated with the microfabrication of devices presented in this chapter was the unusually high aspect ratio of some structures crucial for particle separation. The separation principle in the novel MASCF filter presented earlier in this chapter is based on numerous extremely narrow side slits that connect two parallel much wider microchannels (see Figure 3.2). The width of these side slits was designed to be $\sim 5 \mu\text{m}$. Considering the constant height across most devices ($\sim 55 \mu\text{m}$), such a small width would translate into an aspect ratio of >10 for side slits (see Figure 3.10.a and b). SU-8 has generally been a photoresist of choice for high aspect ratio fabrication purposes; however,

the microfabrication of structures with an aspect ratio of >10 in SU-8 is a challenging task that entails rigorous experimental optimization of the fabrication recipe [242] [243] [244]. In particular, it was found that the soft bake should be done such that no solvent is trapped within the lower layers of SU-8. A partially baked high aspect ratio SU-8 structure with remnant solvent within the structure was particularly prone to collapse and deformation (see Figure 3.10.c). To address this issue, the temperature during the soft bake should be increased slowly and gradually. A sudden heat shock would result in solidification of the surface of SU-8 structures, leaving some solvent trapped in lower layers.

Another issue concerning the fabrication of MASCFE devices was the overexposure of SU-8 at the corners of structures, particularly where side slits connect to the sample microchannel. Due this overexposure, instead of sharp edges at these corners, curved edges were formed (see Figure 3.10.d). These curved corners, in turn, resulted in a relatively wider entrance to side slits. As it is discussed in the next section, this issue partly resulted in cancer cell loss in the MASCFE device, as target cancer cells were able to squeeze through this wide entrance and leave the sample microchannel. The overexposure at corners is an inherent issue in photolithography. While its effect can be reduced by experimental optimization of the exposure dose, it cannot entirely be eliminated. One solution is to use super high-resolution exposure systems, such as electron-beam lithography (EBL), to expose the photoresist, but such techniques are expensive, extremely slow, and not easily applicable to thick photoresist layers.

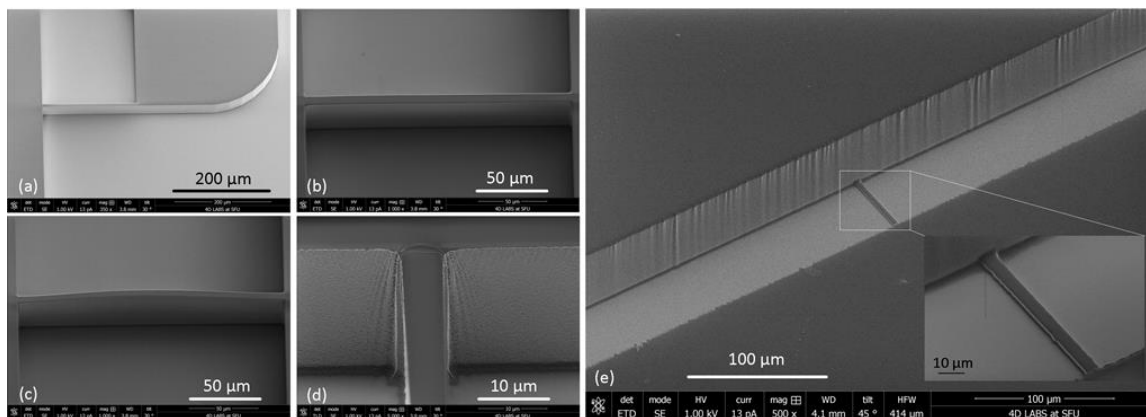
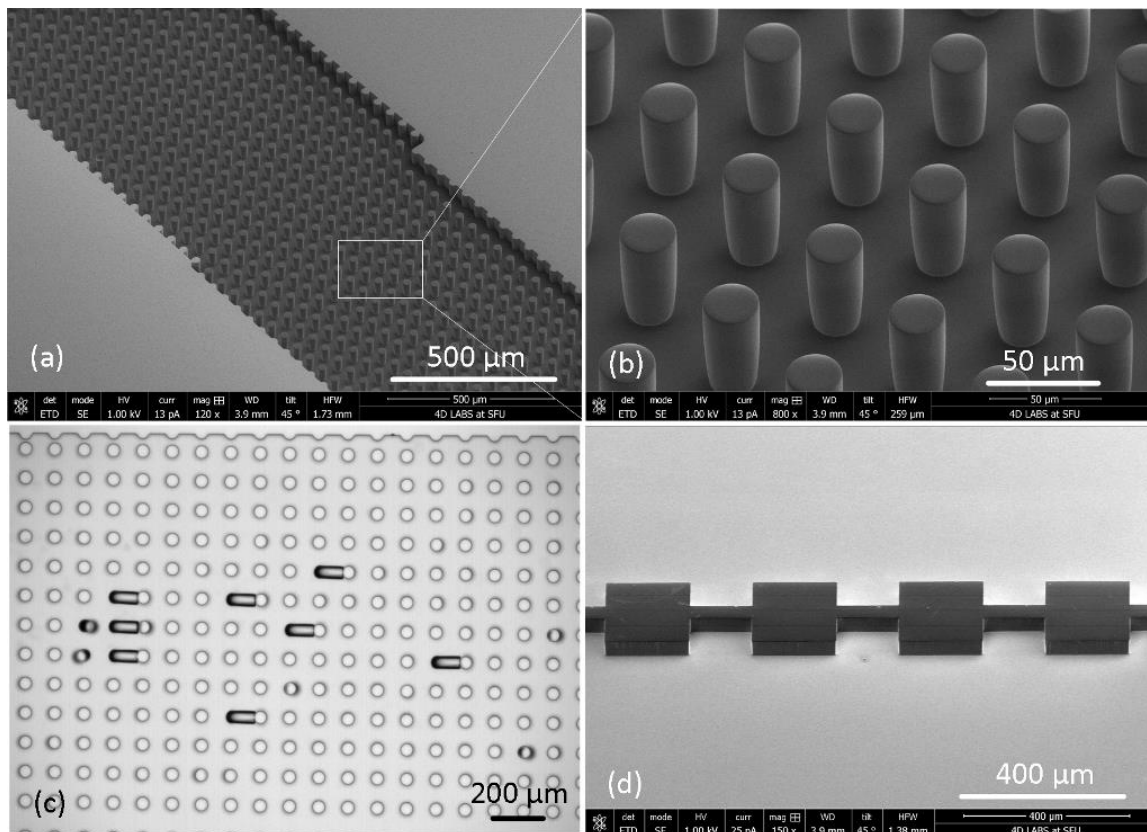


Figure 3.10 Different SEM views of a MASCFE SU-8 mold. (a) View of the first side slit connecting the sample microchannel (partly visible on left) to the collection microchannel (right). (b) A closer view of a functional side slit. (c) A faulty deformed side slit. (d) A close view of wider entrance to side slits caused by overexposure at sharp corners. (e) A MASCFE device with $\sim 5 \times 5 \mu\text{m}$ side slits.

Except for occasional cases in which PDMS microposts in DLD devices collapsed under pressure after the PDMS part was bonded to the glass substrate, no particular issue was observed in the fabrication of DLD and MOFF devices (see Figure 3.11).



Further details of this interfacing

Figure 3.11 (a) SEM view of a typical DLD microchannel. (b) The magnified SEM views of microposts within the DLD microchannel. (c) In some case, microposts collapsed under pressure after the PDMS part was bonded to the glass substrate. (d) SEM view of MOFF contraction/expansion units.

3.5.2. Qualitative Characterization of Efficiency of Filters to Remove Free Magnetic Beads

Several experiments were initially performed to visually evaluate the efficiency of different prototypes to remove unbonded free magnetic beads from the sample and retain target cancer cells. To assess MASCFE prototypes, at a given magnetic field created by a pair of magnets, the flow rate was adjusted until the best magnetic separation was observed. At its best performance, a MASCFE device could remove >50% of beads suspended in a buffer solution at an optimized flow rate of 125 μL/min. However, the particle separation performance was not sustainable for an extended duration of time or

large sample volumes, as some side slits tended to get clogged after >1 mL of sample was processed through the device. More importantly, another major issue with MASCFE filters was the unexpected considerable higher rate of the loss of target cells through side slits. It was observed that some LNCaP cells can pass through 5- μm -wide slits and enter the collection microchannel. The ability of cancer cells to move through such narrow openings, such as capillaries, is a major factor in hematogenous spread of cancer. While using 5 \times 5 μm side slits reduced the cell loss but, due to extremely small size of these slits, they were not as efficient for magnetic bead removal and became clogged rather quickly.

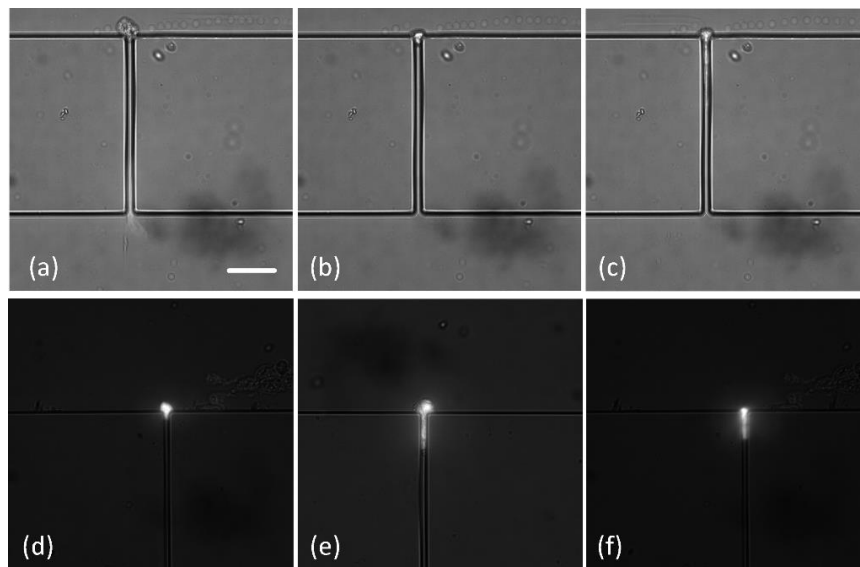


Figure 3.12 Examples of target cell loss in MASCFE devices partly due to the ability of cancer cells to pass through extremely narrow opening (e.g., capillaries in body). (a-c) and (d-f) show the time-lapse passage of two different LNCaP cells through side slits. Bar scale represents 50 μm .

The performance of different DLD prototypes was also investigated at different flow rates. The highest bead removal rate was achieved at $\sim 15 \mu\text{L}/\text{min}$. Under this condition, >75% of beads were removed from the sample and collected at the bead collection outlet while $\sim 70\%$ of target cancer cells were retained and collected at the refined sample outlet. The low throughput of this design could be improved by massive parallelization, where, for example, 20 DLD modules would be incorporated on the single device. Such an approach has been used by other researchers for removal of magnetic beads and RBCs from blood samples [228]. However, implementation of such a design in PDMS is relatively challenging and requires at least three separate layers that would include microposts, inlets/outlets, and microfluidic flow distribution/collection manifolds. Another issue concerning the PDMS-based DLD design was its malfunction once air bubbles entered

the devices. Due to the extremely high surface-area-to-volume ratio of the DLD design and extreme hydrophobicity of PDMS, air bubbles could not be easily removed and affected the separation efficiency (Figure 3.13).

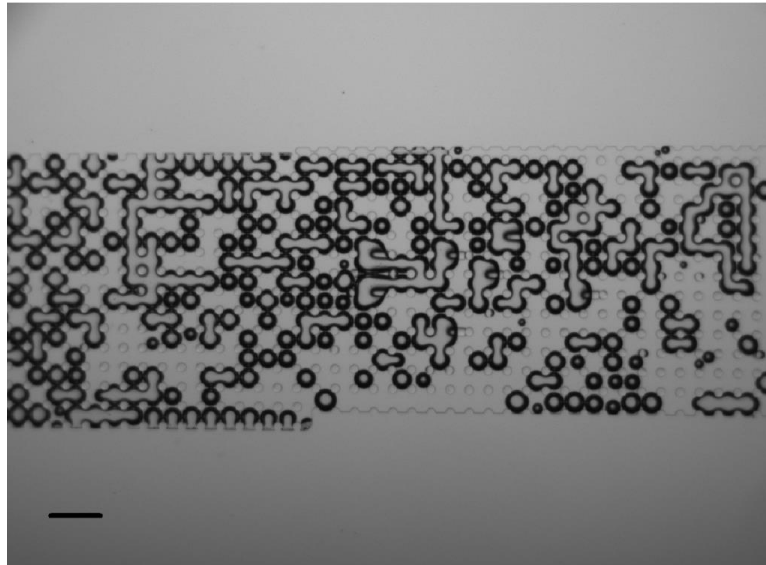


Figure 3.13 DLD malfunction due to accumulation of air bubbles within the device. Bar scale represents 200 μm .

The performance of MOFF prototypes was initially tested at the analytically set flow rate (i.e. 200 $\mu\text{L}/\text{min}$ for each module or ~ 800 $\mu\text{L}/\text{min}$ for four parallel modules). It was observed that at this flow rate, neither magnetic beads nor target cancer cells were focused at expected locations in MOFF microchannels. Instead, all particles were randomly scattered across the microchannel. The flow rate was experimentally adjusted, and the best performance was observed at 200 $\mu\text{L}/\text{min}$ (equal to 50 $\mu\text{L}/\text{min}$ for each module). At this flow rate, $\sim 80\%$ of particles and $\sim 85\%$ of labelled cells were collected at the corresponding outlets. Except for minor cases, no significant clogging was observed, as majority of large particles and debris (>100 μm in size) were stopped at the input filter. The designed hydraulic resistances performed at expected, and the collected fluid volume at each exit matched the designed values.

3.5.3. Quantitative Characterization and Cell Capture Experiments

Experimental Setup and Sample Preparation

Considering that the best overall performance for removing free magnetic beads and retaining cancer cells was observed using the MOFF filter, this design was selected

for further quantitative cell capture studies. For these experiments, the MOFF chip and the magnetic chip were connected in tandem and together formed a microfluidic platform that can be used for isolation of cancer cells from immunomagnetically labelled blood samples (see Figure 3.14). The same experimental setup and sample preparation protocols that explained earlier in Chapter 2 were also used for these experiments.

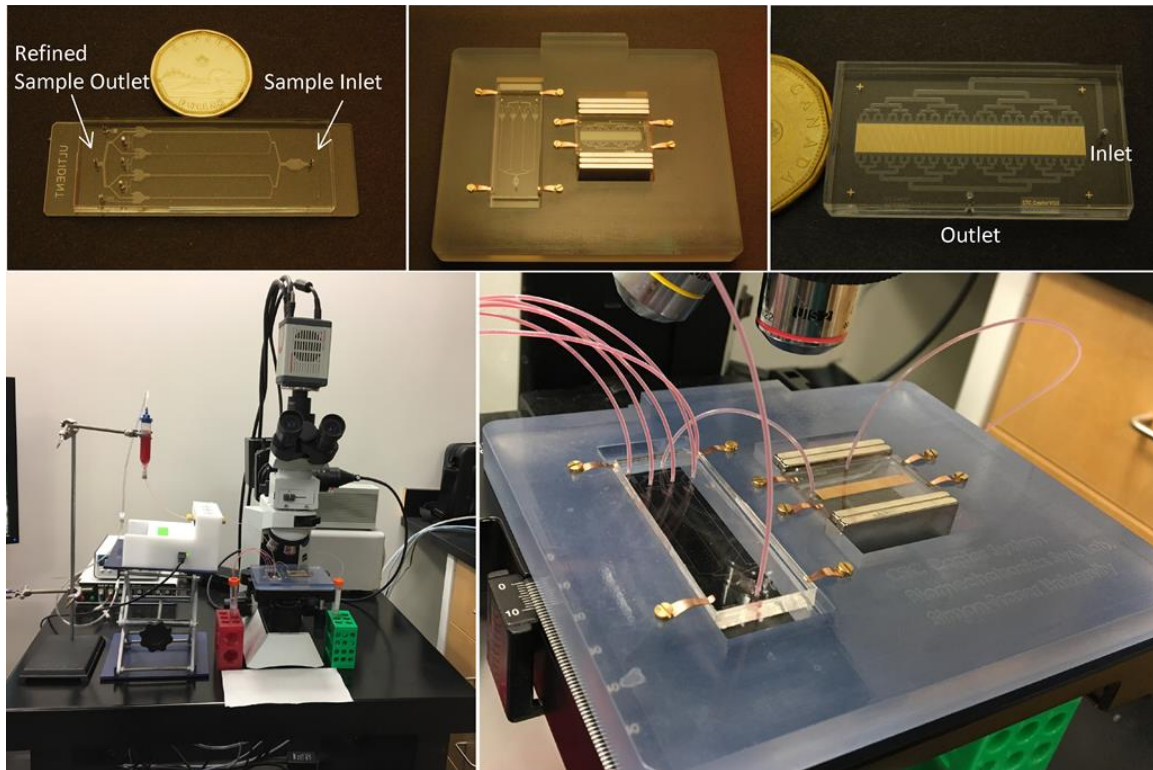


Figure 3.14 The experimental setup and the microfluidic platform for size-based enrichment and immunomagnetic isolation of cancer cells from spiked blood samples. Top row: the platform consists of two microfluidic chips, the hydrodynamic size-based MOFF filter (left) and the magnetic chip (right). The sample first enters the MOFF filter, whose refined sample outlet would be connected to the magnetic chip's inlet via a short piece of tubing. Extra magnetic particles removed by the MOFF filter would be collected at five different outlets. These two chips are placed in a custom-built adaptor that homes a pair of grade N52 NdFeB magnet stacks to create an external magnetic field in the desired direction that magnetically activates the magnetic chip. The platform itself can be integrated and fixed on a microscope stage for *in situ* visual analysis purposes.

Specificity and Sensitivity of MOFF Filter

To accurately evaluate the specificity of MOFF filter, defined as its ability to retain target cancer cells in the refined sample, several experiments were performed. Magnetically labelled LNCaP cells were seeded in the buffer solution at low concentrations (5-50 cells/mL), and the samples were processed at two different flow rates (150 and 200

$\mu\text{L}/\text{min}$, $n=6$ for each condition). Once the sample was processed, the number of LNCaP cells captured on the magnetic chip was counted. The specificity of MOFF filter was defined as the ratio of number of LNCaP cells captured on the magnetic chip to number of LNCaP cells initially seeded in the buffer solution. The recovery rates for samples processed at $150 \mu\text{L}/\text{min}$ and $200 \mu\text{L}/\text{min}$ were $58\pm 6.33\%$ and $77\pm 7.57\%$, respectively (see Figure 3.15.a and b). These results confirmed the earlier observations that the best performance of the MOFF filter is obtained when the sample is processed at $200 \mu\text{L}/\text{min}$.

Next, to evaluate the sensitivity of MOFF filter (percentage of beads removed by the filter) and its effect on overall recovery rate, a number of experiments was carried out, in which magnetically labelled LNCaP cells were seeded in buffer solutions (5-20 cells/mL) that were polluted with free magnetic beads at an average concentration corresponding to optimized labelling protocol for $2.8 \mu\text{m}$ beads ($\sim 1.5 \times 10^7$ beads/mL) ($n=5$). While it was not possible to numerically assess the efficiency of MOFF filter to remove magnetic beads, it was observed that the number of beads that were not removed by the MOFF filter and had made it to the magnetic chip and captured on permalloy structures was not high enough to cover the captured cells and prevent them from being visually detected. The LNCaP recovery rate was $74.7\pm 4.24\%$, which confirms that the LNCaP recovery rate is not significantly affected by extra captured beads (see Figure 3.15.c).

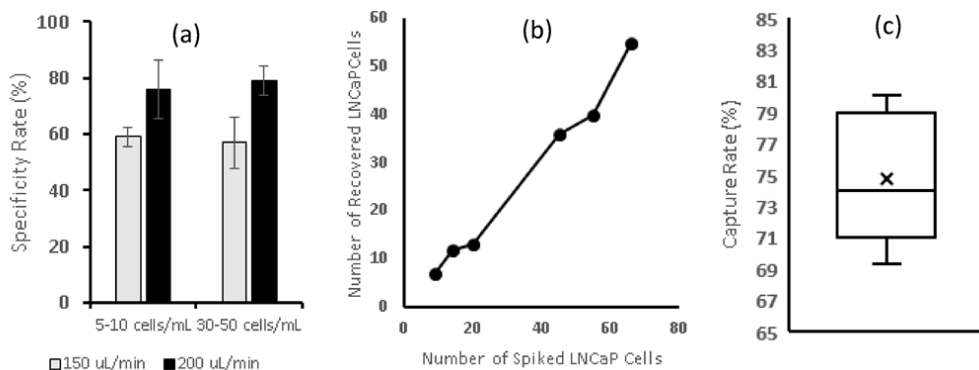


Figure 3.15 (a) The specificity rate (as defined in the text) of MOFF filter at different LNCaP cell concentrations and flow rates ($n=3$ for each concentration). (b) The number of LNCaP cells initially seeded (horizontal axis) versus number of LNCaP cells recovered (vertical axis) at $200 \mu\text{L}/\text{min}$. (c) Capture efficiency for recovery of labelled LNCaP cells from buffer polluted with $\sim 1.5 \times 10^7$ beads/mL ($n=5$).

Effect of Blood Cells on MOFF Filtration Specificity

There are at least a billion RBCs in a millilitre of whole blood. RBCs are disk-shaped and 6-8 μm in diameter. Therefore, based on the critical dimensions of MOFF filters designed to remove free magnetic beads, RBCs may also be focused in the MOFF microchannel and removed from the sample. To evaluate how this interference from RBCs would affect the filtration specificity, several blood experiments were carried out ($n=5$). LNCaP cells were fluorescently and magnetically labelled and seeded in healthy blood samples at low concentrations (5-20 cells/mL). The blood samples were then diluted 10 \times and processed at an average flow rate of 200 $\mu\text{L}/\text{min}$. The recovery rate was $79\pm 3\%$, confirming that blood cells do not affect the performance of the filter (see Figure 3.16).

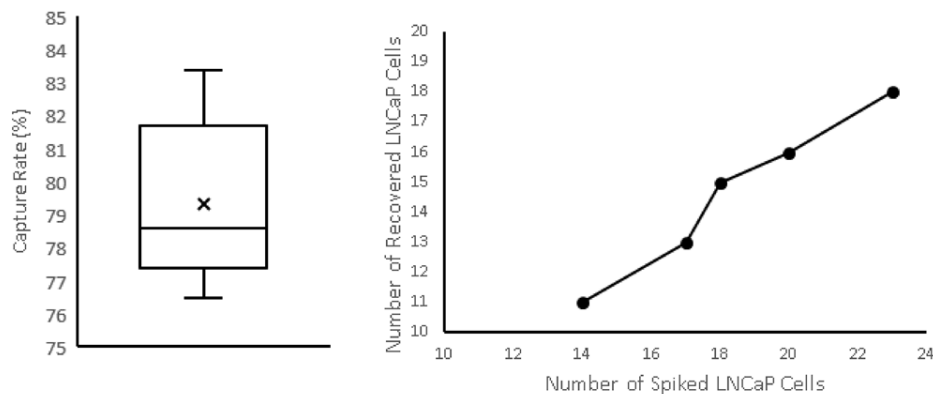


Figure 3.16 Capture efficiency of the platform for labelled LNCaP cells seeded in blood sample

Capture of LNCaP Cells from Spiked Blood Samples

Finally, after studying the performance of individual components of the proposed CTC isolation system, i.e. the immunomagnetic labelling protocol, the magnetic capture mechanism, and the filtration technique to remove free unbonded magnetic beads, to assess the performance of the complete system and fully simulate the isolation of rare CTCs from clinical blood samples a number of spiked blood experiments was performed ($n=5$). LNCaP cells were fluorescently labelled and seeded in healthy blood samples at clinically relevant low concentrations (5-20 cells/mL). The spiked blood samples were then immunomagnetically labelled according to the previously optimized protocol: they were first incubated with biotinylated anti-PSMA antibody (1.25 $\mu\text{g}/\text{mL}$) for 40 minutes followed by incubation with streptavidin-coated 2.8 μm magnetic beads ($\sim 1.5 \times 10^7$ beads/mL) for another 50 minutes on a vortex mixer at the room temperature. The blood samples were

10x diluted with the buffer solution and processed at a flow rate of $\sim 200 \mu\text{L}/\text{min}$. The capture results are summarized in Figure 3.17. The recovery rate was $70 \pm 3.34\%$, which is a function of several parameters, including immunomagnetic labelling efficiency, macro-to-micro interfacing efficiency, MOFF filtration sensitivity and specificity, and the magnetic chip's capture efficiency.

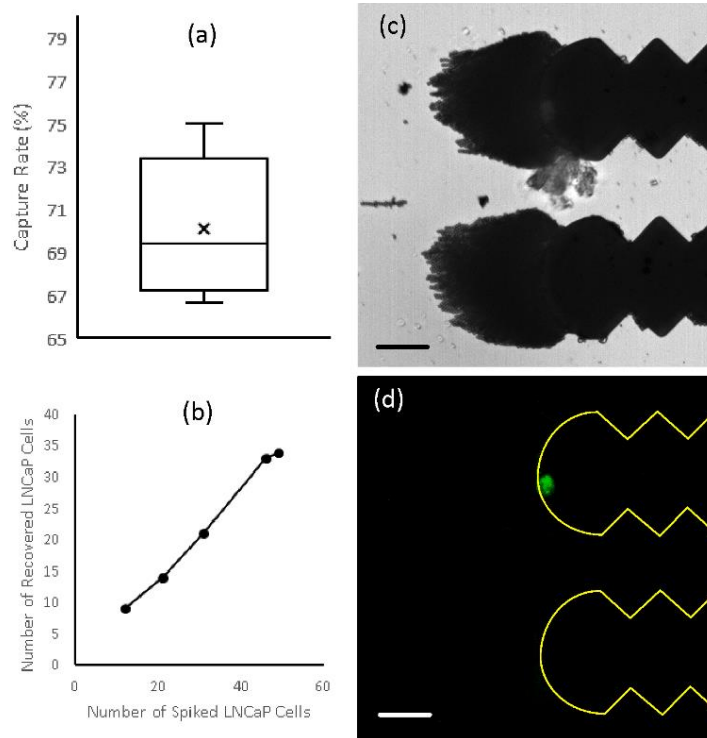


Figure 3.17 (a) Recovery rate of the platform for LNCaP cells spiked in blood (n=5). (b) Number of LNCaP cells originally spiked in blood (horizontal axis) versus number of LNCaP cells recovered (vertical axis). (c) and (d) Magnified views of a captured LNCaP cell on tip of a permalloy structure. Scale bars represent 50 μm .

3.6. Summary and Discussion

Microfluidic immunomagnetic cell separation is one of the most sensitive and specific techniques for rare cell isolation. However, a serious drawback concerning this method is the excessive number of free magnetic particles/beads that remain in the sample after the immunomagnetic labelling process. When a labelled sample is processed, the same mechanism that captures immunomagnetically labelled target cells would also capture these free beads in the sample. These free beads can affect the normal separation function and hamper the visual detection of captured target cells by accumulating on the device and quenching fluorescence signals or burying the capture

cells. Ideally, these free extra magnetic beads should be removed from the sample after the immunomagnetic labelling process. This is a crucial requirement for improving the overall performance of a microfluidic immunomagnetic cell separation system, particularly for rare cell separation, where detection of every single cells is critical. However, except for a single case [228], this issue has rarely been addressed in other works in which immunomagnetic methods have been used for CTC isolation [131] [226] [245] [246] [247].

Three different size-based filters were developed and thoroughly tested for continuously refining immunomagnetically labelled blood samples during my PhD research. The performance of each filter is summarized in Table 4.1. The novel MASCF filter showed an acceptable throughput and sensitivity, but due to the intrinsic plasticity of cancer cells [248] [249], it was concluded that the basic principle of cross flow-fractionation and its novel modified version employed in the MASCF filter does not provide an acceptable specificity for the current application. Experiments using the DLD filter, showed high sensitivity and specificity rates but suffered from a low throughput. Moreover, the proposed DLD devices were fabricated in PDMS, which is highly hydrophobic. Such a property along with the high surface-area-to-volume ratio of the DLD design could harm the normal function of device due to accidental bubble formation and blockage. Compared to MASCF and DLD filters, the MOFF filter displayed the best overall performance.

The final design for the proposed microfluidic platform for size-based enrichment and immunomagnetic isolation of prostate cancer cells from whole blood samples is made of the MOFF filter and the magnetic chip that are integrated in tandem. Rigorous quantitative characterization studies showed that the platform can successfully and consistently remove the majority of free magnetic beads (~80%) while retaining ~75-85% of target cancer cells. This degree of magnetic bead filtration was high enough to allow for visual detection of captured cancer cells on the magnetic chip. Based on the designed parameters, the best performance of the MOFF chip was expected to be achieved at a flow rate of ~800 $\mu\text{L}/\text{min}$. Nevertheless, preliminary experiments showed that the most efficient filtration is attained at a much lower flow rate (~200 $\mu\text{L}/\text{min}$). This discrepancy can be partly due to the microfabrication error. Moreover, the calculated particle Reynolds numbers for free magnetic beads and target cancer cells were not precisely within the range associated with the best performance of MOFF filters [236]. However, the overall

particle separation performance using the MOFF device developed in this work was analogous and comparable to those reported in previous works [236] [237] [240] [241].

Table 3.1 Summary of the filtration performance of MASCF, DLD, and MOFF designs

Filter	Sensitivity*	Specificity**	Throughput ($\mu\text{L}/\text{min}$)***
MASCF	>50%	N/A	125
DLD	75%	70%	15
MOFF	80%	85%	200

* The ratio of the number of magnetic beads removed from the sample by the filter to the number of magnetic beads in the original unfiltered sample.

** The ratio of the number of cancer cells retained in the refined sample and captured on the magnetic chip to the number of cancer cells initially seeded in the sample.

*** The maximum flow rate at which the best performance for each filter is achieved.

Chapter 4.

Retrieval and Propagation of Immunomagnetically Captured Cancer Cells

4.1. Background

The diagnostic and prognostic significance of the frequency of CTCs has initially been the major motivation for their capture from blood samples. However, the qualitative study of CTCs either at the molecular level or via functional assays offers far more valuable information than the mere CTC enumeration does and could provide more insight into the basic biology of metastasis and disease progression and be eventually used in precision oncology for development of personalized therapeutic regimens [250]. Such studies necessitate the retrieval and *in vitro* culture of live CTCs from patients' blood samples. Given the inherent scarcity of CTCs and difficulties associated with culturing them, this aspect of the CTC research has been addressed only by a few researchers [251]. As such, further research on this topic and optimization of current protocols for retrieval and propagation of the captured CTCs is necessary. The retrieval of immunomagnetically captured LNCaP cells on the magnetic chip and their propagation were briefly investigated as a pilot study towards the end of my PhD studies, which is presented in this chapter.

4.2. Effect of Immunomagnetic Labelling on Viability of LNCaP Cells

Prior to the experiments involving retrieval and propagation of captured LNCaP cells, the effect of immunomagnetic labelling on the viability of cells was studied. LNCaP cells were maintained in 10 mm culture plates as explained earlier. Before each experiment, the cells were rinsed with PBS and dissociated using the buffer solution (1% w/v BSA + 3mM EDTA in PBS). The dissociated cells were then collected and resuspended in the buffer solution. For each experiment, cell solutions containing $\sim 10^4$ cells suspending either in the buffer solution or in the culture medium (control) were prepared. The cells in each sample were then either only incubated with the biotinylated anti-PSMA antibody (1 $\mu\text{g}/\text{mL}$ for 40 minutes at the room temperature) or immunomagnetically labelled according to the optimized protocol explained earlier.

Following the above treatments, the cells in each solution were pelleted by centrifugation, resuspended in appropriate volumes of the culture medium, and placed back in the incubator. The cells were inspected daily for up to four days.

Figure 4.1 shows the cells with different treatments after 96 hours. Looking at the results, two major issues are evident. First, in general, the buffer solution used in cell capture experiments negatively affects the viability of LNCaP cells. For experiments carried out during this research, the use of this buffer solution was necessary, as it significantly reduces the cell aggregation and non-specific cell adhesion to the reservoir, tubing, and devices. While the buffer had been supplied with 1% v/w BSA and low concentrations of EDTA, it appears that the relatively short stay (<2 hours) of LNCaP cells in such an environment impair their viability. Second, regardless of the carrying medium (i.e. the cell culture medium or the buffer), the labeling of LNCaP cells with magnetic beads against PSMA can reduce the viability of cells.

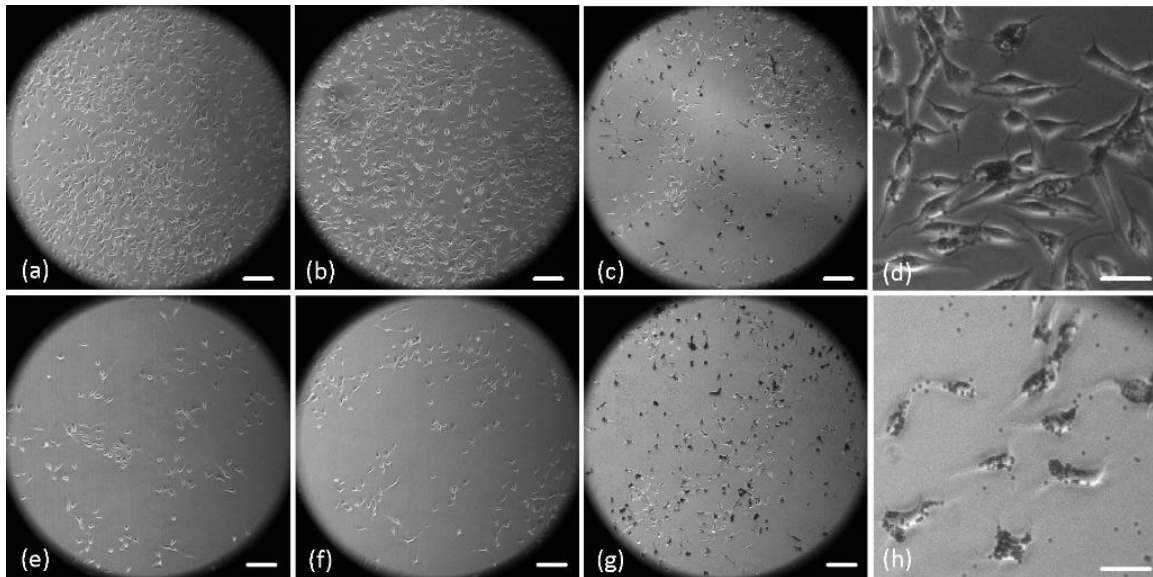


Figure 4.1 Viability of LNCaP cancer cells 96hrs after immunomagnetic labelling. Top row: LNCaP cells treated in the culture medium: (a) control cells, (b) cells labelled with biotinylated anti-PSMA antibody only, (c) cells labelled with the antibody and 2.8 μm magnetic beads, (d) closer view of cells labelled with the antibody and 2.8 μm magnetic beads. Bottom row: LNCaP cells treated in the buffer solution (1% v/w BSA + 3mM EDTA in PBS): (e) control cells, (f) cells labelled with biotinylated anti-PSMA antibody only, (g) cells labelled with the antibody and 2.8 μm magnetic beads, (h) closer view of cells labelled with the antibody and 2.8 μm magnetic beads. Scale bars in (a)-(c) and (e)-(g) represent 100 μm . Scale bars in (d) and(h) represent 50 μm .

4.3. Biocompatibility of the Microfluidic Magnetic Cell Separation System

In addition to the immunogenetic labelling process and conditions under which the cells are initially handled, another factor that may ultimately affect the viability of retrieved LNCaP cells is the interactions between the cells and the cell capture platform. PDMS, the tubing, and the glass substrates are all biocompatible components. To ensure biocompatibility of permalloy structures, they are sheathed by a 200-nm gold layer during the microfabrication. To confirm the biocompatibility of the magnetic chip, LNCaP cells were seeded on a magnetic component placed at the bottom of a 60 mm culture plate. The culture plate was then placed in an incubator and the cells were cultured under normal conditions (37°C and 5% CO₂). The cells were inspected under the microscope after 48 hours and no significant signs of necrotic cell death was observed (see Figure 4.2).

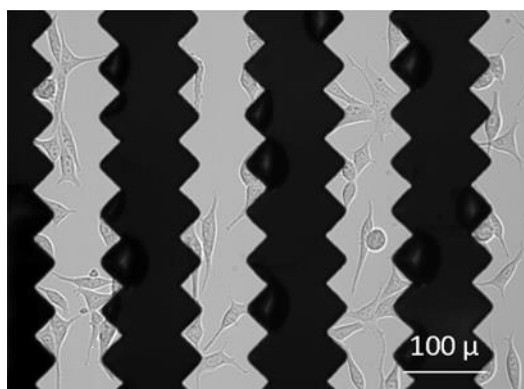


Figure 4.2 Validation of the biocompatibility of the magnetic chip. LNCaP cells seeded and incubated on the magnetic chip for 2 days without any sign of necrotic cell death. Black and gray areas represent permalloy and glass substrate, respectively.

4.4. Retrieval and Propagation of Captured LNCaP Cells

After studying various parameters that could potentially affect the viability of captured cells, the retrieval and propagation of LNCaP cells captured on the chip was attempted (n=3). For each trial, three samples containing $\sim 10^3$ LNCaP cells suspended in the buffer solution were prepared. One was the control, and the other two samples were immunomagnetically labelled using the optimized protocol explained earlier. One of the labelled samples was used as the second control, and the other sample was processed through the magnetic chip at the nominal flow rate of 100 $\mu\text{L}/\text{min}$. Once the entire sample

was processed, the chip was removed from the adaptor and placed on a hot plate set at 40°C. Then, 4 mL of the pre-warmed 0.05% EDTA-Trypsin solution was flushed through the chip at an average flow rate of 300 $\mu\text{L}/\text{min}$. The outflow was collected in a sterilized tube. The collected outflow and the two control samples were pelleted down. The supernatant was removed carefully from each sample and the pelleted cells were resuspended in the culture medium and incubated in a 12 well plate under normal conditions. Figure 4.3 shows the results for one of the trials. The results from the other two trials were similar. While the number of retrieved cells and their viability were not precisely quantified, it was observed that $\sim 75\%$ of captured cells were retrieved, of which $>50\%$ were viable after 48 hours.

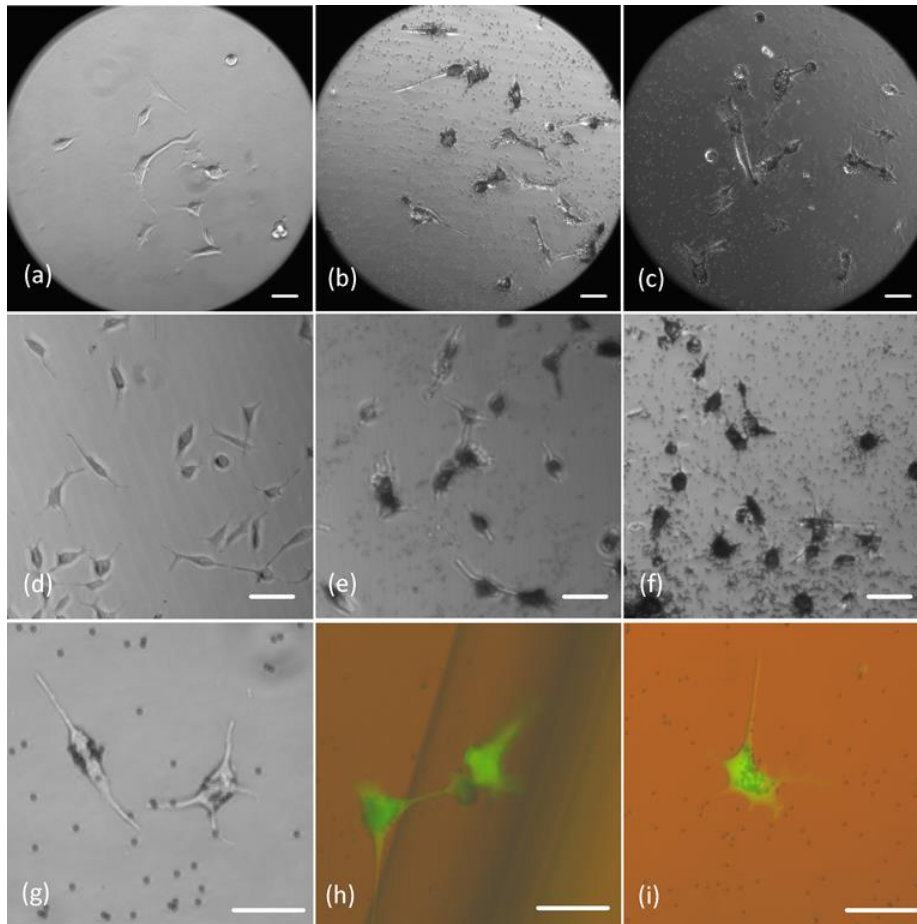


Figure 4.3 Retrieval and propagation of captured LNCaP cells on the magnetic chip. Top row shows cells after 48 hours: (a) non-labelled control cells, (b) immunomagnetically labelled control cells, (c) retrieved cells. Middle row shows cells after 72 hours: (d) non-labelled control cells, (e) immunomagnetically labelled control cells, (f) retrieved cells. (g) A closer view of retrieved cells after 72 hours. (h) and (i) Closer views of retrieved cells after 8 days. The cells were labelled with Calcein to confirm their viability. All scale bars represent 50 μm .

4.5. Summary and Discussion

Given the vast amount of information that can be obtained by studying CTCs, an efficient CTC isolation strategy should be ultimately able to retrieve these cells such that they can be successfully propagated. These CTC cultures then can be used in variety of applications. Therefore, considering the necessity of retrieving captured cancer cells, this topic was briefly studied at the end of my PhD studies. Although sub-optimal, the proposed approach retrieved and successfully cultured LNCaP cells for more than a week. While removing the magnetic chip from the external magnetic field and treating the captured cells with the pre-warmed 0.05% EDTA-Trypsin solution could dislodge majority of them from microtraps, it was observed that ~25% of cells remained captured on the chip. This could be due to either strong remnant magnetism of permalloy structures or strong non-specific adhesion of captured cells to the glass substrate. Further characterization of magnetic properties of deposited permalloy and optimization of the dissociating agent used to remove cells could improve the retrieval rate. Other factors that might affect the viability of cancer cells in the proposed CTC isolation capture method were also studied. Contrary to the common assumption that immunomagnetic labeling would not alter the viability of cells, it was observed that LNCaP cells that were immunomagnetically labelled against PSMA might undergo necrotic or apoptotic cell death.

Chapter 5.

Conclusion and Future Work

CTCs play a pivotal role in cancer metastasis. As such, their analysis may be used as an efficient biomarker for cancer diagnosis and prognosis. The longitudinal screening of CTCs can serve as both an intermediate endpoint for the efficiency of current treatment and a predictive biomarker for selection of the next line of therapy that may improve survival and QOL of cancer patients. Studying CTCs can also improve the existing knowledge regarding the biology of metastasis, enabling the development of more effective personalized therapies. By fully exploiting the high potential of CTCs in context of precision oncology, the envisioned future for clinical cancer management would be a model similar to antimicrobial therapy. In such a framework, the results from a blood test permits the molecular signature of malignancy, the therapeutic targets, and possible modifications in the existing treatments based on the quantitative and qualitative monitoring of CTCs. Thanks to recent advances in biotechnology and clinical computational biology, comprehensive catalogues of cancer genes are becoming increasingly malleable, making the implementation of the idea of genomics-driven cancer medicine possible more than ever. To further investigate such potential applications of CTCs, it is essential to first isolate these cells from the blood. To be useful in cancer research, an ideal method should recover viable cells that can be readily sorted and studied *in situ* at the single-cell level, or be retrieved and further analyzed *in vitro*. During the last decade, detection and isolation of CTCs has gained a considerable and increasing interest, which has resulted in the development of a wide range of technologies. Based on their underlying working principle, the existing CTC detection and isolation techniques can be broadly classified as nucleic acid-based, physical properties-based, and antibody-based methods, the latter of which is the most effective method for both detection and isolation of CTCs.

In this thesis, the development and preclinical testing of a novel microfluidic platform for sensitive and specific size-based enrichment and PSMA-based immunomagnetic isolation of blood-borne prostate cancer cells from cancerous blood sample models was presented. The platform is composed of a size-based microfluidic filter and a novel integrated microfluidic magnetic chip that are connected in tandem. The

filter is designed based on the principle of MOFF, fabricated in PDMS, and employed to continuously remove extra free magnetic beads from an immunomagnetically labelled blood sample before it enters the magnetic chip. The magnetic chip is composed of a permalloy-based magnetic component and a PDMS-based microfluidic counterpart that are irreversibly bonded and together form the integrated microfluidic magnetic chip. The magnetic component of the chip contains thousands of magnetic microtraps fabricated on a glass substrate. These microtraps are made by geometrically modifying 10- μm -thick permalloy strips, creating arrays of numerous sawtooth dentations at both sides of each strip. The microfluidic component of the chip includes a network of PDMS microchannels, bifurcations, diffusers, and a central microchamber that encloses microtraps.

Cell capture experiments using the magnetic chip showed that the proposed device can capture immunomagnetically labelled LNCaP cells with nearly 100% efficiency at very low cancer cell concentrations, demonstrating the efficiency of the magnetic separation mechanism and the macro-to-micro interfacing. The addressable location of microtraps on the chip would allow for automatic enumeration and analysis of captured cells using machine vision. Comparing the efficiency of capturing LNCaP cells from buffer and blood samples proved that blood cells do not significantly affect the capture efficiency. Moreover, minimum nonspecific adhesion of non-target blood cells on the chip was observed. However, since achieving an efficient immunomagnetic labelling of cancer cells spiked in whole blood samples requires incubation of an excessive number of magnetic beads with the sample, the capture and accumulation of numerous unbonded free magnetic beads on the chip did not allow visualization and full detection of captured cells when immunogenically spiked whole blood samples were processed. To address this issue two approaches were investigated: a) reducing the number of beads required for efficient labelling by lysing the blood and reducing the sample volume and b) devising an additional mechanism to continuously remove the unbonded magnetic beads from a sample before it enters the magnetic chip. Experiments using the first approach showed that the relatively harsh preprocessing of sample (i.e. lysing, pipetting, centrifuging, etc.) could result in inadvertent cell loss and reduce the overall recovery rate up to 40%, diminishing the impressive magnetic capture capability of the proposed chip.

To fundamentally address the problem of free unbonded magnetic beads, which is an inherent issue in the micro-scale magnetic cell separation, development of a microfluidic filter for refining immunomagnetically labelled blood samples was studied.

Three different devices were designed, fabricated, and thoroughly tested. While the novel MASCF filter could remove >50% of target particles, the natural plasticity of cancer cells and their ability to pass through extremely small openings made the proposed approach ineffective for this particular application. However, the proposed filtration method would be a practical approach for separation of magnetic particles from diamagnetic entities. The DLD device could remove free beads with a high sensitivity and specificity (>75% and ~70%, respectively), but with a painfully low throughput. Massive parallelization of DLD modules and its fabrication in PDMS was found to be a challenging task, especially considering the combined effect of the undesirable hydrophobicity of PDMS and the extremely high surface-area-to-volume ratio of the DLD design. Both of these issues could be addressed by implementing the parallel design in silicon (using DRIE), but this would be an expensive approach. The MOFF filter showed the best performance and was able to remove ~80% of free beads with close to 85% specificity at a practical throughput (200 μ L/min). Furthermore, blood cells did not affect the filtration performance. The proposed immunomagnetic cell isolation approach, including the labelling protocol, the micro-to-macro interfacing, and the integrated platform, was able to capture prostate cancer cells at clinically relevant concentrations (5-20 cells/mL) with up to 75% efficiency. Although this research was focused on prostate cancer cells, the developed technology is applicable to other cancers as well.

Finally, the retrieval and propagation of captured LNCaP cells on the magnetic chip was briefly studied. Although sub-optimal, the proposed approach retrieved ~75% of captured cells and successfully cultured >50% of them for more than a week.

The proposed microfluidic platform in this thesis has shown reliably high capture efficiency and specificity in preclinical studies. Therefore, the natural next step in evaluating the performance of the platform would involve clinical studies. Accordingly, the proposed future works are as follows:

1) Increasing the recovery rate of the platform by improving the specificity of the MOFF filter

Currently, the MOFF filter can effectively remove at least 80% of free unbonded magnetic beads from immunomagnetically labelled blood samples. In doing so, the filter also non-specifically removes some target cancer cells (15-20%). The overall recovery

rate of the platform can be increased by improving the specificity of the MOFF filter such that it retains all target cancer cells while removing same amount of free magnetic beads from the sample. As mentioned earlier, experimental observations showed that not all cancer cells are precisely focused at the center of MOFF modules in the current design. This leaves some cancer cells focused at both sides of the module, resulting in their non-specific filtration along with free magnetic beads. Further studying the flow dynamics and its interaction with cancer cells and experimental optimization of the outlet design would improve the performance of the MOFF filter.

2) Performing a clinical validation study using blood samples from cancer patients and head-to-head comparison with the clinically-approved CellSearch[®] system

CTCs are known to be highly heterogeneous, showing variations in morphology, genotype, and phenotype even within a single blood draw [8]. Therefore, depending on the physical or molecular characteristics used for isolation of putative CTCs, positive selection techniques, such as the method presented in this thesis, may isolate different populations of CTCs. Thus, it is critical to verify and characterize the clinical significance of captured CTCs based on the criteria employed for CTC isolation by this technique. Currently, the CellSearch[®] system is the only clinically approved assay, but it only captures CTCs expressing sufficient amount of EpCAM. However, several studies have now confirmed that EpCAM expression among cancer cells vary significantly, which may be a direct consequence of the EMT. Given that the EMT has been partially associated with metastasis-initiating cancer cells, it is likely that systems such as CellSearch[®] may neglect an important subpopulation of CTCs, which warrants further investigation.

To evaluate the performance of the proposed platform and compare it with the CellSearch[®] system, a clinical study will be conducted as follows. First, to confirm the specificity of the isolation results, control blood samples from 25 healthy donors will be processed and a cut-off will be set for CTC+ samples. Next, 50 patients with established metastatic prostate cancer (chemo-refractory or castration resistant) with documented metastases via bone scan or CT who are progressing despite continued standard-of-care therapy (to ensure adequate disease burden) will be recruited. In addition, 25 patients with localized early stage disease before or after surgical castration and adjuvant therapy will be accrued (to assess the ability of the proposed platform to isolate CTCs in early stage

cancer). Two 7.5 ml blood samples will be drawn from each subject, one of which for CTC enumeration using the CellSearch® platform and for comparative purposes. The second sample will be processed using the proposed platform in this thesis. The identity of isolated CTCs on the magnetic chip will be confirmed by examining DAPI and Alpha-methylacyl-CoA racemase expression (unique to prostate cells), and epithelial markers (EpCAM, pan-cytokeratin) expression and the lack of CD45 expression (unique to leukocytes). The isolated cells will also be characterized for TMPRSS2-ERG fusion status (FISH), androgen receptor gene amplification (FISH) to confirm malignant origin.

3) Assessing the clinical value of CTC counts using the platform and its association with other clinical markers

4) Studying the molecular heterogeneity of CTCs via *in situ* and/or *in vitro* analysis of the expression of several markers with known implications in disease progression and their clinical significance

In addition to the clinical significance of the frequency of CTCs, there remain other significant issues that need to be studied further. As thoroughly discussed earlier, genomic and proteomic characterization of CTCs offers valuable information about the malignancy and could be employed for developing personalized therapeutic regimens. For example, the over-expression of vimentin, putatively known as an EMT marker, correlates well with accelerated tumour growth, invasion, and poor prognosis. In addition, CTCs expressing CD44, which are not present in all CTCs, have been associated with a lower OS and increased metastatic activity of cancer.

The primary objective of this study will be to prospectively assess the prognostic utility of the frequency of captured CTCs as well as other CTC phenotypes (e.g., PSMA+/EpCAM^{low}/vimentin^{high}) as predictors of OS and PFS. The secondary objective is to explore the concordance of the CTC data with other clinical measures of disease burden (e.g., Gleason score, PSA, alkaline phosphatase, lactate dehydrogenase, and patterns of metastatic spread). A fluorescent imaging protocol will be optimized for visual analysis of various markers (EpCAM, pan-CK, CD44, vimentin, CD45, DAPI). Kaplan-Meier methods, log-rank test, and univariate or multivariate Cox proportional hazard analyses will be used to establish the association of the CTCs data (at baseline and during the follow-up) and other prognostic indicators with PFS and OS and with each other. For OS studies, all

recruited patients with metastatic cancer, and for PFS studies, a cohort of the metastatic patients who are starting a new line of therapy (e.g., enzalutamide, docetaxel, abiraterone acetate, cabazitaxel) will be prospectively followed up for at least 12 months. Primary endpoint will be the disease progression as clinically defined by serum PSA level (according to Prostate Cancer Clinical Trials Working Group 2 (PCWG2) guidelines), bone scan, soft tissue radiography (new lesions or progression of existing lesions), or death (whichever happens first). Blood collection for CTC screening will be performed at the baseline, every two months during the treatment, and also when the primary endpoint is reached. Laboratory and imaging assessments will be performed per discretion of the treating physician, at least every 3 months. Thus, not only their frequency but also the molecular determinants of individual CTCs will be screened and evaluated as potentially more accurate biomarkers for PFS, OS, and treatment efficiency.

5) Optimizing the protocol for retrieval and propagation of the isolated CTCs

Using the proposed protocol in Chapter 4, captured LNCaP cells were retrieved and cultured after isolation on the magnetic chip by removing the external activating magnetic field and flushing the chip with a mild dissociating reagent. However, it is essential to develop and optimize a protocol that can retrieve and propagate the captured CTCs more effectively.

First, development of a decapeptide directed to the immunogenic site mapped on PSMA for the proprietary mouse monoclonal antibody will be studied. This decapeptide would be flushed through the system after CTC capture to compete off the bead-Ab complex from the PSMA expressing cancer cells, thereby releasing the cell from the capture site. Next, a clonogenic assays on collected CTCs will be performed. LNCaP-GFP-AR cells will be seeded into whole mouse blood at various dilutions. The captured cells will be retrieved and cultured in the appropriate medium. Clonogenic cells will be scored after 48 and 72 h to determine viability of the captured cells. Expanded clonogenic cells will be subjected to a battery of validation experiments including quantitative RT-PCR and immunoblotting of cellular lysates to assess PCa marker gene transcript and protein levels (PSA, CGR-A, ENO2, AR, etc.). Application of propagation protocols previously reported for isolating single cells for expansion and engrafting into renal capsule assays will also be studied [252].

References

- [1] B. Brehm-Stecher and E. Johnson, "Single-cell microbiology: tools, technologies, and applications," *Microbiol Mol Biol Rev.*, vol. 68, no. 3, pp. 538-559, September 2004.
- [2] H. Esmailsabzali, K. Sakaki, N. Dechev, R. D. Burke and E. J. Park, "Machine vision-based localization of nucleic and cytoplasmic injection sites on low-contrast adherent cells," *Medical & Biological Engineering & Computing*, vol. 50, no. 1, pp. 11-21, 2012.
- [3] K. Sakaki, H. Esmailsabzali, S. Massah, P. Gratien, N. Dechev, R. D. Burke and E. J. Park, "Localized, Macromolecular Transport for Thin, Adherent, Single Cells via an Automated single Cell Electroporation Biomanipulator," *IEEE Transactions on Biomedical Engineering*, vol. 60, no. 11, pp. 3113-3123, 2013.
- [4] G. 2. M. a. C. o. D. Collaborators, "Global, regional, and national life expectancy, all-cause mortality, and cause-specific mortality for 249 causes of death, 1980-2015: a systematic analysis for the Global Burden of Disease Study 2015," *Lancet*, vol. 388, no. 10053, pp. 1459-1544, 2016.
- [5] K. Pantel and M. Speicher, "The biology of circulating tumor cells," *Oncogene.*, p. doi: 10.1038/onc.2015.192, 2015.
- [6] D. Haber and V. Velculescu, "Blood-based analyses of cancer: circulating tumor cells and circulating tumor DNA," *Cancer Discov.* , vol. 4, no. 6, pp. 650-61, 2014.
- [7] L. H., "Cancer theory faces doubts," *Nature*, vol. 472, no. 7343, 2010.
- [8] A. Powell, A. Talasaz, H. Zhang, M. Coram, A. Reddy , G. Deng , M. Telli, R. Advani, R. Carlson, J. Mollick, S. Sheth, A. Kurian, J. Ford and F. Stockdale, "Single cell profiling of circulating tumor cells: transcriptional heterogeneity and diversity from breast cancer cell lines," *PLoS One*, vol. 7, no. 5, 2012.

- [9] T. Fehm, V. Muller, B. Aktas, W. Janni, A. Schneeweiss, E. Stickeler, C. Lattrich, C. Löhberg, E. Solomayer, B. Rack, S. Riethdorf and C. Klein, "HER2 status of circulating tumor cells in patients with metastatic breast cancer: a prospective, multicenter trial," *Breast Cancer Res Treat.*, vol. 124, no. 2, pp. 403-12, 2010.
- [10] C. Scheel and R. Weinberg, "Cancer stem cells and epithelial-mesenchymal transition: concepts and molecular links," *Semin Cancer Biol.* , vol. 22, no. 5-6, pp. 396-403, 2012.
- [11] A. Singh and J. Settleman, "EMT, cancer stem cells and drug resistance: an emerging axis of evil in the war on cancer," *Oncogene*, vol. 29, no. 34, pp. 4741-51, 2010.
- [12] P. Gupta, C. Chaffer and R. Weinberg, "Cancer stem cells: mirage or reality?," *Nat Med.* , vol. 15, no. 9, pp. 1010-2, 2009.
- [13] J. Visvader and G. Lindeman, "Cancer stem cells: current status and evolving complexities," *Cell Stem Cell*, vol. 10, no. 6, pp. 717-28, 2012.
- [14] C. Eaves , "Cancer stem cells: Here, there, everywhere?," *Nature*, vol. 456, no. 72222, pp. 581-2, 2008.
- [15] A. Mitra, L. Mishra and S. Li, "EMT, CTCs and CSCs in tumor relapse and drug-resistance," *Oncotarget*, vol. 6, no. 13, pp. 10697-711, 2015.
- [16] M. Krebs , R. Metcalf , L. Carter, G. Brady , F. Blackhall and C. Dive , "Molecular analysis of circulating tumour cells-biology and biomarkers," *Nat Rev Clin Oncol.*, vol. 11, no. 3, pp. 129-44, 2014.
- [17] A. Krasnitz, J. Kendall , J. Alexander, D. Levy and M. Wigler, "Early Detection of Cancer in Blood Using Single-Cell Analysis: A Proposal," *Trends Mol Med.* , p. doi: 10.1016/j.molmed.2017.05.005, 2017.
- [18] C. Alix-Panabières and K. Pantel, "Characterization of single circulating tumor cells," *FEBS Lett.* , pp. doi: 10.1002/1873-3468.12662, 2017.

- [19] C. Alix-Panabières and K. Pantel , "Clinical applications of circulating tumor cells and circulating tumor DNA as liquid biopsy," *Cancer Discov.* , vol. 6, no. 5, pp. 479-91, 2016.
- [20] M. Cristofanilli, G. Bud, M. Ellis, A. Stopeck, J. Matera, M. Miller, J. Reuben, G. Doyle, W. Allard, L. Terstappen and D. Hayes, "Circulating tumor cells, disease progression, and survival in metastatic breast cancer," *N Engl J Med.* , vol. 351, no. 8, pp. 781-91, 2004.
- [21] J. Doyen, C. Alix-Panabières, P. Hofman , S. Parks, E. Chamorey , H. Naman and J. Hannoun-Lévi, "Circulating tumor cells in prostate cancer: a potential surrogate marker of survival," *Crit Rev Oncol Hematol.*, vol. 81, no. 3, pp. 241-56, 2012.
- [22] K. Pantel and R. Brakenhoff, "Dissecting the metastatic cascade," *Nat Rev Cancer.* , vol. 4, no. 6, pp. 448-56, 2004.
- [23] Y. Hüsemann , J. Geigl , F. Schubert , P. Musiani , M. Meyer, E. Burghart , G. Forni, R. Eils, T. Fehm, G. Riethmüller and C. Klein, "Systemic spread is an early step in breast cancer," *Cancer Cell.* , vol. 13, no. 1, pp. 58-68, 2008.
- [24] U. De Giorgi , M. Mego, E. Scarpi, M. Giuliano, A. Giordano, J. Reuben, V. Valero , N. Ueno, G. Hortobagyi and M. Cristofanilli, "Relationship between lymphocytopenia and circulating tumor cells as prognostic factors for overall survival in metastatic breast cancer," *Clin Breast Cancer.* , vol. 12, no. 4, pp. 264-9, 2012.
- [25] T. Hiltermann , M. Pore, A. van den Berg , W. Timens, H. Boezen, J. Liesker , J. Schouwink, W. Wijnands, G. Kerner, F. Kruyt , H. Tissing, A. Tibbe, L. Terstappen and H. Groen, "Circulating tumor cells in small-cell lung cancer: a predictive and prognostic factor," *Ann Oncol.* , vol. 23, no. 11, pp. 2937-42, 2012.
- [26] J. Hou, M. Krebs, L. Lancashire , R. Sloane , A. Backen , R. Swain, L. Priest , A. Greystoke , C. Zhou, K. Morris, T. Ward, F. Blackhall and C. Dive, "Clinical significance and molecular characteristics of circulating tumor cells and circulating

- tumor microemboli in patients with small-cell lung cancer," *J Clin Oncol.* , vol. 30, no. 5, pp. 525-32, 2012.
- [27] H. Iinuma , T. Watanabe, K. Mimori, M. Adachi, N. Hayashi, J. Tamura, K. Matsuda, R. Fukushima, K. Okinaga, M. Sasako and M. Mori, "Clinical significance of circulating tumor cells, including cancer stem-like cells, in peripheral blood for recurrence and prognosis in patients with Dukes' stage B and C colorectal cancer," *J Clin Oncol.* , vol. 29, no. 12, pp. 1547-55, 2011.
- [28] G. Vona, L. Estepa, C. Bérout, D. Damotte, F. Capron, B. Nalpas, A. Mineur, D. Franco, B. Lacour , S. Pol, C. Bréchet and P. Paterlini-Bréchet , "Impact of cytomorphological detection of circulating tumor cells in patients with liver cancer.," *Hepatology.*, vol. 39, no. 3, pp. 792-7, 2004.
- [29] L. Zhang, S. Riethdorf , G. Wu, T. Wang, K. Yang, G. Peng, J. Liu and K. Pantel, "Meta-analysis of the prognostic value of circulating tumor cells in breast cancer," *Clin Cancer Res.*, vol. 18, no. 20, pp. 5701-10, 2012.
- [30] A. Lucci , C. Hall, A. Lodhi, A. Bhattacharyya, A. Anderson, L. Xiao, I. Bedrosian, H. Kuerer and S. Krishnamurthy , "Circulating tumour cells in non-metastatic breast cancer: a prospective study," *Lancet Oncol.*, vol. 13, no. 7, pp. 688-95, 2012.
- [31] B. Franken, M. de Groot , W. Mastboom, I. Vermes, J. van der Palen, A. Tibbe and L. Terstappen , "Circulating tumor cells, disease recurrence and survival in newly diagnosed breast cancer," *Breast Cancer Res.* , vol. 14, no. 5, p. R133, 2012.
- [32] L. Devriese, E. Voest, J. Beijne and J. Schellens, "Circulating tumor cells as pharmacodynamic biomarker in early clinical oncological trials," *Cancer Treat Rev.* , vol. 37, no. 8, pp. 579-89, 2011.

- [33] D. Hayes and J. Smerage, "Is there a role for circulating tumor cells in the management of breast cancer?," *Clin Cancer Res.*, vol. 14, no. 12, pp. 3646-50, 2008.
- [34] J. Smerage, W. Barlow, G. Hortobagyi, E. Winer, B. Leyland-Jones, G. Srkalovic, S. Tejwani, A. Schott, M. O'Rourke and D. Lew, "Circulating tumor cells and response to chemotherapy in metastatic breast cancer: SWOG S0500," *J Clin Oncol.* , vol. 32, no. 31, pp. 3483-9, 2014.
- [35] E. Antonarakis, C. Lu, H. Wang, B. Lubber, M. Nakazawa, J. Roeser, Y. Chen, T. Mohammad, Y. Chen and H. Fedor, "AR-V7 and Resistance to Enzalutamide and Abiraterone in Prostate Cancer," *New England Journal of Medicine*, vol. 371, pp. 1028-1038, 2014.
- [36] J. Thiery, "Epithelial-mesenchymal transitions in tumour progression," *Nat Rev Cancer.* , vol. 2, no. 6, pp. 442-54, 2002.
- [37] I. Baccelli, A. Schneeweiss, S. Riethdorf, A. Stenzinger, A. Schillert, V. Vogel, C. Klein and M. Saini, "Identification of a population of blood circulating tumor cells from breast cancer patients that initiates metastasis in a xenograft assay," *Nat Biotechnol.* , vol. 31, no. 6, pp. 539-44, 2013.
- [38] G. Budd , M. Cristofanilli, M. Ellis, A. Stopeck, E. Borden, M. Miller , J. Matera, M. Repollet , G. Doyle, L. Terstappen and C. Hayes, "Circulating tumor cells versus imaging--predicting overall survival in metastatic breast cancer," *Clin Cancer Res.*, vol. 12, no. 21, 2006.
- [39] R. Siegel, K. Miller and A. Jemal, "Cancer statistics, 2017," *CA: Cancer J. Clin.*, vol. 67, no. 1, pp. 7-30, 2017.
- [40] D. Hanahan and R. Weinberg, "Hallmarks of Cancer: The Next Generation," *Cell*, vol. 144, no. 5, pp. 646-74, 2011.
- [41] R. Mathew, V. Karantza-Wadsworth, and E. White, "Role of autophagy in cancer," *Nat Rev Cancer*, vol. 7, no. 12, pp. 961-7, 2010.

- [42] P. Carmeliet and R. Jain, "Angiogenesis in cancer and other diseases," *Nature*, vol. 407, no. 6801, pp. 249-57, 2000.
- [43] J. Pouyssegur , F. Dayan and N. Mazure , "Hypoxia signalling in cancer and approaches to enforce tumour regression," *Nature*, vol. 441, no. 7092, pp. 437-43, 2006.
- [44] Y. Kang and J. Massagué , "Epithelial-mesenchymal transitions: twist in development and metastasis," *Cell*, vol. 118, no. 3, pp. 277-9, 2004.
- [45] D. Micalizzi , D. Haber and S. Maheswaran, "Cancer metastasis through the prism of epithelial-to-mesenchymal transition in circulating tumor cells," *Mol Oncol.* , pp. doi: 10.1002/1878-0261.12081, 2017.
- [46] R. Kalluri and R. Weinberg , "The basics of epithelial-mesenchymal transition," *J Clin Invest.*, vol. 119, no. 6, pp. 1420-8, 2009.
- [47] D. Kong, Y. Li, Z. Wang and F. Sarkar, "Cancer Stem Cells and Epithelial-to-Mesenchymal Transition (EMT)-Phenotypic Cells: Are They Cousins or Twins?," *Cancers (Basel)*, vol. 3, no. 1, pp. 716-29, 2011.
- [48] C. Chaffer and R. Weinberg, "A perspective on cancer cell metastasis," *Science*, vol. 331, no. 6024, pp. 1559-64, 2011.
- [49] G. Gupta and J. Massagué, "Cancer metastasis: building a framework," *Cell*, vol. 127, no. 4, pp. 679-95, 2006.
- [50] A. Rhim , E. Mirek, N. Aiello, A. Maitra, J. Bailey, F. McAllister, M. Reichert, G. Beatty , A. Rustgi , R. Vonderheide, S. Leach and B. Stanger, "EMT and dissemination precede pancreatic tumor formation," *Cell*, vol. 148, no. 1-2, pp. 349-61, 2012.
- [51] S. Frisch and R. Screaton, "Anoikis mechanisms," *Curr Opin Cell Biol.*, vol. 13, no. 5, pp. 555-62, 2001.

- [52] V. Müller , N. Stahmann, S. Riethdorf, T. Rau , T. Zabel , A. Goetz , F. Jänicke and K. Pantel, "Circulating tumor cells in breast cancer: correlation to bone marrow micrometastases, heterogeneous response to systemic therapy and low proliferative activity," *Clin Cancer Res.* , vol. 11, no. 10, pp. 3678-85, 2005.
- [53] A. Chiang and J. Massagué , "Molecular basis of metastasis," *N Engl J Med.* , vol. 359, no. 26, pp. 2814-23, 2008.
- [54] P. Gassmann and J. Haier, "The tumor cell-host organ interface in the early onset of metastatic organ colonisation," *Clin Exp Metastasis.* , vol. 25, no. 2, pp. 171-81, 2008.
- [55] N. Bednarz-Knoll, C. Alix-Panabières and K. Pantel , "Plasticity of disseminating cancer cells in patients with epithelial malignancies," *Cancer Metastasis Rev.* , vol. 31, no. 3-4, pp. 673-87, 2012.
- [56] H. Hugo, M. Ackland, T. Blick, M. Lawrence, J. Clements, E. Williams and E. Thompson, "Epithelial--mesenchymal and mesenchymal--epithelial transitions in carcinoma progression," *J Cell Physiol.*, vol. 213, no. 2, pp. 374-83, 2007.
- [57] A. Al-Mehdi, K. Tozawa , A. Fisher, L. Shientag, A. Lee and R. Muschel , "Intravascular origin of metastasis from the proliferation of endothelium-attached tumor cells: a new model for metastasis," *Nat Med.* , vol. 6, no. 1, pp. 100-2, 2000.
- [58] R. Weinberg, "Mechanisms of malignant progression," *Carcinogenesis*, vol. 29, no. 6, pp. 1092-5, 2008.
- [59] N. Hanna and I. Fidler, "Role of natural killer cells in the destruction of circulating tumor emboli," *J Natl Cancer Inst.* , vol. 65, no. 4, pp. 801-9, 1980.
- [60] D. Páez, M. Labnote, P. Bohanes, W. Zhang, L. Benhanim, Y. Ning, T. Wakatsuki , F. Loupakis and H. Lenz, "Cancer dormancy: a model of early dissemination and late cancer recurrence," *Clin Cancer Res.* , vol. 18, no. 3, pp. 645-53, 2012.

- [61] Y. Chang, E. di Tomaso , D. McDonald, R. Jones, R. Jain and L. Munn, "Mosaic blood vessels in tumors: frequency of cancer cells in contact with flowing blood," *Proc Natl Acad Sci U S A*, vol. 97, no. 26, pp. 14608-13, 2000.
- [62] A. Collins, P. Berry, C. Hyde, M. Stower and N. Maitland, "Prospective identification of tumorigenic prostate cancer stem cells," *Cancer Res.* , vol. 65, no. 23, pp. 10946-51, 2005.
- [63] K. Hyun , J. Kim, H. Gwak and H. Jung, "Isolation and enrichment of circulating biomarkers for cancer screening, detection, and diagnostics," *Analyst.*, vol. 141, no. 2, pp. 382-92, 2016.
- [64] E. van der Toom, J. Verdone, M. Gorin and K. Pienta , "Technical challenges in the isolation and analysis of circulating tumor cells," *Oncotarget*, vol. 7, no. 38, pp. 62754-66, 2016.
- [65] J. Zhang, K. Chen and Z. Fan, "Circulating Tumor Cell Isolation and Analysis," *Adv Clin Chem.* , vol. 75, pp. 1-31, 2016.
- [66] R. Rosenberg, R. Gertler, J. Friederichs, K. Fuehrer, M. Dahm, R. Phelps, S. Thorban , H. Nekarda and J. Siewert, "Comparison of two density gradient centrifugation systems for the enrichment of disseminated tumor cells in blood," *Cytometry*, vol. 49, no. 4, pp. 150-8, 2002.
- [67] B. Naume , E. Borgen, S. Tøssvik , N. Pavlak , D. Oates and J. Nesland, "Detection of isolated tumor cells in peripheral blood and in BM: evaluation of a new enrichment method," *Cytotherapy*, vol. 6, no. 3, pp. 244-52, 2004.
- [68] K. Pachmann, J. Clement , C. Schneider, B. Willen , O. Camara, U. Pachmann and K. Höffken, "Standardized quantification of circulating peripheral tumor cells from lung and breast cancer," *Clin Chem Lab Med.* , vol. 43, no. 6, pp. 617-27, 2005.
- [69] D. Sidransky, "Nucleic acid-based methods for the detection of cancer," *Science*, vol. 278, no. 5340, pp. 1054-9, 1997.

- [70] E. Andreopoulou , L. Yang, K. Rangel, J. Reuben, L. Hsu, S. Krishnamurthy , V. Valero, H. Fritsche and M. Cristofanilli, "Comparison of assay methods for detection of circulating tumor cells in metastatic breast cancer: AdnaGen AdnaTest BreastCancer Select/Detect™ versus Veridex CellSearch™ system," *Int J Cancer.* , vol. 130, no. 7, pp. 1590-7, 2012.
- [71] A. Gervasoni, M. Sandri, R. Nascimbeni , L. Zorzino, M. Cassatella, L. Baglioni, S. Panigara, M. Gervasi, D. Di Lorenzo and O. Parolini , "Comparison of three distinct methods for the detection of circulating tumor cells in colorectal cancer patients," *Oncol Rep.*, vol. 25, no. 6, pp. 1669-703, 2011.
- [72] A. Markou, A. Strati , N. Malamos , V. Georgoulas and E. Lianidou , "Molecular characterization of circulating tumor cells in breast cancer by a liquid bead array hybridization assay," *Clin Chem.* , vol. 57, no. 3, pp. 421-30, 2011.
- [73] V. Zieglschmid, C. Hollmann, B. Gutierrez, W. Albert , D. Strothoff , E. Gross and O. Böcher, "Combination of immunomagnetic enrichment with multiplex RT-PCR analysis for the detection of disseminated tumor cells," *Anticancer Res.*, vol. 25, no. 3A, pp. 1803-10, 2005.
- [74] P. Bossolasco, C. Ricci, G. Farina, D. Soligo, D. Pedretti, A. Scanni and G. Deliliers , "Detection of micrometastatic cells in breast cancer by RT-pCR for the mammaglobin gene," *Cancer Detect Prev.*, vol. 26, no. 1, pp. 60-3, 2002.
- [75] D. Crisan, D. Ruark, D. Decker , A. Drevon and R. Dicarolo, "Detection of circulating epithelial cells after surgery for benign breast disease," *Mol Diagn.*, vol. 5, no. 1, pp. 33-8, 2000.
- [76] K. Pantel , R. Brakenhoff and B. Brandt , "Detection, clinical relevance and specific biological properties of disseminating tumour cells," *Nat Rev Cancer.* , vol. 8, no. 5, pp. 329-40, 2008.

- [77] J. Chelly, J. Concordet, J. Kaplan and A. Kahn, "Illegitimate transcription: transcription of any gene in any cell type," *Proc Natl Acad Sci U S A.*, vol. 86, no. 8, pp. 2617-21, 1989.
- [78] I. Desitter, B. Guerrouahen, N. Benali-Furet , J. Wechsler, P. Jänne, Y. Kuang, M. Yanagita , L. Wang, J. Berkowitz, R. Distel and Y. Cayre , "A new device for rapid isolation by size and characterization of rare circulating tumor cell," *Anticancer Res.* , vol. 31, no. 2, pp. 427-41, 2011.
- [79] M. Hosokawa, T. Hayata, Y. Fukuda, A. Arakaki , T. Yoshino, T. Tanaka and T. Matsunaga, "Size-selective microcavity array for rapid and efficient detection of circulating tumor cells," *Anal Chem.* , vol. 182, no. 15, pp. 6629-35, 2010.
- [80] S. Zheng S, H. Lin, J. Liu, M. Balic, R. Datar , R. Cote and Y. Tai, "Membrane microfilter device for selective capture, electrolysis and genomic analysis of human circulating tumor cells," *J Chromatogr A.* , vol. 1162, no. 2, pp. 154-61, 2007.
- [81] X. Zheng , L. Cheung, J. Schroeder, L. Jiang and Y. Zohar , "A high-performance microsystem for isolating circulating tumor cells," *Lab Chip.* , vol. 11, no. 19, pp. 3269-76, 2011.
- [82] A. Bhagat , H. Bow, H. Hou, S. Tan, J. Han and C. Lim, "Microfluidics for cell separation," *Med Biol Eng Comput.* , vol. 48, no. 10, pp. 999-1014, 2010.
- [83] Z. Chen, S. Zhang, Z. Tang, P. Xiao, X. Guo and Z. Lu, "Pool-dam structure based microfluidic devices for filtering tumor cells from blood mixtures," *Surf Interface Anal.*, vol. 38, no. 6, pp. 996-1003, 2006.
- [84] H. Mohamed, M. Murray, J. Turner and M. Caggana, "Isolation of tumor cells using size and deformation," *J Chromatogr A*, vol. 1216, no. 47, pp. 8289-95, 2009.

- [85] S. Tan, L. Yobas, G. Lee, C. Ong and C. Lim, "Microdevice for the isolation and enumeration of cancer cells from blood," *Biomed Microdevices*, vol. 11, no. 4, pp. 883-92, 2009.
- [86] S. Hur, A. Mach and D. Di Carlo, "High-throughput size-based rare cell enrichment using microscale vortices," *Biomicrofluidics*, vol. 5, no. 2, p. 22206, 2011.
- [87] H. Hou, M. Warkiani, B. Khoo, Z. Li, R. Soo, D. Tan, W. Lim, J. Han, A. Bhagat and C. Lim, "Isolation and retrieval of circulating tumor cells using centrifugal forces," *Sci Rep.* , vol. 3:1256, 2013.
- [88] S. Kuntaegowdanahalli, A. Bhagat, G. Kumar and I. Papautsky, "Inertial microfluidics for continuous particle separation in spiral microchannels," *Lab Chip*, vol. 9, no. 20, pp. 2973-80, 2009.
- [89] J. Sun, M. Li, C. Liu, Y. Zhang, D. Liu, W. Liu, G. Hu and X. Jiang, "Double spiral microchannel for label-free tumor cell separation and enrichment," *Lab Chip*, vol. 12, no. 20, pp. 3952-60, 2012.
- [90] A. Bhagat , H. Hou, L. Li, C. Lim and J. Han, "Pinched flow coupled shear-modulated inertial microfluidics for high-throughput rare blood cell separation," *Lab Chip.* , vol. 11, no. 11, pp. 1870-8, 2011.
- [91] K. Hyun, K. Kwon, H. Han, S. Kim and H. Jung, "Microfluidic flow fractionation device for label-free isolation of circulating tumor cells (CTCs) from breast cancer patients," *Biosens Bioelectron.*, vol. 40, no. 1, pp. 206-12, 2013.
- [92] W. Allard , J. Matera, M. Miller, M. Repollet, M. Connelly, C. Rao, A. Tibbe, J. Uhr and L. Terstappen, "Tumor cells circulate in the peripheral blood of all major carcinomas but not in healthy subjects or patients with nonmalignant diseases," *Clin Cancer Res.*, vol. 10, no. 20, pp. 6897-904, 2004.
- [93] S. Suresh, "Biomechanics and biophysics of cancer cells," *Acta Biomater.* , vol. 3, no. 4, pp. 413-38, 2007.

- [94] S. Kim , S. Han, M. Park, C. Jeon, Y. Joo, I. Choi and K. Han , "Circulating tumor cell microseparator based on lateral magnetophoresis and immunomagnetic nanobeads," *Anal Chem.* , vol. 85, no. 5, pp. 2779-86, 2013.
- [95] P. Gascoyne and J. Vykoukal, "Particle separation by dielectrophoresis," *Electrophoresis*, vol. 23, no. 13, pp. 1973-83, 2002.
- [96] C. Gonzalez and V. Remcho, "Harnessing dielectric forces for separations of cells, fine particles and macromolecules," *J Chromatogr A*, vol. 1079, no. 1-2, pp. 59-68, 2005.
- [97] L. Broche, N. Bhadal, M. Lewis, S. Porter, M. Hughes and F. Labeed, "Early detection of oral cancer — is dielectrophoresis the answer?," *Oral Oncol*, vol. 43, no. 2, pp. 199-203, 43.
- [98] E. Pratt, C. Huang, B. Hawkins, J. Gleghorn and B. Kirby, "Rare cell capture in microfluidic devices," *Chem Eng Sci.*, vol. 66, no. 7, pp. 1508-22, 2011.
- [99] E. Cen, C. Dalton, Y. Li, S. Adamia, L. Pilarski and K. Kaler, "A combined dielectrophoresis, traveling wave dielectrophoresis and electrorotation microchip for the manipulation and characterization of human malignant cells," *J Microbiol Methods*, vol. 58, no. 3, pp. 387-401, 2004.
- [100] S. Fiedler, S. Shirley, T. Schnelle and G. Fuhr, "Dielectrophoretic sorting of particles and cells in a microsystem," *Anal Chem*, vol. 70, no. 9, pp. 1909-15, 1998.
- [101] J. Yang, Y. Huang, X. Wang, F. Becker and P. Gascoyne, "Cell separation on microfabricated electrodes using dielectrophoretic/gravitational field-flow fractionation," *Anal Chem*, vol. 71, no. 5, pp. 911-18, 1999.
- [102] J. Cheng, E. Sheldon, L. Wu, M. Heller and J. O'Connell, "Isolation of cultured cervical carcinoma cells mixed with peripheral blood cells on a bioelectronic chip," *Anal Chem*, vol. 70, no. 11, pp. 2321-26, 1998.

- [103] F. Becker, X. Wang, Y. Huang, R. Pethig, J. Vykoukal and P. Gascoyne, "Separation of human breast cancer cells from blood by differential dielectric affinity," *Proc Natl Acad Sci U S A*, vol. 92, no. 3, pp. 860-64, 1995.
- [104] P. Gascoyne, J. Noshari, T. Anderson and F. Becker, "Isolation of rare cells from cell mixtures by dielectrophoresis," *Electrophoresis*, vol. 30, no. 8, pp. 1388-98, 2009.
- [105] H. Moon, K. Kwon, S. Kim, H. Han, J. Sohn, S. Lee and H. Jung, "Continuous separation of breast cancer cells from blood samples using multi-orifice flow fractionation (MOFF) and dielectrophoresis (DEP)," *Lab Chip*, vol. 11, no. 6, pp. 1118-25, 2011.
- [106] V. Gupta, I. Jafferji, M. Garza, V. Melnikova, D. Hasegawa, R. Pethig and D. Davis, "ApoStream(™), a new dielectrophoretic device for antibody independent isolation and recovery of viable cancer cells from blood," *Biomicrofluidics*, vol. 6, no. 2, p. 24133, 2012.
- [107] A. Ghazani, C. Castro, R. Gorbatov, H. Lee and R. Weissleder, "Sensitive and direct detection of circulating tumor cells by multimarker μ -nuclear magnetic resonance," *Neoplasia*, vol. 14, no. 5, pp. 388-95, 2012.
- [108] J. Viator, S. Gupta, B. Goldschmidt, K. Bhattacharyya, R. Kannan, R. Shukla, P. Dale, E. Boote and K. Katti, "Gold nanoparticle mediated detection of prostate cancer cells using photoacoustic flowmetry with optical reflectance," *J Biomed Nanotechnol.*, vol. 6, no. 2, pp. 187-91, 2010.
- [109] X. Wang, X. Qian, J. Beitler, Z. Chen, F. Khuri, M. Lewis, H. Shin, S. Nie and D. Shin, "Detection of circulating tumor cells in human peripheral blood using surface-enhanced Raman scattering nanoparticles," *Cancer Res.*, vol. 71, no. 5, pp. 1526-32, 2011.
- [110] S. Joosse and K. Pantel, "Biologic challenges in the detection of circulating tumor cells," *Cancer Res*, vol. 73, no. 1, pp. 8-11, 2013.

- [111] Y. Man, Q. Wang and W. Kemmner, "Currently used markers for CTC isolation — advantages, limitations and impact on cancer prognosis," *J Clin Exp Pathol*, vol. 3, no. 6, 2011.
- [112] K. Pantel , C. Alix-Panabières and S. Riethdorf , "Cancer micrometastases," *Nat Rev Clin Oncol.* , vol. 6, no. 6, pp. 339-51, 2009.
- [113] A. Van de Stolpe, K. Pantel, S. Sleijfer, L. Terstappen and J. den Toonder, "Circulating tumor cell isolation and diagnostics: toward routine clinical use," *Cancer Res*, vol. 71, no. 18, pp. 5955-60, 2011.
- [114] F. Coumans, C. Doggen, G. Attard, J. de Bono and L. Terstappen, "All circulating EpCAM + CK + CD45- objects predict overall survival in castration-resistant prostate cancer," *Ann Oncol*, vol. 21, no. 9, pp. 1851-7, 2010.
- [115] M. Magbanua, E. Sosa, J. Scott , J. Simko, C. Collins, D. Pinkel, C. Ryan and J. Park , "Isolation and genomic analysis of circulating tumor cells from castration resistant metastatic prostate cancer," *BMC Cancer.*, vol. 12, no. 78, 2012.
- [116] I. Cruz , J. Ciudad, J. Cruz, M. Ramos, A. Gómez-Alonso, J. Adansa, C. Rodríguez and A. Orfao, "Evaluation of multiparameter flow cytometry for the detection of breast cancer tumor cells in blood samples," *Am J Clin Pathol.*, vol. 123, no. 1, pp. 66-74, 2005.
- [117] M. Yu , S. Stott , M. Toner, S. Maheswaran and D. Haber, "Circulating tumor cells: approaches to isolation and characterization," *J Cell Biol.* , vol. 192, no. 3, pp. 373-82, 2011.
- [118] L. Lowes, D. Goodale, M. Keeney and A. Allan, "Image cytometry analysis of circulating tumor cells," *Methods Cell Biol.* , vol. 102, pp. 261-90, 2011.
- [119] G. Attard, J. Swennenhuis, D. Olmos, A. Reid, E. Vickers, R. A'Hern, R. Levink, F. Coumans, J. Moreira, R. Riisnaes , N. Oommen , G. Hawche , C. Jameson, E. Thompson, R. Sipkema, C. Carden, C. Parker, D. Dearnaley, S. Kaye , C. Cooper , A. Molina, M. Cox, L. Terstappen and J. de Bono, "Characterization of ERG, AR

- and PTEN gene status in circulating tumor cells from patients with castration-resistant prostate cancer," *Cancer Res.* , vol. 69, no. 7, pp. 2912-8, 2009.
- [120] T. Ntouroupi, S. Ashraf, S. McGregor, B. Turney, A. Seppo, Y. Kim, X. Wang, M. Kilpatrick, P. Tsipouras, T. Tafas and W. Bodmer, "Detection of circulating tumour cells in peripheral blood with an automated scanning fluorescence microscope," *Br J Cancer*, vol. 99, no. 5, pp. 789-95, 2008.
- [121] T. Scholtens, F. Schreuder, S. Ligthart, J. Swennenhuis, J. Greve and L. Terstappen, "Automated identification of circulating tumor cells by image cytometry," *Cytometry A*, vol. 81, no. 2, pp. 138-48, 2012.
- [122] P. Pozarowski, E. Holden and Z. Darzynkiewicz, "Laser Scanning Cytometry: Principles and Applications," *Methods Mol Biol.*, vol. 319, pp. 165-92, 2006.
- [123] P. Pozarowski, E. Holden and Z. Darzynkiewicz, "Laser Scanning Cytometry: Principles and Applications—An Update," *Methods Mol Biol.*, vol. 931, pp. 187-212, 2013.
- [124] R. Krivacic, A. Ladanyi , D. Curry, H. Hsieh, P. Kuhn, D. Bergsrud, J. Kepros, T. Barbera, M. Ho, L. Chen, R. Lerner and R. Bruce, "A rare-cell detector for cancer," *Proc Natl Acad Sci U S A.*, vol. 101, no. 29, pp. 10501-4, 2004.
- [125] D. Marrinucci , K. Bethel, A. Kolatkar, M. Luttgen, M. Malchoidi, F. Baehring, K. Voigt , D. Lazar, J. Nieva, L. Bazhenova, A. Ko, W. Korn, E. Schram, M. Coward, X. Yang, T. Metzner , R. Lamy, M. Honnatti, C. Yoshioka , J. Kunken, Y. Petrova , D. sok, D. Nelson and P. Kuhn, "Fluid biopsy in patients with metastatic prostate, pancreatic and breast cancers," *Phys Biol.*, vol. 9, no. 1, 2012.
- [126] E. Cho, M. Wendel, M. Luttgen, C. Yoshioka, D. Marrinucci , D. Lazar , E. Schram, J. Nieva, L. Bazhenova, A. Morgan, A. Ko, W. Korn, A. Kolatkar, K. Bethel and P. Kuhn , "Characterization of circulating tumor cell aggregates identified in patients with epithelial tumors," *Phys Biol.* , vol. 9, no. 1, p. 016001, 2012.

- [127] C. Alix-Panabières, "EPISPOT assay: detection of viable DTCs/CTCs in solid tumor patients," *Recent Results Cancer Res*, vol. 195, pp. 69-76, 2012.
- [128] C. Alix-Panabières, J. Vendrell, M. Slijper, O. Pellé, E. Barbotte, G. Mercier, W. Jacot, M. Fabbro and K. Pantel, "Full-length cytokeratin-19 is released by human tumor cells: a potential role in metastatic progression of breast cancer," *Breast Cancer Res.*, vol. 11, no. 3, p. R39, 2009.
- [129] J. Schenck , "Physical interactions of static magnetic fields with living tissues," *Prog Biophys Mol Biol.*, vol. 87, no. 2-3, pp. 185-204, 2005.
- [130] G. Deng, M. Herrler, D. Burgess, E. Manna, D. Krag and J. Burke, "Enrichment with anti-cytokeratin alone or combined with anti-EpCAM antibodies significantly increases the sensitivity for circulating tumor cell detection in metastatic breast cancer patients," *Breast Cancer Res*, vol. 10, no. 4, p. R69, 2008.
- [131] N. Pamme, "On-chip bioanalysis with magnetic particles," *Curr Opin Chem Biol.* , vol. 16, no. 3-4, pp. 436-43, 2012.
- [132] B. Plouffe , S. Murthy and L. Lewis, "Fundamentals and application of magnetic particles in cell isolation and enrichment: a review," *Rep Prog Phys.* , vol. 78, no. 1, p. 016601, 2015.
- [133] A. Talasz, A. Powell, D. Huber , J. Berbee , K. Roh, W. Yu, W. Xiao, M. Davis, R. Pease, M. Mindrinos, S. Jeffrey and R. Davis, "Isolating highly enriched populations of circulating epithelial cells and other rare cells from blood using a magnetic sweeper device," *Proc Natl Acad Sci USA*, vol. 106, no. 10, pp. 3970-5, 2009.
- [134] K. Hoshino , Y. Huang, N. Lane, M. Huebschman, J. Uhr , E. Frenkel and X. Zhang, "Microchip-based immunomagnetic detection of circulating tumor cells," *Lab Chip.*, vol. 11, no. 20, pp. 3449-57, 2011.

- [135] S. Mikolajczyk, L. Millar, P. Tsinberg, S. Coutts, M. Zomorodi, T. Pham, F. Bischoff and T. Pircher, "Detection of EpCAM-negative and cytokeratin-negative circulating tumor cells in peripheral blood," *J Oncol* , p. 25361, 2011.
- [136] G. Hager , D. Cacsire-Castillo Tong, I. Schiebel , G. Rezniczek, R. Watrowski, P. Speiser and R. Zeillinger, "The use of a panel of monoclonal antibodies to enrich circulating breast cancer cells facilitates their detection," *Gynecol Oncol.* , vol. 98, no. 2, pp. 211-6, 2005.
- [137] N. Karabacak , P. Spuhler , F. Fachin, E. Lim , V. Pai, E. Ozkumur, J. Martel , N. Kojic, K. Smith, P. Chen, J. Yang, H. Hwang, B. Morgan, J. Trautwein , T. Barber, S. Stott, S. Maheswaran, R. Kapur , D. Haber and M. Toner, "Microfluidic, marker-free isolation of circulating tumor cells from blood samples," *Nat Protoc.*, vol. 9, no. 3, pp. 694-710, 2014.
- [138] Z. Liu, A. Fusi, E. Klopocki , A. Schmittel , I. Tinhofer , A. Nonnenmacher and U. Keilholz, "Negative enrichment by immunomagnetic nanobeads for unbiased characterization of circulating tumor cells from peripheral blood of cancer patients," *J Transl Med.*, vol. 9, 2011.
- [139] L. Yang, J. Lang, P. Balasubramanian, K. Jatana, D. Schuller , A. Agrawal , M. Zborowski and J. Chalmers, "Optimization of an enrichment process for circulating tumor cells from the blood of head and neck cancer patients through depletion of normal cells," *Biotechnol Bioeng.*, vol. 102, no. 2, pp. 521-34, 2009.
- [140] S. Sieben, C. Bergemann, A. Lübbe, B. Brockmann and D. Rescheleit, "Comparison of different particles and methods for magnetic isolation of circulating tumor cells," *J Magn Magn Mater*, vol. 225, no. 1-2, pp. 175-79, 2001.
- [141] J. Haun , N. Devaraj , S. Hilderbrand, H. Lee and R. Weissleder , "Bioorthogonal chemistry amplifies nanoparticle binding and enhances the sensitivity of cell detection," *Nat Nanotechnol.* , vol. 5, no. 9, pp. 660-5, 2010.

- [142] K. McCloskey, J. Chalmers and M. Zborowski, "Magnetic cell separation: characterization of magnetophoretic mobility," *Anal Chem.*, vol. 75, no. 24, pp. 6868-74, 2003.
- [143] T. Schneider , L. Moore, Y. Jing, S. Haam, P. Williams, A. Fleischman, S. Roy, J. Chalmers and M. Zborowski , "Continuous flow magnetic cell fractionation based on antigen expression level," *J Biochem Biophys Methods.* , vol. 68, no. 1, pp. 1-21, 2006.
- [144] M. Zborowski and J. Chalmers , "Rare cell separation and analysis by magnetic sorting," *Anal Chem.*, vol. 83, no. 21, pp. 8050-6, 2011.
- [145] C. Alix-Panabières, J. Vendrell, O. Pellé , X. Rebillard, S. Riethdorf , V. Müller , M. Fabbro and K. Pantel, "Detection and characterization of putative metastatic precursor cells in cancer patients," *Clin Chem.* , vol. 53, no. 3, pp. 537-9, 2007.
- [146] L. Flores , D. Kindelberger , A. Ligon, M. Capelletti , M. Fiorentino , M. Loda, E. Cibas, P. Jänne and I. Krop, "Improving the yield of circulating tumour cells facilitates molecular characterisation and recognition of discordant HER2 amplification in breast cancer," *Br J Cancer.* , vol. 2, no. 10, pp. 1495-502, 2010.
- [147] M. Miller, G. Doyle and L. Terstappen, "Significance of Circulating Tumor Cells Detected by the CellSearch System in Patients with Metastatic Breast Colorectal and Prostate Cancer," *J Oncol.* , vol. 617421, 2010.
- [148] M. Krebs , J. Hou, R. Sloane , L. Lancashire, L. Priest, D. Nonaka, T. Ward , A. Backen, G. Clack , A. Hughes, M. Ranson, F. Blackhall and C. Dive, "Analysis of circulating tumor cells in patients with non-small cell lung cancer using epithelial marker-dependent and -independent approaches," *J Thorac Oncol.* , vol. 7, no. 2, pp. 306-15, 2012.
- [149] S. Riethdorf , H. Fritsche, V. Müller , T. Rau, C. Schindlbeck, B. Rack, W. Janni , C. Coith, K. Beck , F. Jänicke, S. Jackson, T. Gornet , M. Cristofanilli and K. Pantel , "Detection of circulating tumor cells in peripheral blood of patients with

- metastatic breast cancer: a validation study of the CellSearch system," *Clin Cancer Res.* , vol. 13, no. 3, pp. 920-8, 2007.
- [150] O. Lara, X. Tong, M. Zborowski and J. Chalmers , "Enrichment of rare cancer cells through depletion of normal cells using density and flow-through, immunomagnetic cell separation," *Exp Hematol.*, vol. 32, no. 10, pp. 891-904, 2004.
- [151] S. O'Hara , J. Moreno , D. Zweitzig, S. Gross, L. Gomella and L. Terstappen, "Multigene reverse transcription-PCR profiling of circulating tumor cells in hormone-refractory prostate cancer," *Clin Chem.*, vol. 50, no. 5, pp. 826-35, 2004.
- [152] R. Zigeuner , R. Riesenberger, H. Pohla , A. Hofstetter and R. Oberneder , "Isolation of circulating cancer cells from whole blood by immunomagnetic cell enrichment and unenriched immunocytochemistry in vitro," *J Urol.* , vol. 169, no. 2, pp. 701-5, 2003.
- [153] N. Pamme, "Magnetism and microfluidics," *Lab Chip*, vol. 6, no. 1, pp. 24-38, 2006.
- [154] J. Kang , S. Krause, H. Tobin, A. Mammoto, M. Kanapathipillai and D. Ingber, "A combined micromagnetic-microfluidic device for rapid capture and culture of rare circulating tumor cells," *Lab Chip.*, vol. 12, no. 12, pp. 2175-81, 2012.
- [155] T. Forbes and S. Forry, "Microfluidic magnetophoretic separations of immunomagnetically labeled rare mammalian cells," *Lab Chip.*, vol. 12, no. 8, pp. 1471-9, 2012.
- [156] B. Plouffe, M. Mahalanabis, L. Lewis, C. Klapperich and S. Murthy, "Clinically relevant microfluidic magnetophoretic isolation of rare-cell populations for diagnostic and therapeutic monitoring applications," *Anal Chem.*, vol. 84, no. 3, pp. 1336-44, 2012.
- [157] S. Wang, H. Wang, J. Jiao, K. Chen, G. Owens, K. Kamei, J. Sun, D. Sherman, C. Behrenbruch , H. Wu and H. Tseng, "Three-dimensional nanostructured

- substrates toward efficient capture of circulating tumor cells," *Angew Chem Int Ed Engl.*, vol. 48, no. 47, pp. 8970-3, 2009.
- [158] T. Didar and M. Tabrizian , "Adhesion based detection, sorting and enrichment of cells in microfluidic Lab-on-Chip devices," *Lab Chip.* , vol. 10, no. 22, pp. 3043-53, 2010.
- [159] J. Smith , A. Barbati , S. Santana, J. Gleghorn and B. Kirby, "Microfluidic transport in microdevices for rare cell capture," *Electrophoresis.*, vol. 33, no. 21, pp. 3133-42, 2012.
- [160] T. Fan, Q. Zhao, J. Chen, W. Chen and M. Pearl, "Clinical significance of circulating tumor cells detected by an invasion assay in peripheral blood of patients with ovarian cancer," *Gynecol Oncol.* , vol. 112, no. 1, pp. 185-91, 2009.
- [161] J. Lu, T. Fan, Q. Zhao, W. Zeng, E. Zaslavsky, J. Chen, M. Frohman , M. Golightly , S. Madajewicz and W. Chen, "Isolation of circulating epithelial and tumor progenitor cells with an invasive phenotype from breast cancer patients," *Int J Cancer.*, vol. 126, no. 3, pp. 669-83, 2010.
- [162] L. Cheung, X. Zheng, L. Wang, R. Guzman, J. Schroeder, R. Heimark, J. Baygents and Y. Zohar, "Kinematics of specifically captured circulating tumor cells in Bio-functionalized microchannels," *J Microelectromech Syst*, vol. 19, no. 4, pp. 752-63, 2010.
- [163] L. Cheung, X. Zheng, L. Wang, J. Baygents, R. Guzman, J. Schroeder, R. Heimark and Y. Zohar, "Adhesion dynamics of circulating tumor cells under shear flow in a bio-functionalized microchannel," *J Micromech Microeng.*, vol. 21, no. 5, p. 054033, 2011.
- [164] M. Nora Dickson, P. Tsinberg, Z. Tang, F. Bischoff, T. Wilson and E. Leonard, "Efficient capture of circulating tumor cells with a novel immunocytochemical microfluidic device," *Biomicrofluidics.*, vol. 5, no. 3, 2011.

- [165] Y. Wan, J. Tan, W. Asghar, T. Kim, Y. Liu and S. Iqbal, "Velocity effect on aptamer-based circulating tumor cell isolation in microfluidic devices," *J Phys Chem B*, vol. 115, no. 47, pp. 13891-6, 2011.
- [166] S. Mittal , I. Wong, W. Deen and M. Toner, "Antibody-functionalized fluid-permeable surfaces for rolling cell capture at high flow rates.," *Biophys J.* , vol. 102, no. 4, pp. 721-30, 2012.
- [167] S. Santana , H. Liu, N. Bander, J. Gleghorn and B. Kirby, "Immunocapture of prostate cancer cells by use of anti-PSMA antibodies in microdevices," *Biomed Microdevices.* , vol. 14, no. 2, pp. 401-7, 2012.
- [168] S. Stott, C. Hsu, D. Tsukrov, M. Yu, D. Miyamoto, B. Waltman, S. Rothenberg, A. Shah,, M. Smas, G. Korir, F. Floyd Jr., A. Gilman, J. Lord, D. Winokur, S. Springer, D. Irimia, S. Nagrath, L. Sequist, R. Lee, K. Isselbacher, S. Maheswaran, D. Haber and M. Toner, "Isolation of circulating tumor cells using a microvortex-generating herringbone-chip," *Proc Natl Acad Sci USA*, vol. 107, no. 43, pp. 18392-97, 2010.
- [169] A. Adams , P. Okagbare, J. Feng, M. Hupert, D. Patterson, J. Göttert, R. McCarley, D. Nikitopoulos, M. Murphy and S. Soper, "Highly efficient circulating tumor cell isolation from whole blood and label-free enumeration using polymer-based microfluidics with an integrated conductivity sensor.," *J Am Chem Soc.*, vol. 130, no. 27, pp. 8633-41, 2008.
- [170] U. Dharmasiri, S. Balamurugan, A. Adams, P. Okagbare , A. Obubuafo and Soper SA, "Highly efficient capture and enumeration of low abundance prostate cancer cells using prostate-specific membrane antigen aptamers immobilized to a polymeric microfluidic device," *Electrophoresis.*, vol. 30, no. 18, pp. 3289-300, 2009.
- [171] U. Dharmasiri , S. Njoroge, M. Witek, M. Adebisi , J. Kamande, M. Hupert , F. Barany and S. Soper, "High-throughput selection, enumeration, electrokinetic

- manipulation, and molecular profiling of low-abundance circulating tumor cells using a microfluidic system," *Anal Chem.* , vol. 83, no. 6, pp. 2301-9, 2011.
- [172] H. Hou , M. Warkiani , B. Khoo , Z. Li, R. Soo, D. Tan, W. Lim, J. Han, A. Bhagat and C. Lim, "Isolation and retrieval of circulating tumor cells using centrifugal forces," *Sci Rep.*, vol. 3, 2013.
- [173] S. Wang, K. Liu, J. Liu, Z. Yu, X. Xu, L. Zhao, T. Lee, J. Reiss, Y. Lee, L. Chung, J. Huang, M. Retting, D. Seligson, K. Duraiswamy , C. Shen and H. Tseng , "Highly efficient capture of circulating tumor cells by using nanostructured silicon substrates with integrated chaotic micromixers," *Angew Chem Int Ed Engl.* , vol. 50, no. 13, pp. 3048-8, 2011.
- [174] L. Sequist, S. Nagrath, M. Toner, D. Haber and T. Lynch, "The CTC-chip: an exciting new tool to detect circulating tumor cells in lung cancer patients," *J Thorac Oncol.*, vol. 4, no. 3, pp. 281-3, 2009.
- [175] J. Gleghorn, E. Pratt, D. Denning, H. Liu, N. Bander, S. Tagawa, D. Nanus, P. Giannakakou and B. Kirby, "Capture of circulating tumor cells from whole blood of prostate cancer patients using geometrically enhanced differential immunocapture (GEDI) and a prostate-specific antibody," *Lab Chip.* , vol. 10, no. 1, pp. 27-9, 2010.
- [176] S. Nagrath, L. Sequist, S. Maheswaran , D. Bell, D. Irimia, L. Ulkus, M. Smith , E. Kwak, S. Digumarthy , A. Muzikansky, P. Ryan, U. Balis, R. Tompkins, D. Haber and M. Toner, "Isolation of rare circulating tumour cells in cancer patients by microchip technology," *Nature*, vol. 450, no. 7173, pp. 1235-9, 2007.
- [177] M. Kurkuri , F. Al-Ejeh, J. Shi , D. Palms , C. Prestidge , H. Griesser , M. Brown and B. Thierry , "Plasma functionalized PDMS microfluidic chips: towards point-of-care capture of circulating tumor cells," *J Mater Chem*, vol. 21, pp. 8841-8, 2011.

- [178] W. Sheng, T. Chen , R. Kamath, X. Xiong, W. Tan and Z. Fan, "Aptamer-enabled efficient isolation of cancer cells from whole blood using a microfluidic device," *Anal Chem.* , vol. 84, no. 9, pp. 4199-206, 2012.
- [179] C. Pecot , F. Bischoff , J. Mayer , K. Wong, T. Pham , J. Bottsford-Miller, R. Stone, Y. Lin, P. Jaladurgam , J. Roh, B. Goodman, W. Merritt , T. Pircher, S. Mikolajczyk , A. Nick, J. Celestino, C. Eng, L. Ellis, M. Deavers and A. Sood, "A novel platform for detection of CK+ and CK- CTCs," *Cancer Discov.* , vol. 1, no. 7, pp. 580-6, 2011.
- [180] A. Saliba, L. Saias, E. Psychari, N. Minc, D. Simon, F. Bidard, C. Mathiot, J. Pierga, V. Fraasier, J. Salamero, V. Saada, F. Farace, P. Vielh, L. Malaquin and J. Viovy, "Microfluidic sorting and multimodal typing of cancer cells in self-assembled magnetic arrays," *Proc Natl Acad Sci USA*, vol. 107, no. 33, pp. 14524-9, 2010 .
- [181] J. Kralj , C. Arya, A. Tona, T. Forbes, M. Munson, L. Sorbara, S. Srivastava and S. Forry, "A simple packed bed device for antibody labelled rare cell capture from whole blood," *Lab Chip.* , vol. 12, no. 23, pp. 4972-5, 2012.
- [182] A. Hughes, J. Mattison , L. Western, J. Powderly , B. Greene and M. King, "Microtube device for selectin-mediated capture of viable circulating tumor cells from blood," *Clin Chem.* , vol. 58, no. 5, pp. 846-53, 2012.
- [183] H. Esmaeilsabzali, T. Beischlag, M. Cox, A. Parameswaran and E. Park, "Detection and isolation of circulating tumor cells: principles and methods," *Biotechnol Adv.*, vol. 31, no. 7, pp. 1063-84, 2013.
- [184] H. Esmaeilsabzali, T. Beischlag, M. Cox, N. Dechev, A. Parameswaran and E. Park , "An integrated microfluidic chip for immunomagnetic detection and isolation of rare prostate cancer cells from blood," *Biomed Microdevices.* 2, vol. 18, no. 22, 2016.

- [185] G. Hatch and R. Stelter, "Magnetic design considerations for devices and particles used for biological high-gradient magnetic separation (HGMS) systems," *J. Magn. Mater.*, vol. 225, no. 1-2, pp. 262-7, 2001.
- [186] Y. Huang, P. Chen, C. Wu, K. Hoshino, K. Sokolov, N. Lane, H. Liu, M. Huebschman, E. Frenkel and J. Zhang, "Screening and molecular analysis of single circulating tumor cells using micromagnet array," *Sci Rep.*, vol. 5, no. 16047, 2015.
- [187] R. Bird, W. Stewart and E. Lightfoot, *Transport Phenomena*, 2 ed., New York: John Wiley & Sons, 2007.
- [188] K. Hoshino, P. Chen, Y. Huang and X. Zhang, "Computational analysis of microfluidic immunomagnetic rare cell separation from a particulate blood flow," *Anal Chem.*, vol. 84, no. 10, pp. 4292-9, 2012.
- [189] W. Grover, A. Bryan, M. Diez-Silva, S. Suresh, J. Higgins and S. Manalis, "Measuring single-cell density," *Proc Natl Acad Sci U S A.*, vol. 108, no. 27, pp. 10992-6, 2011.
- [190] B. Plouffe, L. Lewis and S. Murthy, "Computational design optimization for microfluidic magnetophoresis," *Biomicrofluidics*, vol. 5, no. 1, p. 013413, 2012.
- [191] K. McCloskey, J. Chalmers and M. Zborowski, "Magnetic cell separation: characterization of magnetophoretic mobility," *Anal Chem.*, vol. 75, no. 24, pp. 6868-74, 2003.
- [192] M. Davis, M. Bennet, L. Thomas and P. Bjorkman, "Crystal structure of prostate-specific membrane antigen, a tumor marker and peptidase," *Proc Natl Acad Sci USA*, vol. 102, no. 17, pp. 5981-6, 2005.
- [193] S. Denmeade, "Prostate-Specific Membrane Antigen," in *Encyclopedia of Cancer*, Springer, 2017, pp. 3068-72.

- [194] S. Chang, "Overview of prostate-specific membrane antigen.," *Rev Urol.*, vol. 6, no. 10, pp. S13-8, 2004.
- [195] K. Bouchelouche, P. Choyke and J. Capala, "Prostate specific membrane antigen- a target for imaging and therapy with radionuclides," *Discov Med.* , vol. 9, no. 44, pp. 55-61, 2010.
- [196] J. Ross, C. Sheehan, H. Fisher, R. Kaufman, P. Kaur , K. Gray , I. Webb, G. Gray, R. Mosher and B. Kallakury, "Correlation of primary tumor prostate-specific membrane antigen expression with disease recurrence in prostate cancer," *Clin Cancer Res.* , vol. 9, no. 17, pp. 6357-62, 2003.
- [197] S. Perner , M. Hofer, R. Kim, R. Shah, H. Li, P. Möller, R. Hautmann, J. Gschwend, R. Kuefer and M. Rubin , "Prostate-specific membrane antigen expression as a predictor of prostate cancer progression," *Hum Pathol.* , vol. 38, no. 5, pp. 696-701, 2007.
- [198] B. Kirby , M. Jodari , M. Loftus , G. Gakhar, E. Pratt, C. Chanel-Vos, J. Gleghorn, S. Santana, H. Liu, J. Smith, V. Navarro, S. Tagawa, N. Bander, D. Nanus and P. Giannakakou, "Functional characterization of circulating tumor cells with a prostate-cancer-specific microfluidic device," *PLoS One.* , vol. 7, no. 4, p. e35976, 2012.
- [199] C. Alix-Panabières and K. Pantel, "Circulating tumor cells: liquid biopsy of cancer," *Clin Chem.* , vol. 59, no. 1, pp. 110-8, 2013.
- [200] T. Gorges, I. Tinhofer, M. Drosch, L. Röse, T. Zollner, T. Krahn and O. van Ahsen, "Circulating tumour cells escape from EpCAM-based detection due to epithelial-to-mesenchymal transition," *BMC Cancer*, vol. 12, no. 178, 2012.
- [201] C. C. S. A. C. o. C. Statistics, "Canadian Cancer Statistics 2016," Canadian Cancer Society, Toronto, ON, 2016.
- [202] M. Barry, "Prostate-specific-antigen testing for early diagnosis of prostate cancer," *N Engl J Med.* , vol. 344, no. 18, pp. 1373-7, 2001.

- [203] T. Yap, A. Zivi, A. Omlin and J. de Bono, "The changing therapeutic landscape of castration-resistant prostate cancer," *Nat Rev Clin Oncol.* , vol. 8, no. 10, pp. 597-610, 2011.
- [204] F. Saad, K. Chi, A. Finelli, S. Hotte, J. Izawa, A. Kapoor, W. Kassouf, A. Loblaw, S. North, R. Rendon, A. So, N. Usmani, E. Vigneault and N. Fleshner, "The 2015 CUA-CUOG Guidelines for the management of castration-resistant prostate cancer (CRPC)," *Can Urol Assoc J.*, vol. 9, no. 3-4, pp. 90-6, 2015.
- [205] E. Basch, D. Loblaw, T. Oliver, M. Carducci, R. Chen, J. Frame, K. Garrels, S. Hotte, M. Kattan, D. Raghavan, F. Saad, M. Taplin, C. Walker-Dilks, J. Williams, E. Winquist, C. Bennett, T. Wootton, R. Rumble, S. Dusetzina and K. Virgo, "Systemic therapy in men with metastatic castration-resistant prostate cancer: American Society of Clinical Oncology and Cancer Care Ontario clinical practice guideline," *J Clin Oncol.*, vol. 32, no. 30, pp. 3436-48, 2014.
- [206] D. Suzman and E. Antonarakis, "Castration-resistant prostate cancer: latest evidence and therapeutic implications," *Ther Adv Med Oncol.*, vol. 6, no. 4, pp. 167-79, 2014.
- [207] E. Antonarakis, C. Lu, B. Lubber, H. Wang, Y. Chen, M. Nakazawa, R. Nadal, C. Paller, S. Denmeade, M. Carducci, M. Eisenberger and J. Luo, "Androgen Receptor Splice Variant 7 and Efficacy of Taxane Chemotherapy in Patients With Metastatic Castration-Resistant Prostate Cancer," *JAMA Oncol.* , vol. 1, no. 5, pp. 582-91, 2015.
- [208] C. Hwang, "Overcoming docetaxel resistance in prostate cancer: a perspective review," *Ther Adv Med Oncol.*, vol. 4, no. 6, pp. 329-40, 2012.
- [209] A. Wognum and P. Lansdorp, "Tetrameric antibody complexes for blocking non-specific labeling of antigens". Canada Patent CA2411392 A1, 2003.

- [210] W. Liu, N. Dechev, I. Foulds, R. Burke, A. Parameswaran and E. Park, "A novel permalloy based magnetic single cell micro array," *Lab Chip.*, vol. 9, no. 16, pp. 2381-90, 2009.
- [211] H. Arnold and G. Elmen, "Permalloy, a new magnetic material of very high permeability," *Bell Labs Techn. J.*, vol. 2, no. 3, pp. 101-11, 1923.
- [212] T. Buchheit, S. Goods, P. Kotula and P. Hlava, "Electrodeposited 80Ni–20Fe (Permalloy) as a structural material for high aspect ratio microfabrication," *Mater. Sci. Eng. A* , vol. 432, no. 1-2, pp. 149-57, 2006.
- [213] G. Whitesides, E. Ostuni, S. Takayama, X. Jiang and D. Ingber, "Soft lithography in biology and biochemistry," *Annu Rev Biomed Eng.* , vol. 3, pp. 335-73, 2001.
- [214] J. Chung, *MSc Thesis: Development of a Cell Cross Flow System*, University of Victoria, 2010.
- [215] J. Luo, D. Chu, A. Flewitt, S. Spearing, N. Fleck and W. Milne, "Uniformity control of Ni thin-film microstructures deposited by through-mask plating," *J. Electrochem. Soc.*, vol. 152, no. 1, pp. 36-41, 2005.
- [216] H. Liu, P. Li and J. Lew, "CFD study on flow distribution uniformity in fuel distributors having multiple structural bifurcations of flow channels," *Int J Hydrogen Energ*, vol. 35, no. 17, pp. 9186-98, 2010.
- [217] R. Lovchik , N. Tonna, F. Bianco, M. Matteoli and E. Delamarche, "A microfluidic device for depositing and addressing two cell populations with intercellular population communication capability," *Biomed Microdevices.* , vol. 12, no. 2, pp. 275-82, 2010.
- [218] A. Miguel, "An analytic approach to capillary pressure in tree-shaped networks," *The Open Thermodynamics Journal*, vol. 2, pp. 39-43, 2008.

- [219] D. Emerson, K. Cieřlicki, X. Gu and R. Barber, "Biomimetic design of microfluidic manifolds based on a generalised Murray's law," *Lab Chip* , vol. 6, no. 3, pp. 447-54, 2006.
- [220] X. Wang, A. Mujumdar and C. Yap, "Effect of bifurcation angle in tree-shaped microchannel networks," *J. Appl. Phys.* , vol. 102, no. 7, 2007.
- [221] A. Stroock, S. Dertinger, A. Ajdari, I. Mezic , H. Stone and G. Whiteside , "Chaotic mixer for microchannels," *Science*, vol. 295, no. 5555, pp. 647-51, 2002.
- [222] M. Williams, K. Longmuir and P. Yager, "A practical guide to the staggered herringbone mixer," *Lab Chip.*, vol. 8, no. 7, pp. 1121-9, 2008.
- [223] C. Fredrickson and Z. Fan, "Macro-to-micro interfaces for microfluidic devices," *Lab Chip.*, vol. 4, no. 6, pp. 526-33, 2004.
- [224] J. Horoszewicz, S. Leong, E. Kawinski, J. Karr, H. Rosenthal , T. Chu, E. Mirand and G. Murphy, "LNCaP model of human prostatic carcinoma," *Cancer Res.* , vol. 43, no. 4, pp. 1809-18, 1993.
- [225] K. Haubert, T. Drier and D. Beebe, "PDMS bonding by means of a portable, low-cost corona system," *Lab Chip.*, vol. 6, pp. 1548-9, 2006.
- [226] J. Luo, D. Chu, A. Flewitt, S. Spearing , N. Fleck and W. Milne, "Uniformity control of Ni thin-film microstructures deposited by through-mask plating," *J. Electrochem. Soc.*, vol. 152, no. 1, pp. C36-41, 2005.
- [227] Y. Oh, S. Chung and M. Lee, "Optimization of thickness uniformity in electrodeposition onto a patterned substrate," *Materials Transactions*, vol. 45, no. 10, pp. 3005-10, 2004.
- [228] C. Park and K. Park, "An effect of dummy cathode on thickness uniformity in electroforming process," *Results in Physics*, vol. 4, pp. 107-12, 2014.

- [229] M. Krishnan, J. Nalaskowski and L. Cook, "Chemical mechanical planarization: slurry chemistry, materials, and mechanisms," *Chem. Rev.*, vol. 110, no. 1, pp. 178-204, 2010.
- [230] P. Chen, Y. Huang, K. Hoshino and J. Zhang, "Microscale magnetic field modulation for enhanced capture and distribution of rare circulating tumor cells," *Sci Rep.*, vol. 5, 2015.
- [231] P. Sajeesh and A. Sen, "Particle separation and sorting in microfluidic devices: a review," *Microfluid Nanofluidics*, vol. 17, no. 1, pp. 1-52, 2014.
- [232] E. Ozkumur, A. Shah, J. Ciciliano, B. Emmink, D. Miyamoto, E. Brachtel, M. Yu, P. Chen, B. Morgan, J. Trautwein, A. Kimura, S. Sengupta, S. Stott, N. Karabacak, T. Barber, J. Walsh, K. Smith, P. Spuhler, J. Sullivan, R. Lee, D. Ting, X. Luo, A. Shaw, A. Bardia, L. Sequist, D. Louis, S. Maheswaran, R. Kapur, D. Haber and M. Toner, "Inertial focusing for tumor antigen-dependent and – independent sorting of rare circulating tumor cells," *Sci Transl Med.*, vol. 5, no. 179, 2013.
- [233] J. Kuo, Y. Zhao, P. Schiro, L. Ng, D. Lim, J. Shelby and D. Chiu, "Deformability considerations in filtration of biological cells," *Lab Chip.*, vol. 10, no. 7, pp. 837-42, 2010.
- [234] Y. Chiu, C. Huang and Y. Lu, "Enhancement of microfluidic particle separation using cross-flow filters with hydrodynamic focusing," *Biomicrofluidics.*, vol. 10, no. 1, p. 011906, 2016.
- [235] X. Li, W. Chen, G. Liu, W. Lu and J. Fu, "Continuous-flow microfluidic blood cell sorting for unprocessed whole blood using surface-micromachined microfiltration membranes," *Lab Chip*, vol. 14, no. 14, pp. 2565-75, 2014.
- [236] L. Huang, E. Cox, R. Austin and J. Sturm, "Continuous particle separation through deterministic lateral displacement," *Science*, vol. 304, no. 5673, pp. 987-90, 2004.

- [237] D. Inglis, J. Davis, R. Austin and J. Sturm, "Critical particle size for fractionation by deterministic lateral displacement," *Lab Chip*, vol. 6, no. 5, pp. 655-8, 2006.
- [238] J. McGrath, M. Jimenez and H. Bridle, "Deterministic lateral displacement for particle separation: a review," *Lab Chip*, vol. 14, no. 21, pp. 4139-58, 2014.
- [239] J. Davis, "Microfluidic separation of blood components through deterministic lateral displacement," Princeton University, 2008.
- [240] J. Park and H. Jung, "Multiorifice flow fractionation: continuous size-based separation of microspheres using a series of contraction/expansion microchannels," *Anal Chem.*, vol. 81, no. 20, pp. 8280-8, 2009.
- [241] J. Park, S. Song and H. Jung, "Continuous focusing of microparticles using inertial lift force and vorticity via multi-orifice microfluidic channels," *Lab Chip*, vol. 9, no. 7, pp. 939-48, 2009.
- [242] J. Matas, J. Morris and E. Guazzelli, "Inertial migration of rigid spherical particles in Poiseuille flow," *J. Fluid Mech.*, vol. 515, pp. 171-95, 2004.
- [243] D. Di Carlo, D. Irimia, R. Tompkins and M. Toner, "Continuous inertial focusing, ordering, and separation of particles in microchannels," *Proc Natl Acad Sci USA.*, vol. 104, no. 48, pp. 18892-7, 2007.
- [244] H. Moon, K. Kwon, S. Kim, H. Han, J. Sohn, S. Lee and H. Jung, "Continuous separation of breast cancer cells from blood samples using multi-orifice flow fractionation (MOFF) and dielectrophoresis (DEP)," *Lab Chip.*, vol. 11, no. 6, pp. 1118-25, 2011.
- [245] K. Hyun, K. Kwon, H. Han, S. Kim and H. Jung, "Microfluidic flow fractionation device for label-free isolation of circulating tumor cells (CTCs) from breast cancer patients," *Biosens Bioelectron.*, vol. 40, no. 1, pp. 206-12, 2013.

- [246] N. Shirtcliffe, S. Aqil, C. Evans, G. McHale, M. Newton, C. Perry and P. Roach, "The use of high aspect ratio photoresist (SU-8) for super-hydrophobic pattern prototyping," *J. Micromech. Microeng.*, vol. 14, no. 10, pp. 1384-9, 2004.
- [247] L. Amato, S. Keller, A. Heiskanen, M. Dimaki, J. Emneus, A. Boisen and M. Tenje, "Fabrication of high-aspect ratio SU-8 micropillar arrays," *Microelectronic Eng.*, vol. 98, pp. 783-7, 2012.
- [248] A. del Campo and C. Greiner, "SU-8: a photoresist for high-aspect-ratio and 3D submicron lithography," *J. Micromech. Microeng.*, vol. 17, pp. R81-R95, 2007.
- [249] C. Sun, Y. Hsieh, S. Ma, S. Geng, Z. Cao, L. Li and C. Lu, "Immunomagnetic separation of tumor initiating cells by screening two surface markers," *Sci. Rep.*, vol. 7, 2017.
- [250] Y. Huang, P. Chen, C. Wu, K. Hoshino, K. Sokolov, N. Lane, H. Liu, M. Huebschman, E. Frenkel and J. Zhang, "Screening and molecular analysis of single circulating tumor cells using micromagnet array," *Sci. Rep.*, vol. 5, 2015.
- [251] C. Wu, Y. Huang, P. Chen, K. Hoshino, H. Liu, E. Frenkel, J. Zhang and K. Sokolov, "Versatile immunomagnetic nanocarrier platform for capturing cancer cells," *ACS Nano.*, vol. 7, no. 10, pp. 8816-23, 2013.
- [252] C. Vicente-Dueñas, J. Gutiérrez de Diego, F. Rodríguez, R. Jiménez and C. Cobaleda, "The role of cellular plasticity in cancer development," *Curr Med Chem.*, vol. 16, no. 28, pp. 3676-85, 2009.
- [253] C. Meacham and S. Morrison, "Tumor heterogeneity and cancer cell plasticity," *Nature*, vol. 501, no. 7467, pp. 328-37, 2013.
- [254] B. Khoo, S. Lee, P. Kumar, T. Tan, W. Warkiani, S. Ow, S. Nandi, C. Lim and J. Thiery, "Short-term expansion of breast circulating cancer cells predicts response to anti-cancer therapy," *Oncotarget*, vol. 6, no. 17, pp. 15578-93, 2015.

- [255] S. Maheswaran and D. Haber, "Ex Vivo Culture of CTCs: An Emerging Resource to Guide Cancer Therapy.," *Cancer Res.*, vol. 75, no. 12, pp. 2411-5, 2015.
- [256] H. Cai, S. Memarzadeh, T. Stoyanova, Z. Beharry, A. Kraft and O. Witte, "Collaboration of Kras and androgen receptor signaling stimulates EZH2 expression and tumor-propagating cells in prostate cancer," *Cancer Res.*, vol. 72, no. 18, pp. 4672-81, 2012.
- [257] T. Karantanos, C. Evans, B. Tombal, T. Thompson, R. Montironi and W. Isaacs, "Understanding the mechanisms of androgen deprivation resistance in prostate cancer at the molecular level," *Eur Urol.* , vol. 67, no. 3, pp. 407-9, 2015.

Appendix A.

Machine Vision-Based Localization of Nucleic and Cytoplasmic Injection Sites on Low-Contrast Adherent Cells

Machine vision-based localization of nucleic and cytoplasmic injection sites on low-contrast adherent cells

Hadi Esmailsabzali · Kelly Sakaki ·
Nikolai Dechev · Robert D. Burke ·
Edward J. Park

Received: 4 April 2011 / Accepted: 8 September 2011 / Published online: 27 September 2011
© International Federation for Medical and Biological Engineering 2011

Abstract Automated robotic bio-micromanipulation can improve the throughput and efficiency of single-cell experiments. Adherent cells, such as fibroblasts, include a wide range of mammalian cells and are usually very thin with highly irregular morphologies. Automated micromanipulation of these cells is a beneficial yet challenging task, where the machine vision sub-task is addressed in this article. The necessary but neglected problem of localizing injection sites on the nucleus and the cytoplasm is defined and a novel two-stage model-based algorithm is proposed. In Stage I, the gradient information associated with the nucleic regions is extracted and used in a mathematical morphology clustering framework to roughly localize the nucleus. Next, this preliminary segmentation information is used to estimate an ellipsoidal model for the nucleic region, which is then used as an attention window in a *k*-means clustering-based iterative search algorithm for fine localization of the nucleus and nucleic injection site (NIS). In Stage II, a geometrical model is built on each localized nucleus and employed in a new texture-based region-

growing technique called Growing Circles Algorithm to localize the cytoplasmic injection site (CIS). The proposed algorithm has been tested on 405 images containing more than 1,000 NIH/3T3 fibroblast cells, and yielded the precision rates of 0.918, 0.943, and 0.866 for the NIS, CIS, and combined NIS–CIS localizations, respectively.

Keywords Adherent cells · *k*-means clustering · Machine vision · Nucleic and cytoplasmic micromanipulation · Region growing

1 Introduction

Single-cell research provides precise understanding of cells and their functions by avoiding inaccuracies which are inherent to data-averaging over cell cultures, and caused by intercellular signaling or heterogeneity of cell populations. A fundamental step in many single-cell experiments is to manipulate the genetic or biochemical contents of a live cell using capillary pressure microinjection (CPM) [7] or single-cell electroporation (SCE) [20]. To improve the throughput and efficiency of these methods, automated robotic systems based on CPM [18] and SCE [15] have been developed previously. Machine vision that recognizes single cells or their internal structures (e.g., nucleus) in microscopic images is a basic requirement in these systems. We have reported the development of a proof-of-concept automated single-cell micromanipulation system—now dubbed RoboSCell—in [15], where it was employed for in vitro SCE-based injection of sea urchin eggs, which are large (~80 μm in diameter) and spherical. To generalize the technology, the automated SCE capability of RoboSCell must be applied to other cell types, particularly adherent cells, which are flat, thin, and morphologically irregular. Although a number of

Electronic supplementary material The online version of this article (doi:10.1007/s11517-011-0831-2) contains supplementary material, which is available to authorized users.

H. Esmailsabzali · K. Sakaki · E. J. Park (✉)
Mechatronics Systems Engineering, School of Engineering
Science, Simon Fraser University, 250-13450 102nd Avenue,
Surrey, BC V3T 0A3, Canada
e-mail: ed_park@sfu.ca

N. Dechev · E. J. Park
Department of Mechanical Engineering, University of Victoria,
3800 Finnerty Road, Victoria, BC V8W 2Y2, Canada

R. D. Burke
Department of Biochemistry and Microbiology, University of
Victoria, 3800 Finnerty Road, Victoria, BC V8W 2Y2, Canada

studies have been reported on automatic CPM- and SCE-based micromanipulation of physically or chemically immobilized single suspended cells [15, 18], to our best knowledge, there has been little work done on fully automated micromanipulation of single adherent cells. The main obstacle to full automation has been the need for a human operator to be involved in the selection of the proper *injection site* on the adherent cell, for either the CPM or SCE methods (e.g., [11]).

Recently, the automated localization of injection sites on adherent cells has been partly addressed in [19]. However, their method identifies injection sites only on the nucleus, which is limited to nucleic injection applications (e.g., pronuclear DNA microinjection [5]) that involve the insertion of foreign molecules into the individual nuclei. Alternatively, there are other cytology applications, such as the study of intracellular behavior of nucleic acids or gene therapy [10, 13], in which the external molecules should be inserted into the cytoplasm (i.e., cytoplasmic injection). It has been suggested in the literature pertaining to single-cell micromanipulation systems (e.g., [18]) that such a system should have the capability of injecting cells at various locations (e.g., both nucleus and cytoplasm), yet surprisingly, its implementation and automation have not been addressed.

1.1 Problem statement

Hence, an image processing algorithm to localize injection sites, (i) in the nucleus (nucleic injection site, NIS) and (ii) in the cytoplasm (cytoplasmic injection site, CIS), of an irregularly shaped adherent cell is required. The NIS is defined as a point on the nucleus, whereas the CIS is a point off the nucleus and on the cytoplasmic regions where it is adequately far from the nucleus, but is still thick enough to be injected. These are the criteria that are often used by cell biologists. The algorithm should robustly perform against irregular morphology of adherent cells, object multiplicity (e.g., cellular debris and dead cells in images), occlusion (i.e., laterally touching cells), and more importantly, poor contrast (short range of gray levels) of cell images.

To address this problem, we propose a practical, two-stage model-based algorithm that first performs NIS localization using mathematical morphology and k -means clustering methods. Then, based on the results from the first stage, a geometrical model is built for each cell and used along with a moderated region-growing technique called Growing Circles Algorithm—the main contribution of this study—to localize the CIS. The proposed algorithm can then be employed in CPM- or SCE-based robotic systems for automated high-throughput injection of single adherent cells.

2 Methods

2.1 Stage I: NIS localization

Nuclei detection is a well-known problem in the field of cell image processing and has many applications, such as image cytometry, cell image retrieval systems, etc. [2, 4, 8]. Usually, fluorescence microscopy or staining techniques have been used in most of these applications to increase the image signal-to-noise ratio. However, such techniques cannot be used in the target application, i.e., automated robotic single-cell micromanipulation. Here, the whole cell-sample must be scanned to localize the *live cells* and the injection sites prior to manipulation. Therefore, fluorescence microscopy cannot be employed in this application, due to the possibility of phototoxicity as a result of long-duration exposures. Phototoxicity is caused by the tendency of fluorescent label molecules to react with molecular oxygen, which results in the production of free radicals that can damage subcellular components and compromise the entire cell [16]. In addition, staining techniques cannot be employed, since *live cells* are being studied.

The proposed solution for the NIS localization is based on the fact that the presence of the nucleus containing nucleoli and surrounded by ribosomes and the rough endoplasmic reticulum (RER) gives a higher thickness and refractive index to the nucleic regions of an adherent cell. Therefore, as Fig. 1a shows, these bumpy regions produce a higher contrast in differential interference contrast (DIC) images. The gradient features corresponding to these high-contrast nucleic regions are first extracted and processed to produce single objects associated with each cell's nucleic region. Each segmented region is then estimated with an ellipse that is used as an *attention window* [8] in a k -means clustering-based search algorithm to localize the NIS. It should be noted that, not only are the nucleic regions more distinguishable, but they also rarely touch each other in a confluent cell culture. Hence, the poor contrast and the occlusion problems can be effectively addressed through this approach.

2.1.1 Feature extraction

As shown in the flow chart in Fig. 2, the input image (e.g., Fig. 6a) is first Gaussian-smoothed, and then the following gradient operator is used to highlight the contrast changes:

$$G[x, y] = \sum_{m=-2}^2 \sum_{l=-2}^2 K[l, m] I[x-l, y-m] \quad (1)$$

where I and G are the grayness of the original and the gradient images at pixel (x, y) , respectively, and $K[l, m]$ is a 5×5 Sobel convolution kernel. To draw as much useful gradient information as possible, two orthogonal kernels

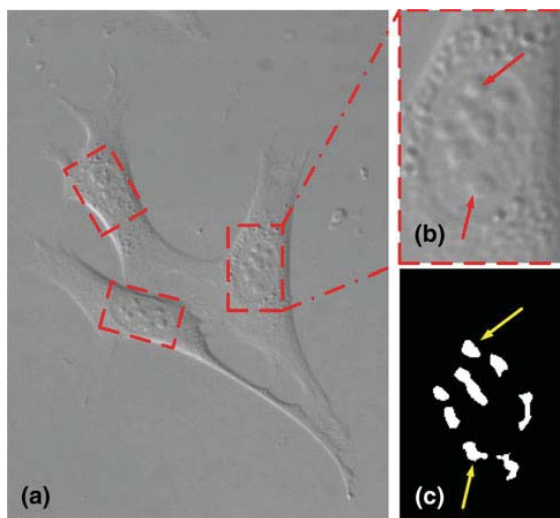


Fig. 1 **a** NIH/3T3 cells under the DIC microscopy. The high-contrast nucleic regions are marked with *dotted boxes*. Notice comparatively lower contrast of the surrounding cytoplasmic regions; **b** zoomed view of the nucleus. *Arrows* show examples of two bright nucleoli. Notice the ellipsoidal layout of the nucleus; and **c** processed (thresholded and filtered) image of **(b)** showing the information used in the *k*-means clustering-based NIS localization

are employed in parallel, and the gradient images in vertical and horizontal directions are produced. The Otsu-clustering method [12] is then used to convert the gradient images to binary images, which represent locally maximal valued pixels in the gradient images. The optimal threshold (T) is calculated by minimizing the intra-class variance in:

$$\sigma_{\text{intra}}^2(T) = n_f(T)\sigma_f^2(T) + n_b(T)\sigma_b^2(T) \quad (2)$$

where $n_f(T)$ and $n_b(T)$ are the number of pixels in the foreground and the background, respectively; $\sigma_{\text{intra}}^2(T)$, $\sigma_f^2(T)$, and $\sigma_b^2(T)$ are the intra-class, foreground, and background variances, respectively. Next, a Ferret diameter filter is applied to the resulting binary images to remove the elongated objects resulting from shadows or reflections in the DIC images that are created by the nucleic regions' height. The size of removable objects by this filter is set according to the optical train's magnification and using the training image library, which is employed to tune the algorithm's parameters. As illustrated in Fig. 2, the resulting binary images from the two parallel processes are then added together to produce a single image containing the information mostly associated with the nucleic regions of each cell (e.g., Fig. 6b).

2.1.2 Mathematical morphology clustering

As it is evident in Fig. 6b, the binary information corresponding to the nucleic regions are in the form of closely segregated pixel sets that should be grouped together to

form a single object representing each nucleic region in the binary image. This is a clustering problem in the field of unsupervised pattern classification that can be addressed using (binary) mathematical morphology operations [14, 17]. The proposed mathematical morphology clustering (MM clustering) algorithm for this purpose is shown in Fig. 2. A dilation step is first employed to *partially* connect the adjacent pixel sets belonging to the same cell's nucleic region to form semi-coherent larger pixel sets. All small in-between particles which are not associated with nucleic regions are then removed. Next, the dilation operation is repeated again to *fully* connect the larger pixel sets. It should be noted that this *dilation-particle removal-dilation* profile is necessary to effectively overcome the occlusion problem and prevent the possible formation of a single object associated with two or more adjacent cells. The remaining gaps in the resulting larger pixel sets are then filled to produce single coherence binary objects which are then eroded to remove their spurious artifacts and produce a single binary object corresponding to each nucleic region (Fig. 6c). 3×3 structuring elements are used for both dilations and the erosion. Since nucleic regions of dividing cells or cells in a highly confluent population could be potentially detected as one object, morphological size and shape filters are also employed to remove these possible erroneous clustering outcomes.

2.1.3 k-means clustering-based NIS localization

In general, the nuclei of most adherent cells have an oval form, which results in an ellipsoidal layout in the 2-D image space (see Fig. 1b). Therefore, each segmented nucleic region from the last step is modeled by an ellipse of the same geometric (i.e., size and length-to-width ratio) and spatial (i.e., orientation and location) properties (Fig. 6c). This way, it can be expected that the ellipse almost encloses the nucleus and the nucleic features (e.g., nucleoli). However, there might be a bias error associated with the position of the estimated *nucleic ellipse* (NE), i.e., the segmented nucleic region (hence, the estimated NE) may not cover parts of the actual nucleus, as shown in Fig. 3a. This is an error that could arise due to non-specificity of the gradient information used in the nucleic region segmentation, and must be properly compensated. In fact, the gradient information associated with some sub-cellular and extracellular structures can sometimes be so significant, that it potentially shifts the centroid of the segmented nucleic region (hence, the estimated NE) toward a fictitious position. Therefore, the estimated NE should be finely relocated until it encloses the nucleus. Referring back to the cell nucleus in Fig. 1b, it can be observed that some parts of the nucleoli inside the nucleus have higher gray-scale intensity than the surrounding regions. The Otsu-

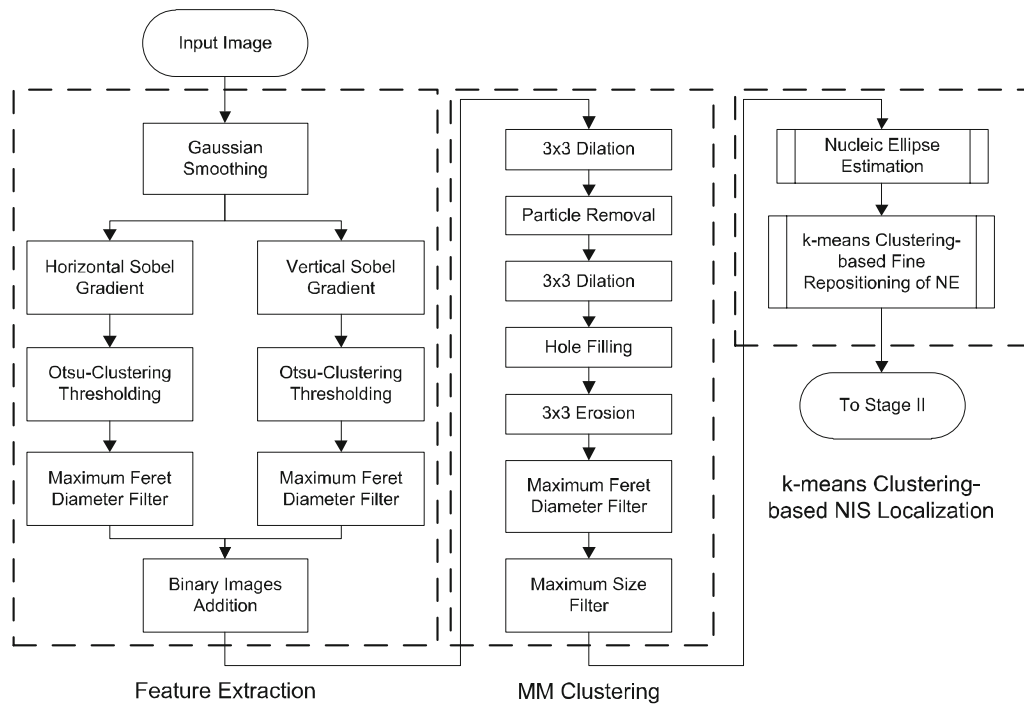


Fig. 2 The block diagram of Stage I: NIS localization

clustering method along with a series of morphological filters is used again to detect these bright nucleoli (see Fig. 1c). Also, the nucleoli are usually distributed evenly inside the nucleus. These characteristics can be used by a k -means clustering-based technique to finely reposition the estimated NE.

The k -means clustering algorithm is a well-known approach in the field of unsupervised data mining, and has been used in a variety of applications, including image processing. It is a fast and easy-to-implement iterative algorithm that alternately switches between two steps (data assignment and relocation of means—see below) until a convergence criterion is satisfied [6]. The main drawback of this method, however, is its initialization, i.e., the selection of the number of clusters and their initial mean values. Nevertheless, in this application, the estimated NEs can be used to effectively address these problems. Using each NE as an attention window applied to the processed (i.e., thresholded and filtered) image (partly shown in Fig. 1c), only one cluster will be handled by the k -means clustering algorithm at a time. Also, the center of the NE is considered as the initial mean value. The k -means clustering algorithm then iteratively performs these two steps: (i) *Step 1-Data Assignment*: all pixels in the processed image that are covered by the NE are assigned to the cluster. (ii) *Step 2-Relocation of Means*: the centroid

(mean) of this cluster is computed as in (3) and the center of the NE is shifted to the calculated centroid.

$$X = \frac{\sum_{i=1}^{i=r} x_i p(x_i)}{\sum_{i=1}^{i=r} p(x_i)}; \quad Y = \frac{\sum_{i=1}^{i=r} y_i p(y_i)}{\sum_{i=1}^{i=r} p(y_i)} \quad (3)$$

where r is the NE's size in pixels, x_i and y_i are the pixel coordinates, and $p(x_i)$ and $p(y_i)$ are the pixel values, respectively. The algorithm stops when the new centroid found in Step 2 coincides the previous one. Hence, this k -means clustering-based algorithm relocates the initial NE to the region where the density of pixels associated with the nucleoli of the cell of interest is the highest (see Fig. 3b). Therefore, the final NE covers the nucleoli and the corresponding nucleus (see Fig. 3c and Online Resource 1). The center of the final NE—which will subsequently be used in Stage II (CIS localization)—is then chosen as the NIS (the red cross marks in Figs. 3c, 6d).

2.2 Stage II: CIS localization

The proposed method for the CIS localization is a pseudo-region-growing algorithm that uses each NE as a *seed region* to perform an iterative search in the 2-D image space to detect the low-contrast cytoplasmic regions to the maximum extent possible. To perform this search, the area around each seed region (i.e., NE) is examined using a

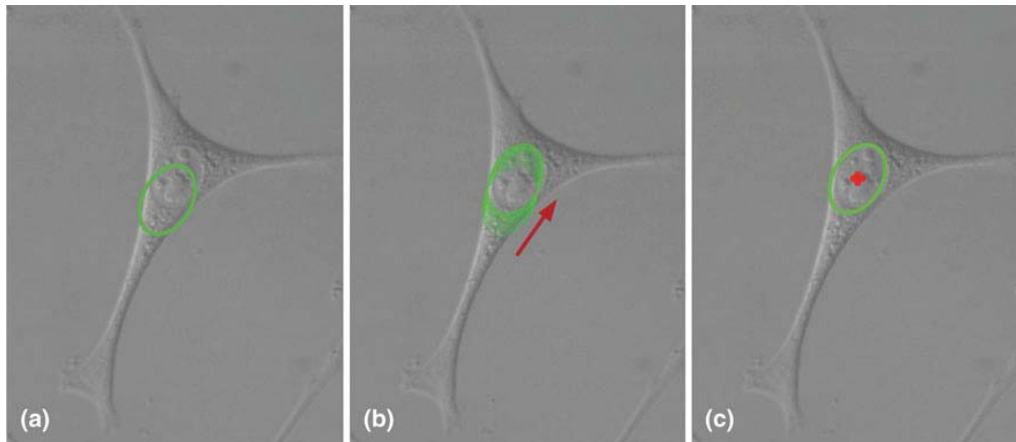


Fig. 3 *k*-means clustering-based fine localization of NE (nucleic ellipse) and NIS: **a** an erroneous initial estimation of NE from the segmented nucleic region; **b** iterative repositioning of the NE via the

k-means clustering-based algorithm. The *arrow* shows the repositioning direction; and **c** final NE and NIS localization results

number of surrounding *probe-circles*, which have been defined using a geometrical model.

2.2.1 Surrounding probe-circles

A geometrical model evenly distributes regions around each NE among a number of probe-circles as illustrated in Fig. 4a and also shown in Fig. 6d. The number and initial area of the circles determine the precision (i.e., the degree to which the cytoplasmic regions surrounding the NE is examined) and the speed of the algorithm. Our experimental trials showed that eight circles provide satisfactory results in both aspects. A fewer number of circles reduces the precision, as some regions will be missed and not assessed by any probe-circle. Using more circles, not only results in a higher computation requirement, but it will also affect the precision, as the probe-circles start to overlap significantly as they grow and duplicate the assessment of some regions. The area of each initial probe-circle (a') is defined based on the area of the estimated NE in Stage I. Again, our experimental trials showed that initializing the area of each probe-circle to be the 16th of that of the corresponding NE will result in locating most of the initiated circles within the cell boundary (e.g., see Fig. 6d).

2.2.2 Low-level information extraction

To assess the cytoplasmic region covered by each probe-circle, some feedback information from that region is required. Looking at Fig. 1a, a slight contrast can be observed over most parts of the cytoplasmic regions around the nucleus. To retrieve this *low-level* information, a highly sensitive edge detection algorithm such as the Canny

method can be employed [3]. The Canny edges vaguely show the outline of each cell, but are too disconnected to define the cell boundaries (see Fig. 6e). Nevertheless, they can be useful to probe the cytoplasmic regions: the higher the edge density in a region, the denser (thicker) the covered portion of the cytoplasm. Therefore, an obvious location for the CIS would be a point on the thickest area covered by initial probe-circles. However, this choice may not be a safe location for cytoplasmic injection, as the subsequent injection at such a region could potentially affect the nucleus contents as well, which is undesirable. Therefore, a point on a relatively thick portion of the cytoplasm that is also sufficiently far from the nucleus would be more appropriate as the CIS. A pseudo-region-growing algorithm that realizes this requirement is proposed next.

2.2.3 Growing Circles Algorithm

The original implementation of the region growing algorithm, such as in [1], is based on expanding homogenous regions by evaluating their adjacent individual pixels. This approach is accurate, but computationally expensive and slow. The targeted application in hand does not require single-pixel precision; therefore, in the proposed algorithm, instead of single pixels, *pixel-crescents* (PCs) are employed and analyzed. A PC is defined as follows:

$$PC = \left\{ p : \bigcup_{j=1}^{j=s} p \cup P_i = P_{i+1} \right\} \tag{4}$$

where p is a pixel, s is a PC's size in pixels, and P_i and P_{i+1} are two consecutive probe-circles, i.e., P_{i+1} is an expanded

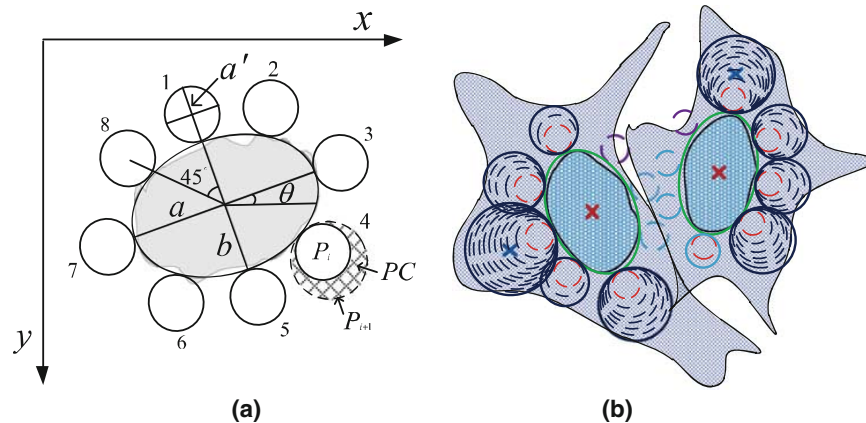


Fig. 4 a Surrounding probe-circles model and a typical pixel-crescent (PC). θ is the orientation of the detected nucleic region (i.e., NE). a and b are semi-major and semi-minor axes of the estimated NE; and **b** an illustration showing the required performance by the Growing Circles Algorithm. The outlier probe-circles (purple) are discarded first. The in-between probe-circles (light-blue) do not

grow further after this state. Other probe-circles grow based on the low-level information provided by the Canny operator. On termination of the algorithm, the center of the NE (red cross) and the centroid of the largest probe-circle (blue cross) are chosen as the NIS and the CIS, respectively. (Color figure online)

version of P_i by a fixed value (i.e., PC) as shown in Fig. 4a. The size of PC affects the precision and the speed of the algorithm. Considering the chosen size of the initial probe-circles for each NE (Sect. 2.2.1), a PC whose size equals that of the initial probe-circle was shown to be satisfactory in our work.

As for the region feature—a characteristic used to describe similar PCs—the Canny edges that provide the texture information are used in the proposed algorithm. The texture information is quantified using Laws' texture measures [9] applied to the Canny edge image: the number of edge pixels (i.e., "1" pixel) in each PC represents the energy of the texture covered by that PC. Also, the homogeneity predicate—the criteria by which PCs are evaluated and integrated—is defined as follows [1]:

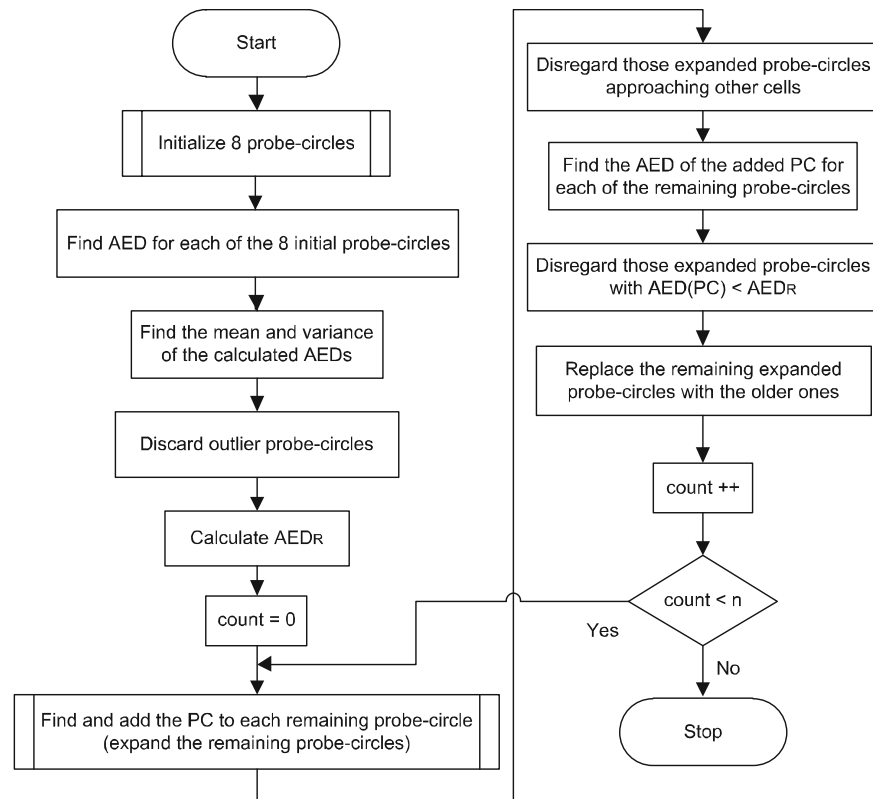
$$\delta(PC) = AED(PC) - AED_R \quad (5)$$

where AED stands for the average edge density, i.e., the average number of Canny edge pixels in a typical region. Therefore, AED(PC) is the average edge density in a PC that is being evaluated. AED_R is a reference measure for each cell's texture and is found by averaging the AED values of those initial probe-circles which are located inside the cytoplasmic region of the cell. Assuming a normal distribution for the AED values of all initial probe-circles, those whose AED is less than one standard deviation are considered to be outliers (i.e., outside the cytoplasmic region); therefore, they are discarded and have not been considered in the calculation of AED_R .

The proposed Growing Circles Algorithm works as outlined in the flowchart in Fig. 5, illustrated in Fig. 4b,

and displayed in Online Resource 1. To improve the algorithm's performance and efficiently address the CIS localization for two or more closely adjacent cells, two practical constraints are placed on the growth of the probe-circles. Suppose n is the factor by which the size of a typical NE is divided to yield the size of its initial probe-circles. (As stated above, in the current implementation, n is set to 16.) First, it has been experimentally observed that the maximum number of n iterations—which according to the chosen size for PCs will produce a probe-circle whose area is the same as for the corresponding NE—is sufficient for an initial circle to grow and completely cover that particular portion of the cytoplasm that is located between the nucleus and the cell boundary. Second, if there are two or more adjacent cells in an image, the in-between probe-circles cannot expand too much to cover other cells' cytoplasmic regions. In other words, for a typical NE, if the mutual distance between the center of each of its probe-circles and the center of other NEs is less than a threshold value, that particular probe-circle cannot grow anymore. The value of this threshold for each NE is set to $3\sqrt{ab}$, where a and b are the NE's semi-major and semi-minor axes, respectively (as shown in Fig. 4a). According to the justification made for the first constraint, this threshold value ensures that a probe-circle will not enter neighboring cells' potential cytoplasmic regions. On terminating the algorithm for each cell, the centroid of the largest probe-circle will be chosen as the CIS (the blue cross marks in Figs. 4b and 6f), which satisfies the requirements stated for the CIS in the original Problem Statement.

Fig. 5 The simplified flow chart of the Growing Circles Algorithm. The algorithm is applied to each NE obtained in Stage I



2.3 Experimental setup

The performance of the developed algorithm was evaluated on NIH/3T3 cells (Cat #: CRL-1658, ATCC, VA, USA), a standard fibroblast cell line commonly used as the growth factor secreting element or as a host in transfection experiments. NIH/3T3 cells represent all the characteristics aforementioned for adherent cells. Cells had been cultured for seven passages in minimum essential medium (MEM) α -medium (1 \times) (Cat #: 12571-063) supplemented with 5% fetal bovine serum (FBS) (Cat #: 16000-036) and 1% Penicillin–Streptomycin (Cat #: 15140-12). All the reagents were purchased from Invitrogen, CA, USA. Cells were plated 10 h prior to being imaged at a concentration of $(60 \pm 2) \times 10^4$ cells/ml.

The image acquisition system consists of an inverted Nikon TE-2000U microscope equipped with a 60 \times Nikon ELWD Plan Flour objective (NA = 0.7) (Nikon, Tokyo, Japan). The DIC mode was employed, and a Retiga EXi Digital CCD camera (QImaging Products, BC, Canada) with the resolution of 1392 \times 1040 pixels was used to capture images. The algorithm was implemented in LabVIEW[®] 9.0 (National Instruments, TX, USA).

3 Results

A library of 405 images—created by manually scanning a square area in four Petri dishes from two different NIH/3T3 cell cultures—was used to perform the localization analysis. The training image library consisted of 30 images taken under the same conditions. The proposed algorithm was applied to all images in the library and the localization results for each image were evaluated manually, as summarized in Table 1. Comparing the total number of objects (Item 1) and the number of actual cells (Item 2), it is observed that 18.9% of the objects in the images are non-cell objects, such as squeezed-shaped dead cells, cell debris aggregates, and large elongated pseudopodia of other cells that are not of interest. This value shows the degree of object multiplicity that was mentioned as one of the main localization challenges in the Problem Statement. Item 3 is the number of actual cells detected by the algorithm, i.e., the number of NEs (and NIS’s) that are associated with actual cells. However, not all of these detections are correct; some of the NEs do not properly enclose the nuclei, which result in erroneous NIS localizations. Therefore, Items 4 and 5 show the number of correct and incorrect

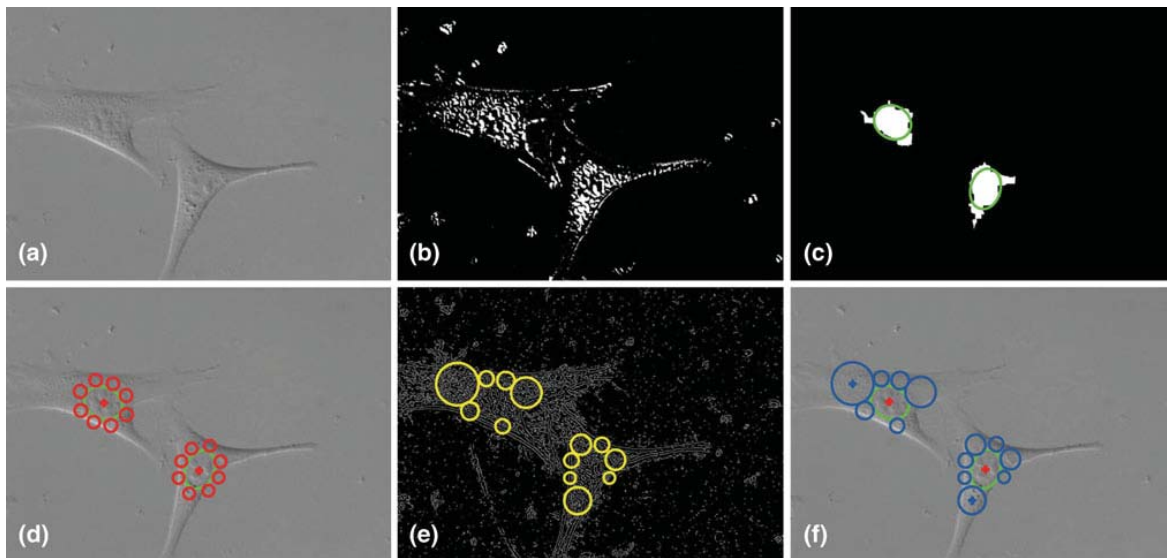


Fig. 6 Live NIH/3T3 cell image sequence of the NIS-CIS localization algorithm: **a** original image; **b** extracted high-contrast information associated with nucleic regions; **c** segmented nucleic regions and the estimated NEs (*green ellipse*); **d** localization of NIS (*red cross*) and initialization of probe-circles model (*red circles*); **e** low-level

edge information in the Canny image and final probe-circles (*yellow circles*) produced by the Growing Circles Algorithm; and **f** final results for CIS and NIS localization (*blue and red crosses*, respectively). (Color figure online)

NIS localizations. The correct NIS detections (as shown in Fig. 6d) refer to those cases where the NE properly encloses the nucleus, implying that the NIS is correctly located within the nucleus of the cell. The incorrect NIS detections are those cases where the identified NE does not cover the nucleus, meaning that the NIS is located either on the periphery or outside of the nucleus. Item 6 shows the number of non-cell objects that an NE has incorrectly been associated with. The last two rows in Table 1 show the number of correct and incorrect CIS localizations that are counted only among those cells for which a correct NIS localization has already been confirmed. The correct CIS localization, as shown in Fig. 6f, refers to the case where the identified CIS is situated on the cytoplasmic region, sufficiently far enough from the nucleus.

To evaluate different aspects of the performance of the proposed algorithm, the aforementioned findings in Table 1 were statistically analyzed, and the results are reported in Table 2. In this table, Item 2 gives the total number of incorrect NIS detections (Item 5 in Table 1) and the number of non-cell objects detected as cells (Item 6 in Table 1), which together are referred to as false positive (FP) NIS localizations. True negative (TN) NIS localizations (Item 3) refer to those situations where non-cell objects have been correctly ignored, whereas false negative (FN) NIS localizations (Item 4) describe those cases in which cells have been incorrectly skipped. These values resulted in NIS localization sensitivity and specificity of

0.730 and 0.771, respectively. The sensitivity (Item 5) states the chance of finding the correct NIS localization among all cells, while the specificity (Item 6) refers to the chance of correctly detecting any incorrect NIS. Finally, the NIS localization precision rate (i.e., positive predictive value) in Item 7 refers to the likelihood of correct NIS localization among all detected NEs. The high value (0.918) of this parameter shows the high performance of the Stage I and, in particular, the *k*-means clustering-based NIS localization algorithm.

Next, the CIS localization results were analyzed statistically. Based on the number of true positive (TP) (Item 8) and FP (Item 9) CIS localizations, the precision rate for CIS localization among TP NIS localizations is 0.943. This value is very promising, as it indicates the good performance of the Growing Circles Algorithm, which is one of the main contributions of this work. It is worth pointing out that in the case of CIS localization, TN and FN concepts are not applicable since the CIS localization algorithm (Stage II) is by default dependent on the NIS localization results of the previous stage, i.e., it performs CIS localization only for those NEs obtained in Stage I.

Finally, the combined NIS and CIS localization statistics were analyzed. Item 11 shows the number of cells for which both the NIS and CIS are correctly localized, whereas Item 12 gives the number of cells for which either the NIS or CIS is localized incorrectly. Therefore, the combined NIS and CIS localization precision rate is calculated to be 0.866,

Table 1 Summary of NIS and CIS localization results for NIH/3T3 cells

Item no.	Item name	Counts
1	Total number of cells and non-cell objects	1,293
2	Number of cells	1,048
3	Number of detected cells	818
4	Number of correct NIS localizations	766
5	Number of incorrect NIS localizations	52
6	Number of non-cell objects detected as cells	16
7	Number of correct CIS localizations	723
8	Number of incorrect CIS localizations	43

Table 2 Summary of statistical analysis of NIS and CIS localization results for NIH/3T3 cells

<i>NIS localization statistics</i>		
1	True positives (TP)	766
2	False positives (FP)	68
3	True negatives (TN)	229
4	False negatives (FN)	230
5	Sensitivity ^a	0.730
6	Specificity ^b	0.771
7	Precision rate ^c (positive predictive value)	0.918
<i>CIS localization statistics</i>		
8	True positives	723
9	False positives (among true positive NIS's)	43
10	Precision rate (among true positive NIS's)	0.943
<i>Combined NIS and CIS localization statistics</i>		
11	True positives	723
12	False positives	111
13	Precision rate	0.866

^a Sensitivity = TP/(TP + FN)

^b Specificity = TN/(TN + FP)

^c Precision rate = TP/(TP + FP)

which is satisfactory for the current application, i.e., robotic automated single-cell micromanipulation.

4 Discussion

High-throughput single-cell assays can benefit from automated bio-micromanipulation systems, particularly for CPM and SCE operations. The automated capability of such systems has been already demonstrated for micromanipulation of suspended cells (e.g., oocytes, blood cells, etc.) [15, 18]. However, in order to generalize the application of automated bio-micromanipulation systems, they must also have the ability to manipulate adherent cells, both on the nucleus and on the cytoplasm. These cells are flat, have irregular shapes, and are usually only 3–6 μm

thick,¹ which makes their automated localization and micromanipulation more challenging. In this article, the underlying machine vision problem was addressed, and a two-stage model-based algorithm based on the concepts of *k*-means clustering and region growing was proposed as a feasible and practical solution. A proof-of-principle demonstration was carried out by testing the algorithm on a library of images taken from live NIH/3T3 cells using DIC microscopy. In the targeted application of this research, the main requirement for the machine vision system is to provide the necessary information to the micromanipulation system that will lead to the highest injection efficiency. To achieve this goal, an ideal localization algorithm should, first, avoid detecting any non-cell objects as cells, and second, choose NIS or CIS locations correctly for injection via the CPM or SCE methods. The results show 0.918, 0.943, and 0.866 precision rates for the NIS, CIS, and combined NIS and CIS localizations, respectively, which confirms the overall performance of the proposed algorithm, and the *k*-means clustering-based NIS localization and the Growing Circles Algorithm, in particular.

The high precision rate and specificity values resulted from the small numbers of incorrect NIS localizations and non-cell object detections, respectively. These values also show the ability of the algorithm to efficiently detect and ignore dividing and dying cells. While dividing, cells share a nucleus that expands until it is separated between the two offspring. The nucleus' (and the nucleic region's) size during this stage is larger than that of a normal cell in the resting state. The morphological size filters employed in the MM clustering step are able to detect and remove the larger nucleic regions associated with dividing cells. Also, dying cells usually look squeezed and do not contain the surrounding cytoplasmic region. Although they could be detected as potential nucleic regions in the NIS localization stage, their surrounding probe-circles cannot grow enough in the CIS localization stage, as there is no cytoplasmic region to provide the required feedback information. A sub-routine always checks the distance between the localized CIS and NIS; if this distance is smaller than a threshold, the detected object is considered to be a dead cell whose probe-circles cannot grow, and will be ignored.

The FP NIS localizations are mainly caused when the image contrast is too low for the nucleoli to be detectable, resulting in the *k*-means clustering-based NIS localization algorithm not performing as expected. In addition, the presence of any intercellular objects with similar morphological and brightness characteristics as nucleoli near the nucleic region sometimes shifts the resulted NE to an

¹ Using a pseudo-patch-clamp technique, an in-progress study by our group has confirmed this range for the thickness of NIH/3T3 fibroblasts.

erroneous location, which in turn leads to incorrect NIS localizations. The FN NIS localization cases mainly happened either due to the highly confluent cell clusters that are ignored by the morphological size filters employed in the MM clustering step or because of extremely low-contrast cells whose gradient features cannot be extracted. The FP CIS localization cases are also caused by the low contrast of the very thin cytoplasmic regions, which is the inherent limitation of the DIC microscopy that is commonly used for *live cell* imaging. In fact, for imaging of *live cells* that are transparent, DIC microscopy is a popular contrast-enhancing technique that renders high-resolution cell morphology and internal content information that are suitable for machine vision; however, when the specimens are very thin cells, as in the present case, even DIC yields relatively poor contrast images. In these cases, there was insufficient low-level information available about the cytoplasmic regions in the Canny image, and the probe-circles did not expand as expected.

Although the proposed algorithm has been tested on NIH/3T3 fibroblast cells, the advantage of the algorithm is its reproducibility and applicability toward a range of other adherent cell lines such as epithelial and endothelial cells. This is due to the fact that the underlying principles of the proposed algorithm are based on the (cell) image features rather than the cell type, and adherent cells generally share the same cellular features that are employed in the proposed algorithm. Hence, the algorithm will work as long as the nuclei and the cytoplasmic regions are actually present and distinctive. The general morphology (i.e., shape) of some adherent cell types, however, could affect the performance of the algorithm, particularly in the CIS localization stage. For example, in cases where the cytoplasmic area is too small (e.g., in some phenotypes whose cytoplasmic regions have not been formed properly) or forms a dendritic shape (e.g., in neuron cells), the algorithm fails to properly localize the CIS. In these cases, the probe-circles simply cannot grow enough because there is not enough feedback information available. As a result, the algorithm either yields a false CIS (i.e., not located within the cytoplasm) or considers these cases as dying cells. The cell concentration could also affect the proper performance of the algorithm. In a cell monolayer where cells are too confluent, such that their nuclei touch each other, some cells could be considered as dividing cells and would be removed. Nevertheless, in the target application that involves automated robotic single-cell micromanipulation, the cells are not required to form a highly confluent culture and can be plated with a proper concentration prior to the manipulation.

In conclusion, the proposed algorithm is a straightforward and easy-to-implement method that will prove useful in a range of cell biology and cancer research applications associated with finding and identifying cellular features

(i.e., nucleic and cytoplasmic) for high-throughput automated micromanipulation of individual adherent cells using CPM and SCE techniques, which is the topic of our future work.

Acknowledgments This study was supported in part by the Simon Fraser University under the President's Research Grants Fund and the National Sciences and Engineering Research Council of Canada. The authors are grateful to Dr. Timothy Beischlag and Mr. Kevin Tam from the Faculty of Health Sciences, Simon Fraser University for their great hospitality and assistance during the experiments performed in Beischlag Lab.

References

- Adams R, Bischof L (1994) Seeded region growing. *IEEE Trans Pattern Anal Mach Intell* 16(6):641–647
- Al-Kofahi Y, Lassoued W, Lee W, Roysam B (2010) Improved automatic detection and segmentation of cell nuclei in histopathology images. *IEEE Trans Biomed Eng* 57(4):841–852
- Canny J (1986) A computational approach to edge detection. *IEEE Trans Pattern Anal Mach Intell* 8(6):679–698
- Gudla PR, Nandy K, Collins J, Meaburn KJ, Misteli T, Lockett SJ (2008) A high-throughput system for segmenting nuclei using multiscale techniques. *Cytometry A* 73(5):451–466
- Ittner LM, Gotz J (2007) Pronuclear injection for the production of transgenic mice. *Nat Protoc* 2(5):1206–1215
- Jain AK, Murty MN, Flynn PJ (1999) Data clustering: a review. *ACM Comput Surv* 31(3):264–323
- Kimura Y, Yanagimachi R (1995) Intracytoplasmic sperm injection in the mouse. *Biol Reprod* 52(4):709–720
- Ko BC, Seo MS, Nam JY (2009) Microscopic cell nuclei segmentation based on adaptive attention window. *J Digit Imaging* 22(3):259–274
- Laws K (1980) Textured image segmentation, PhD Thesis, University of Southern California, Los Angeles, CA, USA
- Lin CL, Evans V, Shen S, Xing Y, Richter JD (2009) The nuclear experience of CPEB: implications for RNA processing and translational control. *RNA* 16:338–348
- Lukkari M, Kallio P (2005) Multi-purpose impedance-based measurement system to automate microinjection of adherent cells. In: *Proceedings of IEEE International Symposium on Computer Intelligence in Robotics and Automation*, Espoo, Finland, pp 701–706
- Otsu N (1979) A threshold selection method from gray-level histograms. *IEEE Transactions on Systems, Manufacturing, and Cybernetics SMC-9*, pp 62–66
- Page R, Butler S, Subramanian A, Gwazdauskas F, Johnson J, Velander W (1995) Transgenesis in mice by cytoplasmic injection of polylysine/DNA mixtures. *Transgenic Res* 4:353–360
- Postaire JG, Zhang RD, Lecocq-Boite C (1993) Cluster analysis by binary morphology. *IEEE Trans Pattern Anal Mach Intell* 15(2):170–180
- Sakaki K, Dechev N, Burke RD, Park EJ (2009) Development of an autonomous biological cell manipulator with single-cell electroporation and visual servoing capabilities. *IEEE Trans Biomed Eng* 56(8):2064–2074
- Schroede T (2008) Imaging stem-cell-driven regeneration in mammals. *Nature* 453:345–351
- Serra J (1983) *Image analysis and mathematical morphology*, 1st edn. Academic Press, Orlando

18. Sun Y, Nelson B (2002) Biological cell injection using an autonomous microrobotic system. *Int J Robotics Res* 21(10–11): 861–868
19. Wang W, Hewett D, Hann C, Chase J, Chen X (2009) Application of machine vision for automated cell injection. *Int J Mechatron Manuf Syst* 2(1):120–134
20. Wang M, Orwar O, Olofsson J, Weber SG (2010) Single-cell electroporation. *Anal Bioanal Chem* 397(8):3235–3248

Appendix B.

Localized, Macromolecular Transport for Thin, Adherent, Single Cells Via an Automated, Single Cell Electroporation Biomanipulator

Localized, Macromolecular Transport for Thin, Adherent, Single Cells Via an Automated, Single Cell Electroporation Biomanipulator

Kelly Sakaki, *Member, IEEE*, Hadi Esmaeilsabzali, Shabnam Massah, Gratien G. Prefontaine, Nikolai Dechev, *Member, IEEE*, Robert D. Burke, and Edward J. Park*, *Member, IEEE*

Abstract—Single cell electroporation (SCE), via microcapillary, is an effective method for molecular, transmembrane transport used to gain insight on cell processes with minimal preparation. Although possessing great potential, SCE is difficult to execute and the technology spans broad fields within cell biology and engineering. The technical complexities, the focus and expertise demanded during manual operation, and the lack of an automated SCE platform limit the widespread use of this technique, thus the potential of SCE has not been realized. In this study, an automated biomanipulator for SCE is presented. Our system is capable of delivering molecules into the cytoplasm of extremely thin cellular features of adherent cells. The intent of the system is to abstract the technical challenges and exploit the accuracy and repeatability of automated instrumentation, leaving only the focus of the experimental design to the operator. Each sequence of SCE including cell and SCE site localization, tip-membrane contact detection, and SCE has been automated. Positions of low-contrast cells are localized and “SCE sites” for microcapillary tip placement are determined using machine vision. In addition, new milestones within automated cell manipulation have been achieved. The system described herein has the capability of automated SCE of “thin” cell features less than 10 μm in thickness. Finally, SCE events are anticipated using visual feedback, while monitoring fluorescing dye entering the cytoplasm of a cell. The execution is demonstrated by inserting a combination of a fluorescing dye and a reporter gene into NIH/3T3 fibroblast cells.

Index Terms—Electroporation, machine vision, microcapillary transfection, microelectrode, robot-assisted manipulation, single cell.

I. INTRODUCTION

TRANSPORTING proteins, DNA, and other metabolites across the cell membrane is a fundamental mechanism used to investigate human processes at the cellular level. However, the cell membrane forms an effective barrier to foreign molecules and alternative means are required to coerce entry [1]. One effective method of overcoming this barrier is single cell electroporation (SCE) via microcapillary, which can be applied to cells directly in culture or to tissue with minimal preparation. SCE, via microcapillary, is a highly localized, repeatable method for gene transfection and molecular uptake for both *in vitro* and *in vivo* single cell manipulation [2]–[6]. SCE induces reversible pores [7] in the membrane by channeling an electric field through a microcapillary [3], [8] and concentrating the electric field at the cell surface [see Fig. 1(a)]. Charged ions and molecules, contained within microliters of solution loaded in a microcapillary, are inserted through the pores via an iontophoretic flow and diffusion. Since the diameter of the tip is small, a high spatial selectivity of the cell and the location on the cell is achievable allowing the tip to be placed on extremely small cell features [4].

SCE is a versatile single cell manipulation method; however, the technical complexity limits its operation to highly trained operators. The complexities of single cell manipulation technologies in general, and the demand for more versatile instrumentation have coupled focused methods of molecular transport using robot-assisted technology. As a result, the capabilities of robot-assisted, single cell manipulation technologies, such as SCE and intracytoplasmic, and capillary pressure microinjection (CPM), have rapidly advanced over the last decade as single cell research evolves.

Robot-assisted manipulation of large, single cells and embryos in suspension (i.e., diameters on the order of 10^2 and 10^3 μm 's) is frequently performed using intracytoplasmic injection techniques. This involves piercing through the cell membrane and using CPM to deliver molecules into the cytoplasm. Suspended cells can be immobilized with one microcapillary. Using visual servoing, a second microcapillary approaches and microinjects the cell in the same focal plane as the holding microcapillary [9]. Others have developed methods combining

Manuscript received March 12, 2013; revised May 23, 2013; accepted June 7, 2013. Date of publication June 12, 2013; date of current version October 16, 2013. This work was supported by the Natural Sciences and Engineering Research Council of Canada under Grant RGPIN/298219-2012 and Grant EQPEQ/406188-2011. The work of K. Sakaki was partly supported under the British Columbia Innovation Scholars Award. *Asterisk indicates corresponding author.*

K. Sakaki and H. Esmaeilsabzali are with the Faculty of Applied Sciences, Simon Fraser University, Surrey, BC V3T 0A3, Canada and also with the Faculty of Health Sciences, Simon Fraser University, Burnaby, V5A 1S6, Canada (e-mail: kelly.sakaki@sfu.ca; hesmaeil@sfu.ca).

S. Massah and G. G. Prefontaine are with the Faculty of Health Sciences, Simon Fraser University, Burnaby, BC V5A 1S6, Canada (e-mail: smassah@sfu.ca; ggp1@sfu.ca).

N. Dechev is with the Department of Mechanical Engineering, University of Victoria, Victoria, BC V8W 3P6, Canada (e-mail: dechev@uvic.ca).

R. D. Burke is with the Department of Biochemistry and Microbiology, University of Victoria, Victoria, BC V8W 3P6, Canada (e-mail: rburke@uvic.ca).

*E. J. Park is with the School of Mechatronic Systems Engineering, Faculty of Applied Sciences, Simon Fraser University, Surrey, BC V3T 0A3, Canada, and also with the Faculty of Health Sciences, Simon Fraser University, Burnaby, V5A 1S6, Canada (e-mail: ed_park@sfu.ca).

Color versions of one or more of the figures in this paper are available online at <http://ieeexplore.ieee.org>.

Digital Object Identifier 10.1109/TBME.2013.2268387

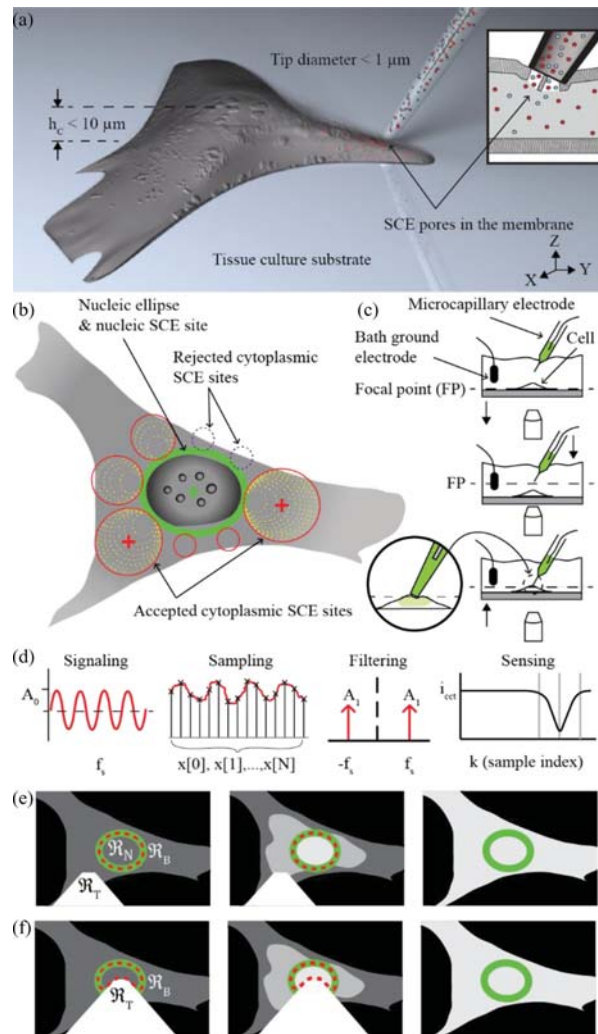


Fig. 1. Automated SCE. (a) Thin features on cells are targeted with microcapillary SCE to create (inset) reversible pores in the membrane used to insert molecules. (b) Nucleic and cytoplasmic SCE sites are localized on the cell using machine vision. (c) SCE site is positioned below the focal point and the tip is localized. The platform rises and brings the cell into contact with the tip. (d) Sinusoidal, sensing signal aids tip-membrane contact detection in the presence of a low SNR environment. Samples are input to the Discrete Fourier Transform. The signal is isolated on the frequency spectrum at f_s producing a measure of the current, i_{cet} , through the electrode to sense changes during tip-membrane contact. i_{cet} is relatively constant when the tip approaches the cell and abruptly decreases upon contact. This abrupt change is detected using statistical process control and tip motion is halted. Fluorescent molecules entering the cell via SCE are measured during (e) cytoplasmic and (f) nucleic SCE. A 1.5 times increase in fluorescent intensity in \mathcal{R}_B (red boundary) signals an end to the SCE routine.

“sensing” capabilities, including machine vision and force data [8], [9]. Further, designs increased throughput by trapping embryos and suspended cells using suction ports [12] and grooves [10] fabricated directly into the substrate.

Manipulating single cells that have been trapped, or adhered to substrates typically require an out-of-plane [13] delivery method, and a framework of high precision instrumentation to

position a microcapillary on a cell with a cross-sectional height h_c as small as several micrometers. Conventional microscopy formats (e.g., upright and inverted microscopes) typically reduce the working environment to a 2-D image and impede the ability to visually detect tip-membrane contact. A CPM system attempted to overcome such challenges using machine vision to estimate the height of the microcapillary with respect to the position of adherent cells [14].

Alternatively, visual servoing methods can be substituted for, or combined with microcapillary-based, microelectrode measurements [3], [15]–[17], which sense the degree of “tip-membrane” contact as the tip indents the membrane. Decreasing the amplitude of a low-potential, sensing signal provides an indication of the seal created between the microcapillary tip and the cell membrane. However, in microcapillary-based methods, the resolution of the sensing signal used during the tip-membrane placement routine is hampered by a poor signal-to-noise ratio (SNR). This is common in electrode-based devices and was demonstrated in our previous work [18]. Large cells provide sufficient membrane deflection distance to achieve significant amplitude changes at a specified threshold beyond the SNR with classic filtering techniques. Therefore, a little chance of damage to the cell or the tip is likely. In contrast, thin cells $10 \mu\text{m}$ or less, are problematic where the distance from the tip to the membrane (i.e., tip-membrane) cannot be accurately resolved and the distance from the initial tip membrane contact to the substrate is small. Subsequently, the use of fixed-threshold contact methods [3], [15], [17] can impede operational throughput as a result of damaged tips, ruptured cell membranes, or false tip-membrane detections, especially where a low SNR is present.

Even after achieving significant advances in automated cell manipulation, the limitations with respect to the size of adherent cells has rarely been discussed. Microcapillary SCE can insert molecules into a cell without piercing the membrane and can be executed, while the microcapillary is in contact with the membrane surface [15], [17], [18] or positioned several micrometers away [8]. Where novel solutions have automated the full sequence or a partial sequence of the stages of SCE, greater efforts are required to localize and manipulate cells with thin cross sections and exploit one of the most significant advantages of microcapillary SCE.

Prior work has achieved significant milestones toward fully automated solutions. Rae and Levis [3] suggested a method of estimating the potential at the membrane during tip-membrane contact for SCE. In [15], a semiautomated solution for SCE was demonstrated by inserting fluorescing dye into aortic endothelial cells. Kallio *et al.*, provides an electrical model describing current flowing through the microcapillary and used microcapillary electrodes [16] to indicate contact in SH-SY5Y cells (mouse neural blastoma) using a CPM robot-assisted manipulator. He also describes conditions for detecting broken and clogged microcapillaries. Our laboratory provided an automated solution to localize and manipulate large, sea urchin eggs that were chemically adhered to a substrate [17] using SCE.

Although many technological milestones have been achieved in microcapillary-based SCE and similar technologies, further

advances are necessary where methods and designs in the literature fall short of, or have not been developed for an automated solution for the SCE of thin, adherent cells. The broad technical requirements and the fragile nature of cell structures limit the efficiency of manual-throughput and subsequently rates of processing are sufficiently slow [5], [6]. Furthermore, the full sequence of tasks have not been adequately achieved by automated efforts, thus the true potential of SCE has not been realized.

In this study, a novel system for fully automated SCE is described. Our system utilizes a machine vision algorithm, developed in our laboratory, to detect low-contrast, thin, adherent cells and SCE sites on cells for molecular delivery [19]. Applying SCE on the most suitable location of a cell is rarely discussed in experimental methods. Therefore, two sites were proposed and include the “nucleic SCE site” and the “cytoplasmic” SCE site [see Fig. 1(b)]. In addition, we demonstrate a more versatile and robust, tip-contact detection algorithm, based on statistical process control [18], for cells less than 10 μm in thickness. This achievement eliminates limitations imposed by thin, adherent cells and provides a transmembrane transport method for a much broader range of applications. Finally, an endpoint for SCE is estimated using visual feedback from fluorescing molecules that are inserted in and diffuse throughout the cytoplasm of a cell during SCE

The operation of the system is demonstrated by inserting a fluorescent dye (Alexa Fluor Hydrazide 488) and a plasmid DNA with a reporter gene (pcDNA6-dsRed, 5.8 kbp) into NIH/3T3 fibroblasts. Two video demonstrations are provided as supplementary downloadable material and demonstrate the automation routine methodologies used in this study.

II. METHODOLOGY

A. Three Stages of Automated SCE

Automated SCE can be partitioned into three, sequential stages including, *Stage 1: cell localization and SCE site determination*; *Stage 2: tip-membrane contact detection*, and *Stage 3: SCE*, which is monitored using visual feedback.

Stage 1 (cell and SCE site localization): Cell and SCE site localizations were executed using a two-step algorithm [see Fig. 2]. First, the nucleus of a cell was localized and modeled as an ellipse, \mathcal{R}_N . The center of the ellipse determined the nucleic SCE site and the ellipse provided a bounded region \mathcal{R}_B , used to monitor visual feedback of the increase in fluorescent dye entering the cell during SCE. The localization of the cells and the corresponding SCE sites on the nucleus or cytoplasm was accomplished by first extracting the relatively high contrast features associated with the nuclei and surrounding rough endoplasmic reticula (RER) of cells in differential interference contrast (DIC) images. A sequence of an adaptive threshold and mathematical morphology operations coarsely located the nucleus of each cell. Next, each segmented nucleic region was estimated by an ellipse of similar geometrical and spatial properties. Fine localization of the nucleus was then realized using an iterative, k -means, clustering-based algorithm. Gradients associated with the nucleoli and other intranuclear organelles were

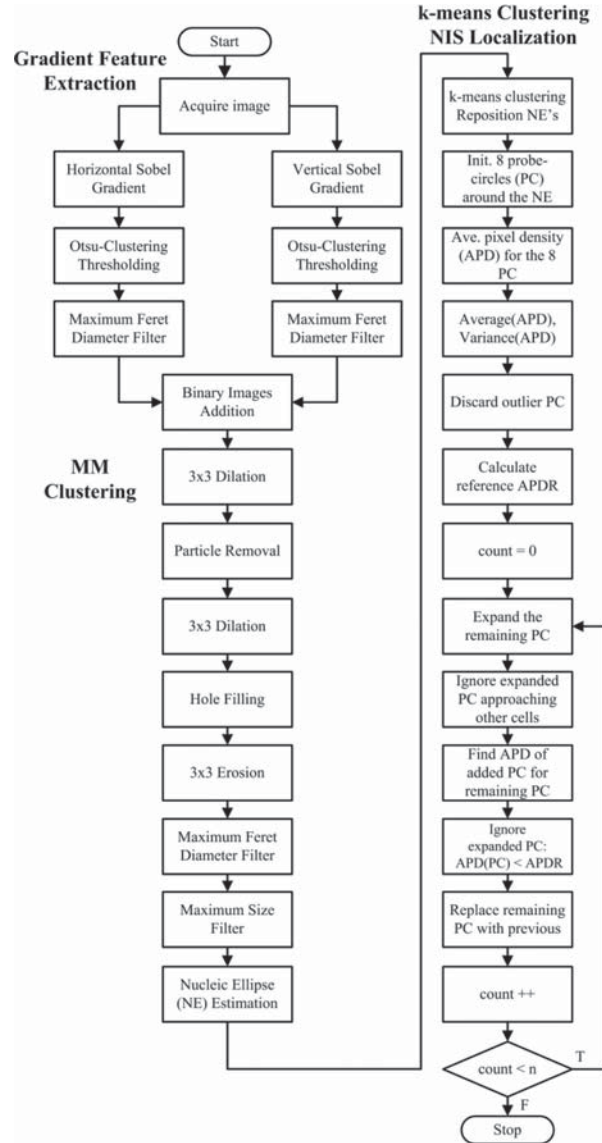


Fig. 2. Cell and SCE site localization. The gradient data associated with the nuclei and surrounding rough endoplasmic reticula in smoothed images is extracted and clustered to produce binary objects corresponding to each nucleus. Each binary object is then estimated with a nucleic ellipse (NE), and a k -means clustering algorithm iteratively repositions each NE until it encloses the nucleus. The final NE will be used to monitor the completion of SCE process, and its center may be selected as a nucleic SCE site. In the second stage, the Growing Circle Algorithm (GCA) uses a number of probe circles initiated around each NE to detect the cytoplasmic regions to the maximum extent possible. Upon completion of the GCA routine for each cell, the center of a probe circle that covers the thickest detected portion of the cytoplasm will be chosen as the cytoplasmic SCE site.

exploited in order to relocate the estimated nucleic ellipse in the image until \mathcal{R}_N enclosed the nucleus. Second, a modified region-growing algorithm called Growing Circles [19], used the results obtained during nucleic localization to localize the cell cytoplasm and determines a suitable SCE site over the cytoplasm

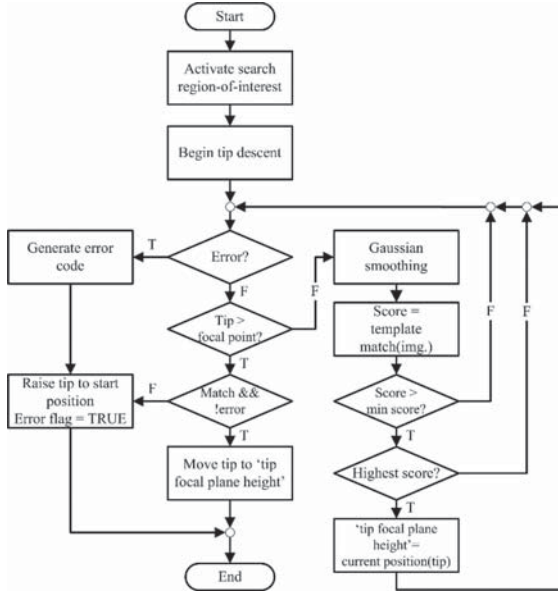


Fig. 3. Tip-template matching. Before the automation sequence begins, a microcapillary is attached to the platform for SCE. The tip is lowered to the focal plane and an image template is created and used for the duration of the automation. Prior to each tip-membrane approach, the tip is accurately located using template matching allowing placement of the tip on thin, cell features. The tip passes through the focal plane by several micrometers and template matching provides the highest correlation score obtained during the descent.

adjacent to the nucleus (i.e., cytoplasmic SCE site localization). Following localization of the cells and SCE sites, the cell is positioned $15 \mu\text{m}$ below the focal point [see Fig. 1(c)]. The tip descends to the focal point and was localized by using template-matching [see Fig. 3]. The SCE site on the localized cell is moved directly beneath the tip and ascends toward the tip at a constant velocity of $1 \mu\text{m/s}$.

Stage 2 (tip-membrane approach sequence): Early detection of tip-membrane contact is a critical requirement for avoiding damage to thin cell structures and to the microcapillary, thus high resolution, tip-membrane placement is a requirement. Tip-membrane contact is achieved by detecting an abrupt decrease in measurements of the current i_{cct} through the microcapillary electrode. $S(t)$ is a low amplitude, sinusoidal “sensing signal” [see Fig. 1(d)], set at a fixed frequency, f_s . $S(t)$ is generated within a circuit that includes the microcapillary electrode, the cell bath solution, a cell bath electrode, and analog and digital circuitry used to measure and amplify the signal. Inherent noise, within electrode-based and electromechanical environments cause i_{cct} to fluctuate randomly about the mean of, i_{cct} , μ_0 , which is relatively constant during the tip-membrane approach.

Data are acquired in the basic form of discrete measurements

$$x_k = \theta_k + e_k \quad (1)$$

where x_k , is the k th measurement that includes θ_k the desired signal and e_k is the noise signal. These measurements are as-

sumed to be a sequence of n independent and random variables $(x_k)_{1 \leq k < n}$ with a mean value, μ_i .

In this study, x_k represents i_{cct} , the current measured through the electrode and μ_i is calculated using the cumulative moving average

$$\mu_i = \frac{1}{k+1} \sum_{k=1}^n x_{k+1} \quad (2)$$

and updated after each sample, k . At the start of the tip-membrane approach sequence, the standard deviation of i_{cct} measurements, σ , is acquired, while the tip is in motion and well before tip-membrane contact occurs (i.e., while i_{cct} is relatively constant).

The standard deviation provides a measure of the SNR,

$$\text{SNR} = \frac{\mu_1 - \mu_0}{\sigma} \quad (3)$$

and defines the signal level required to discern a change beyond the noise about the mean, μ_0 . In this study, μ_0 is calculated as the average of the cumulative sum using (2). The residual (i.e., the difference between the measured data and the average), $x_k - \mu_i$, is normalized with σ ,

$$y_k = \frac{x_k - \mu_i}{\sigma} \quad (4)$$

then y_k is input to the double-sided, cumulative sum [20] or “cusum”—a statistical process control algorithm. The cusum defines two recursive statistics, C_k^+ and C_k^- as follows:

$$C_k^+ = \max [0, C_{k-1}^+ + y_k - \lambda] \quad (5)$$

$$C_k^- = \max [0, C_{k-1}^- - y_k - \lambda] \quad (6)$$

where λ is the slack variable. The value of C_k^+ or C_k^- increases when $y_k > \lambda$ or $-y_k > \lambda$, respectively. If an abrupt change in one direction occurs, an alarm d is signaled when either C_k^+ or C_k^- exceeds the threshold ν ,

$$d = \begin{cases} 0 & \text{if } C_k^+ < \nu \cap C_k^- < \nu \\ 1 & \text{if } C_k^+ \geq \nu \cup C_k^- \geq \nu. \end{cases} \quad (7)$$

A sharp decrease in i_{cct} is observed when tip-membrane contact occurs causing C_k^- to exceed ν signaling a tip-membrane contact condition. Should C_k^+ exceed ν , an alarm is activated indicating a faulty electrode or broken tip. The values of λ and ν are set relative to σ and are discussed in Section II-B. Greater detail on the tip-membrane approach sequence can be found in [18]. A full statistical analysis on the cusum and the parameters are discussed in [20]–[23].

Stage 3 (SCE): Following tip-membrane contact detection, a low duty-cycle, square wave pulse initiating SCE is activated. Fluorescent molecules enter the pores induced by SCE at lower potentials than for larger molecules (e.g., plasmid DNA) and serve as a mechanism to correlate the transmembrane transport of molecules. SCE event detection is monitored by analyzing changes in the relative fluorescent intensity within a bounded region \mathfrak{R}_B in the cell using machine vision [see Fig. 4].

The averaged fluorescent intensity I_k within \mathfrak{R}_B is acquired and compared to the background or initial average fluorescent

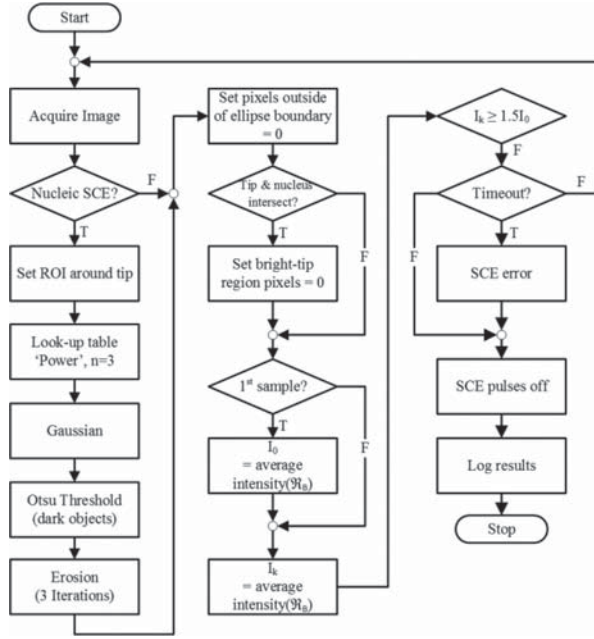


Fig. 4. SCE detection using visual feedback. Nucleic and cytoplasmic SCE are observed, while measuring increases in fluorescent intensity inside the cell during SCE pulses. If nucleic SCE is being performed, the image is applied to a power, lookup table to increase the pixel intensity of the fluorescing tip. This result provides a well-defined area where pixels are saturated due to the fluorescing tip. The tip region, \mathcal{R}_T , can then be removed from the nucleic ellipse, \mathcal{R}_N , using Otsu clustering where overlap of \mathcal{R}_T and \mathcal{R}_N occurs during nucleic SCE. In both cytoplasmic and nucleic SCE, measurements of the average fluorescent intensity, I_K , in \mathcal{R}_B can then be acquired and compared to the initial fluorescent intensity I_0 , measured at the beginning of the routine.

intensity I_0 measured prior to SCE. In addition, a SCE endpoint threshold set to $1.5I_0$ was used in this study. When I_k exceeds this threshold, a signal is issued indicating that SCE is complete. Relative fluorescence intensity measurements occur concurrently as SCE pulses are applied. Analyzing the increasing pixel average I_k during electroporative pulses within \mathcal{R}_B provides an indicator that SCE is occurring.

The nucleic and cytoplasmic SCE routines execute similarly with the exception of nucleic SCE, where the brightly fluorescing tip is excluded from fluorescence measurements. \mathcal{R}_B is represented by one of two bounded regions depending on the type of SCE site selected and are defined for cytoplasmic SCE sites [see Fig. 1(e)] by

$$\mathcal{R}_B = \mathcal{R}_N \quad (8)$$

where \mathcal{R}_N is the localized nucleus, and for nucleic SCE sites [see Fig. 1(f)] by

$$\mathcal{R}_B = \mathcal{R}_N \wedge \overline{\mathcal{R}_T} \quad (9)$$

where \mathcal{R}_T is the bounded region of the fluorescent tip. A rectangular, region of interest surrounding the location of the tip and the entire nucleic ellipse is applied to an exponential lookup table to increase the regions of high fluorescent intensity. The

resulting output was input to an Otsu threshold routine (i.e., clustering) to remove \mathcal{R}_T from \mathcal{R}_N and was followed by an erosion operation. This effectively reduces dispersion effects of the gradient between \mathcal{R}_T and \mathcal{R}_N effectively leaving the remainder of \mathcal{R}_N for analysis.

B. Tip-Membrane Approach and Cusum Initialization

Prior to routine operation, a system calibration routine was performed to estimate suitable values for the threshold ν and the slack variable λ . Adjustments to λ and ν affect the indentation depth of the tip and the cusum algorithm's sensitivity to noise. In general, decreasing λ reduces the indentation depth (i.e., number of samples) before tip-membrane contact detection, but increases the possibility of generating a false tip-membrane contact alarm. Increasing ν gradually increases the indentation depth before detecting tip-membrane contact. The value of σ is estimated at the beginning of each tip-membrane approach sequence.

Six calibration test-runs were performed. Each test-run consisted of executing the tip-membrane contact detection routine to collect i_{cct} data on sample cells with the exception that the tip indentation continued until tip-breakage occurred. Three test runs were executed with the center of the nucleic ellipse as the target and three test runs were performed with the cytoplasmic SCE site used as the target. Sequential i_{cct} data were collected during the approach sequence, during tip-membrane contact (i.e., abrupt decrease in i_{cct}), and during the tip-substrate contact (i.e., abrupt increase in i_{cct}). SCE was purposely omitted throughout these runs.

Following the calibration test runs, offline simulations were performed on the i_{cct} datasets. Each i_{cct} dataset was input to the cusum routine and an iterative routine, described in [18], which stepped through each pair of ν , and λ to evaluate where the cusum would signal an alarm condition. The parameter pairs of λ and ν varied over a wide range to determine suitable pairs for operational use. In this study, the range of values for λ and ν was—[0.1, 30]

After each pair was tested by the iterative routine, a contour plot (i.e., performance surface) was generated using the indentation distances over the λ - ν parameter space. Lower indentation values were generated directly after tip-membrane contact first occurred (i.e., transition from the constant i_{cct} to the abrupt decrease of i_{cct}) and before the tip contacted the substrate (i.e., before the abrupt increase in i_{cct}). Pairs that caused a false tip-membrane contact detection, pairs that failed to detect contact before the tip contacted the substrate, or pairs that did not detect contact at all were assigned a high indentation value to indicate unsuitable parameters. In this study, a value of $20 \mu\text{m}$ was assigned to these pairs, which is greater than twice the average height of the cells measured [18]. The three runs of each group were averaged producing two contour plots—one for the nucleic runs and the other for the cytoplasmic runs shown in Fig. 5(a) and (b), respectively. In this study, parameters for operational use were selected such that the indentation was approximately $1.5 \mu\text{m}$ in depth ($\lambda = 20$, $\nu = 4$).

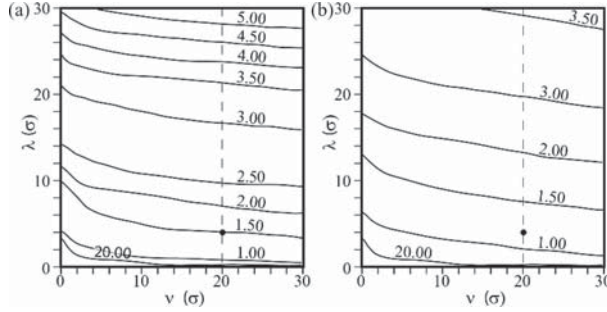


Fig. 5. Performance surface plots generated for the tip-membrane calibration runs. (a) Surface generated for nucleic and (b) cytoplasmic SCE sites. Each plot was generated using the i_{cct} data during three tip-membrane approach sequences. Each set of i_{cct} data is tested once for each pair of parameters (ν, λ) during an offline analysis producing an estimated indentation depth. Plotting the indentation depths over the range of parameters produced a performance surface allowing the selection of suitable system parameters for use. In this study, parameters were chosen such that the tip indentation was approximately $1.5 \mu\text{m}$ ($\nu = 20, \lambda = 4$). Contour units are in μm .

C. Experimental SCE Parameters

The automated routine was validated using two sets of parameters for nucleic and cytoplasmic SCE. A pulse width of 1 ms was used in all sets. Two pulse frequencies, 10 and 40 Hz were used in combination with an SCE pulse potential, V_{SCE} , of -6 and -10 V for nucleic SCE. These parameters have been demonstrated using manual methods of SCE [3]; however, the SCE site in [3] was not specified. For cytoplasmic SCE, only a V_{SCE} of -6 V was used as high potentials and high frequencies adversely affected the NIH/3T3 cells (e.g., -10 V and 40 Hz). A complete analysis relating the efficiency of the SCE parameters, SCE site location, and uptake of electroporated molecules were not the focus of this study.

D. SCE Biomanipulator Platform

The custom platform [see Fig. 6(a)] consisted of an X, Y , and Z linear, direct-drive platform (ALS 1000, Aerotech, Inc.). Each stage was powered by an Aerotech BA-10 amplifier and submicrometer precision was obtained using MXH-500 high-resolution, encoder signal multipliers. Aerotech drivers were interfaced to a National Instruments (NI) NI-7358 and two NI UMI-7774 interfaces. Software control of the motors was performed using the LabVIEW Motion API.

A custom optical train integrating Nikon CFI-60 and DIC elements consisted of a 40X, extra-long working distance objective. Fluorescence observation was performed using epifluorescence illumination with a red filter (Chroma Technology Corp. 49008/ET-Texas Red) for the dsRed and green filter (Chroma Technology Corp. 49002/ET-GFP) for the Alexa Fluor 488, respectively. All images were captured using a 12-bit CCD camera (Retiga, QImaging) at a maximum rate of 10 frames/s using two-times binning.

E. System Control Architecture

The system control software was structured using supervisory control with the automation core designed as a queued state-machine [see Fig. 6(b)] using LabVIEW 2011. Submodules were used to collect data from independent peripherals and execute low-level processing. Information compiled by the submodules was returned to and was collectively processed by the supervisory module. Data transfer latency between the submodules and the supervisory module and the time of the data spent in the queue was negligible.

F. SCE Module

The SCE module is an embedded system designed to generate signals, acquire i_{cct} measurements indicating tip-membrane proximity, and deliver electroporative pulses to induce SCE. The SCE module is comprised of three submodules including the signal generator, the data acquisition module (DAQ), and the data processing module which is integrated into the supervisory module. Signal acquisition and signal generation occurred near the microcapillary. The block diagram is shown integrated into the system control architecture in Fig. 6(b).

A digital signal processor (DSP, Microchip dsPIC 30f3013, Microchip Technology) and LabVIEW coordinated using serial, asynchronous communications at 19.2 kb/s. Signal generation was completed by the DSP, which sent 16-bit words, representing the voltage, to a 16-bit digital-to-analog converter (DAC, Analog Devices AD660) over an 8-bit bus. The DAC output a signal of up to ± 10 V and was amplified by 1.8 times providing a maximum amplitude pulse of ± 17.3 V to the electrode. Hardware filters were avoided to maintain a wide bandwidth reducing pulse signal distortion.

Two signals were generated during the automated sequence. During the tip-membrane approach sequence, $S(t)$ was generated with a peak amplitude, A_0 , of $0.3 V_p$ and at a frequency f_s of 186 Hz. Following tip-membrane contact detection, a unipolar, rectangular wave pulse at a potential of V_{SCE} was activated in order to induce SCE. The low potential sensing signal was applied intermittently between pulses to acquire measurements of i_{cct} during SCE by combining the two signals at the output.

The sensing signal and the pulses for inducing electroporation were output from the DAC to a discrete network of amplifiers in a current-to-voltage (C2V) configuration, and provided a measure of i_{cct} through the electrode. The output of the instrumentation amplifier was reduced to a maximum ± 10 V and was sampled by a NI USB-6009 DAQ at 44 kHz.

Raw data samples of the sinusoidal signal were transferred to LabVIEW in 712 sample windows and were analyzed using the discrete Fourier transform (DFT). The resulting i_{cct} amplitude of the sinusoidal signal, representing x_k in (1), was conveniently isolated on the frequency spectrum at f_s using the DFT. The value of u_0 was updated in (2). x_k was normalized with σ in (4) and output at a rate of 25 Hz to the cusum in (5) and (6), while checking for alarm conditions in (7).

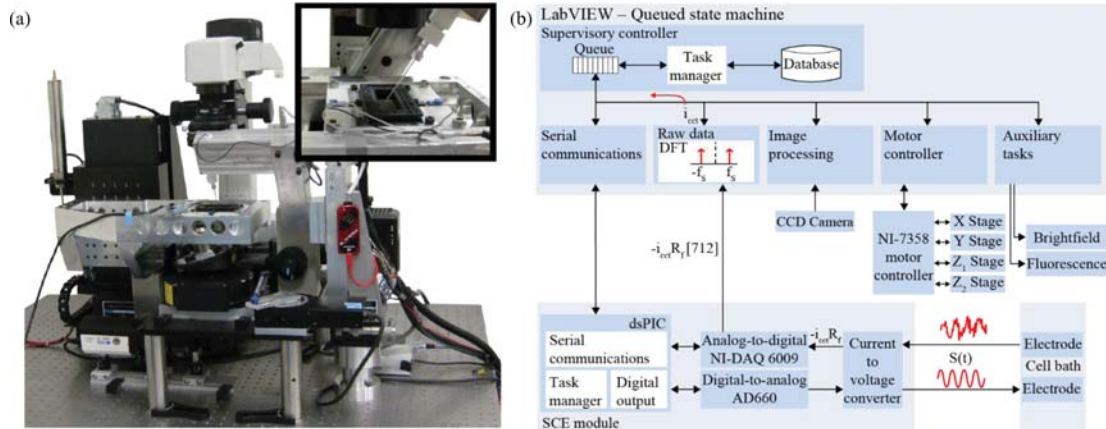


Fig. 6. SCE biomanipulator. (a) Biomanipulator used during experimentation to conduct automated SCE. (inset) A view of the cell chamber and the microcapillary used for SCE during the automated routine. (b) Hardware and software system block diagram.

G. Microcapillaries and Microelectrodes for SCE

Microcapillaries were fabricated on a Flaming/Brown P-97, using fire polished microcapillaries (Sutter BF150-110-10) and the “bee-stinger” protocol [24]. Microcapillaries were backfilled with a 4 μL solution containing 63 $\text{ng}/\mu\text{L}$ dsRed plasmid [25], 150 mM KCl, and 3.8 mM Alexa Fluor 488.

The electrode was fashioned by immersing 0.25-mm diameter silver wire (64-1319, Harvard Apparatus) in bleach for 30 min until an even coating of silver-chloride coated the bare wire. This wire was cleaned with 70% EtOH, washed with distilled water, and allowed to dry. The microcapillary was inserted in an electrode holder (1-HL-U, Molecular Devices) and the tip of the wire was immersed beyond 2 mm of solution from the end of the microcapillary. The electrode assembly was then inserted on the SCE module. After experimentation, the electrode wires were sufficiently rinsed with 70% EtOH followed by distilled water and allowed to dry.

H. Cell and Reagent Preparation

NIH/3T3 cells (ATCC #CRL-1658) were cultured in alpha Modified Eagle Medium (α -MEM, Invitrogen, 32571-028) supplemented with 10% fetal bovine serum (FBS, Invitrogen, 16000-036) and 1% Penicillin–Streptomycin (Invitrogen, 15140-122).

For the purpose of experiments and to achieve high-resolution imaging, the cells were prepared and cultured in a coverslip bottom, cell chamber [Quorum Technologies, Chamlyde, WL-2460-1, Fig. 6(a, inset)]. The complete cell chamber assembly, including a No. 1.5, 24 \times 60 mm coverslip (VWR, CA48383-252-1), were autoclaved prior to use. Cells were cultured in 100 mm Petri dishes for 72 h. At 90% confluence, the cells were rinsed with phosphate buffered saline (PBS) and treated with 0.4 mL of 0.25% Trypsin-EDTA for 1 min in 37 $^{\circ}\text{C}$. After detachment, the cells were diluted by culture media to 8 mL. The concentration of the diluted cell solution was further reduced by addition of the culture media in a 1:10 volumetric ratio. The final cell solution was added to the cell chambers and incubated for

24 h prior to experimentation. Following the incubation period, the cells were rinsed three times with PBS followed by adding fresh media (Invitrogen, 41061-029—no phenol red). The cells were placed back in the incubator for 3 h prior to experimentation. Following the incubation period, a cell chamber was placed on a custom cell heater on the robotic platform. A dual temperature controller (Warner Instruments, TC-344B) was connected to the cell heater maintaining the temperature at 37 $^{\circ}\text{C}$. Cells remained viable for durations greater than 30 min; however, were kept outside the incubator for no longer than 20 min at a time. 10–15 cells were processed during each round of experimentation and were incubated for 24 h prior to inspection.

III. RESULTS

The automated SCE sequence was completed for 200 nucleic SCE and 100 cytoplasmic SCE runs. Examples of data acquired during automation of each type of sequence are shown in Fig. 7. A video demonstration is also provided and shows several cells and SCE sites being localized and then processed using the automated routine (Video 1—supplementary information).

In Fig. 7(a), a localized cell selected for nucleic SCE during *Stage 1*, is shown in *Image i*. The initial localized nucleic ellipse is shown as a green outline around the nucleus. During the tip-membrane approach sequence [see Fig. 7(a)] of *Stage 2*, i_{cct} measurements were constant until the tip-membrane contact was detected (*Image ii*) after approximately 1.3 μm of indentation. An abrupt increase in C_k^- can be seen in Fig. 7(b) as i_{cct} samples decreased in value during contact. At that moment, epifluorescent illumination was activated (see *Image iii*) and the bright fluorescing tip region \mathfrak{R}_T was removed from \mathfrak{R}_N allowing increases in fluorescing intensity to be monitored in \mathfrak{R}_B during SCE. During the SCE pulses in *Stage 3*, relative measurements of the fluorescent intensity within the nucleus increased linearly [see Fig. 7(c)] to the threshold, $1.5I_0$ ending SCE pulses. The change in fluorescent intensity can be observed in coarse pixel plots before SCE pulses begin (see *Image iv*) and directly before SCE pulses end (see *Image v*). The minimum intensity in the 8-bit images is 0 (dark blue) and the maximum pixel intensity

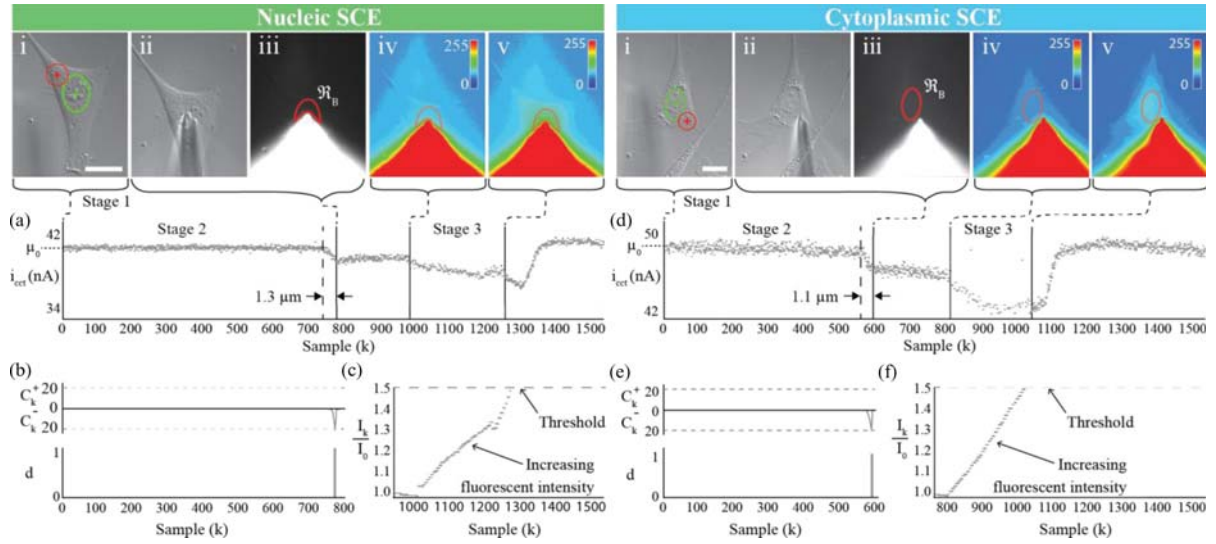


Fig. 7. Examples of the automation SCE sequence. During *Stage 1* nucleic and cytoplasmic SCE sites are localized in *Image i*. (a) i_{cet} samples are shown during the tip-membrane approach sequence (*Stage 2*). (b) During tip-membrane contact, shown in *Image ii*, i_{cet} samples, in (a), decreased from the average current, μ_0 and the negative cusum exceeded the threshold signaling an alarm, *d*, after an estimated indentation of $1.3 \mu\text{m}$. Epifluorescent illumination was activated in *Image iii* and the average fluorescent intensity in \mathfrak{R}_B was measured during SCE pulses. (c) During SCE pulses, relative fluorescence measurements, I_k/I_0 , increased in a linear fashion until the fluorescence intensity reached $1.5 I_0$. Coarse pixel intensity plots are shown in *Image iv*, before pulses began, and in *Image v*, immediately before pulses ended. Similar results are seen for cytoplasmic SCE in (d–f).

TABLE I
TIP-MEMBRANE CONTACT AND FLUORESCENT DYE DETECTION
SUCCESS RATIOS

SCE Site	Tip-membrane contact		Fluorescent dye detection	
	N	Tip-membrane contact success %	N	Fluorescent dye detection success %
Nuc	200	98.5	197	96.5
Cyto	100	99.0	99	86.9

is 255 (red). Following SCE, in *Stage 3*, the tip is raised and i_{cet} returns to the level at the onset of *Stage 2*. Similar data from a sequence for cytoplasmic SCE are shown in Fig. 7(d–f). In Video 2 (supplementary information), the SCE sequences are shown for the nucleic and cytoplasmic SCE datasets from Fig. 7.

In all cells localized for both nucleic and cytoplasmic SCE, tip-membrane contact detection was successful without tip-breakage and 98.8% successful in tip-membrane placement ($N = 300$)—failed runs occurred due to pierced cells and pierced cells exhibited dye immediately prior to SCE pulses (see Table I). The processing time for each run was an average of 81 s per cell. During the tip-membrane placement routine, the average σ measured was 0.44 nA ($SD = 0.38 \text{ nA}$, $N = 300$) and the average i_{cet} measured at the beginning of the run was 39.9 nA ($SD = 10.6 \text{ nA}$, $N = 300$). A total of 24 microcapillaries were used and fabricated using identical “pulling” parameters [24].

When the microcapillary was placed over the nucleus, a success rate of 96.5% electroporation of the dye was achieved ($N = 200$) and was 19.0% successful at transfection and expression of plasmid DNA for all cells. However, when regions lateral to the nucleus are targeted (i.e., cytoplasmic sites), a success rate of 86.9% electroporation of the dye is achieved and no successful

TABLE II
DsRed TRANSFECTION RATIO 24 h AFTER SCE

Set	SCE Site	N	Pulse freq. (Hz)	V_{SCE} (V)	\bar{t}_{SCE} (s)	$t_{SCE} \text{ SD}$ (s)	dsRed %
1	Nuc	50	10	-6	11.1	9.0	10.0
2	Nuc	50	40	-6	4.6	4.8	44.0
3	Nuc	50	10	-10	5.3	3.0	2.0
4	Nuc	50	40	-10	2.1	6.1	20.0
5	Cyto	50	10	-6	14.1	9.2	0.0
6	Cyto	50	40	-6	11.6	8.8	0.0

transfection of plasmid DNA ($N = 100$). The average elapsed time during SCE pulses measured for I_k to reach $1.5I_0$ and the success ratio of detecting dsRed in cells following 24 h after SCE is \bar{t}_{SCE} and summarized in Table II for each parameter set.

A followup study was performed in the absence of viability data validating cytoplasmic SCE due to the lack of dsRed expression in all cells. Cytoplasmic SCE site sequences were repeated for 20 trials. Following cytoplasmic SCE, cells were monitored over a 24-h period and image data were acquired in 6 h intervals to ensure the viability and the continuity of the location of the cells [see Fig. 8]. Continuity of the cells’ location was observed by monitoring bright field images [see Fig. 8(a–e)] and fluorescent microscopy images of the fluorescent dye over a 24-h duration [see Fig. 8(f–i)]. Following the 24-h period, the media was replaced with media containing calcein-AM red. After incubating the cells in calcein-AM for 1 h in 37°C , the media was replaced with media without calcein-AM. The cells were then inspected using epifluorescent microscopy and cells fluorescing under a red filter indicated cell viability [see Fig. 8(j)]. For all cells, the average viability was 60% ($N = 20$)

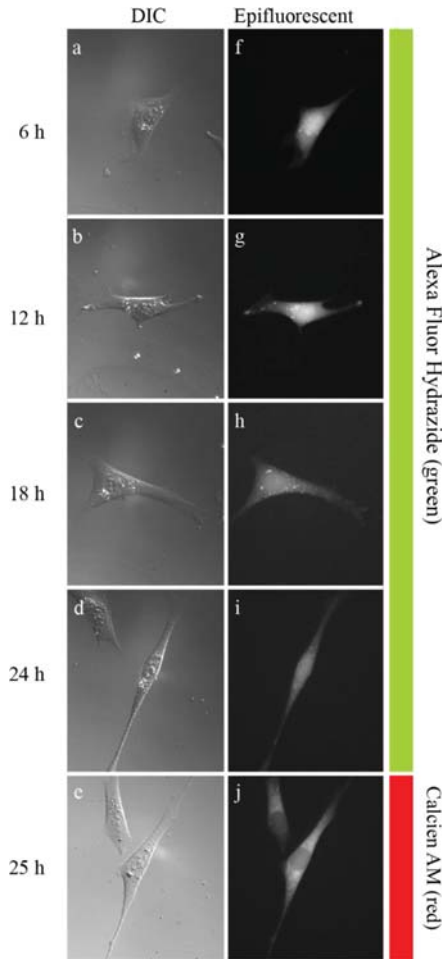


Fig. 8. Cytoplasmic SCE viability test. Viable cells, following cytoplasmic SCE, were observed over 25 h. An example of a cell targeted using cytoplasmic SCE is shown. Images collected using (a–e) DIC and (f–i) epifluorescent microscopy were collected in six h intervals. Green fluorescing dye is observed in the manipulated cell. (j) At 25 h, cells were exposed to calcein red. Viable cells were identified by continuous observation over 24 h and by observing calcein production in the cell after 1 h incubation in calcein AM.

TABLE III
VIABILITY ANALYSIS FOR CYTOPLASMIC SCE SITES

Set	SCE Site	N	Pulse freq. (Hz)	V_{SCE} (V)	\bar{t}_{SCE} (s)	t_{SCE} SD (s)	24-hr viable %
7	Cyto	10	10	-6	26.5	14.8	60.0
8	Cyto	10	40	-6	2.4	1.5	60.0

and for each parameter set the average viability was also 60% ($N = 10$ for each). The data are summarized in Table III.

IV. DISCUSSION AND FUTURE WORK

The system, methods, and instrumentation proposed in this study are intended to provide a seamless transition between the three, sequential stages of automated SCE including localization of cells and SCE sites, tip-membrane contact detection, and

SCE. Our method is capable of precise and repeatable targeting of thin, adherent cells for electroporation with an accuracy of nearly 100% success (see Table I). Our technology achieved new milestones in automated SCE.

Adherent cells less than $10 \mu\text{m}$ and SCE sites were localized using our machine vision algorithm described in [19]. Tip-membrane contact detection was executed using a statistical process control algorithm developed in [18] and visual feedback was implemented during nucleic and cytoplasmic SCE. In this discussion, we identify a site-specific dependence contributing to the success of SCE and identify areas of future work to improve the existing methods.

Targeted delivery of molecules, using SCE, is an effective means for conducting manipulation assays requiring greater access to cellular regions such as the nucleic and cytoplasmic SCE sites. However, little is known or has been reported on what region of the cell is best suited for SCE of macromolecules and specifically DNA of up to 14 kb/s [3]. When the microcapillary was placed over the nucleus, a success rate of 96.5% electroporation of the dye was achieved (see Table I) and was 19.0% successful at transfection of the plasmid DNA (see Table II) for all cells, which is similar to manual efficiencies [2], [3]. However, when regions lateral to the nucleus are targeted (i.e., cytoplasmic sites), a success rate of 86.9% electroporation of the dye is achieved and no successful electroporation of plasmid DNA ($n = 100$) was detected even though subsequent viability tests demonstrated 60% of the cells remained viable 24 h after SCE (see Table III). This demonstrates that the site placement of the microcapillary is a critical factor in successful SCE, and to the best of our knowledge, has not been previously reported in the literature.

Detecting tip-membrane contact is a critical event when processing thin cells to avoid rupturing the cells and breaking the microcapillary tip. At the beginning of each run, a measure of the noise σ was acquired relating noise levels to, λ and ν . As σ varies, the value of λ is scaled accordingly and is less susceptible to fluctuations in noise causing false contact detections. The residual, $x_k - \mu_0$, is normalized with σ , and samples must satisfy $y_k > \lambda$ or $-y_k > \lambda$ to increase C_k^+ or C_k^- , respectively. Variability in σ can influence the indentation distance (i.e., number of samples before the threshold is exceeded) as a low SNR will reduce the ability to discern a change from μ_0 . Greater control and system versatility could be achieved by implementing a control routine in response to variations in σ . Previous tip-membrane approach sequences, or simulated approach sequences based on a model of tip and membrane could be processed between runs to control the number of samples to achieve an alarm condition in response to variations in σ that occur. Performance surfaces, similar to those created during the calibration routine, could be generated or updated each sequence and incorporated with optimization routines to estimate more efficient parameters. Minor adjustments to λ and ν would be updated prior to the next run.

Differences in the compliance between cells and cell structures (e.g., nucleic and cytoplasmic SCE sites) could vary the rate of the formation of a seal. Thus, it is possible for variations between cells and cell lines to influence the tip-membrane

approach sequence. We tested our tip-membrane contact and SCE algorithm briefly on other cell lines including human breast cancer cells (MCF-7) and mouse neural blastoma cells (SH-SY5Y) with positive success. Although an extensive study was not performed, no significant differences were observed in comparison to NIH/3T3 cells during the tip-membrane contact algorithm or SCE while inserting fluorescing molecules. Establishing an electromechanical model of the seal created between a tip and a membrane would be a valuable contribution in future work for microcapillary-based, microelectrode methods of manipulation. This model could be experimentally verified using atomic force microscopy, and provide greater insight and to subtle differences encountered during the seal formation between cells, cell structures, and various cell lines.

Visual feedback was used during SCE which provided an effective indicator for SCE conditions and a suitable endpoint of the automated sequence. Where the light-collecting, capacity of the microscopy methods permits, future methods could visualize SCE using the molecules (e.g., DNA) attached directly to fluorescent molecules indicating SCE. Alternatively, conventional methods [2], [3] of SCE without visual indicators could be applied by modifying *Stage 3*, but lack visual feedback of molecules entering the cell and is nonspecific where the variability observed in $\overline{t_{SCE}}$ indicates SCE varies from cell to cell (see Tables II, and III).

The methods in this study were designed to manipulate thin, adhered cells, allowing cell analysis over extended durations. The utility of the system could be increased by adapting similar infrastructure such as holding microcapillaries [9] or mechanical restraints [10], [12] to restrain and manipulate suspended cells similar to sizes used in this study ($h_C < 10 \mu\text{m}$). Alternatively, chemical methods (e.g., Poly-D-lysine, Poly-L-lysine) may offer a simple method, where cells can be restrained sufficiently on conventional glass or plastic substrates.

V. CONCLUSION

SCE has the potential to drive single cell research where accuracy, repeatability, and higher-than-manual throughput are required. Our system provides a versatile, automated solution with capabilities of accurately localizing cytoplasmic or nucleic SCE sites on single cells and inserting exogenous molecules into cell features with micrometer thicknesses via SCE. Our system exceeded the throughput of manual SCE by reducing the cell processing rate to one-third (81 s/cell) in comparison to rates reported in the literature (e.g., 480 s/cell [5] and 240 s/cell [6]). In addition, we provided a visual feedback to monitor the progress of SCE and reported a site-specific dependence in the transfection ratio when targeting cytoplasmic SCE sites and nucleic SCE sites.

The instrumentation and methods described are intended to provide the framework for a powerful method of manipulation to the scientific community. The engineered architecture is intended as a significant stepping stone in the development of future designs to provide even greater capabilities and a broader selection of methods not achievable by manual processes. While a complete solution for automated SCE has been presented, it is

the opinion of the authors that the technology is only in its infancy and the true power of SCE has yet to be unleashed. Further optimization of our routines, and maturation of automated SCE in general, will inevitably improve the efficiency and latencies of cell-processing reported in this study.

REFERENCES

- [1] N. Blow, "Journeys across the membrane," *Nat. Methods*, vol. 6, no. 4, pp. 305–309, Apr. 2009.
- [2] K. Haas, W. C. Sin, A. Javaherian, Z. Li, and H. T. Cline, "Single-Cell electroporation for gene transfer *in vivo*," *Neuron*, vol. 29, no. 3, pp. 583–591, 2001.
- [3] J. Rae and R. Levis, "Single-cell electroporation," *Pflügers Arch.*, vol. 443, no. 4, pp. 664–670, Feb. 2002.
- [4] P. Lovell, S. H. Jezzini, and L. L. Moroz, "Electroporation of neurons and growth cones in *Aplysia Californica*," *J. Neurosci. Methods*, vol. 151, no. 2, pp. 114–120, Mar. 2006.
- [5] M. Wang, O. Orwar, and S. G. Weber, "Single-cell transfection by electroporation using an electrolyte/plasmid-filled capillary," *Anal. Chem.*, vol. 81, no. 10, pp. 4060–4067, May 2009.
- [6] M. Tanaka, Y. Yanagawa, and N. Hirashima, "Transfer of small interfering RNA by single-cell electroporation in cerebellar cell cultures," *J. Neurosci. Methods*, vol. 178, no. 1, pp. 80–86, 2009.
- [7] E. Neumann, S. Sakorin, and K. Toensing, "Fundamentals of electroporative delivery of drugs and genes," *Bioelectrochem. Bioenerg.*, vol. 48, no. 1, pp. 3–16, 1999.
- [8] K. Nolkranz, C. Farre, A. Brederlau, R. L. Karlsson, C. Brennan, P. S. Eriksson, S. G. Weber, and O. Orwar, "Electroporation of single cells and tissues with an electrolyte-filled capillary," *Anal. Chem.*, vol. 73, pp. 4469–4477, 2001.
- [9] Y. Sun and B. J. Nelson, "Biological cell injection using an autonomous microrobotic system," *Int. J. Robot. Res.*, vol. 21, no. 10/11, pp. 861–868, 2002.
- [10] H. Huang, D. Sun, J. K. Mills, and S. H. Cheng, "Integrated vision and force control in suspended cell injection system: Towards automatic batch biomanipulation," in *Proc. IEEE Conf. Robot. Autom.*, 2008, pp. 3413–3418.
- [11] Y. Xie, D. Sun, H. Y. G. Tse, C. Liu, and S. H. Cheng, "Force sensing and manipulation strategy in robot-assisted microinjection on zebrafish embryos," *IEEE Trans. Mechatronics*, vol. 16, no. 6, pp. 1002–1010, Dec. 2011.
- [12] W. Wang, X. Liu, D. Gelinas, B. Ciruna, and Y. Sun, "A fully automated robotic system for microinjection of zebrafish embryos," *Plos One*, vol. 2, no. 9, p. e862, Sep. 2007.
- [13] H. Huang, D. Sun, J. K. Mills, W. J. Li, and S. H. Cheng, "Visual-based impedance control of out-of-plane cell injection systems," *IEEE Trans. Autom. Sci. Eng.*, vol. 6, no. 3, pp. 565–571, Jul. 2009.
- [14] W. Wang, Y. Sun, M. Zhang, R. Anderson, L. Langille, and W. Chan, "A system for high-speed microinjection of adherent cells," *Rev. Sci. Instrum.*, vol. 79, no. 10, p. 104302, 2008.
- [15] C. Bae and P. Butler, "Automated single-cell electroporation," *BioTechniques*, vol. 41, no. 4, pp. 399–402, Oct. 2006.
- [16] P. Kallio, T. Ritala, M. Lukkari, and S. Kuikka, "Injection guidance system for cellular microinjections," *Int. J. Robot. Res.*, vol. 26, pp. 1303–1313, 2007.
- [17] K. Sakaki, N. Dechev, R. D. Burke, and E. J. Park, "Development of an autonomous biological cell manipulator with single-cell electroporation and visual servoing capabilities," *IEEE Trans. Biomed. Eng.*, vol. 56, no. 8, pp. 2064–2074, Aug. 2009.
- [18] K. Sakaki, H. Esmailsabzali, N. Dechev, R. D. Burke, and E. J. Park, "A generalized tip-membrane contact detection algorithm for automated single cell electroporation using statistical process control," *IEEE Trans. Autom. Sci. Eng.*, vol. 9, no. 2, pp. 226–236, Apr. 2012.
- [19] H. Esmailsabzali, K. Sakaki, N. Dechev, R. D. Burke, and E. J. Park, "Machine vision-based localization of nucleic and cytoplasmic injection sites on low-contrast adherent cells," *Med. Biol. Eng. Comput.*, vol. 50, no. 1, pp. 11–21, Sep. 2012.
- [20] E. S. Page, "Continuous inspection schemes," *Biometrika*, vol. 41, pp. 100–115, Jun. 1954.
- [21] M. Basseville and I. V. Nikiforov, *Detection of abrupt change theory and applications*. Englewood Cliffs, NJ, USA: Prentice-Hall, 1993.

- [22] J. O. Westgard, T. Groth, T. Aronsson, and C. H. De Verdier, "Combined Shewhart-cusum control chart for improved quality control in clinical chemistry," *Clin. Chem.*, vol. 23, no. 10, pp. 1881–1887, 1977.
- [23] D. C. Montgomery, *Introduction to Statistical Quality Control*, 4th ed. New York, NY, USA: Wiley, 2001.
- [24] *P-1000 & P-97 Pipette Cookbook 2011*. Sutter Instrument Company Novato, CA, USA, 2011.
- [25] R. E. Campbell, O. Tour, A. E. Palmer, P. A. Steinbach, G. S. Baird, D. A. Zacharias, and R. Y. Tsien, "A monomeric red fluorescent protein," *Proc. Natl. Acad. Sci.*, vol. 99, no. 12, pp. 7877–7882, 2002.



Kelly Sakaki (M'09) received the Telecommunications Engineering Technologist Diploma degree from the Northern Alberta Institute of Technology, Edmonton, AB, Canada, in 2001, the B.Eng. degree in computer systems engineering, and the M.A.Sc. degree in mechanical engineering from the University of Victoria, Victoria, BC, Canada in 2005 and 2007, respectively, and the Ph.D. degree in mechatronic systems engineering from the School of Engineering Science, Simon Fraser University, BC, Canada, in December 2012. He has recently joined the Brain Research Center

at the University of British Columbia, Vancouver, BC, Canada, as a Postdoctoral Fellow.

His research interests include automation, electrical and mechanical design, signal processing, and machine vision. He is currently investigating novel methods of single cell analysis and manipulation using robotics-assisted instrumentation, microfluidics and MEMS.



Hadi Esmailsabzali received the B.A.Sc. degree in biomedical engineering from the School of Medicine, Shahid Beheshti University of Medical Sciences, Tehran, Iran, in 2003 and the M.A.Sc. degree in control engineering from the School of Electrical Engineering, Iran University of Science and Technology, Tehran, Iran, in 2006. He is currently working toward the Ph.D. degree in mechatronic systems engineering from Simon Fraser University, BC, Canada.

His research interests include immunomagnetic cell manipulation, development of lab-on-a-chip bioMEMS for rare-cell detection, isolation, characterization and point-of-care testing devices, single-cell biomanipulation, and machine vision applied to these areas.



Shabnam Massah received the B.Sc. degree in cell and molecular biology (microbiology), from Azad University of Karaj, Karaj, Iran, in 2006. She is currently working toward the Ph.D. degree in the Faculty of Health Sciences, Simon Fraser University Burnaby, BC, Canada.

Her research interests include understanding the role of epigenetic modifications, specifically, DNA methylation in regulation of gene expression. She is also interested in identification of molecules that can interpret or sense chromatin modifications, and maintain the normal or disease-related gene expression profiles.



Gratien G. Prefontaine received the B.Sc. degree, the M.Sc. degree and the Ph.D. degree in biochemistry in 1993, 1996, and 2001, respectively, all from the University of Ottawa, Ottawa, ON, Canada.

From 2001 to 2008, he was engaged in Postdoctoral Research Training at the University of California, San Diego, USA, and he became an Assistant Project Scientist in 2007. He is currently an Assistant Professor in the Faculty of Health Sciences, Simon Fraser University Burnaby, BC, Canada, and he is also an Associate Member in the Faculty of Science,

Departments of Molecular Biology and Biochemistry as well as Biological Sciences. His research interests include gene regulation, DNA methylation, DNA pyrosequencing, microarray technology, bacterial artificial chromosome recombination technology, and developmental biology.



Nikolai Dechev (M'04) received the B.A.Sc., M.A.Sc., and the Ph.D. degrees in 2004, all from the Department of Mechanical Engineering, University of Toronto, Toronto, Canada, in 1996, 1999, and 2004, respectively.

He is currently an Associate Professor in Mechanical Engineering at the University of Victoria, Victoria, BC, Canada. His research interests include biomedical systems design in the areas of advanced hand prosthesis, implantable sensors and prosthesis control, MEMS sensors, and robotic micromanipulation and automation technologies for MEMS and biological cells.

Dr. Dechev is a Member of the ASME.



Robert D. Burke received the B.Sc. (Hons.) degree, and the Ph.D. degree in 1978, both from the University of Alberta, Edmonton, Canada, in 1974 and 1978, respectively.

He has been at the University of Victoria, Victoria, BC, Canada since 1980, and is currently the Chair of the Department of Biochemistry and Microbiology. His research interests include cellular and developmental biology. He has published more than 100 journal papers in these areas.



Edward J. Park (M'03) received the B.A.Sc. degree from the University of British Columbia, Vancouver, BC, Canada, and the M.A.Sc. and the Ph.D. degrees from the University of Toronto, Toronto, Canada, in 1996, 1999, and 2003, respectively, all in mechanical engineering.

Previously, he was an Assistant Professor at the Department of Mechanical Engineering, University of Victoria, Victoria, BC, Canada, from 2003 to 2008. He is currently an Associate Professor of the School of Mechatronic Systems Engineering at the Simon Fraser University, Surrey, BC, Canada, and the Director of the Biomechatronic Systems Laboratory. He is also an Associate Member of the Faculty of Health Sciences. He has authored/coauthored more than 80 journal and conference papers in these areas. His current research interests include biomechanics and biomedical technologies for life sciences, rehabilitation and medicine, and mechatronics applied to next generation vehicular, robotic, and space systems.

Appendix C.

COMOSL CFD Optimization of the Microfluidic Manifold Structure

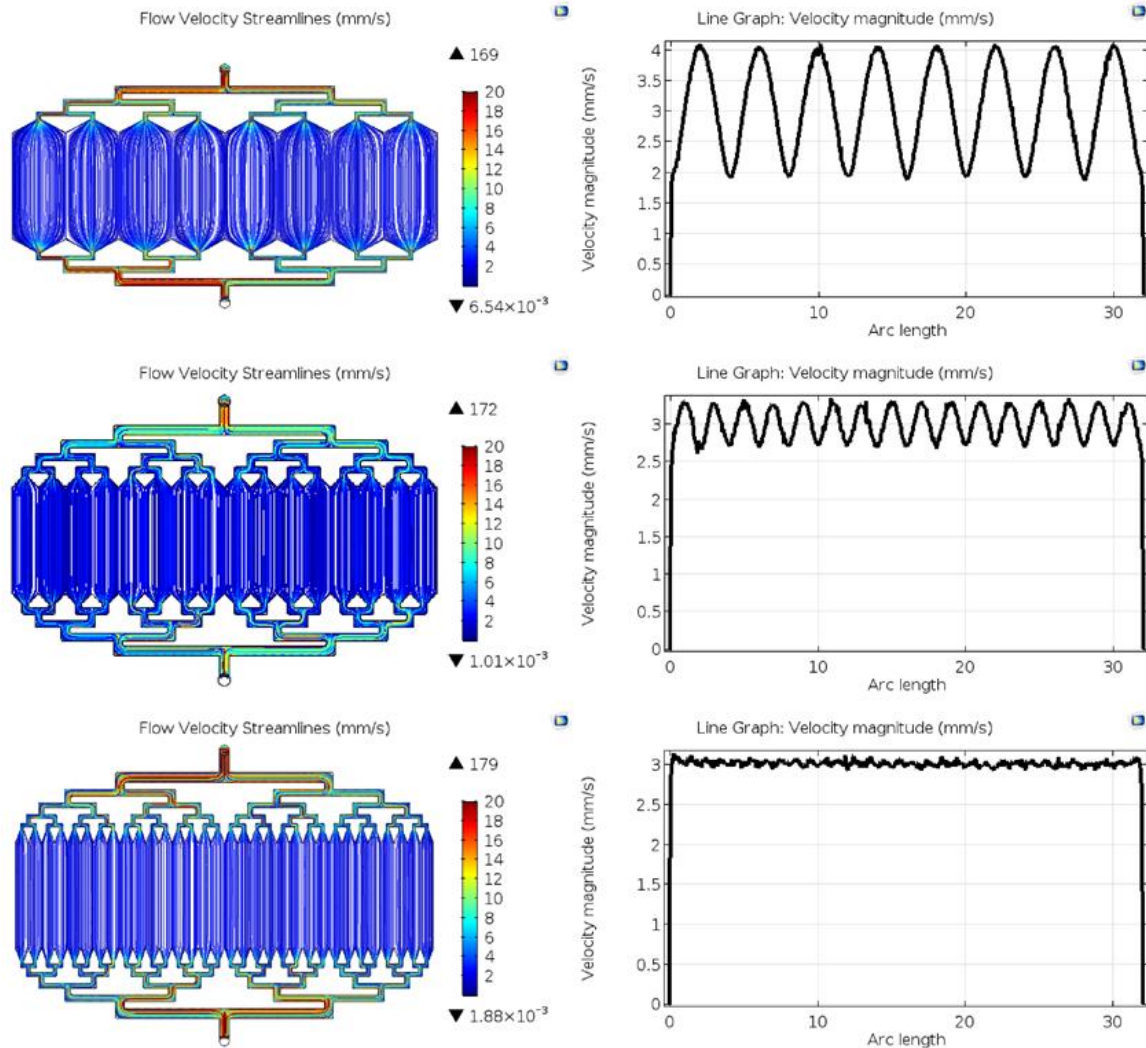


Figure C.1. The effect of the number of diffusers used to feed the microchamber on the flow uniformity. On each row, the left plot shows flow velocity streamlines while the right plot depicts the flow velocity as measured 500 μm below the diffusers across the width of microchambers (32 mm in this case). As it is evident, increasing the number of diffusers improves the flow uniformity.

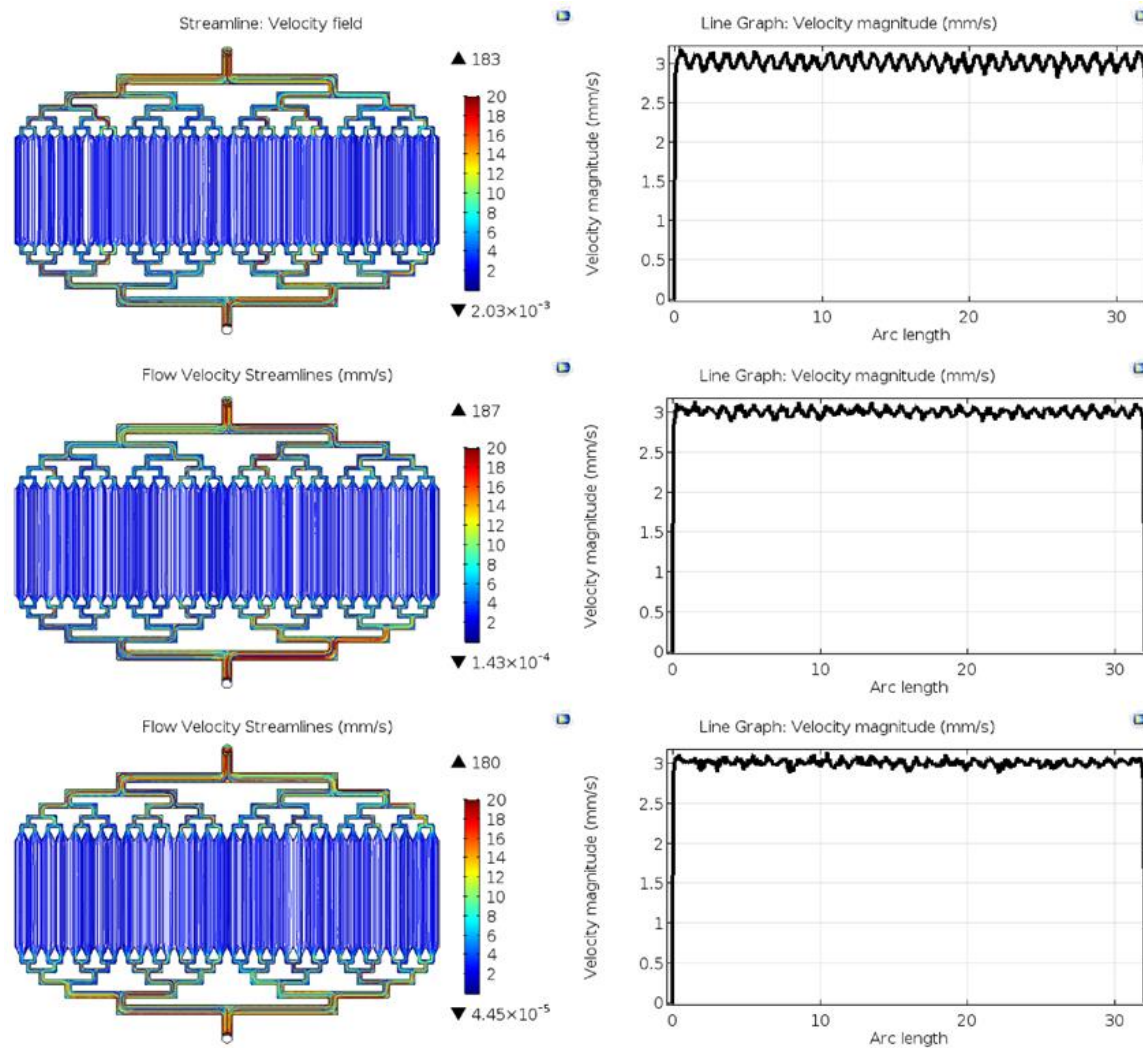


Figure C.2.A. The effect of the length of diffusers used to feed the microchamber on the flow uniformity. On each row, the left plot shows flow velocity streamlines while the left plot depicts the flow velocity as measured 500 μm below the diffusers across the width of microchambers (32 mm in this case). Top row: 250- μm -long diffusers; flow velocity SD: $\pm 6.49\%$. Middle row: 500- μm -long diffusers; flow velocity SD: $\pm 6.41\%$. Bottom row: 750- μm -long diffusers; flow velocity SD: $\pm 6.14\%$.

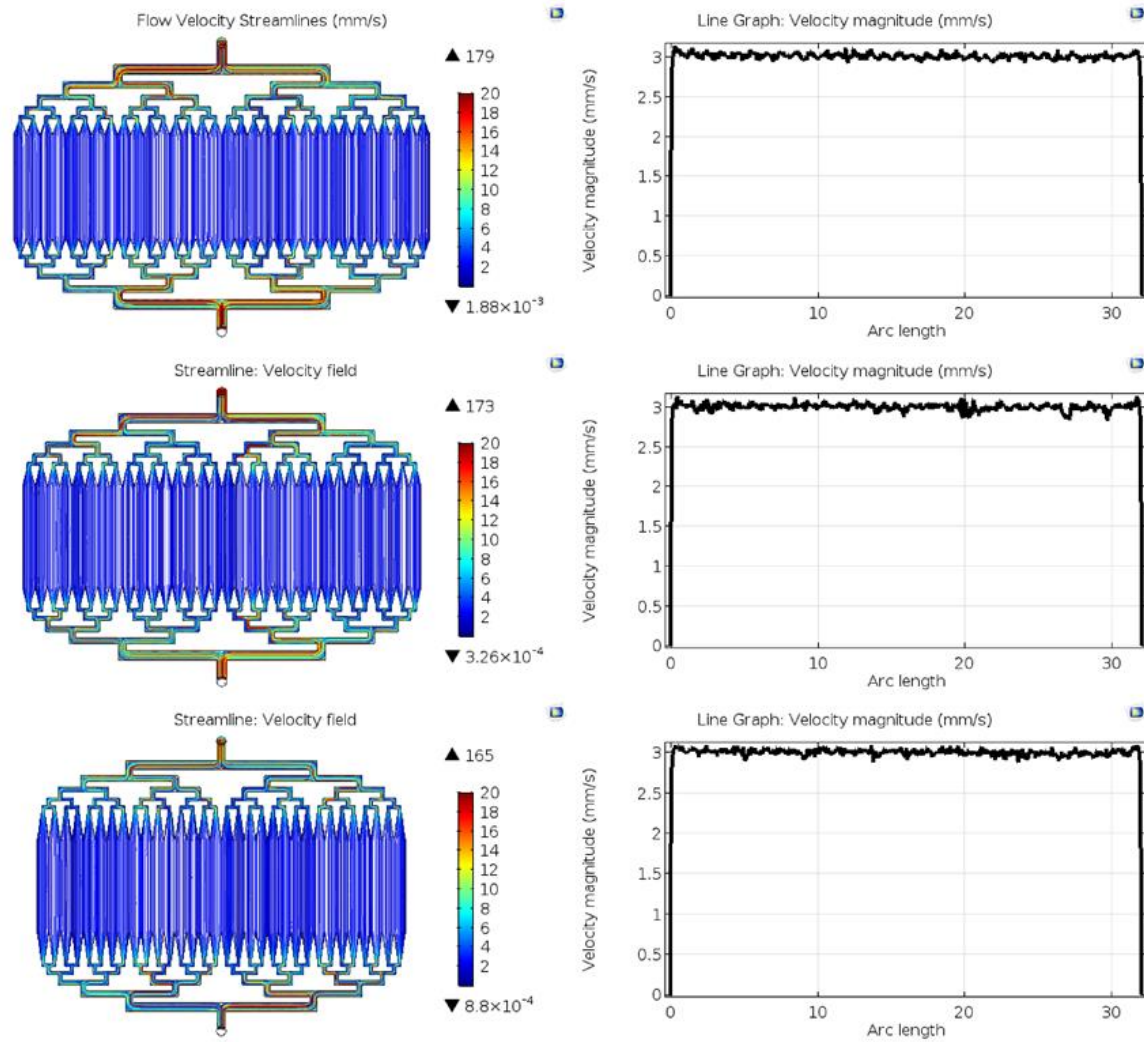


Figure C.2.B. The effect of the length of diffusers used to feed the microchamber on the flow uniformity. On each row, the left plot shows flow velocity streamlines while the left plot depicts the flow velocity as measured 500 μm below the diffusers across the width of microchambers (32 mm in this case). Top row: 1-mm-long diffusers; flow velocity SD: $\pm 6.15\%$. Middle row: 1.5-mm-long diffusers; flow velocity SD: $\pm 6.09\%$. Bottom row: 2.5-mm-long diffusers; flow velocity SD: $\pm 5.90\%$.